ISBN 978-82-326-5540-3 (printed ver.)
ISBN 978-82-326-6764-2 (electronic ver.)
ISSN 1503-8181 (printed ver.)
ISSN 2703-8084 (electronic ver.)

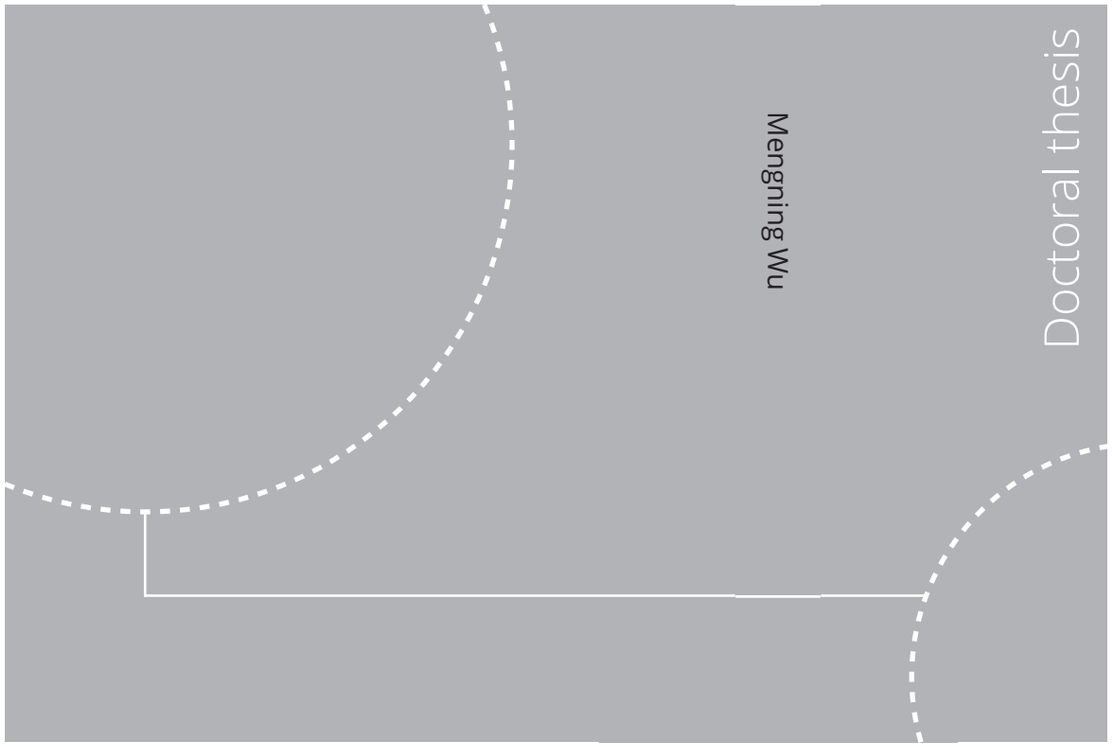

Doctoral theses at NTNU, 2021:325

Mengning Wu

Uncertainty of Machine Learning-Based Methods for Wave Forecast and its Effect on Installation of Offshore Wind Turbines

NTNU
Norwegian University of
Science and Technology

Doctoral theses at NTNU, 2021:325

NTNU
Norwegian University of Science and Technology
Thesis for the degree of Philosophiae Doctor
Faculty of Engineering
Department of Marine Technology

NTNU
Norwegian University of
Science and Technology

Mengning Wu

Uncertainty of Machine Learning-Based Methods for Wave Forecast and its Effect on Installation of Offshore Wind Turbines

Thesis for the degree of Philosophiae Doctor

Trondheim, October 2021

Norwegian University of Science and Technology
Faculty of Engineering
Department of Marine Technology

NTNU
Norwegian University of
Science and Technology

NTNU
Norwegian University of Science and Technology

Thesis for the degree of Philosophiae Doctor

Faculty of Engineering
Department of Marine Technology

ISBN 978-82-326-5540-3 (printed ver.)
ISBN 978-82-326-6764-2 (electronic ver.)
ISSN 1503-8181 (printed ver.)
ISSN 2703-8084 (electronic ver.)

Doctoral theses at NTNU, 2021:325

PRINTED IN NORWAY
NO - 1598

NORDIC SWAN ECOLABEL
Printed matter
2041 0731

Printed by Skipnes Kommunikasjon AS

Abstract

Marine operations, such as offshore lifting and mating, are complex and highly weather-sensitive. When planning these weather-restricted operations, it is necessary to determine the operational limits in terms of sea state variables (i.e., allowable sea states) of the system used in operations. During the execution phase, the allowable sea states could be compared with weather forecasts to decide whether the operation should start or not. In order to do this, it is important to make short-term forecasts of wave conditions that are characterized by significant wave height H_s, peak wave period T_p and so on. Given that there is inherent uncertainty in weather forecasts, how to quantify the forecast uncertainty and reflect it when planning and executing marine operations thus become a key issue.

This thesis first addresses the multi-step-ahead wave forecasting by using machine learning-based methods. Different time series-based machine learning (TSML) methods are developed and established, which rely on correlations between data in time series and consist of different pre-processing techniques, data-driven models and multi-step-ahead strategies. In addition to the TSML method, a new efficient and reliable forecasting method, called the physics-based machine learning (PBML) method is proposed by combining the characteristics of physics-based wave models with machine learning techniques. In the PBML model, physical knowledge from physics-based wave models is utilized as a guide for designing inputs and outputs, and machine learning algorithm is adopted to learn the implicit relationships between them.

These machine learning-based methods are employed to forecast one-day-ahead H_s and T_p at the central part of the North Sea. Uncertainty quantification analysis is carried out to evaluate and compare the forecast performance of different methods. This is done by calculating conventional error measures such as RMSE and carrying out statistical analysis of a pre-defined forecast error factor. Results demonstrate the feasibility of applying machine learning algorithms to forecast wave conditions. However,

the forecast uncertainty of TSML methods generally increases with the forecast horizon. Since the data correlation in time series of sea state variables decreases significantly with the time interval increases, it is difficult to deal with this phenomenon, whether by changing data-driven models or developing more complex TSML methods. By comparison, due to the consideration of physical meaning, the PBML method can generate more accurate wave forecasts in the whole forecast horizon and the forecast uncertainties are quite low. Due to the high forecast performance and low computational cost, the PBML method can be conceived as an efficient tool for wave forecasting.

Then the effect of weather forecast uncertainty on marine operations is investigated. In the thesis, a methodology is proposed to assess the allowable sea states for marine operations, with emphasis on considering weather forecast uncertainty. It consists of uncertainty quantification of weather forecasts, statistical analysis of system dynamic responses of coupled system for marine operations and allowable sea states assessment by means of response-based criteria. Based on the methodology, a new response-based alpha-factor α_R is derived. This is similar to the α-factor proposed by DNV, but it accounts for the effect of forecast uncertainties of both H_s and T_p on the dynamic response of operations. The α_R is defined from the perspective of dynamic response during operation, and depends on the type and duration of marine operations, the characteristics of dynamic system, the weather forecasting method, etc. By applying the α_R, allowable sea states in terms of H_s and T_p for the operation can be assessed, taking into account the weather forecast uncertainty at different lead times.

Finally, the proposed methodology is applied to the blade installation of offshore wind turbines as a case study. The final mating phase between the blade root and hub is considered and the crane tip motion, blade root radial motion and velocity are regarded as the limiting response parameters to illustrate the usage of the methodology in frequency- and time-domain, respectively. The α_R factors for each limiting parameter are established separately in terms of sea state scenarios and forecast lead times. The corresponding allowable sea states are then assessed. It is found that there is a significant difference between the allowable sea states with and without considering weather forecast uncertainty and forecast uncertainties in both H_s and T_p have important contributions to it. If weather forecast uncertainties are not included, the allowable sea states would be over-estimated. As the forecast lead time increases, the allowable sea states gradually decrease.

In summary, the original contributions of this thesis include the establishment and development of machine learning-based forecasting methods

for wave forecast, the quantification analysis of weather forecast uncertainties, and the development of a methodology for assessment of allowable sea states for marine operations including the effect of weather forecast uncertainty. These are meaningful and have great potential applications in marine operations, which can assist decision-making in the execution phase.

Preface

This thesis is submitted to the Norwegian University of Science and Technology (NTNU) for partial fulfillment of the requirements for the degree of philosophiae doctor.

This doctoral work has been performed at Department of Marine Technology, NTNU, Trondheim. Professor Zhen Gao from Department of Marine Technology, NTNU is the main supervisor. Professor Sverre Haver from Department of Mechanical and Structural Engineering and Materials Science, UiS as well as Senior Research Scientist Christos Stefanakos from Department of Environment and New Resources, SINTEF Ocean are the co-supervisors.

Acknowledgment

I would like to express my sincere gratitude to my main supervisor Professor Zhen Gao for giving me the opportunity to carry out my Ph.D. research work at the Department of Marine Technology, NTNU. For a new research field, he could always provide valuable and enlightening suggestions. Without his guidance and support for the development of my work, this Ph.D. would not have been achievable.

I would like to extend my gratitude to my co-supervisor Professor Sverre Haver. His expertise, wisdom, advice and positive energy played a key role and helped me get through the situations when the spirits were low. I am also extremely grateful to Senior Research Scientist Christos Stefanakos, from SINTEF Ocean. Involving him as my co-supervisor is definitely the perfect starting point for my PhD research. He generously shared his expertise and provided me with a lot of help and inspiration for entering the new field. It has been nice working with my three supervisors and a great experience in my academic life.

Many thanks to Dr. Yuna Zhao for her great collaboration and kind explanation when I was struck with software. Many thanks to Prof. Zhengshun Cheng and Prof. Wei Chai for their valuable suggestions when I encountered academic problems. I would also like to appreciate the time and work of my thesis committee members: Prof. Carlos Guedes Soares, Dr. Elzbieta Bitner Gregersen and Prof. Bernt J. Leira.

Thanks to all my dear friends and colleagues at the Department of Marine Technology for making this long study a fun and pleasant experience. All the support and memory have become the highlights of my life.

Finally, I want to express my deep gratitude to my parents and boyfriend. Your love and understanding mean everything to me.

Mengning Wu
October 2021
Trondheim, Norway

List of published Papers

Paper 1:
Prediction of short-term wind and wave conditions for marine operations using a multi-step-ahead decomposition-ANFIS model and quantification of its uncertainty.
Authors: Mengning Wu, Christos Stefanakos, Zhen Gao, Sverre Haver
Published in *Ocean Engineering* 2019, Vol. 188, pp. 106300.

Paper 2:
Multi-step-ahead forecasting of wave conditions based on a physics-based machine learning (PBML) model for marine operations.
Authors: Mengning Wu, Christos Stefanakos, Zhen Gao
Published in *Journal of Marine Science and Engineering* 2020, Vol. 8, pp. 992.

Paper 3:
Methodology for developing a response-based correction factor (alpha-factor) for allowable sea state assessment of marine operations considering weather forecast uncertainty.
Authors: Mengning Wu, Zhen Gao
Published in *Marine Structures* 2021, Vol. 79, pp. 103050.

Paper 4:
Assessment of allowable sea states for offshore blade installation using time-domain numerical models and considering weather forecast uncertainty.
Authors: Mengning Wu, Zhen Gao, Yuna Zhao
Submitted to *Ocean Engineering* 2021.

Paper 5:
Prediction of short-term wind and wave conditions using adaptive network-

based fuzzy inference system (ANFIS) for marine operations.
Authors: Mengning Wu, Christos Stefanakos, Zhen Gao
Published in *Proceedings of the 3rd International Conference on Renewable Energies Offshore (RENEW 2018)*, Lisbon, Portugal, October 8-10, 2018.

Paper 6:
Comparison of machine-learning methods for multi-step-ahead prediction of wave and wind conditions.
Authors: Mengning Wu, Zhen Gao, Christos Stefanakos, Sverre Haver
Published in *Proceedings of International Conference on Time Series and Forecasting (ITISE 2019)*, Granada, Spain, September 25-27, 2019.

Declaration of Authorship

In all these papers, I was the first author and responsible for initiating ideas, establishing models, performing the analysis, providing the results and writing the papers. The co-authors Prof. Zhen Gao, Dr. Christos Stefanakos and Prof. Sverre Haver have contributed to the support, discussions and constructive comments to increase the scientific quality of the publications. Dr. Yuna Zhao is the third author of *paper 4*, and she provided the numerical model of the blade installation and the guidance on numerical simulation.

Glossary

Abbreviations

R^2	Correlation coefficient
ANFIS	Adaptive-Network-based Fuzzy Inference System
ANN	Artificial Neural Network
ARIMA	AutoRegressive Integrated Moving Average
ARMA	AutoRegressive Moving Average
AR	AutoRegressive
AUV	Autonomous Underwater Vehicles
BIC	Bayesian Information Criterion
CDF	Cumulative Distribution Function
CNN	Convolution Neural Network
COG	Center of Gravity
COV	Coefficient of Variation
DLL	Dynamic Link Library
DMI	Danish Meteorological Institute
DNV	Det Norske Veritas

DOF Degree of Freedom

DP Dynamic Positioning

ECMWF European Centre for Medium-Range Weather Forecasts

EMD Empirical Mode Decomposition

FD Frequency Domain

FIS Fuzzy Inference System

FWT Floating Wind Turbine

GBF Gravity Based Foundation

HIRLAM High Resolution Limited Area Model

HLV Heavy Lift Vessel

IEC International Electrotechnical Commission

IMF Intrinsic Mode Function

JIP Joint Industry Project

JONSWAP Joint North Sea Wave Project

LSTM Long Short-Term Memory

MAE Mean Absolute Error

MAPE Mean Absolute Percentage Error

MF Membership Function

MLE Maximum Likelihood Estimation

MOF MetOffice (UK)

MTF MeteoFrance

MTN Norwegian Meteorological Institute

NCEP National Center for Environmental Prediction

NWP Numerical Weather Prediction

OWT Offshore Wind Turbines

PBML Physics-Based Machine Learning

PDF Probability Density Function

RMSE Root Mean Square Error

RNN Recurrent Neural Network

ROV Remotely Operated Vehicle

SHM SHOM-Service hydrographique et océanographique de la Marine, Naval Hydrographic and Oceanographic Service

SI Scatter Index

SPS Subsea Production System

STWAVE Steady State WAve Model

SWAN Simulating WAves Nearshore

TD Time Domain

TLP Tension Leg Platform

TSML Time Series-based Machine Learning

WAM Wave Modeling

Nomenclature

α_R response-based alpha factor

α_{RM} response-based alpha-factor of the blade root radial motion

α_{RV}	response-based alpha-factor of the blade root radial velocity
β	scale parameter of the Gumbel distribution
γ	location parameter of the Gumbel distribution
ε	forecast error ratio
ε_h	forecast error ratio of H_s
ε_M	forecast error factor
ε_t	forecast error ratio of T_p
D_u	wind direction
H	wave height
H_s	significant wave height
H_s^f	forecasted significant wave height
H_s^t	actual significant wave height
H_{max_WF}	characteristic value of maximum wave height taking into account forecast uncertainty in H_s
H_{max}	characteristic value of maximum wave height
$H_{s\_lim\_\alpha}$	allowable H_s for marine operations adjusted by α factor
H_{s_lim}	allowable H_s for marine operations
R_E	characteristic value of the limiting response parameter
R_{E_WF}	characteristic value of the limiting response parameter taking into account weather forecast uncertainty
R_{EM}	characteristic values of blade root radial motion
R_{EV}	characteristic values of blade root radial velocity

R_{root}	radius of blade root
T_C	estimated maximum contingency time
T_E	duration of marine operations
T_L	forecast lead time
T_p	peak wave period
T_p^f	forecasted peak wave period
T_p^t	actual peak wave period
T_R	operation reference period
T_S	sea state reference period
T_{POP}	planned operation period
U_w	mean wind speed
U_{10}	mean wind speed at the reference height of 10 m

Contents

Abstract **i**

Preface **v**

Acknowledgment **vii**

Publication List **ix**

Glossary **xii**

List of Figures **xxiii**

List of Tables **xxvii**

1 Introduction **1**
1.1 Background 1
1.2 Marine operations 3
1.2.1 Weather-restricted and -unrestricted operations 4
1.2.2 Offshore oil & gas 4
1.2.3 Subsea operations 6
1.2.4 Offshore wind turbine installation 7
1.2.4.1 Installation of foundations 7
1.2.4.2 Installation of wind turbine components . . . 11
1.2.5 Criteria for planning and execution of marine operations 13
1.3 Weather forecasting 16
1.3.1 Metocean data 16
1.3.2 Evolution of numerical weather forecasting 18
1.3.3 Physics-based numerical models 19
1.3.4 Data-driven models 20
1.3.5 Application of weather forecasts in marine operations 21
1.4 Weather forecast uncertainty 23

1.5 Aim and scope 24
1.6 Thesis outline 26

2 Machine learning-based weather forecasting methods 29
2.1 Introduction 29
2.1.1 Machine learning 29
2.1.2 Training, testing and validation sets 30
2.1.3 Forecast step 31
2.1.4 Input variable selection 31
2.1.4.1 Univariate TSML method 32
2.1.4.2 Multivariate TSML method 33
2.1.4.3 PBML method 33
2.2 Machine learning techniques 34
2.2.1 Data pre-processing 34
2.2.1.1 Decomposition technique 35
2.2.1.2 EMD 36
2.2.2 Data-driven models 37
2.2.2.1 ARIMA 38
2.2.2.2 ANN 39
2.2.2.3 RNN 40
2.2.2.4 ANFIS 42
2.2.3 Multi-step-ahead forecast strategies 45
2.2.3.1 M-1 model 45
2.2.3.2 M-N model 46
2.2.3.3 M-mN model 47
2.2.3.4 M-1 slope model 47
2.3 Forecasting methods 48
2.3.1 Time series-based machine learning (TSML) method . 49
2.3.2 Physics-based machine learning (PBML) method . . . 52
2.3.2.1 Background 52
2.3.2.2 Model establishment 54
2.4 Forecast performance evaluation 57
2.4.1 Forecasted time series 57
2.4.2 Error measures 58
2.4.3 Forecast errors 58
2.5 Application, assumption and limitation 59

3 Weather forecast results and uncertainty quantification 61
3.1 Offshore site and metocean data 61
3.2 TSML method 63
3.2.1 Decomposition-ANFIS method 63

3.2.1.1 One-step-ahead forecasting . . . 63
3.2.1.2 Multi-step-ahead forecasting . . . 65
3.2.2 Comparison of different TSML methods . . . 70
3.2.3 Summary . . . 73
3.3 PBML method . . . 73
3.3.1 Model architecture determination . . . 74
3.3.2 Forecast of total wave conditions . . . 75
3.3.2.1 Significant wave height . . . 75
3.3.2.2 Peak wave period . . . 79
3.3.3 Forecast of separate wind-generated sea conditions and swell conditions . . . 80
3.3.3.1 Significant wave height . . . 81
3.3.3.2 Mean wave period . . . 84
3.3.4 Summary . . . 86
3.4 Comparison with physics-based wave models . . . 86

4 Methodology for the allowable sea states assessment of marine operations considering weather forecast uncertainty 91
4.1 Alpha-factor proposed by DNV . . . 92
4.2 Response-based alpha-factor . . . 94
4.2.1 Key parameters . . . 94
4.2.2 Framework . . . 96
4.3 Uncertainty quantification of sea state forecast . . . 98
4.4 Extreme response analysis for marine operations . . . 99
4.5 Derivation of the response-based alpha-factor . . . 102
4.6 Application of the response-based alpha-factor . . . 104

5 Allowable sea states assessment of the blade installation of offshore wind turbine 107
5.1 Numerical modelling of blade installation . . . 108
5.2 Uncertainty quantification of weather forecasts . . . 110
5.3 Crane tip motion (FD) . . . 114
5.3.1 Dynamic response analysis of the crane tip . . . 115
5.3.1.1 Spectral analysis . . . 115
5.3.1.2 Extreme response analysis . . . 117
5.3.2 α_R for the crane tip motion . . . 120
5.3.3 Allowable sea states assessment . . . 123
5.4 Blade root radial motion and velocity (TD) . . . 125
5.4.1 Comparison between FD and TD analysis . . . 125
5.4.2 Sensitivity analysis of wind loads . . . 126
5.4.3 Extreme response analysis . . . 129

5.4.3.1 Statistical uncertainty 130
5.4.3.2 Characteristic response values 133
5.4.4 α_R for the final blade mating phase 135
5.4.4.1 Blade root radial motion 135
5.4.4.2 Blade root radial velocity 137
5.4.5 Allowable sea state assessment 137

6 Conclusions and recommendations for future work 141
6.1 Conclusions 141
6.2 Original contributions 143
6.3 Limitations and recommendations for future work 145

References 147

A Analysis of long-term metocean data 169
A.1 Time series plot 171
A.2 Auto-correlation coefficient 171
A.3 Cross-correlation coefficient 174
A.4 Predictability 176

B Forecasted and actual time series based on decomposition-ANFIS method 179

C List of previous PhD theses at Dept. of Marine Tech. 185

List of Figures

1.1 Wind energy development and future trends 2
1.2 Size of offshore wind turbines 2
1.3 Average water depth of offshore wind farms 3
1.4 Average distance to shore of offshore wind farms 3
1.5 Two types of sea transport 5
1.6 Two accidents related to towing operations 5
1.7 Subsea production systems 6
1.8 Illustration of the procedure of subsea lifting operation 7
1.9 Schematic of different foundation types for offshore wind turbines 9
1.10 Illustration of FWTs based on the restoring mechanisms . . . 10
1.11 Installation methods for wind turbine components 12
1.12 Installation vessels for offshore wind turbines 13
1.13 Criteria for planning and execution of marine operations . . . 15
1.14 Wave hindcasting vs. forecasting 17
1.15 The schematic of the modern numerical prediction model . . 18
1.16 The parameterization processes included in NWP models . . 20
1.17 Scope of the thesis 25

2.1 Initial and decomposed time series of H_s in one year 36
2.2 Illustration of using EMD for a H_s time series 37
2.3 Structure of a typical ANN 39
2.4 The structures of RNN and LSTM 41
2.5 Structure of FIS 42
2.6 ANFIS architecture 44
2.7 Structure of the M-1 model 46
2.8 Structure of the M-N model 46
2.9 Structure of the M-N model 47
2.10 Input selection criteria of the M-1 slope model 48
2.11 Flowchart of the TSML method 50

2.12 The sketch of the atmosphere-wave forecasting system 53
2.13 Idea of the PBML method 54
2.14 Illustration of the forecast domain 55
2.15 Illustration of the PBML model architecture 56
2.16 Illustration of forecasted time series generation 57

3.1 North Sea area and the selected offshore site 62
3.2 One-step-ahead forecasting results 64
3.3 Q-Q plots for one-step-ahead weather forecasts 65
3.4 Several cases of H_s forecast by the three models 68
3.5 Statistics of ε_M at different forecast step N 69
3.6 Comparison of forecast uncertainty based on different TSML methods 72
3.7 Illustration of a small forecast domain 73
3.8 Forecast errors of the PBML model with different durations of wind forcing (point 5) 74
3.9 Forecast errors of the PBML model using wind forcing up to (t+N-TU^*) (point 5) 75
3.10 Forecast results of H_s at each lead time based on the PBML model 76
3.11 Error measures of H_s forecasts for all nine grid points 77
3.12 Forecast results of H_s based on the PBML model with one-point domain 78
3.13 Forecast errors of H_s based on the PBML model with one-point domain 79
3.14 Forecast results of T_p based on the PBML model 80
3.15 Forecast results of H_{sw} based on the PBML model 81
3.16 Forecast results of H_{ss} based on the PBML model 82
3.17 Scatter plot of significant wave height and mean wind speed . 83
3.18 Forecast results of T_{mw} based on the PBML model 84
3.19 Forecast results of T_{ms} based on the PBML model 84
3.20 Scatter plot of wave period and mean wind speed 85

4.1 The framework of the methodology for developing the response-based alpha-factor 96
4.2 Illustration of construction of allowable sea states considering weather forecast uncertainty 105
4.3 Illustration of application of allowable sea states considering weather forecast uncertainty 106

5.1 Schematic view of the offshore blade installation system (θ_{wv} is the incident wave angle and θ_{wd} is the wind inflow angle) . 108
5.2 Illustration of the mating phase of offshore blade installation 109
5.3 Forecast error distribution of H_s at different lead times . . . 110
5.4 Forecast error distribution of T_p at different lead times 110
5.5 Statistics of ε_h and trend line analysis for different lead times (TSML method) 111
5.6 Statistics of ε_h and trend line analysis for different lead times (PBML method) 111
5.7 Statistics of ε_t and trend line analysis for different lead times (TSML method) 112
5.8 Statistics of ε_t and trend line analysis for different lead times (PBML method) 112
5.9 Motion transfer functions of the crane tip in the beam sea condition 115
5.10 Wave spectra and power spectra of crane tip motion for different T_p (H_s=2 m) 116
5.11 Characteristic values of crane tip motion for different T_p (H_s=2 m) 117
5.12 Extreme response distributions with and without considering weather forecast uncertainty (H_s=1 m, T_p=7 s, TSML method, T_L=3 hours, 10^{-4} exceedance probability) 118
5.13 Extreme response distributions with and without considering weather forecast uncertainty (H_s=1 m, T_p=7 s, TSML method, T_L=3 hours, 10^{-2} exceedance probability) 118
5.14 α_R vs. H_s in different T_p groups (TSML method) 122
5.15 α_R vs. H_s in different T_p groups (PBML method) 122
5.16 Allowable sea states of the crane tip motion (allowable limit=0.8 m, 10^{-4} exceedance probability) 124
5.17 Allowable sea states of the crane tip motion (allowable limit=0.4 m, 10^{-2} exceedance probability) 124
5.18 Comparison of power spectra of crane tip motion using FD and TD methods (H_s =1 m, T_p =7 s) 126
5.19 Power spectra of blade COG motion with different wind fields (H_s=2 m, T_p=7.5 s) 128
5.20 Standard deviations of blade COG motion with different wind fields (H_s=2 m, T_p=7.5 s) 129
5.21 Comparison of blade root radial motions with different wind fields (H_s=2 m, T_p=7.5 s) 129

5.22 Extreme value distribution estimation of the blade root radial motion (H_s =2 m and T_p =5 s) 130
5.23 Fitted extreme distribution of the blade root radial motion (1000 simulations, H_s=2 m, T_p=5 s) 131
5.24 Variation of the characteristic with the number of simulations (H_s=2 m, T_p=5 s) 132
5.25 Variation of the characteristic values in different sets (H_s=2 m, T_p=5 s) 132
5.26 Fitting surface of Gumbel parameters as a function of H_s and T_p (blade root radial motion) 133
5.27 Fitting surface of Gumbel parameters as a function of H_s and T_p (blade root radial velocity) 135
5.28 α_{RM} with a lead time of 3 hours 136
5.29 Variation of α_{RM} with lead times in different H_s groups . . . 136
5.30 Variation of α_{RV} with lead times in different T_p groups 137
5.31 Allowable sea states of the blade root radial motion 138
5.32 Allowable sea states of the blade root radial velocity 139

A.1 Time plot of metocean variables (one year) 172
A.2 Auto-correlation coefficient of metocean variables (one year) . 173
A.3 Auto-correlation coefficient of metocean variables (summer) . 173
A.4 Auto-correlation coefficient of metocean variables (winter) . . 174
A.5 Scatter plots of metocean data 175
A.6 Cross-correlation coefficient of H_s against U_w 176
A.7 Relation between the coefficient of correlation and forecasting efficiency 176

B.1 Forecasted time series of U_w 182
B.2 Forecasted time series of H_s 183
B.3 Forecasted time series of T_p 184

List of Tables

2.1 Data sources for model establishment and application 59

3.1 Structures of the one-step-ahead ANFIS models 64
3.2 The list of developed forecasting methods 70
3.3 Forecast errors of H_s at each lead time based on the PBML model 77
3.4 Forecast errors of T_p based on the PBML model 80
3.5 Forecast errors of H_{sw} based on the PBML model 81
3.6 Forecast errors of H_{ss} based on the PBML model 82
3.7 Forecast errors of T_{mw} based on the PBML model 83
3.8 Forecast errors of T_{ms} based on the PBML model 85
3.9 Comparison of one-day-ahead H_s forecasts 87
3.10 Comparison of one-day-ahead T_p forecasts 87
3.11 Comparison of the forecast uncertainty in H_s (based on the method from Natskår) 88

5.1 Error mean and standard deviation of forecasts from different institutions (T_L=24 hours) 114
5.2 R_E values (m) of the crane tip motion (10^{-4} exceedance probability) 119
5.3 R_{E_WF} values (m) of the crane tip motion (T_L=3 hours, TSML method, 10^{-4} exceedance probability) 120
5.4 Properties of the correction factors 121
5.5 Properties of TD and FD response analysis methods for blade installation 127
5.6 Statistical uncertainty in extreme response estimation (H_s=2 m, T_p=5 s) 133
5.7 R_E values (m) of the blade root radial motion (R_{EM}) 134
5.8 R_E values (m) of the blade root radial velocity (R_{EV}) 134

Chapter 1

Introduction

1.1 Background

The gradual transition away from fossil fuels towards a carbon-neutral society is one of the greatest challenges of the 21 century [1]. Over the past decade, renewable energy, such as wind energy and solar energy, is the fastest-growing energy source globally. Among them, offshore wind energy is identified as one of the most promising sources [2] since it is more stable and stronger, not being exhausted and produce no emissions, and it is also one of the cheapest ways of generating electricity from renewable energy. With regard to the wind energy, the majority of wind power is produced from onshore wind farms at present. However, practical reasons such as the lack of inexpensive land near major population centers, and visual and noise pollution caused by large onshore wind turbines undoubtedly limit its development. In this case, offshore wind energy is highly attractive and has been developed rapidly in the past decade. From 2009 to 2019, offshore wind capacity has grown from being 1% of global wind installations to over 10% [3]. Moreover, it is believed that offshore wind energy has great potential for further development and will continue to expand impressively over the next two decades [4, 5]. As shown in Figure 1.1, the global cumulative installed capacity for offshore wind is expected to increase to 228 GW by 2030 and to 1000 GW by 2050 [5].

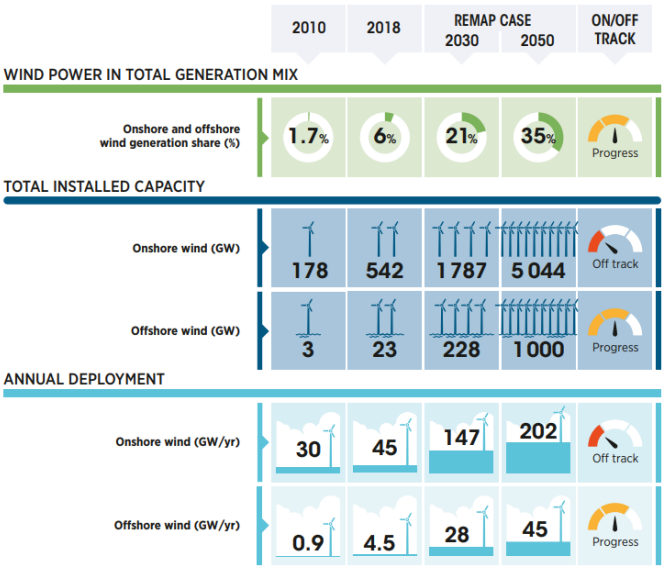

Figure 1.1: Wind energy development and future trends [5]

The rapid development of offshore wind will bring greater challenges to operations related to the installation of offshore wind turbines (OWTs). Figures 1.2 to 1.4 show the evolutions in the size of OWTs, average water depth and distance to shore of offshore wind farms, respectively. It is visible that in order to capture better and stable wind energy, the overall trend of offshore wind energy is toward larger wind turbines, further offshore and deeper waters. Depending on the water depth, bottom-fixed wind turbines and floating wind turbines are the two main types of OWTs at present. The associated operations related to transportation, installation, maintenance, replacement and decommissioning, might be concept-dependent and make the installation of OWTs much more complex and challenging.

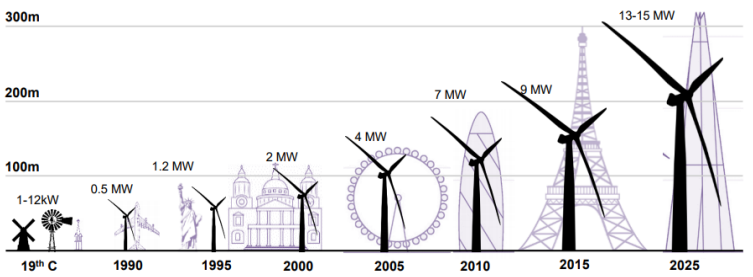

Figure 1.2: Size of offshore wind turbines [6]

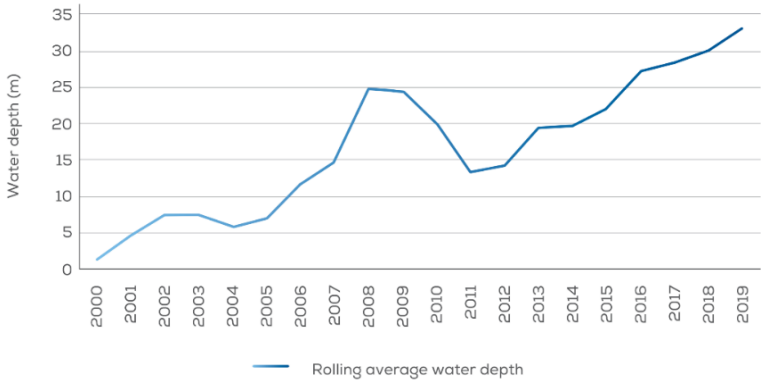

Figure 1.3: Average water depth of offshore wind farms [7]

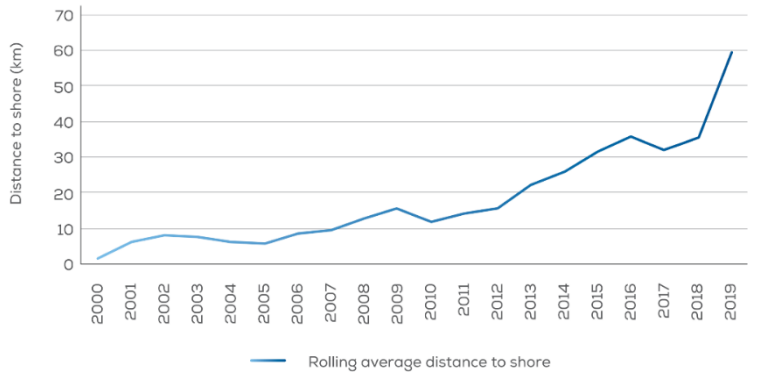

Figure 1.4: Average distance to shore of offshore wind farms [7]

1.2 Marine operations

According to the definition in Det Norske Veritas (DNV) [8], marine operations are non-routine operations of limited duration for handling objects and vessels in the marine environment during temporary phases. Regarding the offshore industry, activities related to transportation, installation, inspection, maintenance and decommissioning of offshore structures are different types of marine operations. This thesis will focus on the installation of OWTs in the case studies. But the overall methodology can be used for different types of marine operations and marine structures. Accordingly, prior to an introduction of various operations related to the OWT installation, a classification of marine operations and a brief overview of marine operations associated with offshore oil & gas and subsea fields are presented.

1.2.1 Weather-restricted and -unrestricted operations

For the planning and execution of marine operations, an important parameter is the operation duration. The duration, which is referred to as the operation reference period (T_R), is normally defined by Eq. (1.1). According to the duration, marine operations can be typically classified into two categories, weather-restricted and weather-unrestricted operations [8]. If T_R of an operation is longer than 96 hours and T_{POP} is longer than 72 hours, this operation is typically defined as a weather-unrestricted operation. Such operation must be able to be performed under any weather that may be encountered for the season. Hence, long-term statistics of environmental conditions are necessary to establish the corresponding environmental limiting criteria. That is, environmental conditions that exceed a given probability need to be considered as the basis for the design of weather-unrestricted operations. As for the operation with T_R less than 96 hours and T_{POP} less than 72 hours, it is usually defined as a weather-restricted operation. When an operation is weather restricted, it could be planned with environmental conditions set by owner, operator or contractor during the planning phase [8]. In the execution phase, weather forecasts instead of long-term statistics are crucial for decision-making. When the weather forecasts do not exceed the limiting criteria within T_R, the operation can be executed safely.

$$T_R = T_{POP} + T_C \tag{1.1}$$

where T_{POP} is the planned operation period and T_C is the estimated maximum contingency time.

1.2.2 Offshore oil & gas

The oil and gas industry deals with the extraction of natural oil and gas from land (onshore) or water (offshore). In the offshore oil and gas industry, various marine operations are involved, including towing and installation of offshore platforms, oil and gas exploration and production, transportation of the oil and gas to land, etc. Unlike operations on land, marine environment is critical for marine operations, such as for the towing operation. It is well known that offshore platforms are very large and heavy. For example, the Troll A platform, built by Norwegian Contractors for Norske Shell and located at the North sea, has an overall height of 472 meters and weighs 656,000 tonnes [9]. To install such large and heavy platforms, offshore structures are usually built onshore to save costs and facilitate construction. After completion, these structures should be loaded out and

transported offshore to the installation site. Correspondingly, sea transport of self-floating objects or large structures by the use of tugs or heavy lift vessels (HLVs) are necessary. Two types of sea transport are shown in Figure 1.5.

(a) Wet tow by a tug [10]

(b) Dry tow by a heavy lift vessel [11]

Figure 1.5: Two types of sea transport

(a) Kolskaya (under tow shortly before it sunk) [12]

(b) Kulluk (aground near Kodiak) [13]

Figure 1.6: Two accidents related to towing operations

Attention should be given to weather conditions during the towing operation. Ignoring or misusing weather information will be prone to lead to accidents and disasters in towing operations. In 2011 and 2012, accidents related to towing operations of the drilling rigs 'Kolskaya' and 'Kulluk' occurred in Arctic waters [13], respectively, which are illustrated in Figure 1.6. The accidents caused loss of lives and economic losses. Harsh weather was a common factor in the development of the 'Kolskaya' and 'Kulluk' accidents scenarios.

1.2.3 Subsea operations

Subsea operations are required for installation of subsea production system (SPS), which is an important component in offshore oil and gas industry. A SPS is an integrated template located on the sea floor, containing the well system (such as the subsea tree), the production system (such as manifolds and subsea processing systems) and the pipeline system (such as tie-ins and production pipelines) [14], see Figure 1.7.

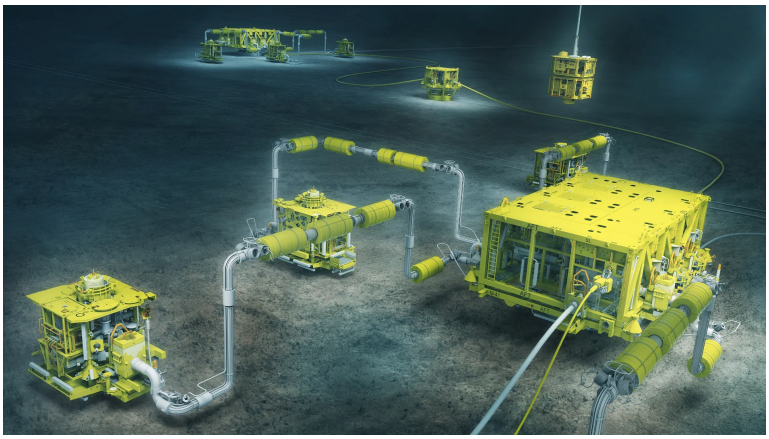

Figure 1.7: Subsea production systems [15]

To install the SPS, several subsea operations are involved, including installation of subsea hardware, riser installation, pipelaying and the use of underwater vehicles such as remotely operated vehicles (ROVs) and autonomous underwater vehicles (AUVs) for subsea inspection, maintenance and repair operations. For most of these operations, subsea structures are transferred from the docks of a shipyard to the seabed at the installation site, that mainly rely on crane and lifting operations. For the lifting operation, subsea modules are lifted off from the deck and hanged in air, lowered through the splash zone, and then lowered further in deep water and landed on the sea bed [16]. This operation, which is illustrated in Figure 1.8 requires a high level of precision and control, to ensure the alignment of modules on the seabed and avoid collisions. However, there are several challenges during the execution of lifting operations. One of them is harsh weather conditions [17]. The dynamic nature of marine environment can cause hydrodynamic loads on subsea modules, especially in the splash zone. Besides, horizontal offset of subsea modules due to current and the crane tip motion due to the vessel motion may also happen. These further introduce

risks and uncertainties in the SPS installation and will have a significant impact on the operational costs and safety at sea. Therefore, decision-making of these operations in the execution phase should be made carefully and low sea states are necessary.

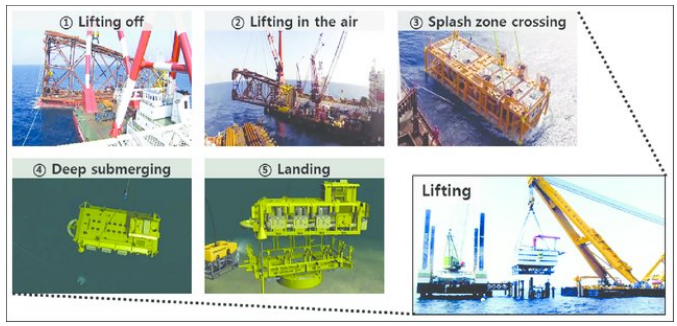

Figure 1.8: Illustration of the procedure of subsea lifting operation [18]

1.2.4 Offshore wind turbine installation

As far as the installation of OWTs is concerned, associated marine operations involve installation of multiple components of OWTs such as foundations, turbine tower, nacelle and blades. Typically operations for each component are weather-restricted with a duration less than one day, while it normally takes months for installation of the whole offshore wind turbine farm. Depending on situations like the site condition, foundation type and turbine size, different installation methods are required in actual OWT installations. An overview regarding the installation methods of each component for OWTs is given below.

1.2.4.1 Installation of foundations

Various types of foundations for OWTs are illustrated in Figure 1.9. Bottom-fixed and floating OWTs are two main categories. To date, offshore wind energy market is dominated by bottom-fixed foundations [19]. The most common types are gravity based foundations (GBFs), monopiles and jackets. Among them, the monopiles have the simplest structure and are widely used in water depths up to 40 m [20]. GBFs are suitable for shallow water where water depths less than 10 m [21] and appropriate for the clay, sandy soil and rock seabed conditions [22]. For relatively deeper waters (50-70 m), the jacket type wind turbine foundations are competitive [23]. Installation procedures for OWT bottom-fixed foundations are inherited from the offshore oil and gas industries [24], which are described below:

Monopile
Monopile is a single steel tube pile. Before installation, it is normally transported on the deck of crane vessels (e.g., jack-up vessels and HLVs) [25]. Besides, the wet towing method has also been applied to transport a floating monopile [26], which is considered economical as the size and weight of the monopile increase. Once it arrives at the installation site, the monopile is lifted-off, upended and lowered to the sea bed by using a crane. Afterwards, a large hydraulic hammer will be used to drive it into the sea bed.

Jacket
Jacket is a foundation that uses a lattice framework with three or four legs set on the sea floor, which can safely anchor the tower of the wind turbine [27]. It can be transported in either an upright or horizontal position on the deck of crane vessels or transportation barges. When on site, the anchor piles are driven into the seabed using a hammer, which is similar to the monopile installation. Afterwards, the crane lifts-off, upends (if the jacket is transported in a horizontal position) and lowers the jacket into the sea. Then the jacket is mated with the pre-installed piles. Finally, a grouting mixture is usually used to fill the annulus between the pile and foundation leg sleeves.

GBF
GBF is a foundation that stands on the seabed with heavy weight (1500-4500 tonnes) to resist the overturning moment [20]. Due to the limited lifting capacities, the traditional method of using HLVs to install GBF faces many challenges. Alternatively, the 'float and submerge' method could be applied for GBF installation [28]. Specifically, a self-floating GBF is produced on land and wet-towed using tug-boats to the installation site. By ballasting and submerging it to the seabed, the installation of the GBF can be completed.

In addition to bottom-fixed OWTs, floating wind turbines (FWTs) have attracted intensive commercial and academic interest over the past two decades, because they tend to be more suitable and cost-effective in deep water locations. As illustrated in Figure 1.9 (b), three typical types of FWTs are spars, semi-submersibles and tension leg platforms (TLPs). Similar to floating platforms in oil and gas industries, FWTs are based on the restoring mechanisms for achieving a hydrostatic equilibrium in deep water. Three restoring mechanisms are shown in Figure 1.10, in which relative positions of several typical FWT concepts are drawn to show their characteristics. Among them, three representative FWTs are introduced to describe the installation procedure of floating foundations for OWTs in the following.

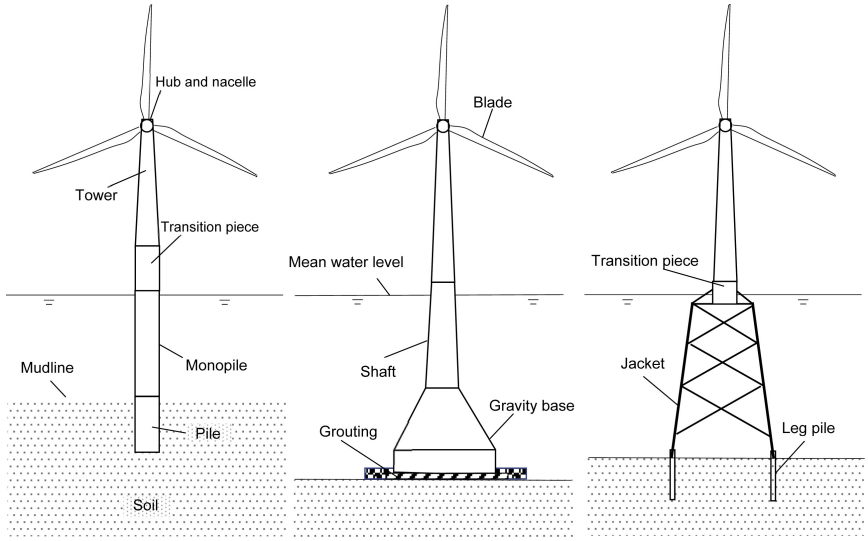

(a) Bottom-fixed types (monopile, GBF and jacket)

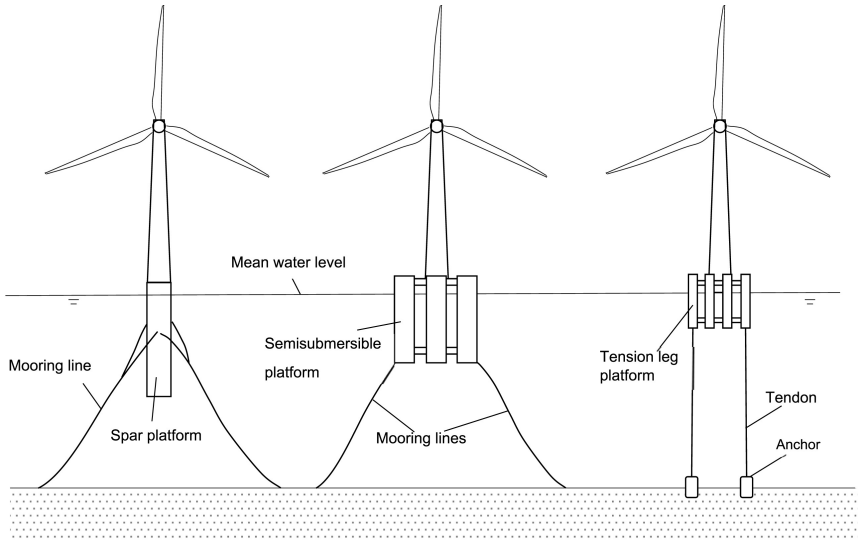

(b) Floating types (spar, semi-submersible and tension leg platform)

Figure 1.9: Schematic of different foundation types for offshore wind turbines [21]

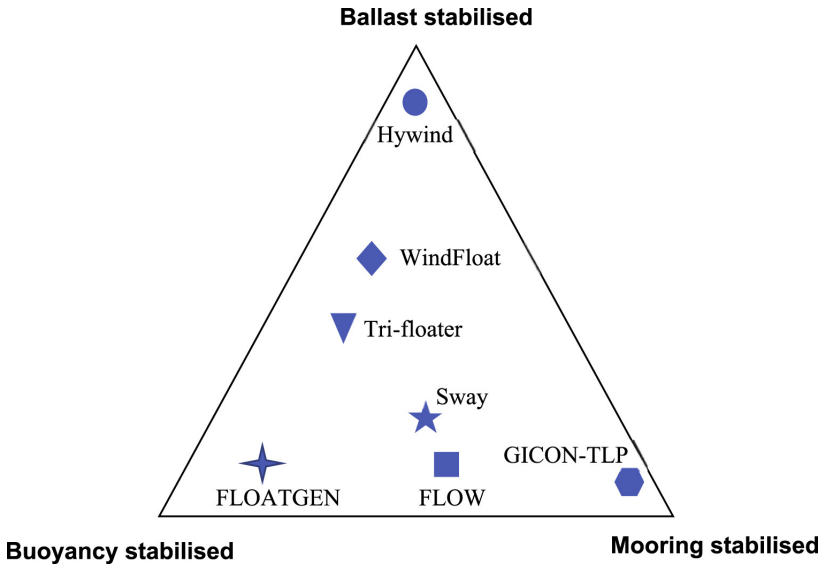

Figure 1.10: Illustration of FWTs based on the restoring mechanisms [21] (Hywind [29], WindFloat [30], Tri-floater [31], S [32], FLOATGEN [33], FLOW [34], GICON-TLP [35])

Spar

Spar is a simple cylindrical column foundation with small waterplane areas. The world's first spar FWT, Hywind Demo [36], was installed in 2009. In the installation procedure, the spar foundation was wet-towed by tugboats from Finland to Norway and upended by pumping water into it. Then solid ballasting and water de-ballasting were carried out to install it and maintain draft, respectively. After installing the spar, the tower and rotor assembly were mated with it offshore.

Semi-submersible

Semi-submersible is a type of foundation composed of three or four columns, which has increased waterplane area compared with the spar. Hence, it has better hydrodynamic behaviour to resist wave loads. Besides, superior towability is another advantage of semi-submersible FWTs [37]. In recent years, many semi-submersible foundations [38–42] have been designed, tested or installed. For instance, for the WindFloat [38], the entire semi-submersible FWT was assembled on shore in a dry dock and then towed by three tugboats to the installation site. With the assistance of an anchor handling vessel, the whole system was moored at seabed.

TLP

TLP is a floating foundation that keeps station-keeping by anchoring heavy

steel rods on the seabed using suction anchors or suction caissons [43]. Compared to spar and semi-submersible, the traditional installation procedure of TLPs is complicated. Normally, the tendons are dry-towed by a cargo and pre-installed by a crane vessel. Alternatively, they could also be welded with buoyancy modules and wet-towed to the site together. Then, the towed assembled TLP FWT is secured to the tendons based on a ballast operation. Finally, de-ballasting of water is performed to pre-tension the tethers. In recent years, some new installation methods have been proposed, such as the installation procedure of GICON TLP [44]. During transportation, a floating slab was used to support the GICON TLP, and then the whole system was towed to the offshore location by a tugboat. By ballasting the slab, the GICON TLP was submerged to its final draft during the installation.

1.2.4.2 Installation of wind turbine components

In addition to foundations, the installation of OWT substructures is important. A wind turbine normally consists of six main components, that are tower, nacelle, hub and three blades [45]. Different from transportation and installation of foundations, the wind turbine components can only be dry-towed by crane vessels or transportation barges, and their installation is mainly based on lifting and mating operations. Compared to the conventional operations in the offshore oil and gas industries, OWT operations generally face more challenges. This is mainly because in addition to wave loads considered in conventional operations, wind loads have a significant impact for installation of OWTs due to large installation height. Presently, the offshore assembly of wind turbine components is normally required after the foundation is installed. According to the number of pre-assembled components, different installation methods can be applied, which have been summarized in various researches [45–47]. Figure 1.11 shows an example, listing six main installation methods [46]. Among them, onshore pre-assembly and a single lift procedure (i.e., method 6 in Figure 1.11) is generally preferred in the past, since it reduces the number of offshore lifts and minimizes offshore assembly. Correspondingly, the challenging operations such as offshore mating processes will be reduced. However, this method requires large-capacity cranes. As the size of turbines increases, this method becomes less competitive and unattractive [48]. In this case, the installation trend of offshore wind turbines is to assemble more turbine components offshore, such as methods 1 and 2 in Figure 1.11.

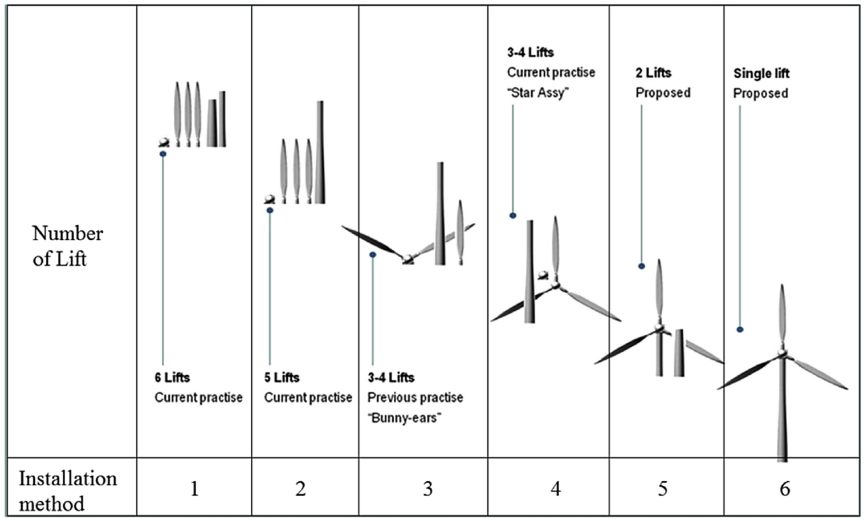

Figure 1.11: Installation methods for wind turbine components [46]

Tower

Installation of an OWT tower requires lifting and mating operations. Similar to the installation of monopile foundations, the tower is normally lifted by a crane vessel and then mated onto a pre-installed foundation. In addition, some novel ideas of tower assembly installation for OWTs have been proposed [48, 49] with a special subsea structure or an upending frame.

Blade

In recent years, single blade installation has drawn great interests [21]. Refer to methods 1 and 2 in Figure 1.11, each blade should be lifted separately and the entire wind turbine installation requires five to six lifts. One advantage of single blade installation is that the required deck space of installation vessels is small. Nevertheless, there are many challenges during the installation process. For instance, the blade installation is quite weather-sensitive. Both wave-induced motion of foundation and installation vessel and wind-induced blade motion make the blade mating process rather difficult. Therefore, dynamic responses of the actual installation process should be studied. Kuijken [50] focused on single blade lifting operation and applied the horizontal single blade mounting (HSBM) technique to study dynamic behaviour of the blade. Jiang et al. [51] concentrated on the mating process for single blade installation, and investigated motions of the blade root, hub, guide pin and flange hole when a blade is mated on a monopile foundation. Zhao et al. [52–54] conducted a series of studies about offshore blade installation. They developed an integrated dynamic analysis method for the single blade

installation and identified critical events and response limiting parameters. It was found that the final mating phase is critical, and the corresponding limiting parameters are the blade root radial motion and velocity. In addition, Verma et al. [55–57] developed an approach to estimate limiting sea states and operability of the blade lifting operation and conducted impact analysis on the blade root.

For offshore blade installation, two types of installation vessels are commonly employed, which are the jack-up crane vessels and the floating crane vessels (see Figure 1.12). The jack-up crane vessels can set legs down to the seabed and then elevate the hull above the sea surface to minimize the impact of waves. Hence, one obvious advantage is that a stable working platform is provided for operations like lifting and mating. Small workable water depth and the large time consumption of the lowering and retrieval processes of jack-up legs are main drawbacks limiting the usage of jack-up crane vessels. In this case, the floating crane vessel could be regarded as an alternative. Compared to jack-up crane vessels, the floating crane vessels can be located and relocated easier and faster during the installation process. Moreover, due to the wider range of applicable water depths, they have greater flexibility in marine operations. However, the installation by floating crane vessels will be more sensitive to waves. When performing operations with floating installation vessels, it is necessary to investigate the effect of weather conditions on the installation process.

(a) Jack-up crane vessel (Swire Blue Ocean) [58]

(b) Floating crane vessel (Jan DE Nul) [59]

Figure 1.12: Installation vessels for offshore wind turbines

1.2.5 Criteria for planning and execution of marine operations

Marine operations are normally carried out at offshore sites and some key issues deserve particular attention, such as environmental conditions, structural integrity, metocean-induced load effects, operational criteria, weather

forecast, etc. Generally, the planning and execution of an operation must follow certain guidelines and standards. DNVGL-ST-N001 [60] and ISO 29400:2020 [61] are comprehensive standards that give general guidance for marine operations. In addition, there are other guidelines focusing on environmental conditions [62], and for specific marine operations [63, 64] or offshore structures [65].

The basic criterion for safely performing a marine operation is that dynamic responses of the system during the operation should not exceed its allowable limit [66]. This refers to the operational limit of the operation, which should be determined in the planning phase. Guachamin Acero et al. [67] proposed a general methodology for assessment of operational limits of marine operations using response-based criteria. The methodology consists of the identification of critical events and limiting parameters of a given operation, dynamic response analysis of limiting parameters for all possible sea states and estimation of corresponding characteristic values. To assess dynamic responses, a detailed numerical modeling of actual operations is required. Depending on the operation properties, frequency domain (FD) or time domain (TD) method can be applied. In general, for operations that can be considered under a linear assumption, it is possible to study the dynamic response in frequency domain to significantly reduce computational cost. Whereas for complex non-linear systems, time domain response analysis approach is more suitable. At present, this approach is widely used to study dynamic responses of operations with floating systems [68–70]. For instance, Hassan and Soares [71] proposed a novel concept of using a floating vessel to install a pre-assembled offshore floating wind turbine and studied it based on time domain simulations. Li et al. [72] studied an over-boarding operation for a subsea template by performing numerical simulations in time domain under various sea states. In addition, TD method is also applied to structural design [73, 74] and fatigue analysis [23, 75, 76] of offshore structures, planning [77] and operability analysis [67, 78] of marine operations, etc. By performing numerical simulations of the actual operations, dynamic responses of the relevant limiting parameters can be analyzed and its characteristic value can be estimated based on extreme value distributions for a target exceedance probability. According to the comparison between the characteristic value and the allowable limit of the limiting parameter, operational limits in terms of environmental variables such as significant wave height H_s, peak wave period T_p and mean wind speed U_w (i.e., allowable sea states) of the operation can be assessed. This procedure is illustrated in Figure 1.13. Regarding the OWT installation, Guachamin Acero et al. established allowable sea states of transition piece mating [79] and fully as-

sembled turbine installation [66]. In addition, allowable sea states of the monopile hammering process and blade mating process were established by Li et al. [80] and Verma et al. [81], respectively.

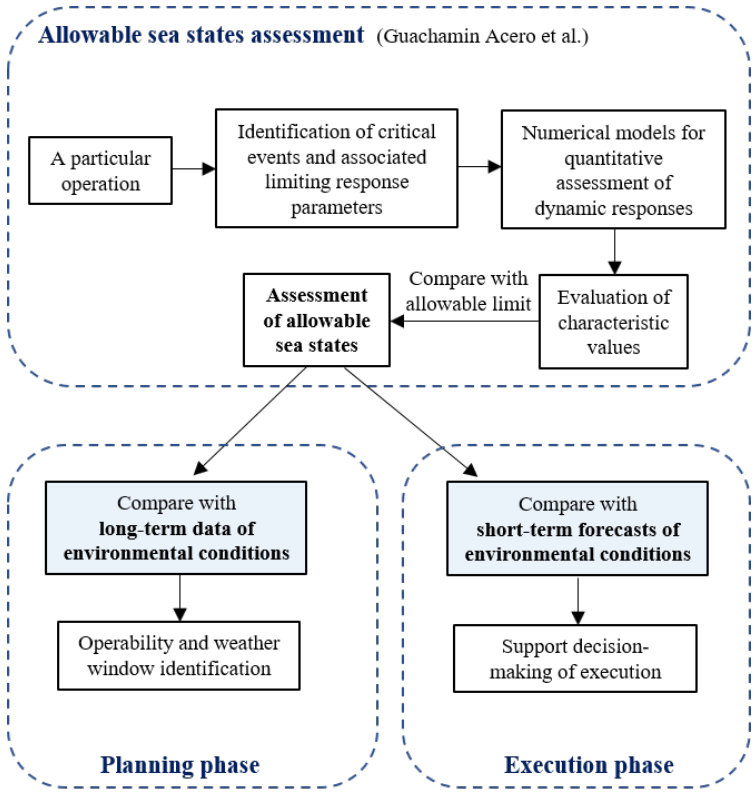

Figure 1.13: Criteria for planning and execution of marine operations

Once allowable sea states are assessed, they should be used in combination with different types of environmental data in planning and execution phases of marine operations. In the planning phase, long-term historical data of environmental conditions at an offshore site can be compared with the allowable sea states to address the operability of an operation. The operability [66] measures the percentage of available time for execution of a marine operation during a reference period (e.g., all year, seasons or months). This is essential for the selection of the suitable season for executing the operation. In addition, if low operability and long downtime are observed, it is possible to update the relevant equipment and vessel during the planning phase to further improve the operability. During the execution phase, the allowable sea states together with weather forecasting can provide a basis

for operation decision-making. The operation is considered to be safe if the short-term forecasts of environmental conditions are lower than the allowable sea states. According to the comparison results, decisions on whether to start the operation can be made and specific execution time can be determined.

1.3 Weather forecasting

As aforementioned, weather forecasts are important for execution of weather-restricted marine operations. In this section, metocean data required for marine operations is first summarized. Then weather forecasting methods and application of weather forecasts in marine operations are presented.

1.3.1 Metocean data

Due to the random nature of wind and wave fields, statistical descriptions are normally used to describe their properties. The most widely used statistical weather parameters in marine operations are H_s, T_p and U_w, which describe the wave and wind field characteristics over a certain period of time (e.g., 1 hour or 3 hours). In order to support different phases of marine operations, three types of metocean data are commonly adopted [82]:

- Measurements
- Hindcast data
- Forecast data

Among them, long-term historical measurements or hindcast data for a given site is necessary in the planning phase of marine operations to provide a description of weather at the location of interest. As illustrated in Figure 1.13, they are able to assess the operability of an operation by comparison with the allowable sea states of the operation. Measurements can be collected by different kind of sensors like satellites, buoys, ships, radars and so on [83]. Alternatively, long-term hindcast data could also be possible to use. In addition to the measurements and hindcast data, another important type of metocean data is the forecast data. At the execution phase, it is necessary to assist decision-making on whether an operation can be started and continued safely. The start time of weather-restricted operations is normally determined by the forecasted weather windows.

Presently, hindcast and forecast data are normally produced by physics-based numerical models. The difference between hindcasting and forecasting

regarding waves is briefly illustrated in Figure 1.14. Wave hindcasting [84] refers to reconstructing the historical wave conditions based on historical winds by applying numerical wave models. For wave forecasting, numerical wave models are identical to those used for wave hindcasting. However, in this case the model must be driven by forecasted wind conditions, instead of its historical values. In order to use hindcast and forecast data, they should be thoroughly calibrated and validated against measurements to demonstrate their accuracy. Various institutions have investigated physics-based numerical models over the years, and validation results have indicated that hindcast data have sufficient reliability [85–88]. Therefore, if in-situ measurements are not available, the accuracy of forecast data can also be evaluated by comparison with high quality hindcast data. Based on the comparison result, the uncertainty in forecasting models will be assessed.

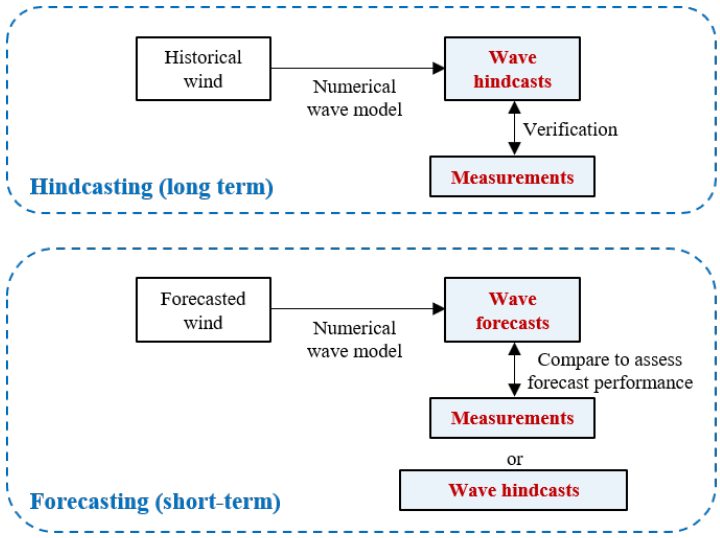

Figure 1.14: Wave hindcasting vs. forecasting

Regarding weather forecasting, the timescales of forecast data required for marine operations may differ. In this thesis, forecasting of short-term environmental statistical variables like H_s and T_p is investigated, and the overall length of forecast data is one-day-ahead, taking into account the typical execution time of OWT installations. Given that wave conditions are more important for marine operations using floating installation vessels, the main focus of this thesis is wave forecasting. In addition to environmental statistical variables, some applications also require forecasting of wave elevations (such as the use of feedforward control in marine operations like

motion compensation, crane operation, etc.). The corresponding forecast timescale is seconds ahead [89–92]. This topic is beyond the scope of the thesis, and the following descriptions of weather forecast refer to the forecasting of environmental statistical variables.

1.3.2 Evolution of numerical weather forecasting

Numerical weather forecasting is defined as the application of science and technology to predict environmental conditions at a given location and time in the future [93]. Researchers have tried to predict weather based on empirical rules since the 19th century. As early as 1904, Vilhelm Bjerknes [94] proposed an idea of using a set of equations of fluid mechanics based on the laws of physics to estimate the state of the atmosphere in the future through numerical methods. This idea was attempted to be realized manually by Richardson [95] to predict the global weather in the 1920s. Due to the scale of the forecast and suitable fast computing was unavailable at the time, the idea was not successfully implemented until the 1950s by a scientific team [96]. They used the ENIAC digital computer to solve barotropic vorticity equations numerically [97]. This was the first weather forecast implemented by computers, that provided a basis for current numerical weather prediction methods.

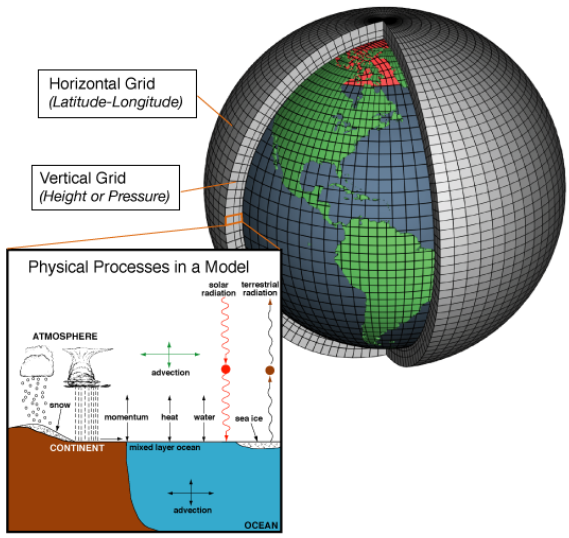

Figure 1.15: The schematic of the modern numerical prediction model [98]

Since then, computers have been widely used in the simulation of weather,

and several groups have begun to engage in the numerical weather prediction [99–102]. With the advent of more powerful computers, the improvement of forecasting methods and the increasement of spatial and temporal resolutions, numerical weather prediction techniques have been gradually developed on a global scale. The schematic of the modern numerical weather forecasting model is given in Figure 1.15. In brief, by dividing the surface of the Earth into discrete grid cells and entering the current weather conditions as input into the numerical prediction model, approximate solutions of future state of the weather in each cell are calculated using finite difference or spectral methods.

1.3.3 Physics-based numerical models

At present, the Numerical Weather Prediction (NWP) is the most popular physics-based numerical model for wind forecasting. It provides a detailed physical description of the atmosphere by utilizing a set of partial differential equations called the primitive equations [103]. For some atmospheric processes that are too small-scale or too complex to be explicitly expressed, NWP models adopt parameterization scheme to represent and reflect them in the primitive equations. Figure 1.16 provides an illustration of different parameterized processes approximated in the model. For more detailed information on parameterization schemes for different processes, refer to [104–106]. To simulate the future state of the atmosphere, the NWP model uses current observations such as wind speed and pressure at the bottom, lateral and top of the atmosphere to initialize equations which are known as the initial boundary conditions. Then the primitive equations are solved numerically by discretization in space and in time, and atmospheric parameters such as surface pressure, three-dimensional wind components, temperature in the future can be obtained.

Regarding wave forecasting, physics-based wave models aim to utilize physical variables to find precise equations that mimic the behavior of wave evolution, and then predict the evolution of the wave energy using numerical techniques. According to the level of parameterization of generation, dissipation and nonlinear wave-wave interactions, the physics-based wave models can be further classified into first-, second- and third-generations [108]. With the increase of computational capacity, the most mature one, namely the third-generation wave models has presently become the most powerful tool for hindcasting and forecasting wave conditions. It applies the wave energy balance equation for describing the evolution of wave spectra in time, geographical and spectral spaces. In addition, it does not impose any priori shapes of the spectrum and considers nonlinear wave-wave interactions [109].

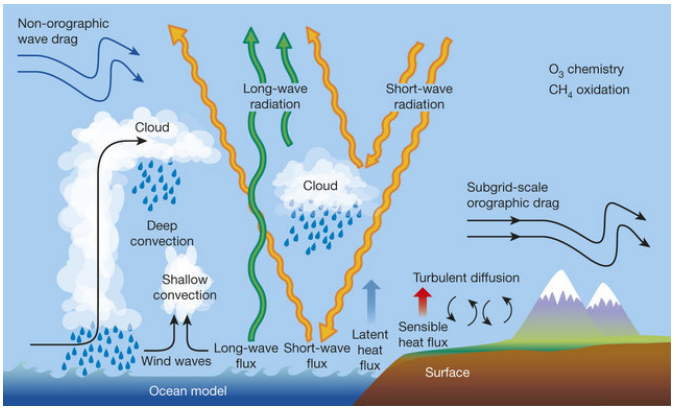

Figure 1.16: The parameterization processes included in NWP models [107]

The most popular of such models are WAM (Wave Modeling) [109], Wave Watch III [108], SWAN (Simulating WAves Nearshore) [110] and STWAVE (Steady State WAve Model) [111]. Among them, WAM and WaveWatch III are ocean scale models which are predominantly used for predictions in deep water, while SWAN and STWAVE are coastal or shelf-sea models which include the wave modifications in the nearshore area and are more oriented towards predictions in shallow water [112]. To drive physics-based numerical wave models for wave forecasting, the forecasted mean wind speed and direction at 10 m above mean sea level are the key inputs. Initial and boundary conditions of the wave field are also needed. Numerical techniques such as the finite difference method are employed for spectral wave computation. Typical forecasted wave parameters are short-term (for example, one-hour or three-hour) wave spectra, from which H_s and T_p for total sea, wind-generated sea and swell can be obtained.

Overall, physics-based numerical models can capture deep existing knowledge based on physical phenomena. However, they are complicated mathematical systems, which include differential and integral equations, parameterization schemes, highly nonlinear empirical expressions, etc. In fact, selection the perfect parameterization schemes to approximate physical processes is challenge. Besides, they normally require large computational and storage resources, which may limit their applications.

1.3.4 Data-driven models

In addition to the physics-based numerical models, some novel machine learning algorithms have been proposed and utilized in weather forecasting

in recent years. Instead of solving differential equations by numerical techniques, machine learning applies data-driven models to provide forecasts by the relation directly found from the historical time series. Therefore, modeling simplicity and high cost efficiency are their significantly advantages. One conventional type of data-driven models is the statistical model, such as the autoregressive (AR) model [113–116], the autoregressive moving average (ARMA) model [114,117–120] and the autoregressive integrated moving average (ARIMA) model [121–124], which expresses the future weather as a linear function of its previous data. However, one issue of statistical models is that they generally show limitations in modeling nonlinear patterns [125]. For complex systems like the atmospheric and wave conditions, it may not be enough to express the system as linear functions. By contrast, neural networks express more comprehensive input-output relationships through a network on the basis of a large amount of historical data of both inputs and outputs. This relationship can be a relation between data at different time steps in a single time series or a relation between different variables with an implicit physical background. At present, the most popular model for weather forecasting is the artificial neural network (ANN) [126–135]. In addition to ANN, wave and wind forecasting by other advanced neural networks, such as the recurrent neural network (RNN) [136, 136, 137], the convolution neural network (CNN) [138] and the adaptive-network-based fuzzy inference system (ANFIS) [139–141], have also been investigated. However, due to the fluctuation and randomness of weather conditions, most of the above studies have mainly focused on one-step-ahead forecasting of weather conditions, while multi-step-ahead forecasting has rarely been studied. Wu et al. [142] proposed a decomposition-ANFIS method to forecast 24-step-ahead wind and wave conditions with relatively good performance. Similar studies [126, 143–145] were also conducted to forecast weather conditions with multiple forecast steps. Although the time scale of weather forecasting has been expanded to a certain extent, multi-step-ahead forecasting of weather conditions is typically faced with growing uncertainties. As a result, the forecast performance of the adopted data-driven models decreased significantly with the increasing forecast time horizon. This implies that although highly capable of training on data, the complexity and randomness of wind and waves still challenge the usage of machine learning algorithms.

1.3.5 Application of weather forecasts in marine operations

As aforementioned, in the execution phase of marine operations, it is necessary to use weather forecasts produced from physics-based numerical methods or machine learning-based methods. The wave and wind forecasting is

strongly dependent on what input information that are available up to the current time. In practice, whether it is possible to get real time measurements or numerical data of wave and wind conditions should be considered. The ideal condition is that all input information up to the current time are available and accurate. If not, the forecast can only rely on the data up to a time instant in the past. In this case, there will be additional uncertainty. However, this issue is not addressed and discussed in the thesis. It is assumed that the weather forecasts utilized in marine operations come from forecasting models with all accurate and known inputs. In the following, three possible applications of weather forecasts in marine operations are described, that are the system response prediction, operational weather windows assessment and response-based operational limit correction.

System response prediction

The forecasted variables, such as H_s, T_p, U_w and wave spectrum, can be used to generate future weather conditions. By means of numerical modelling and dynamic response analysis, dynamic motion responses (such as crane tip motion and blade root motion) and structural responses (such as lift wire tension or stress in structural components) of operation systems can be predicted under these conditions. According to the properties of the operation, two kinds of analysis (i.e., frequency-domain and time-domain response analysis) can be applied. For the former, weather forecasts are combined with transfer functions of the structure to obtain corresponding response spectra and response statistics, such as extreme value of a given reference period. In contrast, for response analysis in time domain, one has to simulate the operation multiple times under the forecasted weather condition and obtain time series of responses, and then process them to get the response spectrum and statistics. Obviously, the quality of weather forecasts greatly affects the accuracy of system responses.

Weather window assessment

For execution of weather-restricted marine operations, the workable weather window is essential to assist the operation decision-making. Weather window is the time interval when marine operations can be performed safely. Normally, it depends on the duration of an operation, allowable sea states and weather forecasts. By means of the comparison results between weather forecasts and allowable sea states, the weather window can be identified. Once the weather window is provided, it is convenient to decide whether and when the operation can be safely performed. In this procedure the quality of weather forecasts is important.

Response-based operational limit correction

In the above two applications, the uncertainty in weather forecasts is not

taken into account. However, ignoring the weather forecast uncertainty will increase the risk of marine operations and increase the possibility of waiting on suitable weather. Furthermore, unpredicted extreme sea states may even cause accidents and casualties during the operation. Therefore, the uncertainty in weather forecasts and their effect on marine operations should be addressed. One possible way is to correct the response-based operational limit more conservative by evaluating and quantifying weather forecasts. This is also one of the objectives of this thesis. The description related to the weather forecast uncertainty will be given in Sec. 1.4

1.4 Weather forecast uncertainty

It is well known that there are uncertainties in weather forecasts, no matter which forecasting method is employed. The accuracy of weather forecasts is normally assessed by comparing forecasted data with reference data from measurements or hindcasts. Then, the forecast error statistics can be calculated to quantify the forecast uncertainty at different forecast lead times. Typical error statistics include mean value and standard deviation, root mean square error (RMSE), correlation coefficient, etc.

Furthermore, how to reflect weather forecast uncertainty when performing marine operations is a key issue. So far, only a few studies have been published on investigating the effect of weather forecast uncertainty on marine operations. At present, an alpha-factor α (a normalized factor less than 1) proposed by DNV [146], is normally used to address the uncertainty in weather forecasts for marine operations. It is determined by evaluating H_s forecasts and the aim of it is to reduce the initial design limit of H_s to a certain extent and therefore making the operation limit more conservative. In practical applications, DNV [8] provides tabulated α-factors for European waters, allowing users to select one for weather-restricted operations based on the operation duration, design wave height, the quality of weather forecasts, whether meteorologists or measurement equipment are available on site, etc. The selected factor can subsequently be used to correct the allowable H_s to include the weather forecast uncertainty. Following this method, a similar study was carried out by Wilcken [147] to generate alpha-factors in the Barents Sea.

Although tabulated alpha-factors for H_s are explicitly given in the standard, tabulated alpha-factors for other wave variables are not provided. It is well known that floating offshore structures are increasingly used for marine operations, and such structures are sensitive to wave periods. For marine operations involving floating systems, forecast uncertainty in wave periods

such as T_p is also important and should be taken into account. Furthermore, the alpha-factor is derived from simple sea state variables without considering the characteristics of offshore systems. In other words, it is independent of the type of marine operations. However, the failure of marine operations is in principle related to the physical response of offshore structures during operations. The extreme response essentially decides whether a specific operation can be safely performed during the execution phase. Therefore, it is necessary to define a response-based factor to quantify the effect of forecast uncertainties in both H_s and T_p on marine operations.

1.5 Aim and scope

The primary aim of the research is to investigate the effect of weather forecast uncertainty on marine operations. In order to achieve this, the main objectives of this thesis are summarized as follows:

- Develop and establish different machine learning-based methods for multi-step-ahead forecasting of wave conditions.
- Assess and compare forecast performance of different forecasting methods and quantify their forecast uncertainty.
- Propose a correction factor to reflect the effect of weather forecast uncertainty on dynamic responses of the system used for marine operations.
- Develop a methodology for assessment of allowable sea states for marine operations, with emphasis on considering the effect of weather forecast uncertainty.
- Take the blade installation of offshore wind turbines as an example to verify the methodology. Generate related correction factors, assess correspondingly allowable sea states and identify workable weather windows for the blade installation.

The scope of this thesis is shown in Figure 1.17, where main topics and the interconnection between different parts are illustrated.

The first part focuses on the use of machine learning algorithms to forecast wave conditions. Two related methods, i.e., the time series-based machine learning (TSML) method and the physics-based machine learning (PBML) method are developed and established. With regard to the forecast horizon, one-step-ahead forecasting is carried out first, in order to verify the

applicability of machine learning algorithms in the scope of weather forecast. Afterwards, multi-step-ahead forecasting is performed, to take into account the operation duration required in the execution of marine operations. On the basis of the multi-step-ahead forecast results, the forecast uncertainty at each forecast step of the models is quantified.

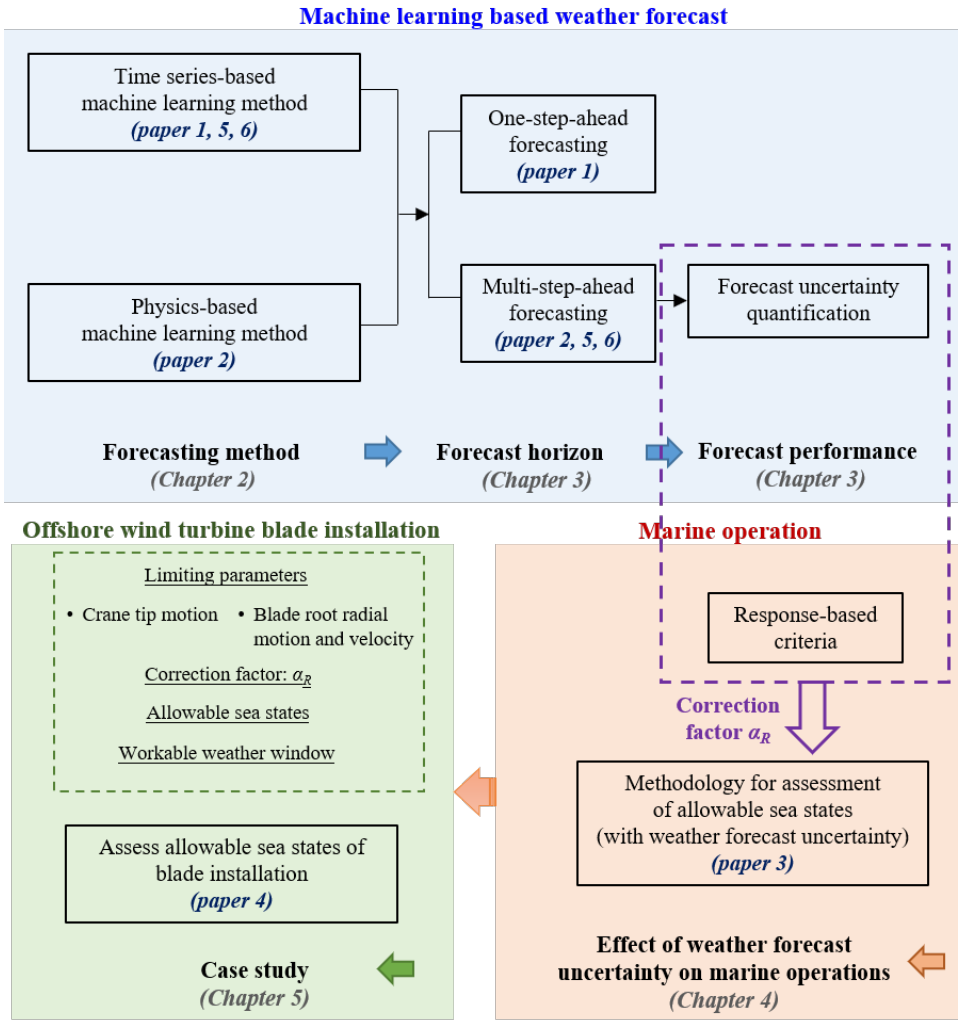

Figure 1.17: Scope of the thesis

Subsequently, the effect of weather forecast uncertainty on marine operations is investigated. By combining uncertainty quantification of weather forecasts with response-based operational limiting criteria for an operation,

a correction factor α_R is derived and generated in terms of the forecast lead time. This factor makes the operational limit more conservative by taking weather forecast uncertainty into account. In addition, a general methodology for assessment of allowable sea states for marine operations is proposed, with emphasis on considering weather forecast uncertainty. It consists of uncertainty quantification of the sea state forecast, statistical analysis of dynamic responses of the coupled system for marine operations and allowable sea state assessment using response-based criteria.

Finally, based on the methodology, the blade installation for offshore wind turbines using a semi-submersible crane vessel is performed as a case study. Typical limiting response parameters, namely the crane tip motion, and blade root radial motion and velocity are selected to illustrate the feasibility of the method using frequency- and time-domain response analysis approaches, respectively. The α_R of each limiting parameter is generated first. Then, the allowable sea states of the blade installation are assessed, including the effect of the weather forecast uncertainty on the operation decision-making. By comparison the allowable sea states with weather forecasts in the execution phase of installation, workable weather windows can be further identified and selected.

1.6 Thesis outline

This thesis is composed of six chapters. The content of each chapter is briefly summarized below.

Chapter 1:
This chapter introduces background, aim and scope, and outline of the thesis. An overview of marine operations, weather forecasting, and weather forecast uncertainty is also presented.

Chapter 2:
This chapter introduces machine learning-based weather forecasting methods. A brief introduction of machine learning is given, focusing on the key issues that should be considered in weather forecasting. Then several machine learning techniques utilized in the thesis are introduced. Afterwards, two machine learning-based weather forecasting methods are developed, and approaches of forecast performance evaluation are presented.Finally, how to apply machine learning-based weather forecasting methods in reality as well as their assumption and limitation are discussed.

Chapter 3:
This chapter first presents a brief description of the study area and used metocean data. Subsequently, weather forecast results based on two types

of machine learning-based forecasting methods are summarized and their forecast uncertainties are quantified. In addition, a comparison analysis between machine learning-based methods and physics-based numerical methods is performed.

Chapter 4:

This chapter introduces a methodology for developing a response-based alpha-factor α_R and assessing allowable sea state of marine operations considering weather forecast uncertainty. The key parameters, framework, and the relevant techniques are also given.

Chapter 5:

The blade installation of offshore wind turbines by a semi-submersible crane vessel is performed. Following the proposed methodology, the α_R factors of limiting response parameters (i.e., crane tip motion, blade root radial motion and velocity) are derived respectively. In addition, the allowable sea states of the blade installation are assessed.

Chapter 6:

Conclusions, highlight of original contributions and recommendations for future work are provided in this chapter.

Chapter 2

Machine learning-based weather forecasting methods

This chapter introduces weather forecasting methods utilized in the thesis, with an emphasize on adopting machine learning algorithms. It starts from an overview regarding basic information of machine learning and types of datasets required for development of data-driven models. Meanwhile, some key issues in developing weather forecasting methods are highlighted, including the selection of input variables and classification of forecast steps. Afterwards, several machine learning techniques are briefly introduced. Two forecasting methods, i.e., time series-based machine learning (TSML) method and physics-based machine learning (PBML) method, are subsequently developed and established. Application, assumption and limitation of these weather forecasting methods will be summarized at last.

2.1 Introduction

2.1.1 Machine learning

Machine learning, which belongs to the field of computer science, is the application of artificial intelligence techniques to automatically learn from historical data and make predictions of future data. The origin of machine learning can be traced back to the 1950s. This term was proposed by an American computer scientist Arthur Samuel in 1959 [148], who defined machine learning as a 'Field of study that gives computers the ability to learn without being explicitly programmed'. Compared with traditional models with explicit equations, machine learning can quickly and automatically generate models by analyzing higher-dimensional and more complex data,

finding relationships between the system state variables (i.e., inputs and outputs) and then make predictions on new input based on the relationships. In recent years, with cheaper and more powerful computing processing, the growing volumes and varieties of available data, as well as affordable data storage, machine learning has become more popular than ever. At present, machine learning has been widely used in various fields, such as speech recognition [149–152], processing images [153–156] and automatically translations [157–159]. In the field of marine engineering, machine learning has also tried to be applied to response prediction [160–162], damage detection [163–165], reliability assessment [166] and fatigue analysis [167, 168] of offshore structures in recent years.

The thesis focuses on exploring and applying machine learning algorithms to forecast wave conditions. The machine learning-based forecasting model can be simply expressed as Eq. (2.1), in which X and Y are the input and output variables, respectively. For weather forecasting, input and output variables can be selected relying on the correlation between data of a single environmental variable, or based on physics so that the selected input and output variables have a clear physical relationship. This will be discussed in detail in Sec. 2.1.4. In addition, f is an algorithm that is employed to learn the mapping function from input to output. In order to establish f and evaluate the forecast performance of the model, different types of datasets are required.

$$Y = f(X) \tag{2.1}$$

2.1.2 Training, testing and validation sets

According to the purpose of data usage, three types of datasets are required in machine learning, which are the training data, validation data and testing data. All of them consist of pairs of inputs and outputs.

- **Training data:** A set of dataset used to train the model, i.e., to fit the parameters in f. The corresponding procedure is called training process.
- **Validation data:** A set of dataset used to tune the model's hyperparameters, in order to prevent the model from overfitting during the training process.
- **Testing data:** A set of dataset used to test the performance of the trained model. The corresponding procedure is called testing process.

When using machine learning, the training process needs to be performed first to learn the model based on the training and validation data. Then the trained model is checked with a new set of data (i.e., testing data) in the testing process. In this process, the forecast performance of the models can be evaluated through comparison between forecasted data and actual data.

2.1.3 Forecast step

For weather forecast based on machine learning algorithm, it is important to point out the forecast step. According to the number of forecast steps, forecasting can be divided into two types, which are one-step-ahead forecasting and multi-step-ahead forecasting. At present, most of the studies related to the machine learning-based weather forecast are focused on the former one. One-step-ahead forecasting only generates one value at the next time step, and therefore, it provides weather for the time-step immediately following the current time and no information about the behavior of weather conditions for longer time. In comparison, multi-step-ahead forecasting aims to generate multiple time steps forecasts in the future, i.e., the future time series of weather. This is of great significance for marine operations, since it can provide overall information about the future weather covering their execution duration. However, multi-step-ahead forecasting is challenging, since it typically faces a growing amount of uncertainties, such as error accumulation, lack of enough input information and so on.

2.1.4 Input variable selection

As illustrated in Eq. (2.1), there are two important components required to be determined, i.e., input and output variables, and machine learning techniques. The following part discusses the input variable selection, with special emphasis on issues related to the weather forecast.

The selection of input and output variables is an initial step for developing a forecasting model and has a significant impact on forecast performance. Regarding wave forecasting, there could be various options for the input-output combination. For instance, input and output data can be selected just based on possible correlation in time series of the forecast variable. This means that the future data merely depends on its relationship with the past data, which does not reflect a physical process. In addition, past data from other variables related to the output variable can be additionally introduced. Accordingly, the effect of past data of other variables on the future data of the forecast variable is included, and physical phenomena in wave fields can be implicitly considered to a certain degree. But in principle,

the above two options make forecasts by capturing the correlation between data in one or more time series. Thus, they are called the time series-based machine learning (TSML) method in the thesis, which are introduced in Secs 2.1.4.1 and 2.1.4.2, respectively.

Furthermore, the input-output relationship can also be selected based on explicit physical processes. The method of selecting input and output through physical phenomena and using machine learning to train the model and make forecast is called the physics-based machine learning (PBML) method. From the perspective of wave evolution, variables related to wave generation may be considered as inputs. If all necessary input information are included, such system is typically causal that can result into a better forecasting. However, the completeness of the input variable and availability of input information should also be taken into account.

According to different input-output combinations, machine learning-based weather forecasting methods developed in the thesis are classified into following three types. For the sake of illustration, one-step-ahead H_s forecasting is taken as an example to describe them respectively in Secs 2.1.4.1 to 2.1.4.3.

- Univariate time series-based machine learning (TSML) method
- Multivariate time series-based machine learning (TSML) method
- Physics-based machine learning (PBML) method

2.1.4.1 Univariate TSML method

This method has been commonly used to make prediction in a wide variety of industries for years. This is the simplest one of the three, since it only relies on auto-correlations in a single time series. One example can be seen in Eq. (2.2), which shows the univariate TSML model for H_s forecasting. In the equation, t is assumed as the current time. The current data $H_s(t)$ and past data $H_s(t-1)$, $H_s(t-2)$, ... are used as inputs to forecast the next value $H_s(t+1)$.

$$H_s(t+1) = f(H_s(t), H_s(t-1), ...) \tag{2.2}$$

For this method, the input data can be selected by checking auto-correlation functions of the forecast variable, in order to decide how much information in the past will affect the future data. No physical phenomena is explicitly taken into account in such a model. Wave and wind fields generally show complex and non-stationary patterns, and the statistical

variables such as H_s and T_p will change irregularly and dynamically with time. This makes the weather forecasting much more difficult to handle compared with other prediction problems. For one-step-ahead forecasting, the univariate TSML method can perform well. Whereas it may not have sufficient capacity to provide accurate weather forecasts when the forecast horizon expands, since the correlation between data in time series will be decreased significantly.

2.1.4.2 Multivariate TSML method

In addition to considering time series of the forecast variable, it is also possible to add time series of other variables to assist in forecasting. The method of using past data of multiple variables as input is called multivariate TSML method. One example is shown in Eq. (2.3), which uses the past and current U_w and H_s to forecast future H_s.

$$H_s(t+1) = f(H_s(t), U_w(t), H_s(t-1), U_w(t-1), ...) \tag{2.3}$$

Obviously, compared with the previous method, the multivariate TSML method adds wind field information (i.e., past and current mean wind speed data) to help forecast. This means that in addition to using auto-correlations of data in the H_s time series, the cross-correlation between previous U_w and future H_s is also considered to build the forecasting model. Since there is an intrinsic physical relationship between U_w and H_s in nature, the physical properties of the wave field can be included in the forecasting model to a certain extent by this method. Nevertheless, it essentially belongs to a time series forecasting method, not a method based on physical phenomena.

2.1.4.3 PBML method

The above two methods assume the future H_s can be completely determined by the past H_s and/or U_w. The lack of causality is a potential disadvantage of them. Alternatively, the forecasting model can take physical background into account by applying the primary inputs in physics-based wave models to design the model structure. With reference to the physics-based wave forecasting system, two primary inputs are included in the PBML method, namely the initial condition and the wind forcing. On one hand, the model is initialized with the wave condition characterized by H_s and T_p at the current time t. On the other hand, the wind conditions from the past to the time of forecast, characterized by mean wind speed U_w and wind direction D_u at different time steps, should be involved as the wind forcing in the

wave forecasting system. By doing these, the input variables of this method are similar to the physic-based wave models but with the help of machine learning to make forecast. It should be mentioned that this is a simplification of physical modelling because only wind is considered as forcing. The input wind forcing reflects the physical process of wave generation, while other processes like wave dissipation and wave-wave interactions considered in physical modelling could be automatically learned by machine learning algorithms from data. The corresponding forecasting model based on the PBML method can be shown in Eq. (2.4).

$$H_s(t+1) = f(H_s(t), T_p(t), U_w(t+1), U_w(t), D_u(t+1), D_u(t), ...) \quad (2.4)$$

Depending on the utilized wind forcing, the PBML model can be a quasi-static system or a mixed system. If the wind forcing only has the wind speed and direction at the same time as the output, the PBML model is represented as a quasi-static system. Besides, it is also possible to additionally include the wind forcing at several previous time steps before the forecast step, in attempting to capture the dynamic characteristics of the wind field (e.g., $U_w(t)$, $D_u(t)$ in Eq. (2.4)). In this case, the forecasting model is a combination system, considering both quasi-static and dynamic processes. The most essential difference between this method and the multivariate TSML method is that the former adds future forcing as inputs, while the TSML method only includes past variable information.

2.2 Machine learning techniques

After determining the input and output variables, machine learning techniques should be employed to learn the inherent relationship between them based on the training data. Several machine learning techniques which are used for weather forecasting in the thesis are introduced. Firstly, two data pre-processing techniques are described, that can help to extract the useful information from the data and improve the learning ability of the model. Afterwards, four data-driven models utilized for weather forecasting are presented. Finally, a description of multi-step-ahead forecast strategies is given.

2.2.1 Data pre-processing

Data pre-processing is a data mining technique whose main purpose is to transform raw data into an understandable format [169]. In this subsection, two pre-processing techniques, which are decomposition technique and empirical mode decomposition (EMD), are described separately.

2.2.1.1 Decomposition technique

The decomposition technique was developed by Athanassoulis and Stefanakos [170], which is able to eliminate the non-stationary influence in weather prediction process. It converts the initial time series to stationary ones by extracting the monthly mean value vector and the covariance matrix. Based on this technique, Stefanakos [141,171,172] processed the wind and wave data and successfully employed adaptive-network-based fuzzy inference system (ANFIS) to make one-step-ahead forecast at the North Atlantic Ocean. The decomposition model for multivariate time series [173] is defined as

$$\begin{array}{ccccccc} \mathbf{Y}(t) & = & \mathbf{M}(t) & + & \mathbf{\Sigma}(t) & \mathbf{W}(t) \\ (N \times 1) & & (N \times 1) & & (N \times N) & (N \times 1) \end{array} \tag{2.5}$$

or, in matrix notation

$$\begin{bmatrix} Y_1(t) \\ Y_2(t) \\ \vdots \\ Y_n(t) \\ \vdots \\ Y_N(t) \end{bmatrix} = \begin{bmatrix} M_1(t) \\ M_2(t) \\ \vdots \\ M_n(t) \\ \vdots \\ M_N(t) \end{bmatrix} + \begin{bmatrix} \Sigma_{11}(t) & \Sigma_{12}(t) & \cdots & \Sigma_{1N}(t) \\ \Sigma_{21}(t) & \Sigma_{22}(t) & \cdots & \Sigma_{2N}(t) \\ \vdots & \vdots & \vdots & \vdots \\ \Sigma_{n1}(t) & \Sigma_{n2}(t) & \cdots & \Sigma_{nN}(t) \\ \vdots & \vdots & \vdots & \vdots \\ \Sigma_{N1}(t) & \Sigma_{N2}(t) & \cdots & \Sigma_{NN}(t) \end{bmatrix} \begin{bmatrix} W_1(t) \\ W_2(t) \\ \vdots \\ W_n(t) \\ \vdots \\ W_N(t) \end{bmatrix} \tag{2.6}$$

where N is the number of time series. ***Y(t)*** and ***W(t)*** represent the initial and corresponding stationary time series, respectively. ***M(t)*** and $\mathbf{\Sigma}(t)$ are the monthly mean value vector and the covariance matrix with period of one year respectively, which represent the 'seasonal patterns' of the initial time series. They can be estimated by averaging the monthly mean values $M_{3,n}(j,m)$ and the covariance matrix $S_{3,nl}(j,m)$ over J years [174], which are shown as Eqs. (2.7) and (2.8), respectively. In these two equations, $Y_n(j,m,\tau_k)$ is a re-parameterized expression of $Y_n(t)$, shown as Eq. (2.9).

$$\tilde{M}_{3,n}(m) = \frac{1}{J}\sum_{j=1}^{J} M_{3,n}(j,m) = \frac{1}{J}\sum_{j=1}^{J}\frac{1}{K_m}\sum_{k=1}^{K_m} Y_n(j,m,\tau_k) \tag{2.7}$$

$$\begin{aligned} &\tilde{S}_{3,nl}(m) = \tfrac{1}{J}\sum_{j=1}^{J} S_{3,nl}(j,m) = \\ &\tfrac{1}{J}\sum_{j=1}^{J}\sqrt{\tfrac{1}{K_m}\sum_{k=1}^{K_m}[Y_n(j,m,\tau_k) - M_{3,n}(j,m)][Y_l(j,m,\tau_k) - M_{3,l}(j,m)]}\,, \\ &n,l = 1,\cdots,N \end{aligned} \tag{2.8}$$

$$\left\{ Y_n(j,m,\tau_k), \quad \begin{array}{c} j=1,\cdots,J \\ m=1,\cdots,12 \\ k=1,\cdots,K_m \end{array} \right\}, \quad n=1,\cdots,N \tag{2.9}$$

where j is the year index, m is the month index and τ_k is the k^{th} observation in the m^{th} month. The number of observations in the m^{th} month is K_m.

The aim of the decomposition technique is to reduce the seasonal effects in the metocean data. One example is illustrated in Figure 2.1, where the initial time series and the corresponding decomposed time series of H_s in one year are shown in subfigure (a) and (b), respectively. It is visible that the decomposed time series becomes a zero-mean stochastic process and the seasonal effects in the data could be reduced to a certain degree. By using the decomposed time series, it is easier to train the forecasting model and then generate forecasts.

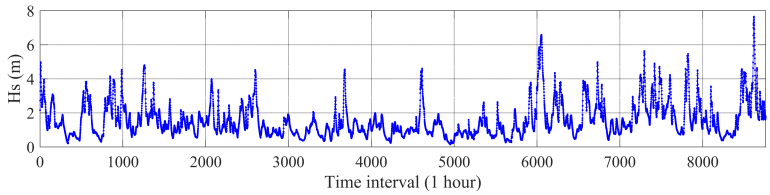

(a) Initial time series

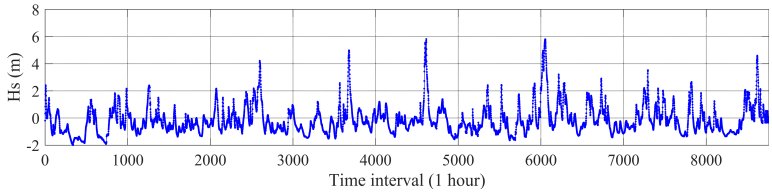

(b) Decomposed time series

Figure 2.1: Initial and decomposed time series of H_s in one year

2.2.1.2 EMD

Empirical mode decomposition (EMD) is a self-adaptive time series decomposition technique which usually analyzes non-linear and non-stationary signals [175]. The basic idea of EMD is to decompose a signal into a set of oscillatory components called intrinsic mode functions (IMFs) and a residue by sifting process [176]. An IMF is a complete and nearly orthogonal basis for the signal and it needs to fulfill two basic conditions:

a) the number of zero-crossings and extremes must be equal or differ at the most by one in the entire data set;

b) the mean value of the envelope defined by local minima and the envelope defined by local maxima is zero at any point in the IMF.

According to the above definitions, an initial time series $Y(t)$ can be decomposed as

$$Y(t) = \sum_{i=1}^{n-1} I_i(t) + r_n(t) \tag{2.10}$$

where $I_i(t)$ is the i^{th} IMF and $r_n(t)$ is the residue of the initial signal.

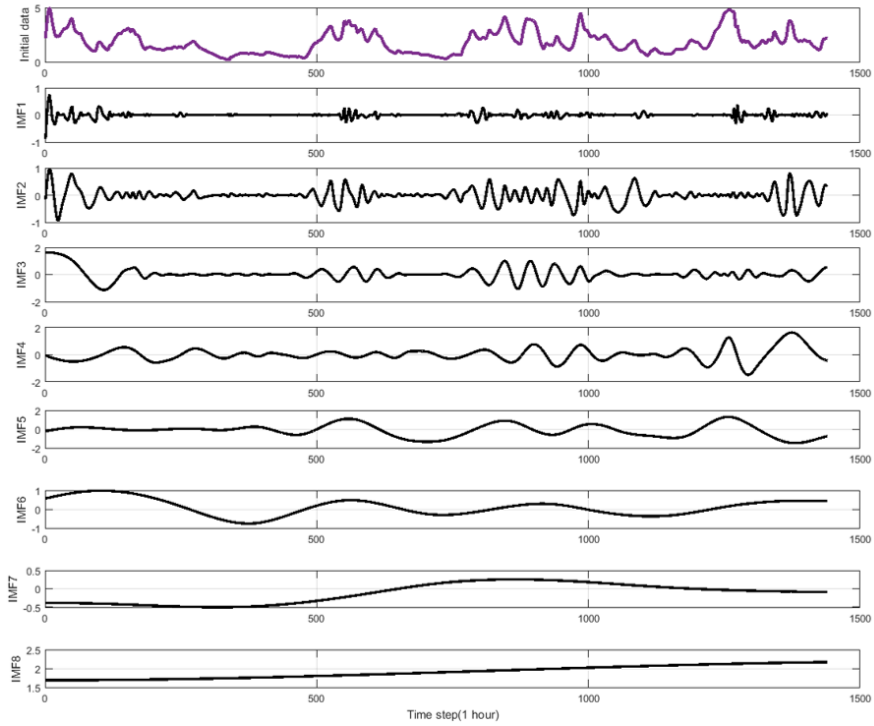

Figure 2.2: Illustration of using EMD for a H_s time series

Figure 2.2 shows an example of the decomposition result of a H_s time series based on the EMD. After decomposition, forecasting model for each IMFs or residue is developed to make forecast. Afterwards, all generated forecasts will be recombined to get the final result.

2.2.2 Data-driven models

In this subsection, four representative data-driven models are introduced, which are the autoregressive integrated moving average (ARIMA), artifi-

cial neural network (ANN), recurrent neural network (RNN) and adaptive-network-based fuzzy inference system (ANFIS).

2.2.2.1 ARIMA

Autoregressive integrated moving average (ARIMA) model is one classical forecasting technique based on the time series statistical analysis. It expresses the future data of a variable as a linear combination of its past behavior by analyzing the correlation between values in a time series. ARIMA is the combination of autoregressive (AR), integrated (I) and moving average (MA) processes. In order to reflect the structure of an ARIMA model, it is generally denoted as ARIMA (p, d, q), where:

a) p is the order of the AR model, representing the number of lags of the past data.

b) d is the order of the differencing, which is used to stable the initial data.

c) q is the order of MA model, representing the number of lags of the past errors.

An AR model is a model where the output depends linearly on its own lags and a MA model is the one that the output depends linearly on the lagged forecast errors. The AR (p) model and MA(q) model can be written as Eqs. (2.11) and (2.12), respectively.

$$Y(t) = c + \sum_{i=1}^{p} \phi_i Y(t-i) + \varepsilon(t) \tag{2.11}$$

$$Y(t) = \mu + \sum_{j=1}^{q} \theta_j \varepsilon(t-j) + \varepsilon(t) \tag{2.12}$$

where $Y(t)$ is the output at time t. $Y(t-i)$ and $\varepsilon(t-j)$ are the past data and white noise error at time $t-i$ and $t-j$, respectively. ϕ_i and θ_j are the i^{th} and j^{th} coefficients of the AR and MA models, respectively. c and μ are a constant value and the mean of the series, respectively.

A typical ARIMA model which expresses the data at time t as a linear function of previous data and white noise errors can be defined in the form

$$\hat{Y}(t) = c + \sum_{i=1}^{p} \phi_i \hat{Y}(t-i) + \sum_{j=1}^{q} \theta_j \varepsilon(t-j) + \varepsilon(t) \tag{2.13}$$

where $\hat{Y}(t)$ is the predicted data at time t. It should be noted that the data $\hat{Y}(t)$ in Eq. (2.13) are stationary after making a d-order difference to the initial data. The description of other parameters is the same as above.

2.2.2.2 ANN

Artificial neural network (ANN) is a typical machine learning algorithm that mimics the process of biological neurons system for receiving, processing and transmitting information [177]. Generally, an ANN model consists of three types of layers, namely an input layer, one or more hidden layers and an output layer. All layers are composed of several neurons. Neurons in different layers are simple but highly interconnected, in order to simulate the processing and transmission of information in the human brain. An ANN model with one hidden layer is illustrated in Figure 2.3 as an example.

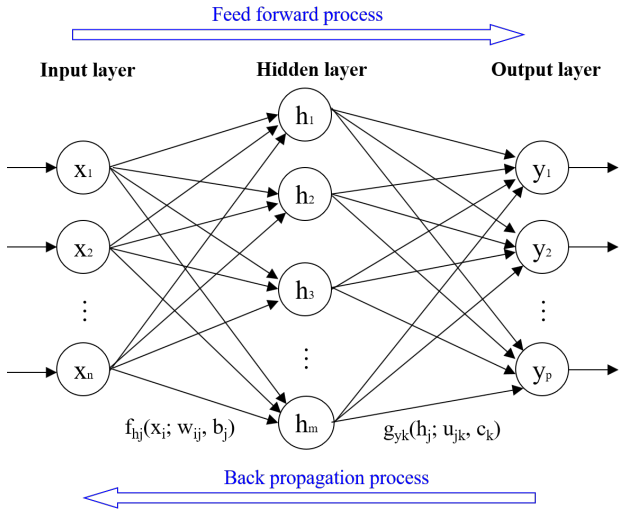

Figure 2.3: Structure of a typical ANN

The input and output layers contain n and p neurons representing the input and output variables, respectively. The middle layer connecting the input and output layers is the hidden layer, which contains m neurons. The neuron in each layer receives input information (from the neurons in the previous layer based on the corresponding weight, bias and activation function) and then further propagates it forward to the neurons in the following layer. Eqs. (2.14) and (2.15) show the calculations of the hidden neuron and output neuron, respectively.

$$h_j = f_{jh}\left(\sum_{i=1}^{n} w_{ij}x_i + b_j\right) \quad , \quad j = 1, \cdots, m \tag{2.14}$$

$$y_k = g_{yk}\left(\sum_{j=1}^{n} u_{jk} h_j + c_k\right) \quad , \quad k = 1, \cdots, p \tag{2.15}$$

where f and g are activation functions of the hidden and output layers, respectively. The commonly used types of activation functions are linear, sigmoid, hyperbolic tangent and so on. w_{ij} and u_{jk} are weights from input neuron x_i to hidden neuron h_j and from hidden neuron h_j to output neuron y_k, respectively. b_j and c_k are biases of neurons h_j and y_k, respectively.

During the training process, the optimal weights and biases can be determined by using the error back propagation algorithm [178, 179]. This algorithm aims to minimize the difference between actual and forecasted values by updating the weights and biases of the network. In the training phase, the initial weights and bias are selected arbitrarily. Then, they are adjusted iteratively to reduce the error rate by an optimization algorithm (e.g., the gradient descent method). When the overall error is within an acceptable range, the training process stops and the optimal neural network is determined. In the subsequent testing phase, the forecasts can be generated directly by using this optimal neural network with new inputs.

The ANN model has proven to be a powerful tool in a wide variety of weather applications since the late 1980s. More recently, advanced neural networks have been proposed to improve the efficiency of the algorithms and utilize more computational power. Among them, RNN and ANFIS are two representative networks. The following parts of this subsection will introduce them separately.

2.2.2.3 RNN

Recurrent neural network (RNN) is an advanced neural network which is especially designed for analyzing sequential data [180]. Compared to a classical ANN, RNN can preserve the intrinsic temporal dependencies in the time series based on the existence of loop structure where the current output depends on the previous hidden neurons. As illustrated in Figure 2.4(a), x_t is the input, y_t is the output and h_t is the hidden output at time step t. U, V and W are the input weights, output weights and recurrent layer weights, respectively. As shown in Eq. (2.16), the hidden state h_t is computed not only based on the current input x_t, but also on the previous hidden state h_{t-1}, from which it can make use of the information of the previous sequence.

$$h_t = \tanh(Ux_t + Wh_{t-1}) \tag{2.16}$$

where tanh is the hyperbolic tangent function.

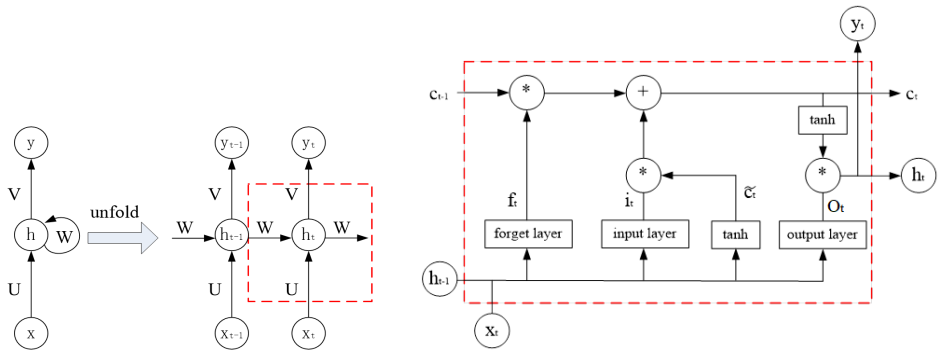

(a) RNN (b) LSTM

Figure 2.4: The structures of RNN and LSTM

However, RNN may suffer from the vanishing gradient problem during the training process, especially in long sequence [181]. In this case, long short-term memory (LSTM) as an extended version of RNN and proposed by Hochreiter and Schmidhuber [182], is able to tackle this problem through its special structure of hidden layers. In contrast to a standard RNN, three gate structures, namely forget gate, input gate and output gate, are incorporated in the hidden layer in LSTM, to control information flow between different time steps and avoid the long-term dependencies problem. Figure 2.4(b) shows a typical structure of LSTM, where i_t, f_t, and o_t represent the input, forget and output gates at time t, respectively. c_t and $\tilde{c}(t)$ represent the memory cell and the updated memory cell at time t, respectively. To be specific, the forget gate f_t decides the proportion of old information to be forgot in the new memory cell c_t through Eq. (2.17). The input gate i_t and the updated memory cell $\tilde{c}(t)$ decide the proportion of new information to be added in the memory cell c_t through Eqs. (2.18) and (2.19), respectively. The output gate o_t controls the proportion of new information to be exported through Eq. (2.20). Based on those, memory cell c_t is calculated by Eq. (2.21). Finally, the output y_t can be expressed as Eq. (2.22). In Eqs. (2.17) to (2.22), σ represents the sigmoid function. w and b are the weight and bias, respectively.

$$f_t = \sigma(w_f x_t + u_f h_{t-1} + b_f) \tag{2.17}$$

$$i_t = \sigma(w_i x_t + u_i h_{t-1} + b_i) \tag{2.18}$$

$$\tilde{c}_t = \tanh(w_c x_t + u_c h_{t-1} + b_c) \tag{2.19}$$

$$o_t = \sigma(w_o x_t + u_o h_{t-1} + b_o) \tag{2.20}$$

$$c_t = f_t c_{t-1} + i_t \tilde{c}_t \tag{2.21}$$

$$y_t = o_t \tanh(c_t) \tag{2.22}$$

2.2.2.4 ANFIS

Adaptive-network-based fuzzy inference system (ANFIS) is a hybrid model that is a combination of a fuzzy inference system (FIS) and an ANN. FIS is a process mapping inputs to an output based on the membership functions (MFs) and IF-THEN rules. MFs characterize fuzziness, which provides a measure of the similarity of the element to a fuzzy set. For example, if X is a universe of discourse (such as H_s) and x is an element of X, then a fuzzy set O (such as 'High') on X can be described as Eq. (2.23). In addition, IF-THEN rules represent the conditional statements containing fuzzy logic and the expression form is 'If x is A, then y is B'. An example is shown in Eq. (2.24).

$$O = \{(x, \mu_O(x)) \ , \quad x \in X \ \} \tag{2.23}$$

where $\mu_O(x)$ is the membership function that is associated with x in fuzzy set O and expresses the degree to which a value of H_s belongs to set 'high'. The most common types of MFs are triangular, Gaussian and sigmoid.

$$\begin{array}{ll} IF & x_1 \ \ is \ \ S_r^{(1)}, \quad x_2 \ \ is \ \ S_r^{(2)} \ , \ \cdots \\ THEN & y = p_r x_1 + q_r x_2 + \cdots \end{array} \tag{2.24}$$

where x_i and y are the inputs and output, respectively. $S_r^{(n)}$ is a linguistic value (such as 'low' or 'high' for H_s), which is represented by a fuzzy set. p_r and q_r are parameters that control the rule.

A basic structure of a FIS is illustrated in Figure 2.5, which is generally composed of four components:

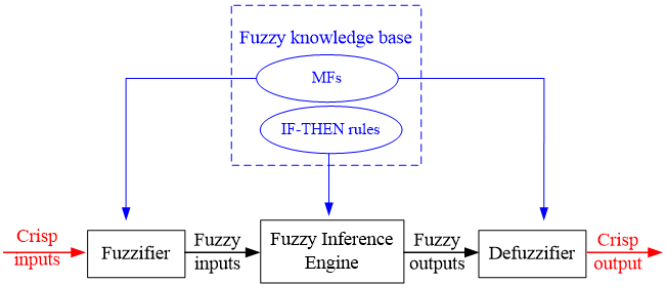

Figure 2.5: Structure of FIS

- Fuzzy knowledge base, that contains the MFs and IF-THEN rules;

- Fuzzifier, that fuzzifies the crisp inputs into fuzzy inputs by using the MFs;
- Inference engines, that maps fuzzy inputs to fuzzy outputs according to the IF-THEN rules;
- Defuzzifier, that defuzzifies the fuzzy outputs into a crisp output.

In the FIS, parameters in both MFs and IF-THEN rules can only be determined based on the experience of experts or past available data of the system. Since they cannot be adjusted automatically and may cause poor forecast performance, a new strategy called ANFIS was proposed by Jang [183] that uses ANN together with FIS. In the ANFIS, ANN is introduced to optimize the parameters of IF-THEN rules and MFs using a hybrid learning algorithm of the gradient descent and the least-squares estimate. Thus, ANFIS can make use of the advantages of both FIS and ANN. In practice, the structure of ANFIS is similar to that of a multi-layer neural network. ANFIS has an input layer, an output layer and three hidden layers that are related to MFs and IF-THEN rules. To illustrate it, the structure of a simple ANFIS that consists of two inputs, namely, x_1 and x_2, and one output, namely, y, is presented in Figure 2.6.

In the ANFIS architecture, the first layer is the input layer, which contains crisp inputs x_1 and x_2. The second layer is the fuzzifying layer, in which the inputs x_i are fuzzified into the membership values $\mu_{Aj}(x_i)$ based on the MFs of linguistic labels A_j, as expressed in Eq. (2.25). This layer is considered as an adaptive layer since the outputs depend on the parameters in the MFs. For example, the MFs, which are denoted as μ_{Aj}, can be selected as Gaussian-type functions and their parameters should be determined.

$$O_{i,j} = \mu_{Aj}(x_i) \ , \quad for \quad i,j = 1,2 \tag{2.25}$$

If the number of crisp inputs exceeds one, the weight of each rule must be determined by using fuzzy operators. To estimate the weights, the third layer is further divided into two layers, which are called the implication and normalizing layers. In these two layers, the firing strength $w_{i,j}$ and the normalized firing strength $\bar{w}_{i,j}$ for each rule are calculated by Eqs. (2.26) and (2.27), respectively.

$$w_{i,j} = \prod_i \mu_{Aj}(x_i) \ , \quad for \quad i,j = 1,2 \tag{2.26}$$

$$\bar{w}_{i,j} = \frac{w_{i,j}}{\sum w_{i,j}} \ , \quad for \quad i,j = 1,2 \tag{2.27}$$

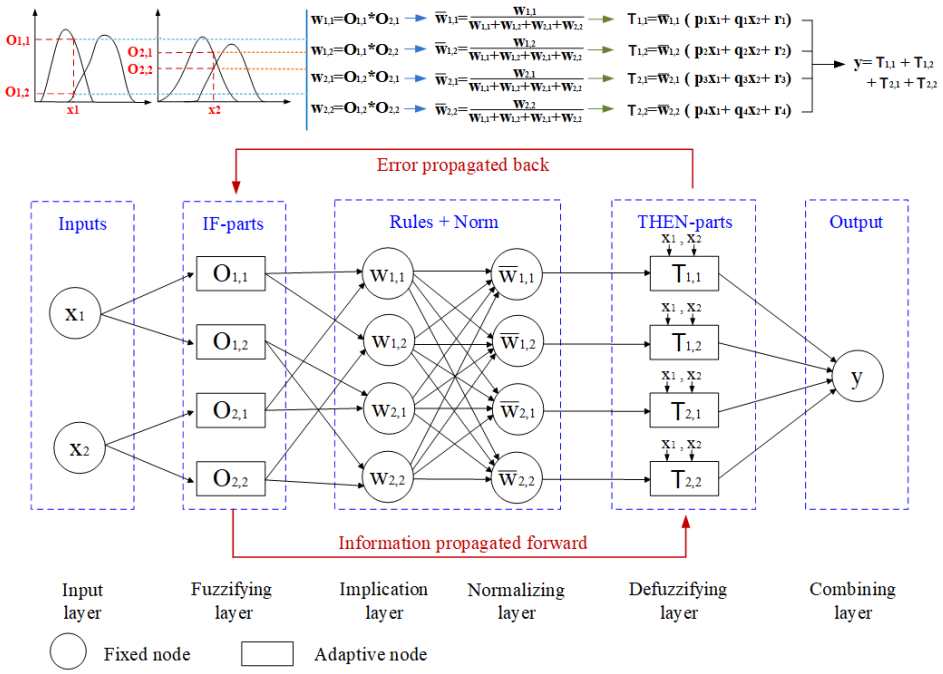

Figure 2.6: ANFIS architecture

Then, the outcome $T_{i,j}$ of each rule can be calculated in the defuzzifying layer using the corresponding IF-THEN rule with specific weights as expressed in Eq. (2.28). Likewise, this layer is also an adaptive layer because parameters p, q and r in the IF-THEN rules should be determined based on the training data.

$$\begin{aligned} T_{i,j} &= \bar{w}_{i,j} \cdot y_{i,j} = \bar{w}_{i,j} \cdot (p_r x_1 + q_r x_2 + r_k), \\ for \quad & i,j = 1,2, \quad k = 1,2, \quad \cdots, i*j \end{aligned} \tag{2.28}$$

By summing all outcomes $T_{i,j}$, the overall output y can be finally estimated based on Eq. (2.29).

$$y = \sum T_{i,j} \tag{2.29}$$

In this process, an adaptive neural network is applied to determine the parameters in the two adaptive layers, which is represented by the red cycle in Figure 2.6. By performing this procedure based on the training data, the corresponding optimal ANFIS can be identified.

2.2.3 Multi-step-ahead forecast strategies

For weather forecasting, a key issue is the forecast horizon. Given that execution of one or a series of continuous marine operations usually takes a few hours to a few days, forecasting a sequence of weather conditions in the future (i.e., multi-step-ahead forecasting) is required. Four strategies used in the thesis for multi-step-ahead forecasting are introduced, which are named M-1, M-N, M-mN and M-1 slope models. The difference between these models is the way to select input-output pairs. It's difficult to conclude which model is the best, since all models have their advantages and disadvantages. To maintain the consistency of the variables, t is assumed as the current time and $X(t)$ denotes data at time t. Besides, N and M denote the number of forecast steps (i.e., the forecast horizon) and input data, respectively.

2.2.3.1 M-1 model

The M-1 model is defined as applying the previous M data of a time series to forecast the next data based on a one-step-ahead forecasting model, as shown in Eq. (2.30), in which f_1 denotes the M-1 model.

$$X(t+1) = f_1(X(t), X(t-1), \cdots, X(t-M+1)) \tag{2.30}$$

To obtain N-step-ahead forecasts, the above model needs to be executed N times recursively. In this procedure, the forecasted value of the previous step is used as one input for the next step forecasting. The mechanism is illustrated in Figure 2.7. Considering H_s as an example, after establishing the M-1 model, one-step-ahead forecast $\hat{H}_s(t+1)$ is obtained by:

$$\hat{H}_s(t+1) = f_1(H_s(t), H_s(t-1), \cdots, H_s(t-M+1)) \tag{2.31}$$

Then, $\hat{H}_s(t+1)$ is considered as a part of input data for forecasting the next-step value $\hat{H}_s(t+2)$ based on the same forecasting model f_1:

$$\hat{H}_s(t+2) = f_1(\hat{H}_s(t+1), H_s(t), H_s(t-1), \cdots, H_s(t-M+2)) \tag{2.32}$$

The same procedure is repeated N times and correspondingly, $\hat{H}_s(t+1)$ to $\hat{H}_s(t+N)$ are forecasted iteratively. The main advantage of the M-1 model is that it is relatively easy since only one training process is required for establishing the forecasting model and this model does not change between steps. Therefore, the computational efficiency is high. However, the iteration process may lead to accumulated errors since the forecasted data is also involved in the next step forecasting. Especially when N exceeds M,

the input set does not contain any actual data after M-step-ahead forecasting, but only forecasted values. In such cases, the forecasts may suffer from low performance.

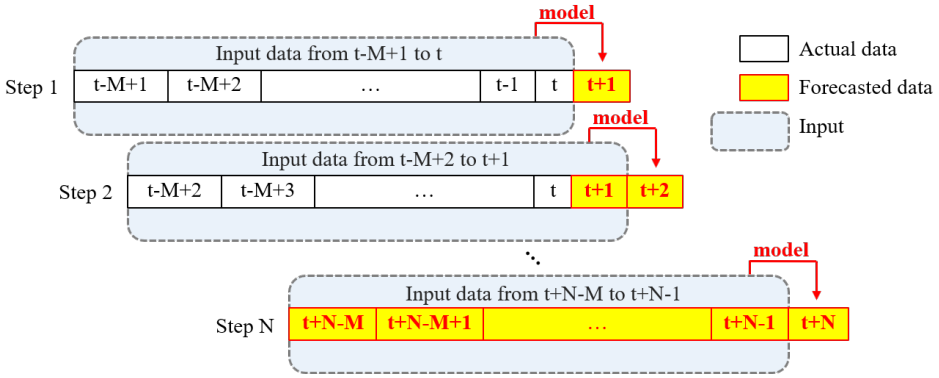

Figure 2.7: Structure of the M-1 model

2.2.3.2 M-N model

In the M-N model, it is necessary to develop specific forecasting models for each forecast step within the forecast horizon. The model is expressed as:

$$X(t+N) = f_N(X(t), X(t-1), \cdots, X(t-M+1)) \tag{2.33}$$

where f_N denotes the forecasting model at forecast step N.

Figure 2.8 shows the mechanism of the M-N model. It is seen that the input set always consists of the last M data up to the current time t in the time series that are known. Therefore, in contrast to the M-1 model, the M-N model does not use any forecasted value as input and thus, prevents error accumulation. However, this model is time-consuming since N models need to be developed in order to generate N-step-ahead forecasts. In addition, the correlation between inputs and output gradually weakens as N increases, thereby increasing the difficulty of learning their relationship.

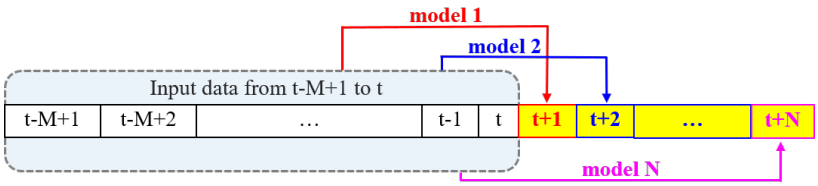

Figure 2.8: Structure of the M-N model

2.2.3.3 M-mN model

The previous two models can produce one output each time. By contrast, the M-mN model is a multiple-output model. The forecasting model is expressed as Eq. (2.34) and its architecture is sketched in Figure 2.9.

$$[X(t+1), X(t+2), \cdots, X(t+N)] = f_{mN}(X(t), X(t-1), \cdots, X(t-M+1)) \tag{2.34}$$

where f_{mN} denotes the M-mN model.

By means of the M-mN model, the previous M data are used to forecast the next N values simultaneously. This implies that compared with the M-1 model, this model can avoid the accumulation of errors. In fact, the implicit principle between M-N and M-mN models is the same. For some machine learning algorithms that can only be designed for one output (such as ANFIS), only the M-N model can be utilized. While for other algorithms such as ANN and RNN, multi-step-ahead forecasts can be generated by the M-mN model, which significantly reduces the computational time.

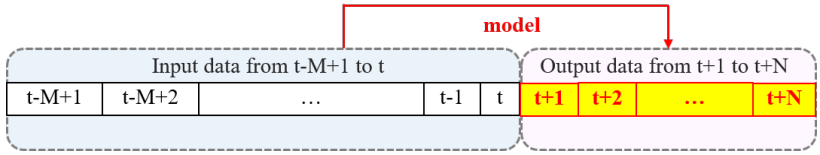

Figure 2.9: Structure of the M-N model

2.2.3.4 M-1 slope model

The M-1 slope model is a relatively complex model by adding a step of manually selecting the input data set. It is similar to the M-1 model, which is also based on a recursive process to make multi-step-ahead forecasts. However, there are several differences between these two models in the selection of training data. In the M-1 model, when forecasting $X(t+1)$, all pairs of inputs and output during the training period are selected as training data to establish the forecasting model. Afterwards, forecast is made based on the trained model and current inputs $[X(t-M+1), \cdots, X(t)]$. By comparison, in the M-1 slope model, only data during the training period that have similar properties to the current inputs can be selected, and pairs of these selected data together with corresponding output are assembled into the training dataset. The selection criteria is that historical data need to have a similar (not exceeding a certain allowable error) value and slope to the current input, which is simplified illustrated in Figure 2.10. As displayed, only limited data (red points), that have similar value and slope

as the current input (black point), are selected to develop the forecasting model.

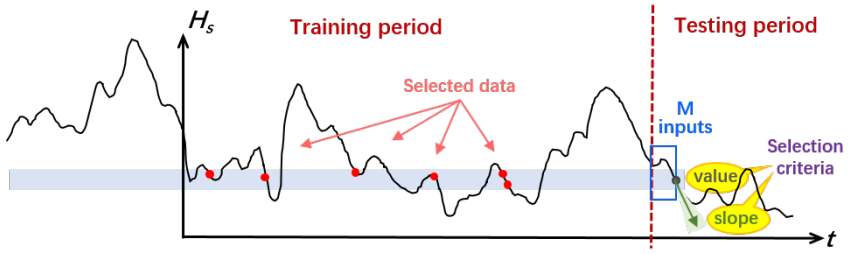

Figure 2.10: Input selection criteria of the M-1 slope model

After establishing the forecasting model based on the selected training dataset, it is used to perform one-step-ahead forecasting. The forecasted data $\hat{X}(t+1)$ is utilized as part of the input to forecast data at next time step and the training dataset needs to be re-selected. The selection process is the same. Subsequently, the forecasting model based on the new training dataset is applied to generate the two-step-ahead forecast. When there is not enough training data available, the process stops. Otherwise, the process is iterated until the N-step-ahead forecast, namely, $\hat{X}(t+N)$ is obtained. For detailed description of the M-1 slope model, refer to Wu et al. [142].

The advantage of this model is that it only extracts historical weather conditions that have similar characteristics of the value at the current time to establish the forecasting model, which may remove many irrelevant sea conditions and improve the forecast efficiency. In addition, compared with the M-1 model, the M-1 slope model may accumulate less error since the model will be updated at each step ahead. However, it is more complicated by involving a judgement process and new models are required to be trained for different steps ahead forecasting. Besides, another disadvantage is that there may not be sufficient training data especially for harsh weather, which will interrupt the training process.

2.3 Forecasting methods

After introducing machine learning techniques, two types of machine learning-based forecasting methods are developed and established. The first one is the TSML method, which is consistent with ideas in Secs. 2.1.4.1 and 2.1.4.2. The second one is the PBML method, which is briefly mentioned in Sec. 2.1.4.3. The following subsections will introduce the details of these two methods respectively.

2.3.1 Time series-based machine learning (TSML) method

This section focuses on the TSML method for wind and wave forecasting. The forecast variables are significant wave height H_s, peak wave period T_p and mean wind speed U_w. Since the core principle of the TSML method is to capture the correlation in time series of wave and wind variables, there is not much difference in forecasting models between different forecast variables.

For multi-step-ahead forecasting, a certain multi-step-ahead strategy should be involved in the method. Data pre-processing may also be considered to better capture data properties and reduce forecast complexity. The flowchart of the TSML method for multi-step-ahead forecasting is illustrated in Figure 2.11. The procedure for developing TSML models is summarized in the following steps:

- **Data preparation**

  To develop data-driven models, long-term time series need to be prepared. Either hindcast data produced by physics-based numerical methods or measurements extracted from wave buoys, ships, platforms or satellites can be used. The obtained dataset is divided into two parts. Most of the data is classified as the training dataset (including a small part of data to validate model), and the rest is classified as the testing dataset.
  Afterwards, it is necessary to determine input and output variables in the training and testing dataset. To forecast mean wind speed U_w, only past wind information is utilized, which means that inputs are current and/or past U_w and wind direction D_u. One example is shown in Eq. (2.35). For wave forecasting, the forecast information of H_s and T_p are desired to be provided. The corresponding input variables can be solely past wave data (e.g., Eq. (2.36)) or both wave and wind data (e.g., Eq. (2.37)). Normally, a sensitivity study of different input-output combinations is required to determine the optimal combination.

$$U_w(t+1) = f_u(U_w(t), D_u(t), U_w(t-1), D_u(t-1)) \tag{2.35}$$

$$H_s(t+1) = f_h(H_s(t), H_s(t-1)) \tag{2.36}$$

$$T_p(t+1) = f_t(H_s(t), U_w(t), T_p(t), H_s(t-1)) \tag{2.37}$$

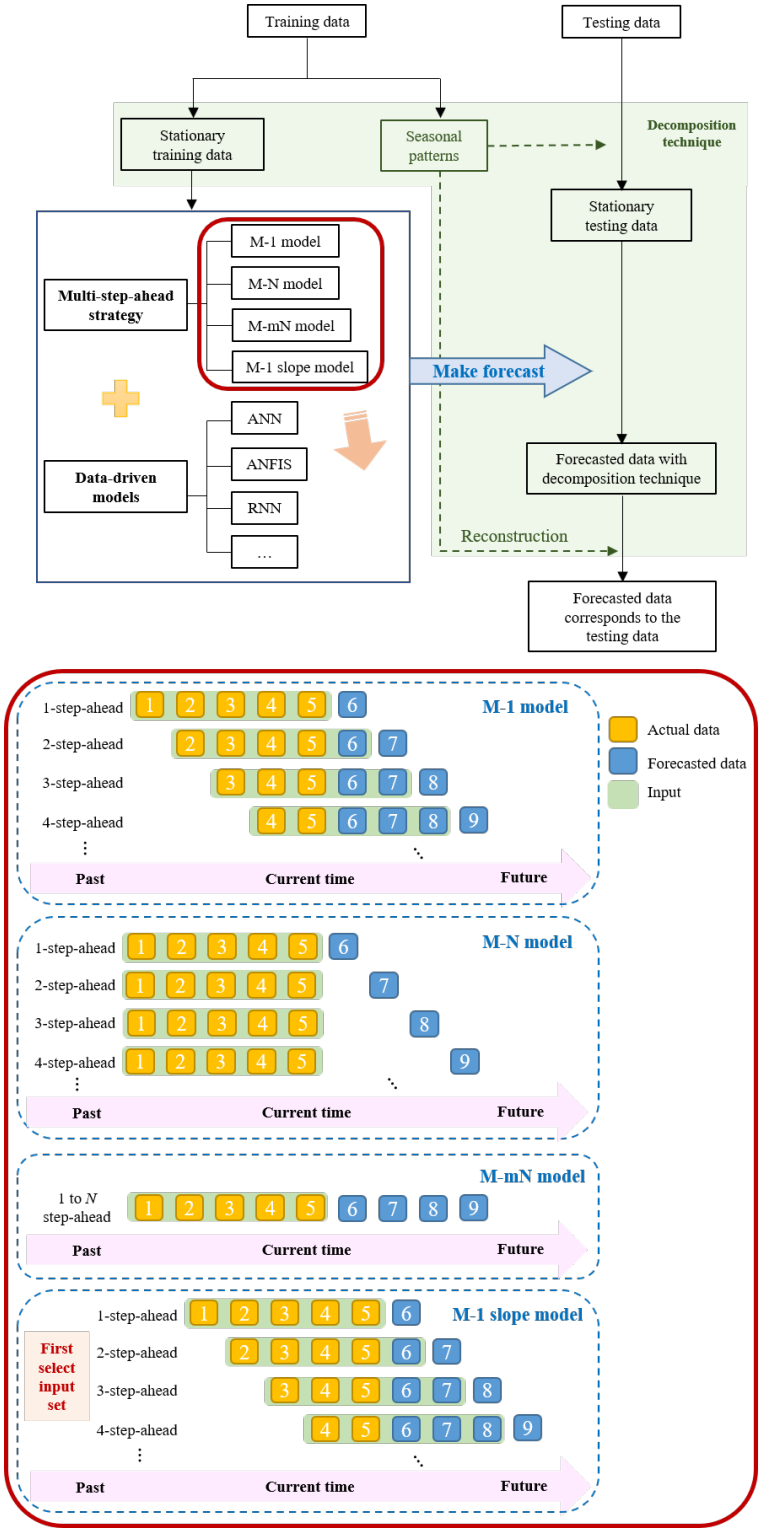

Figure 2.11: Flowchart of the TSML method

- **Model establishment**

  After preparing training and testing dataset, the TSML model needs to be determined. The model illustrated in Figure 2.11 includes the decomposition technique for data pre-processing that is displayed by green shading. The decomposition technique is utilized to transfer the initial training data to the stationary one by extracting seasonal patterns. In practice, the seasonal patterns of future data cannot be determined in advance, and thus the testing data is converted to the corresponding stationary data using the seasonal patterns obtained from the training data. By doing this, the stationary training and testing data can be prepared, which are applied to establish and assess the forecasting model, respectively. It should be emphasized that Figure 2.11 only illustrates an example of the TSML model used in the thesis. Alternatively, the TSML model can also be established without data pre-processing or with other data pre-processing techniques such as EMD.

  Subsequently, a certain multi-step-ahead strategy is selected to determine the input-output pair for each forecast step. Four multi-step-ahead strategies, i.e., M-1, M-N, M-mN and M-1 slope models can be selected, and the difference among them can be seen in the red frame of Figure 2.11.

  One data-driven model is then applied to train the input-output relationship. Depending on the characteristics of the forecast variable, different algorithms can be considered, such as ANN, RNN, ANFIS and so on. Based on the training data, the forecasting model can be learned automatically. One should note that it is necessary to conduct sensitivity studies on model's parameters (e.g., the M value, the number of hidden layers, the number of neurons in each hidden layer, etc.), in order to determine the optimal model structure for the data.

- **Forecast generation**

  When the forecasting model is trained successfully, the forecast can be made using the testing data. This can be done by employing the trained model with new inputs in the testing dataset to generate outputs. These outputs are ensembled as forecasted time series. For the forecasting method including the decomposition technique, the forecasted data should be further converted to the one corresponds to the initial testing data with the seasonal patterns. Finally, the forecasts are compared with the corresponding true values in the testing dataset

to evaluate the forecast performance. This will be introduced in Sec. 2.4.

Generally, TSML forecasting methods are highly flexible in adapting to data. However, it should be pointed out that the establishment of TSML models lacks a clear physical meaning, and therefore interpretability is identified as a potential weakness. In this case, another kind of machine learning-based method, that is the PBML method is further proposed and developed in the thesis.

2.3.2 Physics-based machine learning (PBML) method

The purpose of this section is to introduce the PBML method for forecasting wave conditions. As mentioned in Sec. 2.1.4.3, the PBML method selects input and output variables accounting for physical meaning rather than purely based on time series analysis. In the thesis, the main consideration is the physical process of wind generating waves. That is, the wind field data are the most important input, and their contribution to the wave field is established through machine learning, so as to achieve the purpose of forecasting wave data. To train the model, measurements or numerical data can be used. For measurements, the physical meaning is implicit in the measured wind and wave data, and machine learning is used to exploit their relationship. Numerical data are generated through physical modelling using explicit equations to describe the physical processes, and machine learning can replace this modelling procedure through pure data processing. In the study, numerical data are applied and the background of the physics-based numerical forecasting system is first presented in Sec. 2.3.2.1. After that, the PBML model is described. It should be mentioned that only the model establishment part is introduced since other parts (i.e., data preparation and forecast generation) are similar to those presented in Sec. 2.3.1.

2.3.2.1 Background

At present, forecasting of wave and wind conditions is mainly based on the physics-based numerical forecasting system, containing physics-based atmospheric and wave models. The schematic is shown in Figure 2.12, which illustrates the primary inputs and outputs of the atmosphere-wave forecasting system. In brief, the atmospheric model belongs to the initial value problem, in which initial observations are the critical input. For the wave model, it could be classified as a forced damping problem, where the main forcing comes from the surface winds.

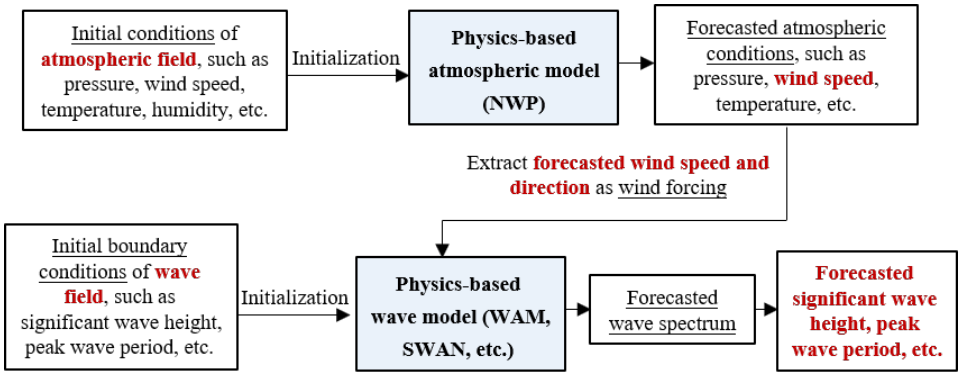

Figure 2.12: The sketch of the atmosphere-wave forecasting system

The idea of the atmosphere-wave forecasting system is simplified described as follow:

- Apply explicit physical equations and empirical parameterizations to represent evolutions of the atmosphere and waves
- Import the initial state and/or forcing in the models
- Use different numerical techniques to solve the models in discrete space and time to estimate the future state of weather conditions

The physics-based numerical forecasting system is complicated. In practice, it is generally developed and operated by large organizations and institutions. Correspondingly, professional teams with highly-skilled scientists are required to simulate and study each components of the models. For instance, for wind forecasting, the High Resolution Limited Area Model (HIRLAM) [184] is a NWP forecast system developed by several European meteorological institutes like Norwegian Meteorological Institute (MET-Norway), Danish Meteorological Institute (DMI) and so on. Similar NWP models have also been developed at other centers [185–187]. For wave forecasting, different forecast products [188–191] are provided by various institutes, such as the European Centre for Medium-Range Weather Forecasts (ECMWF), MET-Norway, National Center for Environmental Prediction (NCEP) and so on.

Besides, although both physics-based atmospheric and wave models explicitly simulate physical phenomena, they demand to solve a set of mathematical equations describing complex atmospheric and wave conditions based on numerical techniques. Inevitably, these models would have some

challenges, such as the difficulty of solving equations, the need for a series of assumptions and parameterizations, long computational time, large archive resources and so on. These challenges provide a potential for the application of the machine learning algorithms, which can be utilized to avoid these shortcomings and simplify the complicated modeling process. However, most of data-driven models for wave forecasting are pure time series-based. Lack of a clear physical background and difficulty in interpretation challenge their reliability. Therefore, a PBML forecasting method is proposed, which attempts to combine the advantages of both physics-based wave models and machine learning algorithms.

2.3.2.2 Model establishment

Unlike the TSML model, the PBML model determines its structure with reference to the physical processes that occur in the wave field. In the model, physical knowledge from the physics-based numerical model is utilized as a guide for designing inputs and outputs, and machine learning algorithm is adopted to learn their relationship automatically. The physics-based wave model reveals that the wind field is the main energy source of the wave field. Thus, wind properties such as the mean speed and direction are introduced as the input variables in the PBML model to forecast wave conditions. In addition, initial wave boundary conditions are added in the model as well. The wave-wave interaction and wave dissipation effects are implicit in the learned relationship. The idea of the PBML method is illustrated in Figure 2.13 and introduced as follows.

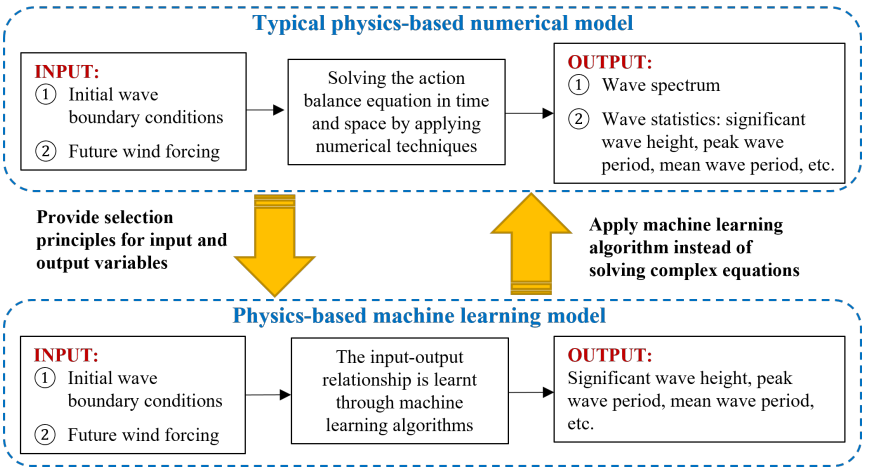

Figure 2.13: Idea of the PBML method

1) Input and output variables

A typical forecast domain is shown as the blue part in Figure 2.14. To make N-step-ahead forecasting of wave conditions , H_s and T_p at time $(t + N)$ at all grid points are the outputs. H_s and T_p at the initial time t at the highlighted grid points (by the red lines) characterize the initial wave boundary conditions in the PBML model. U_w and D_u at all grid points covering the past, the current and the whole forecast time horizon are the wind forcing inputs. These can be obtained from the wind forecasting models such as NWP models.

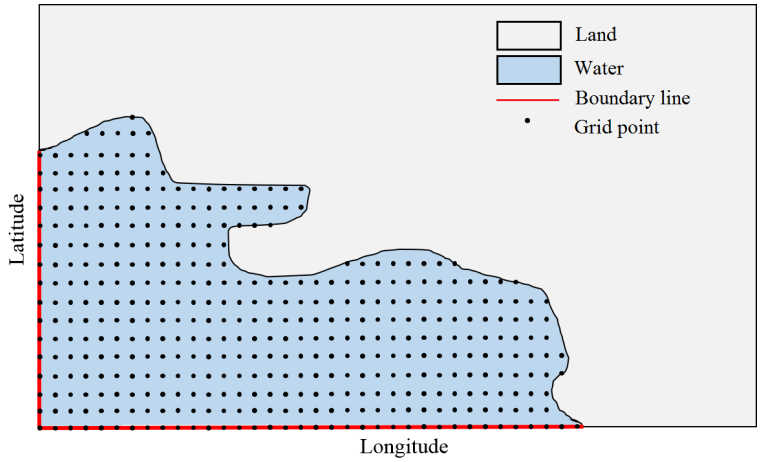

Figure 2.14: Illustration of the forecast domain

2) Calculation algorithm

Differently from the action balance equation employed in the physics-based wave model, the PBML model provides an alternative method, directly establishing the input-output relationship through machine learning algorithms. In this process, the computational cost can be significantly decreased due to no need to solve partial differential equations by an iteration process. Several machine learning algorithms are available, such as ANN, ANFIS and RNN.

3) Creating the forecasting model

After deciding the input and output variables and the calculation algorithm, the forecasting model can be established. To illustrate this, a N-step-ahead forecasting model of H_s is taken as an example in Eq. (2.38),

and its architecture is shown in Figure 2.15.

$$
\begin{aligned}
&[H_{s1}(t+N), H_{s2}(t+N), \cdots, H_{sn}(t+N)] \\
&= f_{hN}(H_{s1}(t), T_{p1}(t), \cdots, H_{sm}(t), T_{pm}(t), U_{w1}(t+N), D_{u1}(t+N), \cdots, \\
&\quad U_{wn}(t+N), D_{un}(t+N), U_{w1}(t+N-TU+1), D_{u1}(t+N-TU+1), \\
&\quad \cdots, U_{wn}(t+N-TU+1), D_{un}(t+N-TU+1))
\end{aligned}
\tag{2.38}
$$

where t is the current time and N is the forecast step. n and m are the number of grid points in the forecast domain and along the boundary lines, respectively. TU is the time range of wind speeds and directions used as wind forcing.

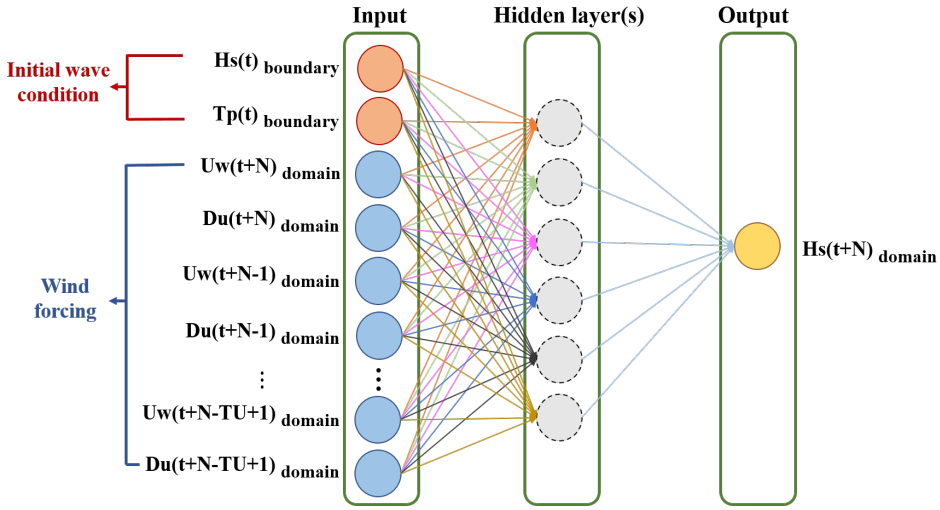

Figure 2.15: Illustration of the PBML model architecture

As displayed in Eq. (2.38) and Figure 2.15, outputs of the model are N-step-ahead H_s in the forecast domain. The inputs include the initial wave boundary conditions (H_s and T_p) at time t and the wind forcing (U_w and D_u) in the forecast domain from $(t+N-TU+1)$ to $(t+N)$. The value of TU denotes how many previous steps of wind conditions up to the forecast step will be used. It should be determined based on sensitivity studies. f_{hN} represents the forecast system at N-step-ahead, which depends on the selected machine learning algorithm. In the thesis, ANN is used. In addition, for the requirement of on-site marine operations, only a small forecast domain is considered, and the corresponding forecast performance of the PBML model will be summarized and discussed in the next chapter.

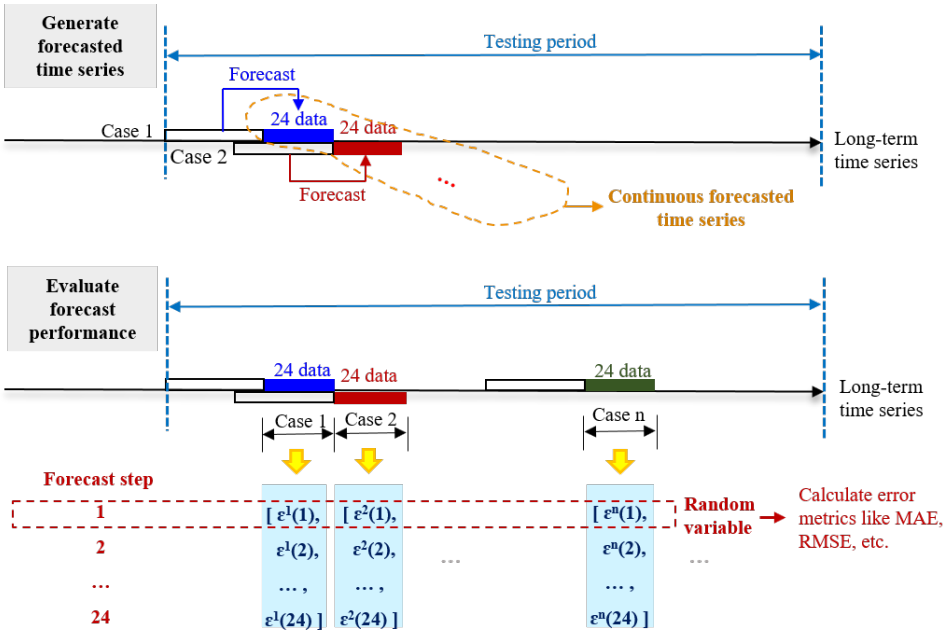

Figure 2.16: Illustration of forecasted time series generation

2.4 Forecast performance evaluation

2.4.1 Forecasted time series

After the forecasting model is trained successfully, it is utilized to generate forecasted time series. The procedure is illustrated in Figure 2.16, which takes 24-step-ahead forecasting as an example. For each case during the testing period, the trained model is used to forecast next 24 data with appropriate inputs (depending on the selected input variables and multi-step-ahead forecast strategy). After one case ends, the next case will start immediately with new inputs. As a result, each case contains forecasts from 1- to 24-step-ahead, and different cases constitute a continuous forecasted time series. By comparing the forecasted time series with the actual one from the testing dataset, the forecast performance of the model at each forecast step can be evaluated. The performance is generally assessed in terms of different error metrics. In the thesis, two kinds of metrics are considered. One is conventional error measures, such as bias and correlation coefficient. The other one is statistics of forecast errors, from which an uncertainty model can be established. These will be presented separately below.

2.4.2 Error measures

Error measures are commonly used in various meteorological centers to evaluate the quality of forecast products. In this thesis, six typical error measures, namely MAE (mean absolute error), RMSE (root mean square error), bias, R^2 (correlation coefficient), SI (scatter index), MAPE (mean absolute percentage error) are utilized, which are expressed as Eqs. (2.39) to (2.44).

$$MAE = \frac{1}{n}\sum_{i=1}^{n}|f_i - a_i| \tag{2.39}$$

$$RMSE = \sqrt{\frac{1}{n}\sum_{i=1}^{n}(f_i - a_i)^2} \tag{2.40}$$

$$bias = \frac{1}{n}\sum_{i=1}^{n}(f_i - a_i) \tag{2.41}$$

$$R^2 = \frac{\sum_{i=1}^{n}(f_i - \bar{f})(a_i - \bar{a})}{\sqrt{\sum_{i=1}^{n}(f_i - \bar{f})^2} \cdot \sqrt{\sum_{i=1}^{n}(a_i - \bar{a})^2}} \tag{2.42}$$

$$SI = \sqrt{\frac{\sum_{i=1}^{n}\left[(f_i - \bar{f}) - (a_i - \bar{a})\right]^2}{\sum_{i=1}^{n}{a_i}^2}} \tag{2.43}$$

$$MAPE = \frac{1}{n}\sum_{i=1}^{n}\left|\frac{a_i - f_i}{a_i}\right| \times 100 \tag{2.44}$$

where n is the number of forecasts. a_i and f_i are i^{th} actual and forecasted data, respectively. $\bar{a}$ and $\bar{f}$ are the mean values of the actual and forecasted data, respectively.

2.4.3 Forecast errors

Most of above error measures are non-negative and the direction of the errors is not considered. For marine operations, the direction of forecast errors in various sea states are of great importance. Ignoring the directions of the error would increase the risk of decision-making during the execution phase. Thus, statistical information of forecast errors are applied as well to

investigate models' forecast performance. The thesis considers three different forecast errors, that are called the forecast error Δ, the forecast error factor ε_M and the forecast error ratio ε, expressed as Eqs. (2.45) to (2.47) respectively. They correspond to the error of the i^{th} forecasted data. When all errors during the testing period are calculated, an uncertainty model can be derived on the basis of their statistics. This model uses the mean value and standard deviation of Δ, ε_M or ε to quantify the uncertainties in weather forecasts at each time step. In addition to the error measures in Sec. 2.4.2, this uncertainty model is necessary for studying the effect of weather forecast performance on marine operations.

$$\Delta_i = f_i - a_i \tag{2.45}$$

$$\varepsilon_{M_i} = \frac{f_i - a_i}{a_i} \tag{2.46}$$

$$\varepsilon_i = \frac{a_i}{f_i} \tag{2.47}$$

2.5 Application, assumption and limitation

The sources of data for establishing and using forecasting models are summarized in Table 1. To train a machine-learning based weather forecasting model, it is necessary to prepare long-term historical data. Both measurements and numerical data of wind and wave conditions can be selected. In the thesis, only hindcast numerical data are used, with an aim to establish forecasting models and investigate their forecast accuracy.

Table 2.1: Data sources for model establishment and application

Model	Establishment	Application
TSML PBML	Long-term measurements or numerical data	Read-time measurements or numerical data
		Real-time measurements or numerical data and wind forecast

In the process of applying machine learning-based methods to make weather forecast, the availability of inputs including both wind and wave data is essential since real-time data are required. In reality, the input information may not easy to obtain. However, this issue is not addressed in the thesis. The assumptions and limitations of the forecasting models are described as follows:

- Assume that all inputs are known. For the TSML models, it means that both wind and wave data up to the current time can be obtained, such as by on-site measurements of a buoy or numerical data generated through physics-based numerical models. For the PBML models, in addition to wave and wind data up to the current time, it is also assumed that the wind data in the future (i.e., the wind forecasts) have been provided by other type of forecasting techniques, such as from NWP models.

- Assume that all inputs in the machine learning-based forecasting models are correct. That is, when the numerical data is utilized, it is assumed to be consistent with the measurement data and uncertainties in the model input are not considered.

- One limitation of the PBML method is that the model needs wind forecasts to drive it. When the forecasted wind conditions can be obtained from atmospheric forecasting models, the PBML model is able to act as a surrogate for the physics-based wave model and provide an efficient way for generating wave forecasts. However, how to quickly get the future wind information to use the PBML method is also an issue worthy of further consideration and discussion in real applications.

Chapter 3

Weather forecast results and uncertainty quantification

Machine learning-based forecasting methods have been introduced in Ch. 2. Based on these methods, this chapter summarizes corresponding weather forecast results. In order to train and test forecasting models, knowledge of the utilized metocean data at the target offshore site is first introduced in Sec. 3.1. Meanwhile, initial data analysis is carried out and included. Secs. 3.2 and 3.3 present results of one-day-ahead wave and/or wind forecasts as well as forecast uncertainties in TSML and PBML methods. Finally, a comparison of forecast performance between machine learning-based methods with physics-based numerical methods is given.

3.1 Offshore site and metocean data

The North Sea is considered to have great potential for offshore wind energy development [192]. In the thesis, the North Sea center is the main focus, as highlighted in Figure 3.1. In this area, various marine operations have been studied and analyzed, such as the installation of monopiles and transition pieces [67], and single blade [51–54] of offshore wind turbines.

Given that data-driven models require long-term historical data and high quality of hindcast data, ten-years (2001-2010) hindcast time series of wind and wave variables are utilized to train and test TSML and PBML models. Data sources from two different institutions are considered:
1) Dataset 1: Hourly hindcast time series of U_w, H_s, T_p and D_u at a single location from the National and Kapodistrian University of Athens (NKUA) [193].
2) Dataset 2: Three-hourly hindcast time series of U_w, H_s, T_p and D_u in

a small area with a spatial resolution of 0.125° from ECMWF CERA-20C datasets [194].

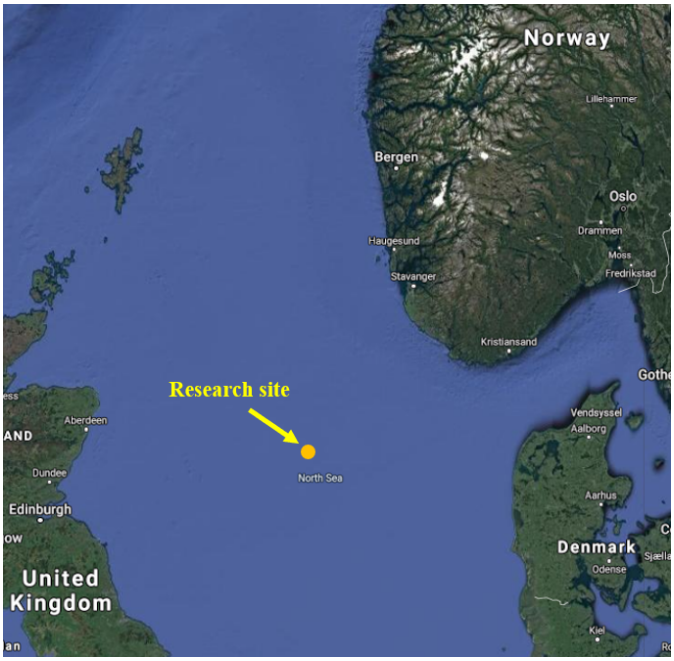

Figure 3.1: North Sea area and the selected offshore site

For TSML models, metocean data at one location is enough for providing input information, and Dataset 1 is mainly used to develop them. By contrast, PBML models are able to forecast spatial wave conditions and thus, spatial data of wind and waves are required. The Dataset 2 is utilized to develop the PBML models, that provides metocean data in a small area.

Each dataset is divided into two parts. The data of the first nine years (from 2001 to 2009) is considered as the training data for establishing the model, in which 10% of the data is selected as the validation data. The data of the last year (2010) is the testing data for evaluating the forecast performance of the model. All machine learning-based forecasting models are developed in MATLAB using the toolboxes or in Python using TensorFlow. Regarding the typical duration of marine operations, the aim is to perform one-day-ahead wave forecasting, that is, twenty-four-step-ahead forecasting and eight-step-ahead forecasting correspond to the Dataset 1 and 2, respectively.

For the long-term datasets, the data analysis is carried out first to provide an overall view of the environmental conditions at the specific site.

This is an important step in designing a weather forecasting model. The relevant analysis is shown in Appendix A. In summary, with reference to the correlation of time series, environmental conditions have a certain degree of predictability. However, it is not easy to make forecast for a long horizon since the correlation between data would decrease significantly as the time interval increases.

3.2 TSML method

3.2.1 Decomposition-ANFIS method

A hybrid decomposition-ANFIS model is developed to illustrate the forecast performance of the TSML method. According to the procedure described in Sec. 2.3.1, the training and testing data are pre-processed by the decomposition technique first. Then, the model combining ANFIS and a multi-step-ahead strategy (if multi-step-ahead forecasting is expected) is built based on the training data. The forecast performance of the forecasting model is evaluated on the testing data at each forecast lead time.

3.2.1.1 One-step-ahead forecasting

For one-step-ahead forecasting, simple forecasting models are developed for U_w, H_s and T_p, which are expressed in Eqs. (3.1) to (3.3), respectively. The basic idea is to use data at the current time as input to forecast the next-step data. This is sufficient for one-step-ahead forecasting, since there is a strong correlation between one metocean data to the next, as analyzed in Appendix A.

$$U_w(t+1) = f_1(U_w(t)) \tag{3.1}$$

$$H_s(t+1) = f_2(U_w(t), H_s(t)) \tag{3.2}$$

$$T_p(t+1) = f_3(H_s(t), U_w(t), T_p(t)) \tag{3.3}$$

Their structures are summarized in Table 3.1. In each model, all input variables are partitioned into two fuzzy sets ('Low' and 'High'), and Gaussian-type MFs are selected for inputs and linear-type for the output. As a result, the total numbers of IF-THEN rules in the U_w, H_s and T_p forecasting models are 2, 4 and 8, respectively. The optimal parameters in MFs and IF-THEN rules are determined in the training phase.

Table 3.1: Structures of the one-step-ahead ANFIS models

Forecast variable	Input variable	Membership functions (MFs)			IF-THEN rules	Output
		Type	Number	Fuzzy sets	Number	MF type
$U_w(t+1)$	$U_w(t)$	Gaussian	2	'low', 'high'	2	Linear
$H_s(t+1)$	$U_w(t)$	Gaussian	2	'low', 'high'	4	Linear
	$H_s(t)$	Gaussian	2	'low', 'high'		Linear
$T_p(t+1)$	$U_w(t)$	Gaussian	2	'low', 'high'	8	Linear
	$H_s(t)$	Gaussian	2	'low', 'high'		Linear
	$T_p(t)$	Gaussian	2	'low', 'high'		Linear

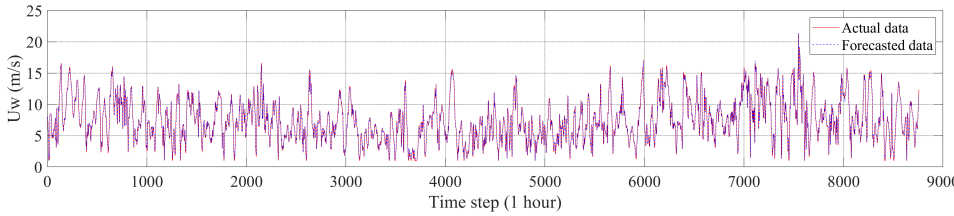

(a) U_w

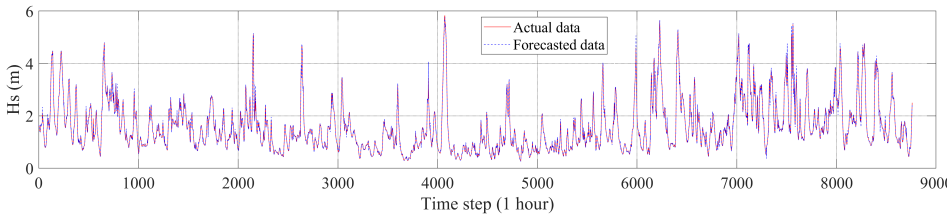

(b) H_s

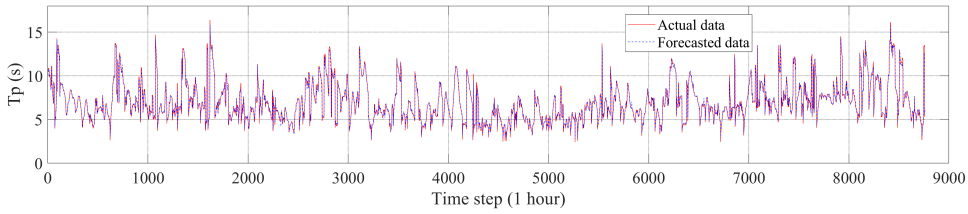

(c) T_p

Figure 3.2: One-step-ahead forecasting results

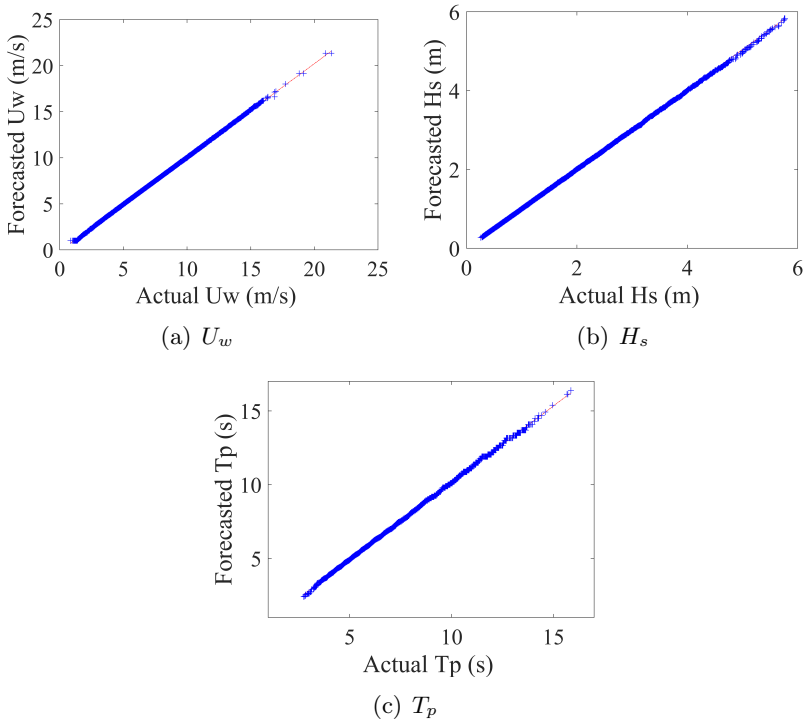

(a) U_w (b) H_s

(c) T_p

Figure 3.3: Q-Q plots for one-step-ahead weather forecasts

After establishing the optimal ANFIS, the testing process is performed. The forecasted U_w, H_s and T_p and the corresponding actual data are plotted in Figure 3.2 (a), (b) and (c), respectively. In each subfigure, the blue line contains forecasted data and the red line contains corresponding actual data. Meanwhile, Quantile-Quantile (Q-Q) plots for relevant results are plotted in Figure 3.3. As displayed in Figure 3.2, the forecasted data are close to the actual data for all three environmental variables throughout the entire testing period. The Q-Q plots in Figure 3.3 further prove the reliability of the forecasts. These results indicate that the adopted TSML method can generate accurate one-step-ahead forecasts of weather conditions.

3.2.1.2 Multi-step-ahead forecasting

To generate multi-step-ahead forecasts, more complicated models with different multi-step-ahead strategies should be developed. Correspondingly, the optimal structure of the forecasting model must be investigated, such as which metocean variables are selected as input and how much past data

(i.e., M values in Eqs. (2.30 - 2.33)) are used separately. In practice, the optimal structure is not easy to determine. Typically, if a large amount of input data is utilized, more historical information can be available and thus, forecasts are expected to be more accurate. However, the training time of the forecasting model would increase dramatically with the number of inputs, especially when optimization techniques are required during the training phase. In the thesis, the model structure is determined by the sensitivity study of various input variables and corresponding M values, starting from M=1. The one corresponds to the minimum statistics of forecast error factors is regarded as the optimal model. Detailed comparison procedure is illustrated in Wu et al. [142]. Optimal decomposition-ANFIS models with three multi-step-ahead strategies are summarized below:

M-1 model:

$$U_w(t+1) = f(U_w(t), U_w(t-3)) \tag{3.4}$$

$$H_s(t+1) = f(H_s(t), H_s(t-1)) \tag{3.5}$$

$$T_p(t+1) = f(T_p(t), T_p(t-1)) \tag{3.6}$$

M-N model:

$$U_w(t+N) = f(U_w(t), D_u(t), U_w(t-3), U_w(t-6), U_w(t-9)) \tag{3.7}$$

$$H_s(t+N) = f(H_s(t), U_w(t), D_u(t), H_s(t-1), U_w(t-3)) \tag{3.8}$$

$$T_p(t+N) = f(T_p(t), H_s(t), U_w(t)) \tag{3.9}$$

M-1 slope model:

For the M-1 slope model, since it is essentially an iterative approach, U_w, H_s and T_p forecasting models are the same as shown in Eqs. (3.4) to (3.6).

In above equations, for the sake of simplicity, f represents the forecasting model. However, it should be emphasized that it is different for each model. In addition, input terms related to U_w are all three-hour intervals, since the time series of wind speed in Dataset 1 are actually three-hourly data. When D_u is considered as input, it is recommended to transform it to a range between 0 and 1 [195] according to Eq. (3.10).

$$Dir = \begin{cases} 1 - \left(\frac{\theta}{180}\right), & if \quad 0^\circ \leq \theta \leq 180^\circ \\ \frac{\theta - 180}{180}, & if \quad 180^\circ \leq \theta \leq 360^\circ \end{cases} \tag{3.10}$$

Overall, all selected models are relatively simple, without containing a lot of input data. This is because sensitivity studies showed that the

accuracy of the models is not very sensitive to the amount of past data included. By contrast, the types of variables that are included in M-N models have a strong impact on the accuracy for wind and wave forecast. Thus, to improve calculation efficiency and decrease the forecast uncertainty in multi-step-ahead forecasts, a small M value is selected and variables that are related to the forecasted variable should be included if possible.

Forecasted time series of U_w, H_s and T_p during the testing period and the corresponding actual series are plotted in Appendix B. To present the characteristics of the forecasting models clearly, considering H_s as an example, several cases of forecast results (250 data) based on the M-1, M-1 slope and M-N models are extracted from Figure B.2 and shown in Figure 3.4. In each subfigure, the black line depicts actual time series and the forecasted time series is represented by the red line. The forecasted time series is composed of multiple one-day-ahead forecast cases. Each one-day-ahead forecast case is obtained by the trained model with appropriate inputs from the testing dataset, and contains twenty-four forecasts, from one-step-ahead to twenty-four-step-ahead. The green and blue points represent one- and twenty-four step-ahead forecast values respectively, representing the beginning and end of one forecast case. The next case starts when the previous one ends. By observing Figure 3.4(b), it can be found that the M-1 slope model cannot perform the 24-step forecast in all cases, especially near the peaks of high sea states. However, compared to the results in Figure 3.4(a) and (c), the M-1 slope model can capture the data variation better, although the positions of peaks/troughs may not be captured exactly.

As displayed, the proposed models can predict the environmental conditions to a certain extent. However, due to the randomness in the occurrence of waves and wind, it is difficult to realize high accuracy in forecasting all points, especially for high sea states. The uncertainty quantification analysis is subsequently performed to evaluate and compare the accuracy of the three multi-step-ahead strategies.

Figure 3.5 presents statistics of the forecast error factor ε_M of U_w, H_s and T_p in terms of the forecast step N. Black, red and blue lines represent results based on the M-1 model, the M-N model and the M-1 slope model, respectively. To distinguish the statistics, the mean values are represented by asterisk marks and the circles correspond to the standard deviations. It is visible that the forecast error of the M-N model exhibits monotonic behavior with respect to N. This is consistent with the phenomenon that the correlation decreases with the increase of the lag number. Whereas, the forecast errors of the other two models exhibit variations because forecasted values are used to further make forecast. Overall, the forecast uncertainties

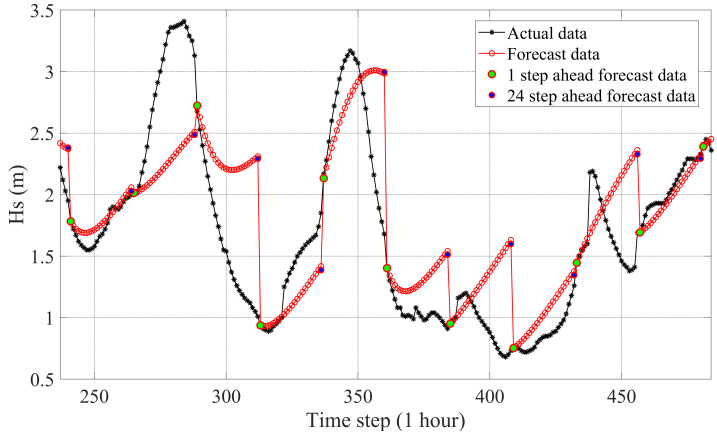

(a) M-1 model

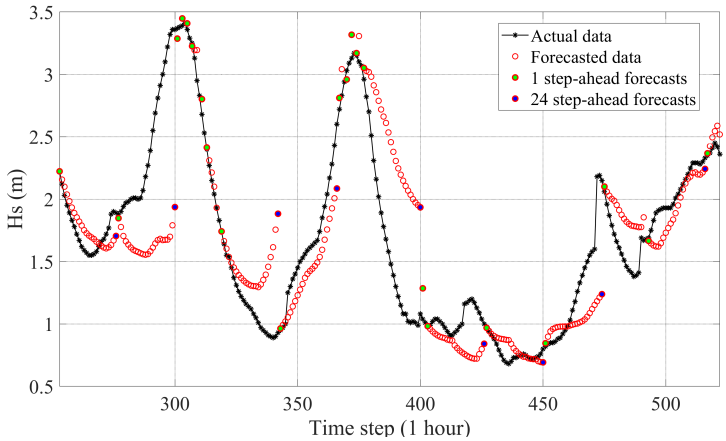

(b) M-1 slope model

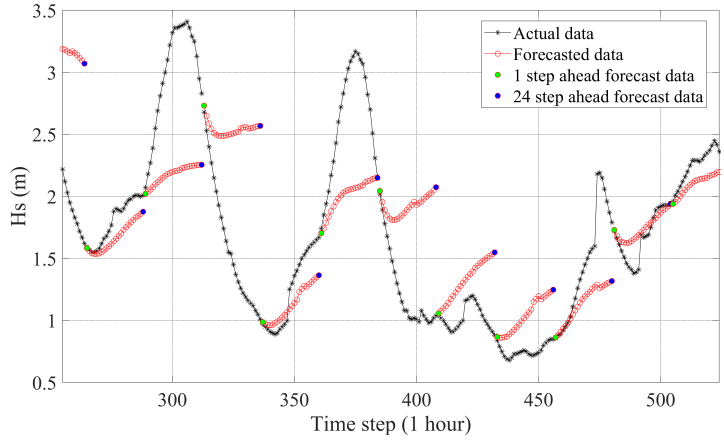

(c) M-N model

Figure 3.4: Several cases of H_s forecast by the three models

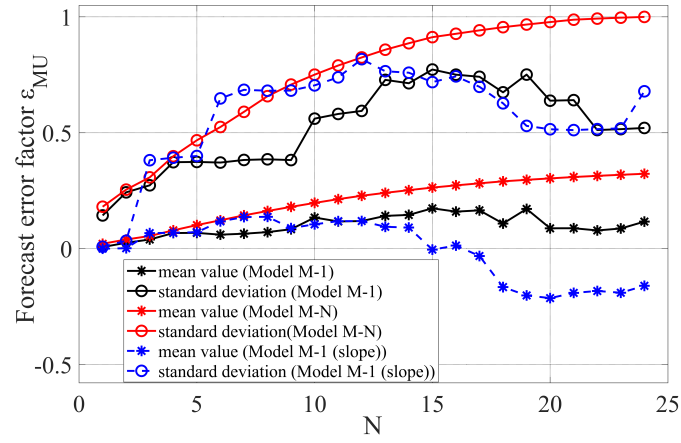

(a) U_w

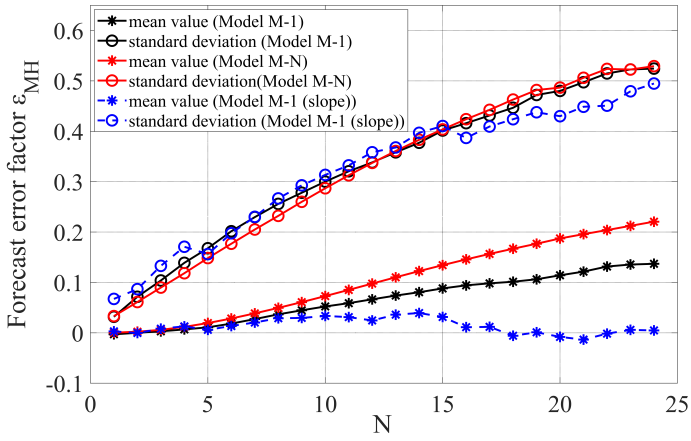

(b) H_s

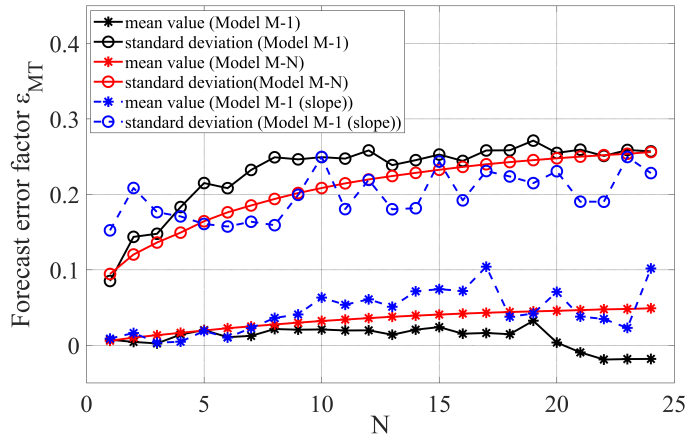

(c) T_p

Figure 3.5: Statistics of ε_M at different forecast step N

of the three models are low at the first forecast step, as reflected in the near-zero mean values and standard deviations. With the increase of the forecast horizon, the forecast uncertainty of all forecasting models significantly increases. In summary, the proposed decomposition-ANFIS methods can be applied for the short-term prediction of wave and wind conditions, and have application potential in marine operations. However, due to the error accumulation problem of the M-1 and M-1 slope models and the uncorrelated input-output sample in the M-N model, it is highly difficult to generate accurate weather forecasts for longer forecast horizons.

3.2.2 Comparison of different TSML methods

This section presents a comparison of different TSML methods for multi-step-ahead wave forecasting. One-day-ahead H_s forecasting is taken as an example to illustrate their forecast performance.

Table 3.2: The list of developed forecasting methods

No.	Method	Pre-processing technique		Data-driven model						
		Decom -position	EMD	ARIMA	ANN	RNN	ANIFS	M-1	M-N	M-mN
1	D-ARIMA	O		O						
2	D-ANN-M-1	O			O			O		
3	D-ANN-M-N	O			O				O	
4	D-ANN-M-mN	O			O					O
5	D-EMD-ANN-M-1	O	O		O			O		
6	D-EMD-ANN-M-N	O	O		O				O	
7	RNN-mN					O				O
8	D-ANFIS-M-1	O						O		
9	D-ANFIS-M-N	O							O	
10	D-EMD-ANFIS-M-1	O	O				O	O		
11	D-EMD-ANFIS-M-N	O	O				O		O	

Table 3.2 summaries the developed 11 TSML methods, which contain different combinations of pre-processing techniques, data-driven models and multi-step-ahead strategies. Since the effectiveness of the decomposition technique has been successfully verified in the time series forecasting of weather conditions [141], all methods except 7 apply it as the data pre-processing technique. In order to investigate the influence of pre-processing techniques, EMD is applied to continue decompose the obtained data in methods 5, 6, 10 and 11. In addition, both ANN and RNN -based methods use M-mN model (i.e., methods 4 and 7), while ANFIS-based method does not because ANFIS can only contain one output variable. The ARIMA model, ANN-based model and ANFIS-based model are performed by using Matlab, and RNN-based model is performed by using TensorFlow.

The optimal structure and characteristic of each TSML model are studied in Wu et al. [196] separately and briefly summarized as follows:
ARIMA-based:

- ARIMA(p, q, 2) is applied and values of p and q are determined by the Bayesian Information Criterion (BIC) for specific training sets. The model yielding the minimum BIC value is selected.

ANN-based:

- ANN models with one hidden layer is applied.
- Based on a sensitivity study, the M value is selected as 24.
- Based on the comparison result, an ANN-based method with double pre-processing techniques (decomposition technique and EMD) is not necessary. This may because after performing the double data pre-processing, the obtained time series are very sensitive to noise and may run into the problem of mode mixing. So methods 5 and 6 are not included in the following comparison.

RNN-based:

- LSTM network is utilized, that consists of two LSTM layers and the size of hidden neurons for each LSTM layer is 32.
- The M value is 24.
- Since LSTM is specially suitable to handle sequence dependence, only M-mN strategy is considered.

ANFIS-based:

- Since ANFIS belongs to the single-output approach, only M-1 and M-N models are considered. The structure is consistent with the ones described in Sec. 3.2.1.2.
- ANFIS-based methods with double pre-processing techniques are also constructed to study the impact of data pre-processing technique on the ANFIS model.

A comparative analysis on the forecast performance among different TSML methods is carried out. This is done by evaluating the forecast uncertainty (characterized by statistics of the forecast error factor ε_M) at each forecast lead time. The results are plotted in Figure 3.6 and described below. Noted that the 'D' is omitted from the legend in the figure.

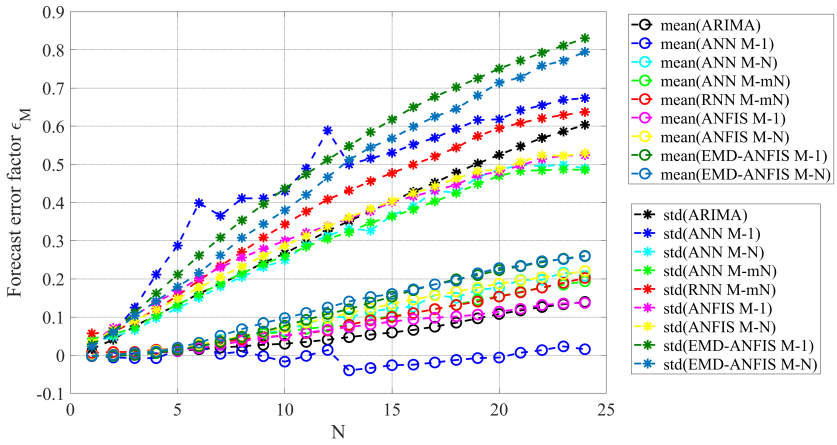

Figure 3.6: Comparison of forecast uncertainty based on different TSML methods

1) ANFIS-based methods with double pre-processing techniques, i.e., EMD-ANFIS M-1 and EMD-ANFIS M-N, results in the worst performance. This indicates that the forecast performance is very sensitive to the nature of the data and using double pre-processing techniques may not be helpful for forecasting, at least for the study area and adopted data.

2) Beside these two methods, the RNN-mN model without any pre-processing techniques (red line) has a higher forecast uncertainty than other models with the decomposition technique. This implies that suitable pre-processing techniques can assist in the time series forecasting.

3) In the remaining methods, the ARIMA model (black line) exhibits a higher forecast uncertainty at longer forecast horizons, indicating that the linear function employed in the ARIMA model have difficulty in capturing the rapidly changing waves when the forecast horizon is relatively long.

4) There is not a clear evidence to show which of the remaining three ANN-based methods and two ANFIS-based methods is the best one for multi-step-ahead forecasting of H_s. From all methods, means and standard deviations of ε_M in the first ten steps are less than 0.1 and 0.3, and around 0.2 and 0.5 at the 24^{th} step, respectively.

Overall, Figure 3.6 demonstrates that the forecast uncertainty generally increases with the forecast horizon, no matter which TSML method is adopted. This is a reasonable observation. In fact, the correlation in data is quite low when the time interval exceeds 7 hours, which makes it difficult for machine learning to find a general relationship between input and output.

3.2.3 Summary

Regarding the TSML method, a hybrid decomposition-ANFIS method is developed in detail for forecasting both wave and wind conditions. In addition, the performance of different TSML methods for one-day-ahead H_s forecasting is investigated and compared. The statistics of forecast error factors are utilized for quantifying their forecast uncertainty. Results demonstrate that all TSML methods have better performance for forecasting significant wave height from first several steps ahead due to the lower forecast uncertainty level. As the number of forecast step further increases, their forecast ability would decrease significantly. This is a common phenomenon and can not be improved obviously by changing data-driven models or developing a more complex hybrid method (including double data pre-processing techniques). Under this circumstance, one may conclude that it is difficult to get accurate weather forecasts for long horizon by the TSML method with purely time series analysis. In order to improve the quality of weather forecasts, unlike the TSML methods that only take historical time series in consideration, it is necessary to develop a hybrid method combining both physical process and data-driven model.

3.3 PBML method

One-day-ahead forecasting of wave conditions (H_s and T_p) by the PBML method is performed. PBML models are developed based on the Dataset 2. With reference to typical physics-based wave models, wind forcing in a selected area as well as initial boundary wave conditions are taken into account as inputs to drive the PBML model and forecast wave conditions in this area. Given that on-site marine operations are normally carried out at a selected position, forecasting in a large domain is not necessary and thus, the focus of the thesis is on a small area. As shown in Figure 3.7, the forecast domain contains nine grid points numbered from 1 to 9.

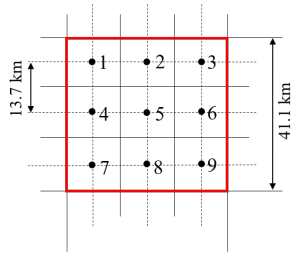

Figure 3.7: Illustration of a small forecast domain

3.3.1 Model architecture determination

Similar to the development of TSML models, the optimal structure of the data-driven model (i.e., ANN in the thesis) employed in the PBML method should be determined first. According to the sensitivity study (described in detail in Wu et al. [197]), the ANN with three hidden layers, twenty neurons in each layer and the tansig type activation function is adopted. In addition, the time range of the input wind field also deserves consideration. As shown in Eq. (2.38), when performing the N-step-ahead forecasting, the wind forcing from $(t+N-TU+1)$ to $(t+N)$ are considered as input. To investigate the impact of wind forcing at different time steps on H_s forecasts, the ANN is developed in terms of the optimal structure described above, and the TU value is selected from one to eight. When TU is equal to 1, only the wind field at the same time as the forecasted H_s is considered. With the increase in TU, an increasing number of past wind fields are taken into account. The results of the sensitivity study of the TU values are shown in the Figure 3.8.

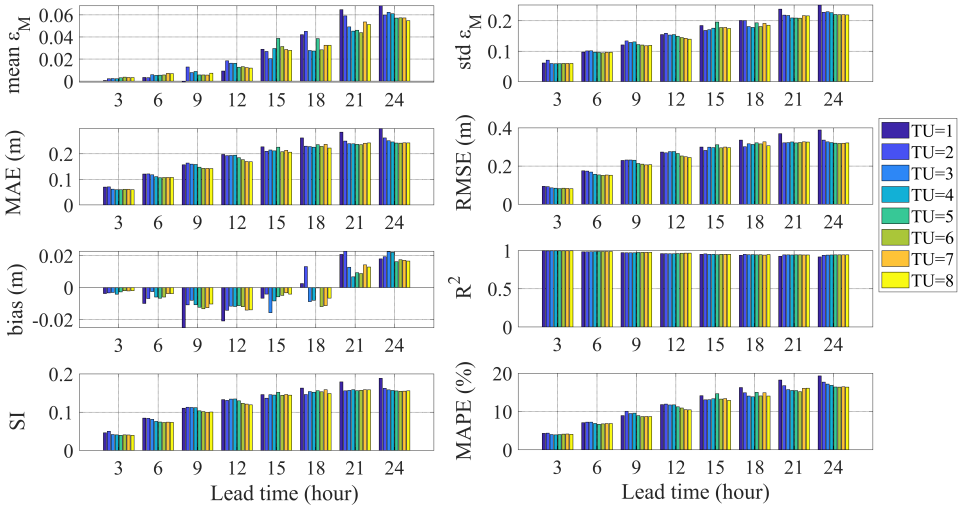

Figure 3.8: Forecast errors of the PBML model with different durations of wind forcing (point 5)

As displayed in Figure 3.8, in general, the forecast performance increases with increasing TU values, indicating that the wind variation should be taken into account in wave forecasting by the PBML model. However, the level of improvement in model performance gradually decreases as the TU increases from 2. Given that increasing the TU value will increase the

number of inputs, which makes the model more complicated and requires longer training time, TU=2 is chosen in the PBML model. That is, the dynamic characteristics of the winds are provided in the model by applying wind speeds and directions at two consecutive time steps.

In addition, it is interesting to see the importance of the future wind forcing. Figure 3.9 shows the forecast performance of the model using wind forcing up to (t+N-TU^*) when forecasting wave conditions at $(t + N)$, where TU^* ranges from 0 to 7. From the sensitivity study, it is clear that the forecast performance will gradually decrease as TU^* increases. In order to forecast the wave conditions at $(t + N)$ accurately, the wind conditions at $(t + N)$ should be included.

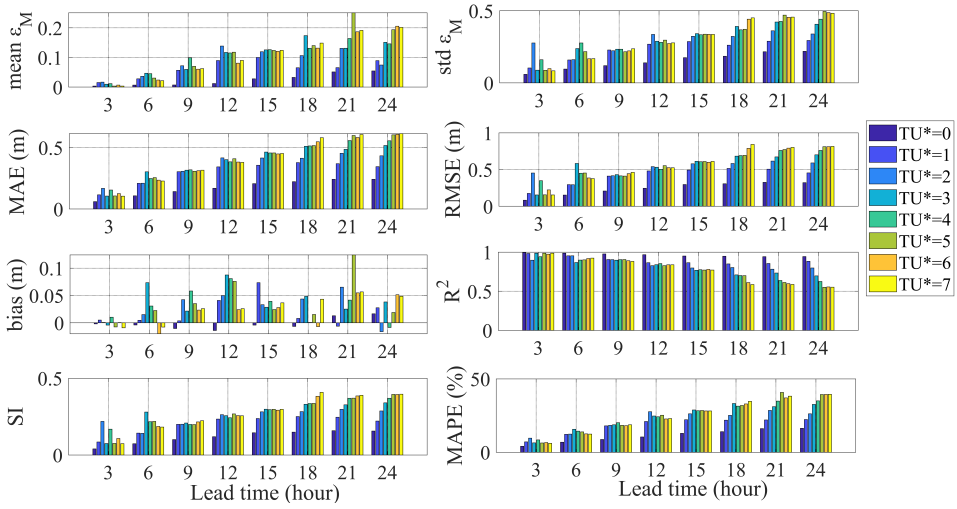

Figure 3.9: Forecast errors of the PBML model using wind forcing up to (t+N-TU^*) (point 5)

3.3.2 Forecast of total wave conditions

3.3.2.1 Significant wave height

Based on the above sensitivity analysis results, the forecasting model of H_s can be set up as follows:

$$\begin{aligned}&[H_{s1}(t+N), H_{s2}(t+N), \cdots, H_{s9}(t+N)]\\ &= f_{hN}(H_{s1}(t), T_{p1}(t), \cdots, H_{s9}(t), T_{p9}(t), U_{w1}(t+N), D_{u1}(t+N), \cdots,\\ &\quad U_{w9}(t+N), D_{u9}(t+N), U_{w1}(t+N-1), D_{u1}(t+N-1),\\ &\quad \cdots, U_{w9}(t+N-1), D_{u9}(t+N-1)) \ , \quad N = 1, \cdots, 8\end{aligned} \tag{3.11}$$

where $H_{s1}(t+N), H_{s2}(t+N), \cdots, H_{s9}(t+N)$ are the outputs, which are N-step-ahead forecasts of H_s for points 1 to 9. f_{hN} is the ANN model at the N-step-ahead. The inputs include the initial boundary wave conditions (i.e., $H_s(t)$ and $T_p(t)$ at points 1, 2, 3, 4, 6, 7, 8 and 9) and the wind forcing at two consecutive time steps in the forecast domain (i.e., U_w and D_u for all nine points at time $t+N$ and $t+N-1$). As a result, it can be seen that in this case, the model for each forecast step has a total of 52 inputs and 9 outputs.

The forecast results during the testing period at the grid point 5 (in Figure 3.7) are plotted in Figure 3.10, in which the actual and forecasted time series are represented by black and red lines, respectively. To reveal the forecast performance more clearly, two short-time windows are also shown in Figure 3.10, in which the meaning of points with different colors are similar to those described in Figure 3.4. That is, each one-day-ahead forecast case contains eight forecasted data from one-step-ahead (green points) to eight-step-ahead (blue points), which are generated by the trained model with appropriate inputs. To illustrate the forecast uncertainty, forecast error metrics including conventional error measures and the forecast error factor at each forecast lead time are summarized in Table 3.3.

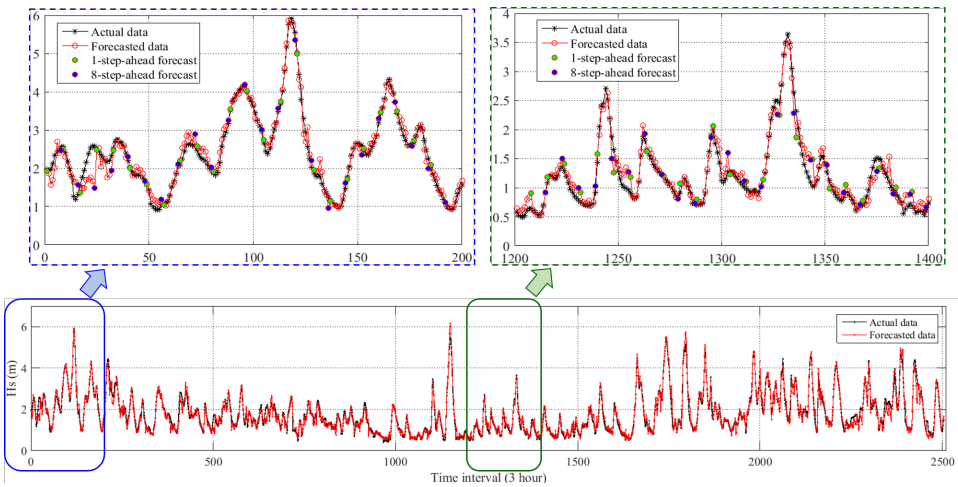

Figure 3.10: Forecast results of H_s at each lead time based on the PBML model

Overall, a good agreement between the forecasted and actual data is observed throughout the entire testing period, which reveals the reliability of the PBML method for H_s forecasting. In addition, there is no significant difference in forecast performance between the two windows, indicating

that the model is suitable for any time of year. In Table 3.3, it is observed that the forecast accuracy decreases with the forecast lead time, reflected in the decrease in R^2 and the increase in other error metrics. Nevertheless, all 8-step-ahead forecasts can be considered satisfactory because the corresponding errors are quite small. For example, the RMSE and R^2 for all steps are less than 0.3 m and higher than 96%, respectively. Furthermore, regarding the computational time, the PBML model can be quickly trained and used to make forecasts extremely fast. The training process of the PBML model on a common server typically takes few minutes.

Table 3.3: Forecast errors of H_s at each lead time based on the PBML model

Error	**Lead Time (hour)**							
Measures	**3**	**6**	**9**	**12**	**15**	**18**	**21**	**24**
m_{ε_M}	0.0050	-0.0039	0.0054	0.0176	0.0171	0.0158	0.0183	0.0239
std_{ε_M}	0.0676	0.0862	0.1008	0.1088	0.129	0.1576	0.1618	0.1741
MAE (m)	0.0617	0.096	0.114	0.1303	0.1525	0.1693	0.1827	0.1961
RMSE (m)	0.0927	0.1375	0.1573	0.1828	0.2213	0.238	0.2587	0.2727
bias (m)	0.0009	-0.0071	-0.0043	0.013	0.0085	0.0047	-0.0009	-0.0008
R^2	0.9975	0.9903	0.9866	0.982	0.9742	0.9711	0.9646	0.9611
SI	0.0447	0.0665	0.0767	0.0887	0.1072	0.1155	0.1256	0.1318
MAPE (%)	4.1138	5.9599	7.2648	8.0594	9.4332	10.8368	11.5503	12.6979

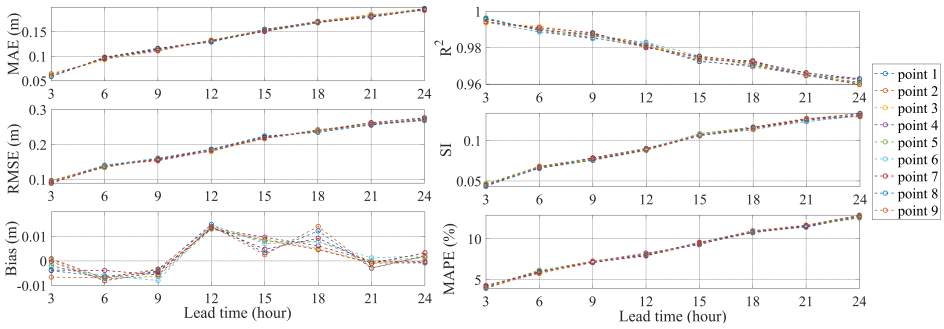

(a) MAE, RMSE, bias (b) R^2, SI, MAPE

Figure 3.11: Error measures of H_s forecasts for all nine grid points

The above results only display the forecast at the grid point 5 in the forecast domain. Figure 3.11 further summarizes the error measures at all nine grid points in the forecast domain by different colors. Little difference

in error measures is found among all nine grid points, which proves that the PBML model is suitable and reliable in a small forecast domain.

In addition to a small forecast domain, the forecast performance for a single point is investigated. This situation is very important to explore whether the PBML method is applicable to the measurement data, since measurements may only be available at limited positions. The forecasting model for a single point is simplified to Eq. (3.12). In this case, the inputs are the initial wave conditions and wind forcing at the position of interest (point 5 in Figure 3.7 is selected as an example here), and the outputs are the future wave conditions at the same position. That is, the model is simplified to have six inputs and one output. The results of forecasted time series and forecast errors are illustrated in Figures 3.12 and 3.13, respectively.

$$H_{s5}(t+N) = f_{h5N}(H_{s5}(t), T_{p5}(t), U_{w5}(t+N), D_{u5}(t+N), \\ U_{w5}(t+N-1), D_{u5}(t+N-1)), \quad N = 1, \cdots, 8 \tag{3.12}$$

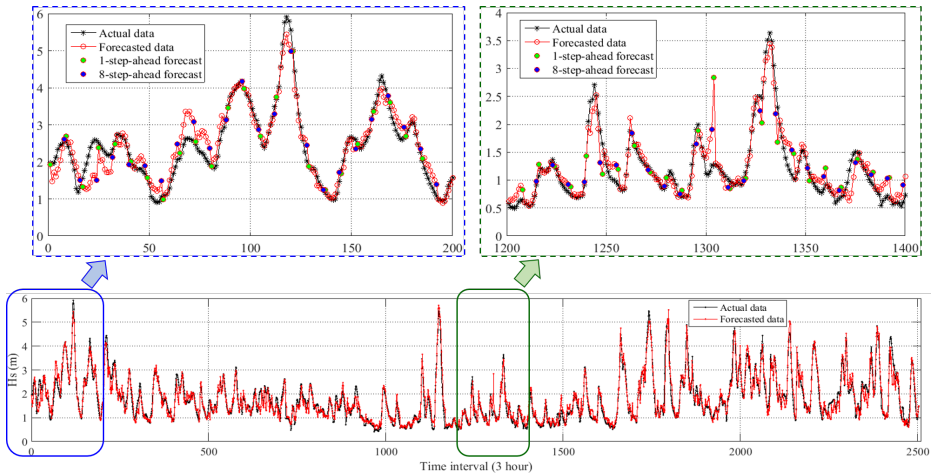

Figure 3.12: Forecast results of H_s based on the PBML model with one-point domain

Compared with the results shown in Figure 3.10, forecast accuracy for this simple model is reduced to some extent due to significant reduction of the input information. Nevertheless, this model still exhibits good forecast performance. As displayed in Figure 3.13, the R^2 and RMSE of all 8-step-ahead forecasts are higher than 94% and lower than 0.33 m, respectively. This indicates that the proposed PBML model can forecast H_s with relatively high accuracy based on weather data of a single position.

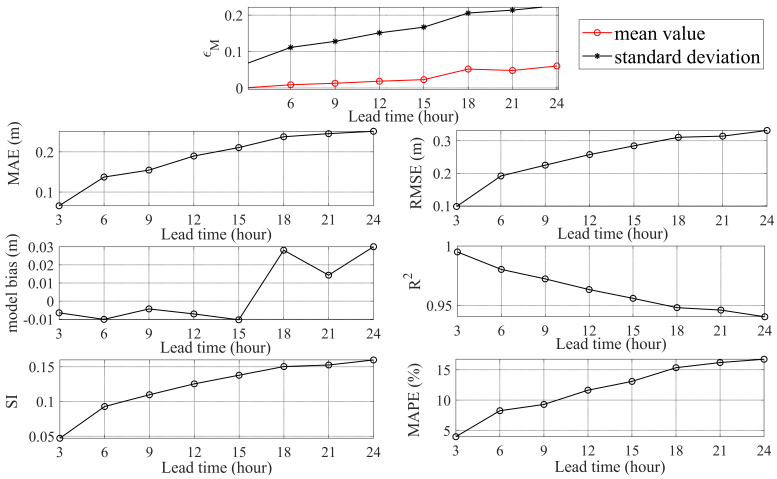

Figure 3.13: Forecast errors of H_s based on the PBML model with one-point domain

3.3.2.2 Peak wave period

Forecast performance of the PBML method for T_p is investigated in this section. The forecasting model of T_p is expressed in Eq. (3.13). The generated forecasted time series are shown in Figure 3.14, and the errors are summarized with respect to the lead time in Table 3.4.

$$\begin{aligned}&[T_{p1}(t+N), T_{p2}(t+N), \cdots, T_{p9}(t+N)]\\ &= f_{tN}(H_{s1}(t), T_{p1}(t), \cdots, H_{s9}(t), T_{p9}(t), U_{w1}(t+N), D_{u1}(t+N), \cdots,\\ &\quad U_{w9}(t+N), D_{u9}(t+N), U_{w1}(t+N-1), D_{u1}(t+N-1),\\ &\quad \cdots, U_{w9}(t+N-1), D_{u9}(t+N-1)) \ , \qquad N = 1, \cdots, 8\end{aligned} \tag{3.13}$$

In general, from Figure 3.14, it is visible that the PBML model can generate acceptable T_p forecasts. The R^2 and RMSE at all lead times are higher than 71% and lower than 1.30 s respectively, which are shown in Table 3.4. However, by comparing Tables 3.4 and 3.3, it can be found that the forecast uncertainty level of T_p is much higher than that of H_s. Significant fluctuation in T_p time series might be the key reason for this phenomenon. Differently from H_s, T_p is associated with the highest energetic waves in the total wave spectrum, and it can be predominated by either wind-generated sea or swell. This uncertainty increases the instability of the series of T_p and further challenges the development of the forecasting model. To further explore the factors that affect T_p forecast performance, in Sec. 3.3.3, the total sea are separated into wind-generated sea and swell, and PBML models

are utilized to forecast these two components separately.

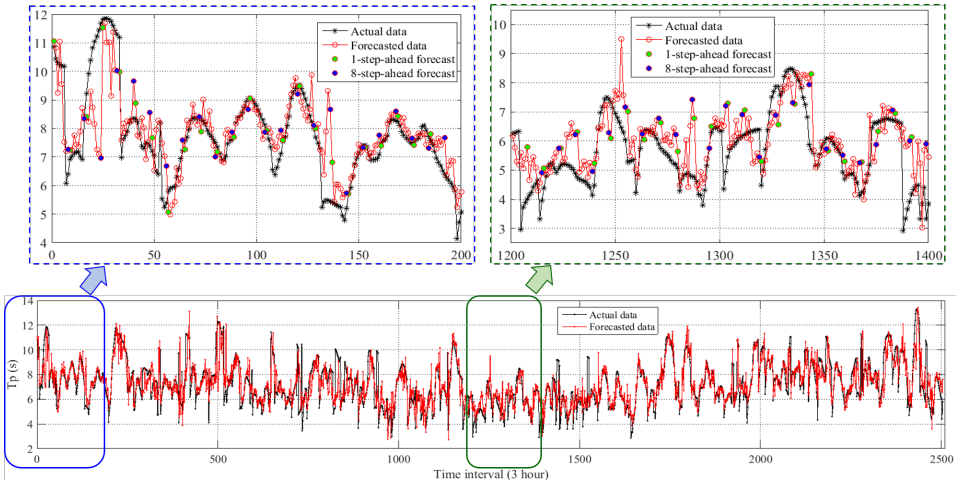

Figure 3.14: Forecast results of T_p based on the PBML model

Table 3.4: Forecast errors of T_p based on the PBML model

Error	Lead Time (hour)							
Measures	3	6	9	12	15	18	21	24
m_{ε_M}	0.0088	-0.0004	0.0231	0.0081	0.0335	0.0397	0.0321	0.0514
std_{ε_M}	0.1302	0.1347	0.1412	0.1769	0.1737	0.1868	0.1774	0.1891
MAE (s)	0.3617	0.5276	0.6151	0.7172	0.7771	0.8859	0.9136	0.9605
RMSE (s)	0.729	0.8633	0.9498	1.1201	1.1186	1.2355	1.2351	1.3026
bias (s)	-0.0038	-0.1092	0.0463	-0.1207	0.0669	0.0575	0.0157	0.1195
R^2	0.9196	0.8855	0.8585	0.8043	0.7941	0.753	0.7405	0.7125
SI	0.0964	0.1133	0.1259	0.1476	0.1496	0.1655	0.1648	0.1724
MAPE (%)	5.4973	7.6696	8.9811	10.3773	11.6007	13.3601	13.2666	14.1797

3.3.3 Forecast of separate wind-generated sea conditions and swell conditions

To forecast significant wave height and mean wave period of wind-generated sea and swell, the historical data are also extracted from CERA-20C with the same forecast domain, resolution and duration as those of the total sea. The extracted variables are significant wave heights and mean wave periods of wind-generated sea (i.e., H_{sw} and T_{mw}) and swell (i.e., H_{ss} and T_{ms}).

The corresponding forecast performances are discussed in the following subsections, respectively.

3.3.3.1 Significant wave height

The PBML models of wind-generated sea and swell are similar to those of total sea, except that the initial wave conditions. Given that all nine grid points have similar forecast performance that is revealed in Sec. 3.3.2.1, only forecast results of the point 5 (in Figure 3.7) are shown in Figures 3.15 and 3.16. Meanwhile, Tables 3.5 and 3.6 give the forecast errors of H_{sw} and H_{ss} with respect to the lead time, respectively.

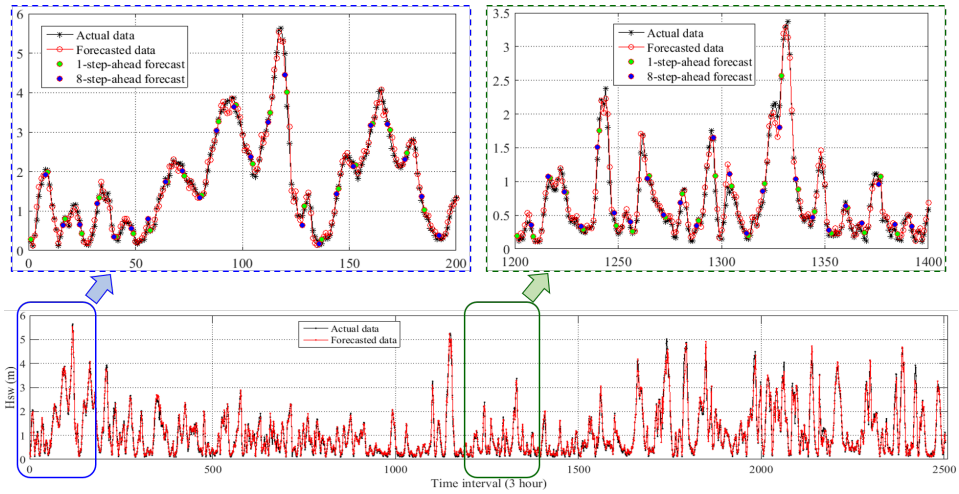

Figure 3.15: Forecast results of H_{sw} based on the PBML model

Table 3.5: Forecast errors of H_{sw} based on the PBML model

Error	Lead Time (hour)							
Measures	3	6	9	12	15	18	21	24
m_{ε_M}	0.073	0.0671	0.106	0.0646	0.0417	0.116	0.0618	0.0888
std_{ε_M}	0.1449	0.1799	0.1836	0.1562	0.1647	0.2362	0.1982	0.232
MAE (m)	0.0747	0.0892	0.1001	0.0888	0.1095	0.1174	0.091	0.1001
RMSE (m)	0.1027	0.1277	0.1428	0.1283	0.1782	0.1779	0.1356	0.1548
bias (m)	0.0422	0.0405	0.0558	0.0224	-0.0102	0.0028	-0.0098	-0.0036
R^2	0.9951	0.9926	0.99	0.9917	0.9855	0.9898	0.9919	0.9908
SI	0.0619	0.081	0.0892	0.0848	0.1178	0.1173	0.0891	0.1011
MAPE (%)	10.9096	12.7095	14.7157	12.008	12.5973	17.4128	13.58	15.3229

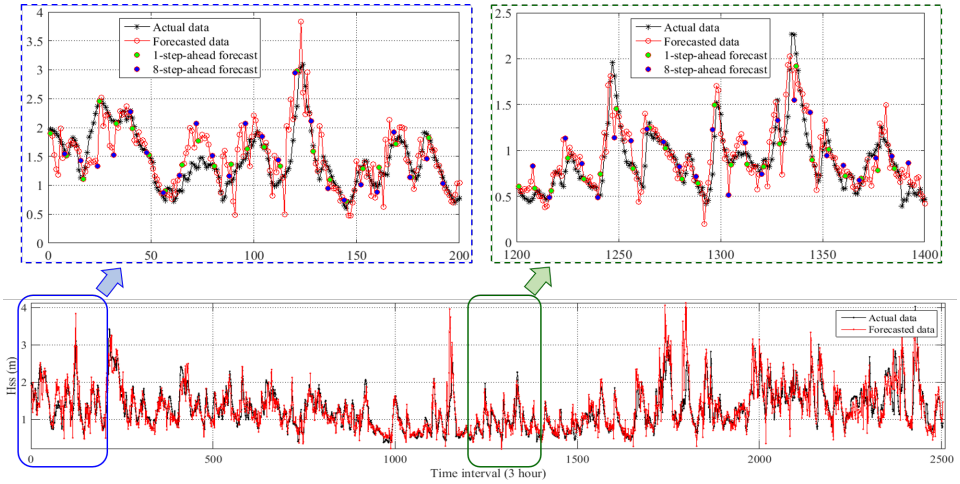

Figure 3.16: Forecast results of H_{ss} based on the PBML model

Table 3.6: Forecast errors of H_{ss} based on the PBML model

Error	**Lead Time (hour)**							
Measures	**3**	**6**	**9**	**12**	**15**	**18**	**21**	**24**
m_{ε_M}	0.0238	-0.0057	-0.0234	0.044	0.078	0.0741	0.0941	0.0919
std_{ε_M}	0.1552	0.1636	0.18	0.2319	0.3136	0.3333	0.2992	0.3328
MAE (m)	0.1129	0.1342	0.1652	0.204	0.2584	0.2846	0.273	0.3011
RMSE (m)	0.1758	0.2008	0.2404	0.3031	0.4013	0.445	0.3848	0.4446
bias (m)	0.0129	-0.0179	-0.0383	0.0372	0.067	0.0685	0.0661	0.0634
R^2	0.9456	0.9337	0.9087	0.8613	0.7821	0.7438	0.7573	0.7041
SI	0.1283	0.144	0.1701	0.2156	0.286	0.3199	0.2775	0.3228
MAPE (%)	9.9648	11.2799	13.1894	16.5625	20.8705	22.8518	22.6173	24.6826

Figure 3.15 shows excellent forecast performance of H_{sw}. For instance, R^2 values for all lead times are higher than 98.5% in Table 3.5. In contrast, the H_{ss} results presented in Figure 3.16 have relatively low forecast accuracy. The weak relation between the output (swell) and input (wind forcing) is the main reason for this phenomenon. Figure 3.17 shows scatter diagrams of the mean wind speed and different significant wave heights (i.e., H_s, H_{sw} and H_{ss}) at the same time and position, based on the hindcast data from year 2001 to 2009. The color depicts the absolute frequencies of occurrence. Obviously, the correlation between the mean wind speed and significant wave height for swell (Figure 3.17(c)) is much weaker than that for wind-generated sea (Figure 3.17(b)). The weaker relationship challenges

development of the forecasting model for H_{ss}. In addition, it is visible from Figure 3.17(a) that despite the existence of swell, the correlation between H_s and U_w in the total sea is still relatively obvious. This guarantees the good performance of the PBML model for forecasting H_s.

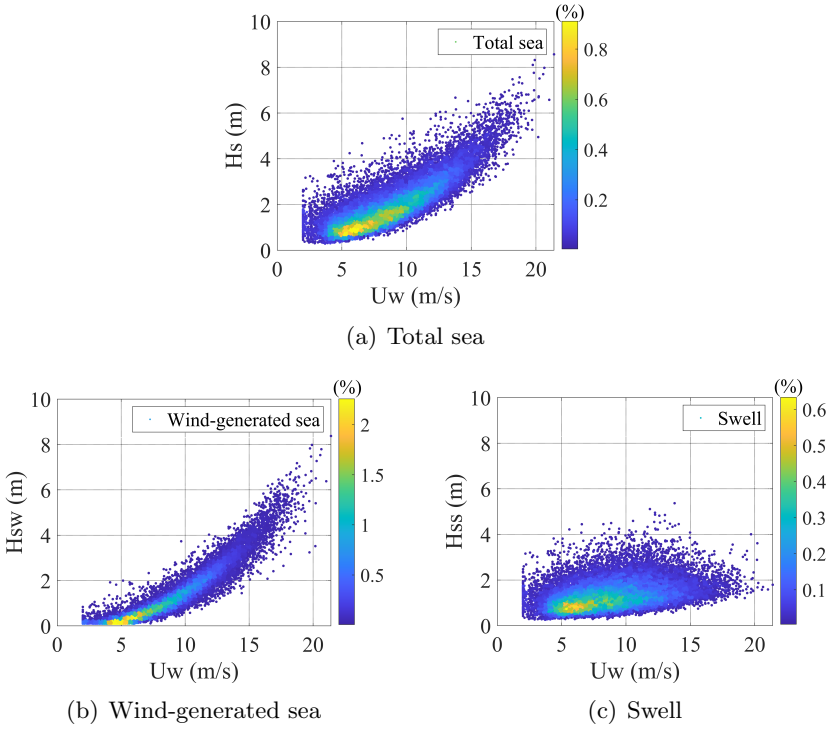

(a) Total sea

(b) Wind-generated sea

(c) Swell

Figure 3.17: Scatter plot of significant wave height and mean wind speed

Table 3.7: Forecast errors of T_{mw} based on the PBML model

Error	**Lead Time (hour)**							
Measures	**3**	**6**	**9**	**12**	**15**	**18**	**21**	**24**
m_{ε_M}	0.0073	0.0027	0.0087	0.006	0.0107	0.0051	0.0057	0.0032
std_{ε_M}	0.0486	0.0601	0.0653	0.068	0.0685	0.0646	0.0691	0.0716
MAE (s)	0.1061	0.1671	0.1803	0.1938	0.1953	0.1994	0.2076	0.2203
RMSE (s)	0.1572	0.2354	0.241	0.2551	0.2581	0.2746	0.2791	0.3054
bias (s)	0.021	-0.0009	0.0168	0.0061	0.0221	-0.0058	0.0037	0.0003
R^2	0.9944	0.9873	0.9864	0.9851	0.9849	0.9825	0.9824	0.9793
SI	0.0342	0.0517	0.053	0.0562	0.0567	0.06	0.0611	0.0669
MAPE (%)	2.8555	4.2903	4.6335	4.9302	4.9289	4.7782	5.1044	5.2865

3.3.3.2 Mean wave period

T_{mw} and T_{ms} are forecasted by PBML models, to further investigate the reasons for the higher uncertainty level in T_p forecasts. The corresponding forecast results of the point 5 are shown in Figures 3.18 and 3.19, respectively. Meanwhile, Tables 3.7 and 3.8 summarize the forecast errors of T_{mw} and T_{ms}, respectively.

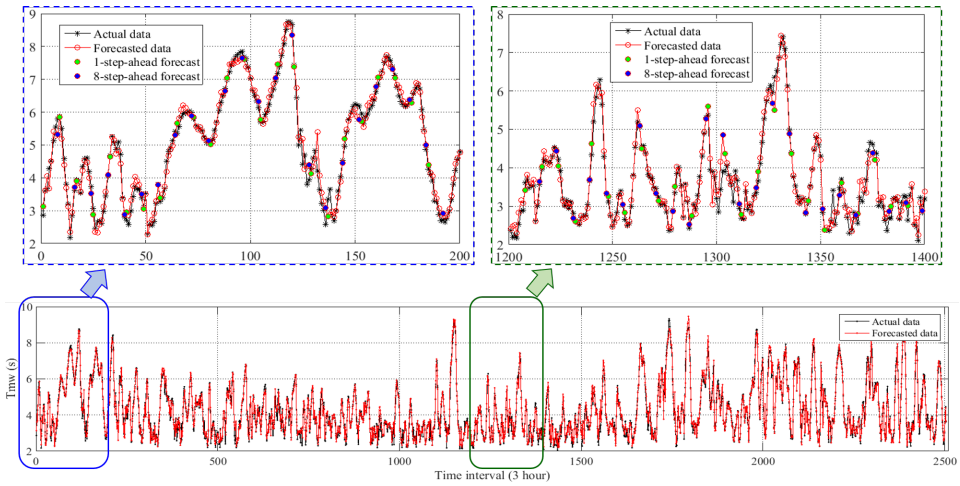

Figure 3.18: Forecast results of T_{mw} based on the PBML model

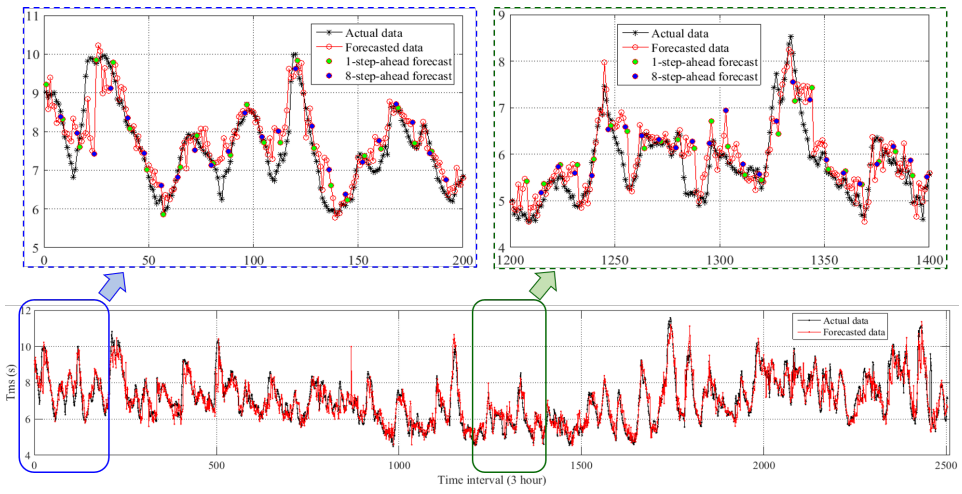

Figure 3.19: Forecast results of T_{ms} based on the PBML model

Table 3.8: Forecast errors of T_{ms} based on the PBML model

Error Measures	Lead Time (hour) 3	6	9	12	15	18	21	24
m_{ε_M}	-0.0013	-0.0046	-0.0017	0.0098	0.0030	0.0171	0.0126	0.0082
std_{ε_M}	0.0386	0.0515	0.0625	0.0779	0.0766	0.0822	0.0901	0.0960
MAE (s)	0.1471	0.2541	0.3130	0.4186	0.4011	0.4523	0.4969	0.5340
RMSE (s)	0.3164	0.4106	0.4707	0.5595	0.5693	0.6024	0.6648	0.7136
bias (s)	-0.0153	-0.0504	-0.0386	0.0139	-0.0095	0.0695	0.0273	-0.0070
R^2	0.9713	0.9528	0.9373	0.9103	0.9033	0.8870	0.8621	0.8382
SI	0.0438	0.0565	0.0650	0.0777	0.0792	0.0833	0.0926	0.0995
MAPE (%)	2.0241	3.4833	4.3740	5.9968	5.6001	6.4784	7.063	7.5135

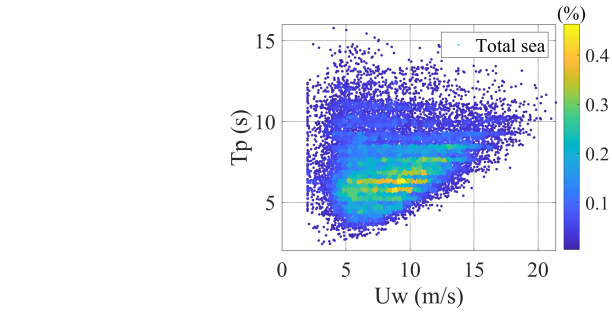

(a) Total sea

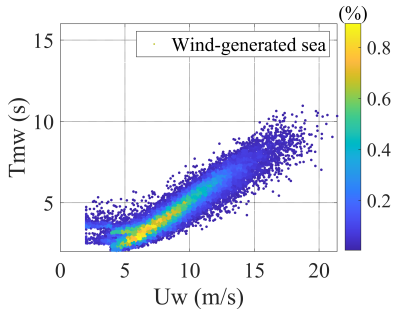

(b) Wind-generated sea

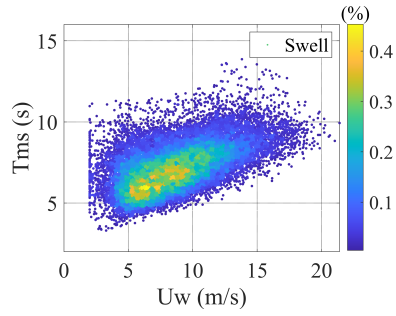

(c) Swell

Figure 3.20: Scatter plot of wave period and mean wind speed

Figures 3.18 and 3.19 present similar findings to those shown in Figures 3.15 and 3.16. That is, the forecast performance of the PBML model for wind-generated sea is better than that for swell. Similar to Figure 3.17, scatter diagrams of the mean wind speed and different wave periods (i.e.,

T_p, T_{mw} and T_{ms}) are illustrated in Figure 3.20. The different correlations shown in Figure 3.20(b) (strong correlation between U_w and T_{mw}) and Figure 3.20(c) (weak correlation between U_w and T_{ms}) can explain these forecast performances to a certain extent. Furthermore, the correlation between U_w and T_p (Figure 3.20(a)) is much lower than the one between U_w and H_s (Figure 3.17(a)), which leads to worse forecast performance of T_p than H_s.

3.3.4 Summary

Forecast performance of the PBML method for one-day-ahead forecasting of wave conditions is investigated in this section. Compared with widely used physics-based numerical methods, high computational efficiency is its primary advantage. On one hand, the PBML model is capable of using environmental conditions in a small area or even from a single position to make forecast. On the other hand, the training process of machine learning is performed mainly through matrix operations rather than solving partial differential control equations. Furthermore, once the model is trained based on the site-specific data, making forecasts on new inputs is straightforward and extremely fast without any new simulations. The forecast results indicate that the forecast performance of H_s is extremely good, while that of T_p is slightly worse due to the weaker implicit relationship between the selected input and output. This is further proved by forecasting wave conditions of wind-generated sea and swell separately. Overall, the PBML method can be conceived as an efficient way for wave forecasting in a small area, which is particularly suitable for on-site marine operations.

Moreover, it must be emphasized that, similar to the physics-based wave model, the PBML model needs future wind forcing to drive it as well. The research conducted in the thesis assumes that the future wind forcing is known and accurate. In real applications, the availability of wind forecasts as well as its uncertainty should also be considered.

3.4 Comparison with physics-based wave models

The application potential of using machine learning-based methods for forecasting environmental conditions have been investigated. Furthermore, it is meaningful to compare them with commonly used physics-based numerical weather forecasting methods. In this section, the comparison of wave forecast performance between TSML model, PBML model and physics-based wave models is performed, which is summarized in Tables 3.9 to 3.11.

Table 3.9: Comparison of one-day-ahead H_s forecasts

Forecasting method		Error measures			
		bias	RMSE	SI	R^2
Physics-based numerical methods	ECMWF	-0.15	0.32	0.21	0.94
	MOF	-0.08	0.25	0.17	0.96
	MTF	-0.22	0.42	0.24	0.91
	SHM	-0.27	0.44	0.21	0.93
	DMI	-0.11	0.27	0.20	0.94
	MTN	-0.17	0.29	0.20	0.94
Machine learning-based method	TSML	-0.36	0.83	0.39	0.26
	PBML	-0.0008	0.27	0.13	0.96

Table 3.10: Comparison of one-day-ahead T_p forecasts

Forecasting method		Error measures			
		bias	RMSE	SI	R^2
Physics-based numerical methods	ECMWF	-0.35	0.84	0.28	0.64
	MOF	-0.08	0.84	0.27	0.62
	MTF	-0.22	1.02	0.29	0.60
	SHM	-0.44	0.84	0.28	0.57
	DMI	-0.28	1.26	0.28	0.64
	MTN	-0.26	0.84	0.29	0.60
Machine learning-based method	TSML	-0.22	1.65	0.22	0.49
	PBML	0.12	1.30	0.17	0.71

Given that the forecast performance of different TSML methods is similar, the ANN M-1 model is utilized as the TSML method due to the high computational efficiency. The results shown in Figures 3.10 and 3.14 are used to represent the forecast performance of the PBML method. Tables 3.9 and 3.10 summarize the forecast performance of H_s and T_p in terms of four error measures (bias, RMSE, SI and R^2). In these two tables, physics-based numerical methods from six forecast modelling institutions are considered, namely ECMWF, MOF (MetOffice), MTF (MeteoFrance), SHM (SHOM - Service hydrographique et océanographique de la Marine, Naval Hydrographic and Oceanographic Service), DMI (Danish Meteorological Institute) and MTN (MET-Norway). The results are extracted from a report [198], which evaluated the forecast accuracy of H_s and T_p by com-

paring the forecasts against measurements at different North Sea buoys. In addition, Natskår et al. [199] developed a statistical model to account for uncertainty in H_s forecasts. He compared forecasted H_s at the Norwegian Sea with hindcast data and quantify the forecast uncertainty by analyzing statistics of errors in terms of the maximum significant wave height during the forecast period, as shown in Eq. (3.14). The relevant results are summarized in Table 3.11. We treated H_s forecasts generated by the TSML and PBML methods following the same procedure and made a comparison in this table. It is noted that physics-based numerical methods normally generate weather forecasts within a relatively long forecast horizon (a few days). In order to be consistent with the horizon of forecasts generated by the machine learning-based methods in the thesis, only one-day-ahead results are focused.

$$\chi_{H_s,\max}(T_R) = \frac{H_{s,hc,\max}}{H_{s,fc,\max}} \tag{3.14}$$

where χ is a stochastic variable describing the ratio between hindcasted and forecasted maximum significant wave heights during the operation reference period T_R.

Table 3.11: Comparison of the forecast uncertainty in H_s (based on the method from Natskår)

Forecasting method	T_R (h)	$\mu_{ln\chi}$	$\sigma_{ln\chi}$
by Asle Natskår		0.06	0.11
TSML	24	0.08	0.37
PBML		-0.02	0.10

The comparison between the two machine learning-based methods shows that by accounting for the physical process of wave field, the forecast performance of the PBML method is better than that of the TSML method for both H_s and T_p. By comparing them with the physics-based numerical methods, it is visible that the uncertainty level of the TSML method is the largest. In addition to it, the forecast uncertainty level of the PBML method and physics-based numerical methods is similar. Thus, it could be inferred that when long-term historical wave and wind data are available at a given offshore site, the PBML method can be considered as an alternative to provide multi-step-ahead wave forecasts, since the cost and time consuming of running the PBML model are quite low.

Nevertheless, it must be emphasized that this is only a preliminary comparison to explore the feasibility of using machine learning-based methods

for wave forecasting. The conditions of different forecasting methods are not exactly the same. First, the time duration and location of weather forecasts are different. The analysis time for physics-based wave models in Tables 3.9-3.10 and 3.11 are three months (May 2017 to July 2017) and one year (year 2011), respectively. By comparison, that for machine-learning based models is one year (year 2010). Besides, physics-based wave models from different forecasting centers correspond to different sites in the North Sea area and Norwegian Sea, while the offshore site of interest in the thesis is a location near the North Sea center. Additionally, the sources of validation data used to quantify the uncertainty are different. Physics-based wave models shown in Tables 3.9 and 3.10 are validated by measurements, and the one shown in Table 3.11 uses hindcast data for validation. By comparison, forecasts generated by the TSML and PBML models in the thesis are validated with hindcast data. Finally, physics-based wave models are forced with 10 m forecasted winds. Whereas hindcast winds are used as inputs in machine learning-based models. Nevertheless, the findings from the above comparison analysis still can provide a general sense of the application potential of machine learning methods in weather forecasting.

Chapter 4

Methodology for the allowable sea states assessment of marine operations considering weather forecast uncertainty

During the execution phase, it is necessary to make decisions on whether marine operations can be carried out safely by comparing operational limits with weather forecasts. Accordingly, uncertainty in weather forecasts is an important issue required to be addressed. This chapter investigates the effect of weather forecast uncertainty on marine operations, and proposes a methodology to deal with weather forecast uncertainty in operational planning and execution phases.

First, a brief introduction of the alpha-factor, a correction factor developed by DNV to take into account weather forecast uncertainty for marine operations, is presented. It is determined by the probability analysis of maximum wave height and used to correct the H_s limit of marine operations. Subsequently, a new defined response-based correction factor, called the response-based alpha-factor α_R, is introduced. It is designed to account for the effect of forecast uncertainties in sea states (characterized by H_s and T_p) on dynamic responses of the coupled system for marine operations. α_R is determined from the perspective of system responses to ensure that the safety level for marine operations (e.g., 10^{-4} per operation) is kept the same with and without considering weather forecast uncertainty. The

general methodology for the development of α_R will be described in detail. Finally, the application of the derived response-based alpha-factor for assessment of allowable sea states for marine operations will be discussed.

4.1 Alpha-factor proposed by DNV

The alpha-factor α [146] is estimated by dividing the maximum wave height with a defined probability level to the same level maximum wave height accounting for H_s forecast uncertainty. The expression is shown in Eq. (4.1).

$$\alpha = \frac{H_{\max}}{H_{\max\_WF}} \tag{4.1}$$

where H_{max} is the characteristic value of maximum wave height, that is defined as the extreme wave height during a given reference period (e.g., 3 hours) with an exceedance probability of 10^{-4}. H_{max_WF} is the characteristic value of maximum wave height with the same exceedance probability taking into account the forecast uncertainty in H_s. For clarity, the symbols H_s^t and H_s^f are used to denote the actual (true) and forecast H_s in the following introduction, respectively.

When a forecasted h_s^f value is given and its forecast uncertainty is not considered, it can be regarded as the true H_s, i.e., h_s^t. Then the probability density function (PDF) of maximum wave height with the given significant wave height is defined as $f_H(h')$. Based on the cumulative distribution function (CDF) of maximum wave height (Eq. (4.2)), the characteristic value H_{max} can thereby be calculated by Eq. (4.3).

$$F_H(h) = \int_0^h f_H(h')dh' \tag{4.2}$$

$$1 - F_H(H_{\max}) = 10^{-4} \tag{4.3}$$

By contrast, when forecast uncertainty in the h_s^f value is considered, the true significant wave height should be described as a distribution rather than a deterministic value, accounting for all possible h_s^t values and the corresponding individual wave height distribution under the given h_s^f value. As a result, a joint PDF of H and H_s^t is established as

$$f_{HH_s^t}(h', h_s^t) = f_{H|H_s^t}(h' \,|h_s^t) \cdot f_{H_s^t}(h_s^t) \tag{4.4}$$

where $f_{H|H_s^t}(h' \,|h_s^t)$ is the conditional PDF of maximum wave height with a given actual significant wave height. $f_{H_s^t}(h_s^t)$ is the PDF of actual significant wave height for the given forecasted significant wave height value,

that is evaluated from the uncertainty analysis of the forecasting model. For different forecasted significant wave heights, this distribution will be different.

Through integration, the marginal CDF of the maximum wave height can be obtained, as shown in Eq. (4.5).

$$F_H^{WF}(h) = \int_0^h \int_0^{+\infty} f_{H|H_s^t}(h' \,|\, h_s^t) \cdot f_{H_s^t}(h_s^t) dh_s^t dh' \tag{4.5}$$

In Eq. (4.5), it is important to quantify the weather forecast uncertainty and establish $f_{H_s^t}(h_s^t)$. In the technical report of the joint industry project (JIP) published in 2007 [146], the forecast uncertainty of H_s is characterized by the forecast error Δ_h, which is defined as Eq. (4.6). This is a random variable which is assumed to follow a Gaussian distribution. According to Eq. (4.6), for a given forecasted significant wave height value, the actual significant wave height is also a Gaussian variable and its distribution $f_{H_s^t}(h_s^t)$ can be transformed from the relevant error distribution. That it, its mean value is the forecasted significant wave height adjusted by the error bias and its standard deviation is the same as that of the forecast error. It is important to emphasize that the forecast uncertainty can also be defined in other ways. Subsequently, the characteristic value H_{max_WF} can be determined by solving Eq. (4.7), which is used to generate the α-factor by Eq. (4.1) together with H_{max}.

$$\Delta_h = h_s^f - H_s^t \tag{4.6}$$

$$1 - F_H^{WF}(H_{max\_WF}) = 10^{-4} \tag{4.7}$$

Following the above procedure, α-factors can be estimated and tabulated for different weather forecast scenarios. Although the alpha-factor is obtained based on the extreme wave height, it is used as a ratio of the significant wave height for marine operations, assuming that the extreme wave height is proportional to the significant wave height and disregarding the effect of wave period and system responses. In practice, for the execution phase of an operation, the specific alpha-factor needs to be selected from the tabulated values in terms of the operation duration, the forecast lead time, the quality of weather forecasts, etc. This selected factor can then be used to correct the allowable H_s (i.e., $H_{s\_\lim}$) of the operation by Eq. (4.8) to account for the weather forecast uncertainty.

$$H_{s\_\lim\_\alpha} = \alpha \cdot H_{s\_\lim} \tag{4.8}$$

where $H_{s\_\lim\_\alpha}$ is the new H_s limit accounting for the forecast uncertainty. In real marine operations, the forecasted value of H_s will be compared to

this new H_s limit to determine whether a safe operation can be performed. If the forecasted H_s is smaller than the new H_s limit, the marine operation can be safely performed.

4.2 Response-based alpha-factor

In this section, the methodology for derivation of the response-based alpha-factor α_R is proposed and introduced. It aims to consider the effect of forecast uncertainties in sea states (characterized by H_s and T_p) on marine operations from a perspective of the system responses. A detailed description of the methodology framework, the key parameters as well as involved analytical techniques are introduced in the following subsections.

4.2.1 Key parameters

Considering the properties of marine operations and weather forecasting, the α_R is presented as a function of:

- The type of marine operation and the relevant operational limiting response parameter
- The duration T_E of the selected operation, i.e., the time used in the extreme response analysis. The characteristic value used to define and calculate the α_R is the extreme response value with a certain exceedance probability (e.g., 10^{-4} or 10^{-2}) during the T_E.
- The sea state reference period T_S, such as 1 hour, 3 hours, etc., is the period used to define a stationary sea state, to quantify the forecast uncertainty and to derive the allowable sea states. It is also the same period that α_R will be applied in marine operations to correct the allowable sea states when forecast uncertainty is considered.
- The forecast variable of weather conditions, e.g., H_s, T_p, etc.
- The weather forecasting method
- The lead time T_L of weather forecasts (i.e., the forecast horizon)
- The forecast uncertainty model

Among the above factors, the type of marine operation must first be selected. It decides the critical events during the operation and the corresponding operational limiting response parameters. The identification

method of critical events and limiting parameters refers to Guachamin Acero et al. [67]. By means of numerical modeling of the selected operation during the operational duration T_E, the dynamic responses of the limiting parameters can be studied. The corresponding extreme value distribution and the characteristic value can subsequently be determined by statistically analyzing the dynamic responses. For operations such as offshore wind turbine blade installation, the critical event may be more concentrated in the final mating phase between blade root and turbine hub opening. T_E is only a few minutes in this case, and the extreme response should be analyzed from the numerical simulation with such short period. In contrast, for operations such as towing operation and sea transports, they generally take several hours/days, and the dynamic response should be simulated during this relatively long period of time. In such cases, it is more complicated. One needs to deal with the sequence of the sea states during operation and the worst sea state might be considered to achieve a conservative result.

Regarding weather conditions, T_S refers to a time interval in which the sea state can be assumed to be stationary. In this period, the statistics (such as the mean value and standard deviation) of a realization of the wave elevation are considered to be independent of time. For marine operations, T_S is normally 1 hour or 3 hours. The other three factors, i.e., the forecast variable of weather conditions, the weather forecasting method and the lead time T_L of weather forecasts, determine the uncertainty related to the weather forecasts. Regarding the forecast variable, significant wave height H_s and peak wave period T_p which are utilized to describe sea states are considered. For operations sensitive to wind loads, forecast uncertainty in the wind fields may also be included and related variables (e.g., mean wind speed U_w) can be regarded as other forecast variables. With regard to the lead time T_L, it could range from one- or three-hours-ahead (depending on T_S) to several-days-ahead, taking into account the execution time of the selected marine operation. As for the forecasting method, different methods (e.g., physics-based numerical method, statistical method or machine learning method) can be adopted to generate forecasts. After obtaining weather forecasts, a forecast uncertainty model is utilized to quantify uncertainties in sea state forecasts.

4.2.2 Framework

The framework of the proposed methodology is illustrated in Figure 4.1 and described in the following steps.

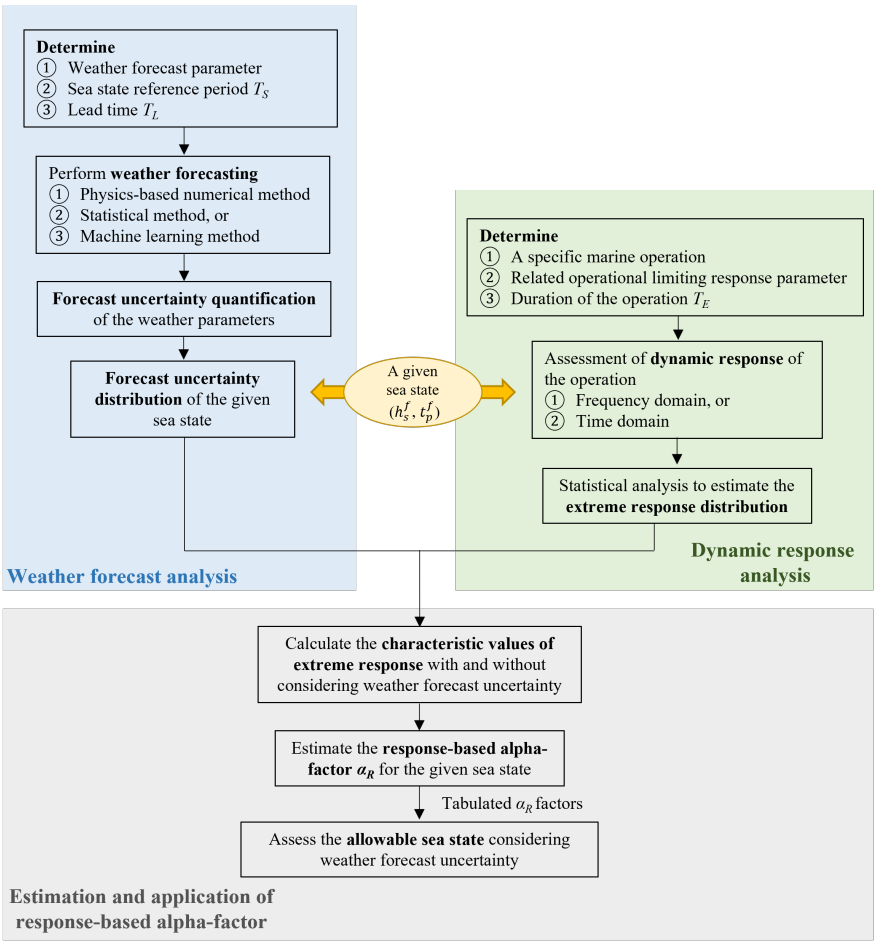

Figure 4.1: The framework of the methodology for developing the response-based alpha-factor

Weather forecast and uncertainty quantification

1. Determine the weather variable that needs to be forecasted, the sea state reference period T_S and the lead time T_L.

2. The selected weather parameters are then forecasted through the physics-based numerical method (such as WAM), the statistical method (such

as ARIMA) or the machine learning method (such as ANN). In the thesis, the weather forecasting is carried out for both H_s and T_p to describe the sea state. In order to better illustrate the weather forecast analysis, the actual sea state is termed as (H_s^t, T_p^t) and the forecasted sea state is presented as (H_s^f, T_p^f). Normally, for the forecast uncertainty analysis, the amount of forecasted data should be as large as possible.

3. The forecast uncertainty quantification is performed to establish error distributions. Similar to the alpha-factor method, this can be done by analyzing the statistical characteristics of a pre-defined forecast error ratio in terms of T_L.

4. Finally, for a given forecasted sea state, the distribution of the actual sea state can be established by transforming the error distribution. This distribution reflects all possible true sea states for a given forecast, and illustrates the weather forecast uncertainty. The method and details for forecast uncertainty quantification will be presented in Sec. 4.3.

Dynamic response analysis

1. A specific marine operation is determined. For this operation, the critical events and operational limiting response parameters as well as the operational duration T_E should be identified.

2. For the sea state considered in the weather forecast analysis, the dynamic response of the limiting response parameter can be simulated and assessed based on frequency- or time-domain response analyses, depending on the properties of the selected operation.

3. Finally, by statistically analyzing the dynamic responses, the extreme response distribution can be estimated. A description of the extreme response analysis will be given in Sec. 4.4.

Estimation and application of the response-based alpha-factors

1. Once the forecast uncertainty distribution and the extreme response distribution for a given sea state are determined, the characteristic values of the limiting parameter in the condition with and without considering weather forecast uncertainty can be calculated respectively. The characteristic value corresponds to the extreme response for a target exceedance probability (e.g., 10^{-4}) of the extreme response distribution within the period T_E.

2. By dividing the two calculated values, the α_R for this given sea state can be estimated. The details for calculating the α_R will be presented in Sec. 4.5.

3. Followed by this procedure, the tabulated α_R can be generated for various sea states. Based on it, the allowable sea states associated with the operation could be assessed, accounting for the weather forecast uncertainty. This will be discussed in Sec. 4.6.

4.3 Uncertainty quantification of sea state forecast

In this section, the procedure for quantifying the uncertainty in sea state forecasts is described. It is assumed that forecast uncertainties of H_s and T_p are independent. Therefore, the PDF of actual sea state with a given forecasted sea state (h_s^f, t_p^f) can be expressed as Eq. (4.9).

$$f_{H_s^t T_p^t}(h_s^t, t_p^t) = f_{H_s^t}(h_s^t) \cdot f_{T_p^t}(t_p^t) \tag{4.9}$$

where $f_{H_s^t}(h_s^t)$ and $f_{T_p^t}(t_p^t)$ describe the probability that actual H_s and T_p may occur under given forecasted significant wave height and peak wave period, respectively.

To establish the PDF of actual sea state, the PDF of the forecast error should be first determined, and then the PDF of the actual sea state is obtained by converting that of the forecast error for a given forecasted sea state. In previous chapters, the forecast error factor, defined as Eq. (2.46), has been applied to quantify the forecast uncertainty. To facilitate the transformation of distributions, the forecast error ratio ε (defined as Eq. (2.47)) will be used in Chs. 4 and 5. Corresponding to H_s and T_p, ε_h and ε_t are expressed by Eqs. (4.10) and (4.11) respectively.

$$\varepsilon_h = \frac{H_s^t}{h_s^f} \tag{4.10}$$

$$\varepsilon_t = \frac{T_p^t}{t_p^f} \tag{4.11}$$

Since marine operations are normally executed in relatively low sea states, it is reasonable to analyze the forecast uncertainty with respect to the range of H_s and T_p. For this purpose, forecasted data as well as corresponding forecast error ratios are categorized. Subsequently, error distribution for each group can be established. Both ε_h and ε_t are modelled

as Gaussian distributed, whose parameters should be estimated separately in each group. Correspondingly, the PDFs of the forecast error ratios can be expressed as Eqs. (4.12) and (4.13) respectively.

$$f_{E_h}(\varepsilon_h) = \frac{1}{\sqrt{2\pi}\,\sigma_{\varepsilon h}} \exp\left[-\frac{1}{2}\left(\frac{\varepsilon_h - \mu_{\varepsilon h}}{\sigma_{\varepsilon h}}\right)^2\right] \tag{4.12}$$

$$f_{E_t}(\varepsilon_t) = \frac{1}{\sqrt{2\pi}\,\sigma_{\varepsilon t}} \exp\left[-\frac{1}{2}\left(\frac{\varepsilon_t - \mu_{\varepsilon t}}{\sigma_{\varepsilon t}}\right)^2\right] \tag{4.13}$$

where mean value $\mu_{\varepsilon h}$ and standard deviation $\sigma_{\varepsilon h}$ are functions of h_s^f and T_L. Mean value $\mu_{\varepsilon t}$ and standard deviation $\sigma_{\varepsilon t}$ are functions of t_p^f and T_L.

$$\mu_{\varepsilon h} = \mu_{\varepsilon h}(h_s^f, T_L) \tag{4.14}$$

$$\sigma_{\varepsilon h} = \sigma_{\varepsilon h}(h_s^f, T_L) \tag{4.15}$$

$$\mu_{\varepsilon t} = \mu_{\varepsilon t}(t_p^f, T_L) \tag{4.16}$$

$$\sigma_{\varepsilon t} = \sigma_{\varepsilon t}(t_p^f, T_L) \tag{4.17}$$

Based on the expressions of ε_h and ε_t, actual H_s and T_p are also Gaussian distributed. They are described as Eqs. (4.18) and (4.19) and also functions of forecasted sea state values and T_L. They reflect the forecast uncertainty in sea states.

$$h_s^t = \varepsilon_h \cdot h_s^f = N(h_s^f \cdot \mu_{\varepsilon h}, h_s^{f2} \cdot {\sigma_{\varepsilon h}}^2) \tag{4.18}$$

$$t_p^t = \varepsilon_t \cdot t_p^f = N(t_p^f \cdot \mu_{\varepsilon t}, t_p^{f2} \cdot {\sigma_{\varepsilon t}}^2) \tag{4.19}$$

4.4 Extreme response analysis for marine operations

In this section, the method for evaluating the conditional distribution of the extreme response for a given sea state will be briefly summarized. Normally, the extreme response distribution is built based on the dynamic responses analysis of marine operations. According to the nature of the problem, two methods are mainly applied, i.e., frequency domain (FD) and time domain (TD) methods. Regarding marine operations, for problems that can be considered under a linear assumption, it is possible to study the dynamic response in frequency domain to significantly reduce computational cost. Whereas for complex nonlinear systems, time domain response analysis approach is more suitable.

Frequency domain analysis

When analyzing the dynamic response of an offshore structure subjected to wave loads in frequency domain, it is assumed that the response amplitude y_a varies linearly with the wave amplitude ξ_a for each frequency, and the transfer function $h_{\xi Y}(\omega)$ is utilized to characterize this deterministic relationship. Correspondingly, the response spectrum $S_{YY}(\omega; h_s^t, t_p^t)$ can be given by

$$S_{YY}(\omega; h_s^t, t_p^t) = |h_{\xi Y}(\omega)|^2 \cdot S_{\xi\xi}(\omega; h_s^t, t_p^t) \tag{4.20}$$

where $S_{\xi\xi}(\omega; h_s^t, t_p^t)$ is the wave spectrum for a given sea state (h_s^t, t_p^t). $|h_{\xi Y}(\omega)|$ is the absolute value of transfer function.

Given that the wave surface process can be modelled as a Gaussian process, the response process can also be modelled as a Gaussian process due to the linearity assumption. Correspondingly, it is reasonable to model the global response maxima R_o (i.e., the largest value between zero up-crossings) as a Rayleigh distribution under a given sea state, as shown in Eq. (4.21).

$$F_{R_0|H_s^t T_p^t}(r_0 \,|h_s^t, t_p^t) = 1 - \exp\left[-\frac{1}{2}\left(\frac{r_0}{\sigma_Y(h_s^t, t_p^t)}\right)^2\right] \tag{4.21}$$

where $\sigma_Y^2(h_s^t, t_p^t)$ is the variance defined by Eq. (4.22), in which $m_{YY}^{(0)}(h_s^t, t_p^t)$ is the $zero^{th}$ order spectral moment.

$$\sigma_Y^2(h_s^t, t_p^t) = m_{YY}^{(0)}(h_s^t, t_p^t) \tag{4.22}$$

The j^{th} order spectral moments $m_{YY}^{(j)}(h_s^t, t_p^t)$ can be defined by

$$m_{YY}^{(j)}(h_s^t, t_p^t) = \int_0^\infty \omega^j S_{YY}(\omega; h_s^t, t_p^t) d\omega \tag{4.23}$$

Assume that all individual global response maxima of the given sea state are independent and identically distributed, the CDF of extreme response R can be given by Eq. (4.24), where n is the expected number of global maxima during the given period T_E, calculated by Eq. (4.25).

$$F_{R|H_s^t T_p^t}(r \,|h_s^t, t_p^t) = \left\{1 - \exp\left[-\frac{1}{2}\left(\frac{r}{\sigma_Y(h_s^t, t_p^t)}\right)^2\right]\right\}^n \tag{4.24}$$

$$n = \frac{T_E}{T_{m02}} \tag{4.25}$$

where T_{m02} is the mean zero up-crossing period, given by

$$T_{m02} = 2\pi\sqrt{\frac{m_{YY}^{(0)}}{m_{YY}^{(2)}}} \tag{4.26}$$

As n increases, this CDF can be reasonably approximated by the Gumbel distribution, which is shown in Eq. (4.27).

$$F_{R|H_s^t T_p^t}(r\,|h_s^t, t_p^t) = \exp\left\{-\exp\left[-\frac{r-\gamma}{\beta}\right]\right\} \tag{4.27}$$

where γ and β are the location and scale parameters, respectively. They are expressed as Eqs. (4.28) and (4.29), based on the Rayleigh assumption of the global response maxima.

$$\gamma = \sigma_Y(h_s^t, t_p^t)\sqrt{2\ln n} \tag{4.28}$$

$$\beta = \frac{\sigma_Y(h_s^t, t_p^t)}{\sqrt{2\ln n}} \tag{4.29}$$

Finally, based on Eq. (4.27), the characteristic value of the dynamic response corresponding to a target exceedance probability can be calculated.

Time domain analysis

For marine operations like mating operation of offshore blade installation, there exists a number of non-linear sources such as second-order wave forces on floating vessel, aerodynamic loads on blade and so on. Hence, dynamic response of the system should be addressed in time domain. In this case, the assumption of Rayleigh distributed global maxima is no longer valid. Nevertheless, a Gumbel extreme value distribution is still valid for most cases [200], but the expressions of Gumbel parameters shown in Eqs. (4.28) and (4.29) need to be modified. To find Gumbel parameters, it is necessary to fit the extreme response distribution based on the response time series by time domain simulations. The procedure is described as follows:

1. For a given sea state, perform the time domain simulation of the operation during the operational duration T_E (e.g., 10 min) and get a realization of the dynamic response. From the realization, the response maxima r_1 can be extracted.

2. To better fit the tail of the extreme response distribution, multiple simulations under the same sea state should be performed to extract a sufficient number of maxima. Hence, repeat the simulation k times with random wave seeds, and k independent response maxima $\{r_1, r_2, r_3, \ldots, r_k\}$ can be obtained.

3. According to the series of response maxima, the Gumbel distribution can be fitted by different methods, e.g., the method of moments, maximum likelihood estimation and so on. Based on the fitted Gumbel distribution, the related characteristic value can be calculated, corresponding to a target exceedance probability from the extreme response distribution.

4. Repeat the procedure for a large number of different sea states, the corresponding Gumbel parameters can be obtained, which are functions of H_s and T_p.

$$\gamma = \gamma(h_s^t, t_p^t) \tag{4.30}$$

$$\beta = \beta(h_s^t, t_p^t) \tag{4.31}$$

4.5 Derivation of the response-based alpha-factor

Followed by the weather forecast analysis and the extreme response analysis, the response-based alpha-factor α_R for a given sea state can be calculated by Eq. (4.32):

$$\alpha_R = \frac{R_E}{R_{E\_WF}} \tag{4.32}$$

where R_E is the characteristic value of the limiting response parameter within an operational duration T_E. It is defined as the extreme response with an exceedance probability (e.g., 10^{-4}) from the extreme response distribution. The definition of R_{E_WF} is similar to R_E but considering the forecast uncertainty in the sea state.

1) Calculation of R_E

When a forecasted sea state (h_s^f, t_p^f) is given and its uncertainty is not considered, the forecasted sea state is regarded as the true value, i.e., (h_s^t, t_p^t). Under this sea state, the extreme response distribution of a specific operation can be estimated directly by frequency- or time-domain response analyses. The PDF of the extreme response R is denoted as $f_{R|H_s^t T_p^t}(r' \,|h_s^t, t_p^t)$, and its CDF can be expressed as Eq. (4.33).

$$F_R(r) = \int_0^r f_{R|H_s^t T_p^t}(r' \,|h_s^t, t_p^t) dr' \tag{4.33}$$

By solving Eq. (4.34) with a certain exceedance probability (e.g., 10^{-4} shown in the equation), the R_E value under the sea state can be determined.

It should be noted that the target exceedance probability depends on the type of operation and consequences of failure events.

$$1 - F_R(R_E) = 10^{-4} \tag{4.34}$$

For marine operations, the exceedance probability of the extreme response is normally set to 10^{-4}. However, the selection of such exceedance probability level is subjected to discussion. The target level can reflect the consequences of operation failure and one may also consider for example 10^{-2} for marine operations if the consequence of failure is not significant. For instance, for the mating operation by an installation vessel, the motion response of the crane tip can be regarded as a limiting response parameter. It is not a structural response parameter like lift wire tension. Large crane tip motion will lead to unsuccessful operation, but may not cause any structural and component damage or operation failure. Operator may try a second operation, if the first operation is not possible. Therefore, in this case, the characteristic values of the limiting parameter can be derived on the basis of extreme response analysis corresponding to a relatively high exceedance probability level.

2) Calculation of R_{E_WF}

When the weather forecast uncertainty is taken into account, the forecasted sea state cannot be regarded as the true value directly. Instead, for the forecasted sea state $(h_s^f,\, t_p^f)$, there are many possibilities for the actual sea state. Therefore, it is of importance to establish the PDF of actual sea state under the given forecasted sea state, expressed as $f_{H_s^t T_p^t}(h_s^t, t_p^t)$. In this case, the characteristic value R_{E_WF} can be determined by a joint PDF of the extreme response R and the actual sea state (H_s^t, T_p^t), that is established as

$$f_{RH_s^t T_p^t}(r', h_s^t, t_p^t) = f_{R\left|H_s^t T_p^t\right.}(r' \left| h_s^t, t_p^t \right.) \cdot f_{H_s^t T_p^t}(h_s^t, t_p^t) \tag{4.35}$$

where $f_{R\left|H_s^t T_p^t\right.}(r' \left| h_s^t, t_p^t \right.)$ is the conditional PDF of the extreme response with a given actual sea state. $f_{H_s^t T_p^t}(h_s^t, t_p^t)$ reflects the uncertainty in actual sea states for a given forecasted sea state.

Through integration, the marginal CDF of R can be obtained, as shown in Eq. (4.36).

$$F_R^{WF}(r) = \int_0^r \int_0^{+\infty} \int_0^{+\infty} f_{R\left|H_s^t T_p^t\right.}(r' \left| h_s^t, t_p^t \right.) \cdot f_{H_s^t T_p^t}(h_s^t, t_p^t) dh_s^t dt_p^t dr' \tag{4.36}$$

By solving Eq. (4.37), the corresponding R_{E_WF} value with the same exceedance probability as R_E can be determined.

$$1 - F_R^{WF}(R_{E\_WF}) = 10^{-4} \tag{4.37}$$

3) Calculation of α_R

For the given sea state, by substituting R_E and R_{E_WF} values, the corresponding α_R value can be calculated by Eq. (4.32). α_R depends on the type and duration of the marine operation, the forecasting method, etc., mentioned in Sec. 4.2.1. For a specific marine operation, repeating this procedure in different sea states, the tabulated α_R can be obtained.

4.6 Application of the response-based alpha-factor

According to the α-factor proposed by DNV, the allowable sea states in terms of H_s can be adjusted directly by the selected α. In comparison, the α_R proposed in this thesis is from the perspective of dynamic responses, and it also depends on the type of operations. Besides, α_R takes into account the forecast uncertainty in both H_s and T_p. Correspondingly, it should be more comprehensive and reliable in the application of marine operations. However, the α_R is a response-based criterion and cannot be used directly to correct sea state limits. In this case, allowable sea states have to be re-assessed considering explicitly the forecast uncertainty and depending on the forecast horizon. The procedures of applying the α_R in marine operations are summarized as follows:

- **Construction**
  In the planning phase of a specific operation, the allowable sea states of the relevant limiting response parameter should be assessed. In principle, this could be done by comparing characteristic values of the response with the allowable limit value. Based on the aforementioned procedure, characteristic values R_E of the limiting parameter for various sea states can be evaluated by carrying out dynamic response analysis. Then different sea states under which R_E is equal to the allowable limit can be found. These sea states form a contour line to represent the maximum sea states that the operation can be safely executed. One example is illustrated in Figure 4.2. Assuming that the allowable response limit of an operation is R_E^0, a black solid line can be generated, showing the maximum allowable sea states for the operation. For all sea states along this line, the corresponding characteristic value R_E of the system will be equal to the allowable limit value. For instance, at the point A, the characteristic value R_E^A under the sea state (h_s^A, t_p^A), is equal to the R_E^0.

  This is the case without considering uncertainty in sea state forecasts. If forecast uncertainty is considered, the allowable sea states should

be reduced to a certain degree. For instance, when a 3 hours-ahead sea state forecast is (h_s^{Af}, t_p^{Af}) (i.e., at point A), due to the uncertainty of the forecast, the true sea state should be described by the distribution $f_{H_s^t T_p^t}(h_s^t, t_p^t)$ instead of a single value. This distribution is represented by the red circles around the point A. By considering all possible true sea states and corresponding system responses, the characteristic value $R_{E\_WF}^A$ can be calculated by Eqs. (4.36) and (4.37). The $R_{E\_WF}^A$ becomes larger than the R_E^A, and their ratio is the α_R with respect to this sea state and forecast lead time. This means that the operation can no longer be carried out safely for the forecasted sea state (h_s^{Af}, t_p^{Af}), and the sea state should be reduced to a certain level to ensure that the characteristic value of the extreme response is equal to the allowable response limit (i.e., R_E^0). Correspondingly, the blue dash line can be generated, that is the allowable sea states of the operation considering weather forecast uncertainty with T_L of 3 hours. For example, at the point B, the characteristic value $R_{E\_WF}^B$ corresponding to the forecasted sea state (h_s^{Bf}, t_p^{Bf}) with the lead time of 3 hours, will be equal to the allowable response limit R_E^0.

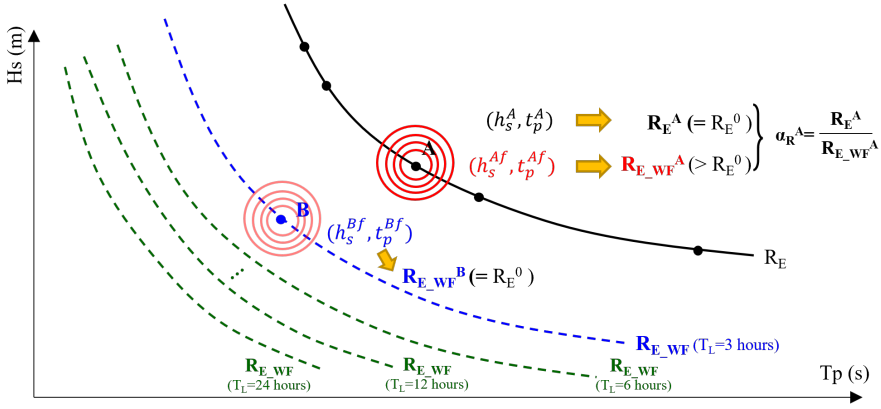

Figure 4.2: Illustration of construction of allowable sea states considering weather forecast uncertainty

Following this procedure for various forecasted sea states and forecast lead times, allowable sea states of the operation including sea state forecast uncertainties at different T_L can be produced. These are plotted as blue and green dash lines in Figure 4.2.

- **Application**
  Once these allowable sea states are constructed in the planning phase, they can be used directly to assist decision-making during the execution phase of the operation, without any new simulations. This is done by comparing updated sea state forecast values with these contour lines. An example is illustrated in Figure 4.3.

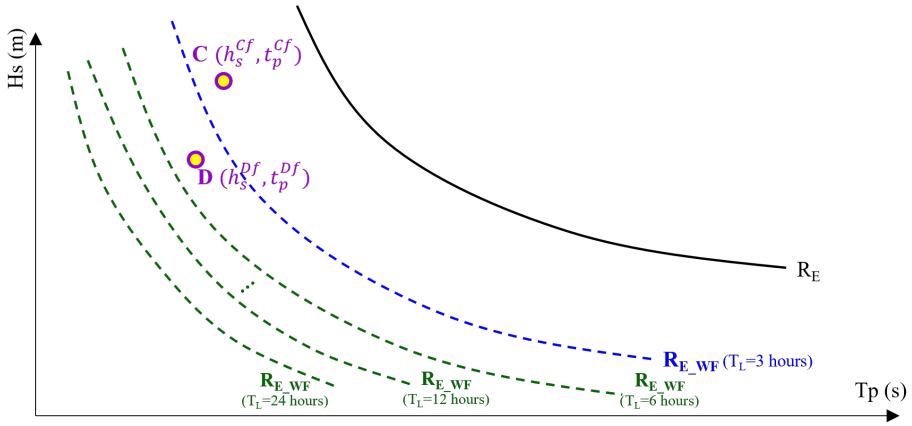

Figure 4.3: Illustration of application of allowable sea states considering weather forecast uncertainty

If a 3 hours-ahead forecasted sea state is (h_s^{Cf}, t_p^{Cf}), by checking its location in Figure 4.3 (that is at the point C), one can conclude that the operation cannot be executed since it is above the blue line. By contrast, if a 3 hours-ahead forecasted sea state is at point D, i.e. (h_s^{Df}, t_p^{Df}), which is below the blue line, the operation is considered executable.

It is clear that once these contour lines are generated, they can be used easily and directly. According to the relative position of the weather forecast value of a certain lead time and the corresponding allowable sea states, the decision on whether or not to start the operation can be quickly made.

Chapter 5

Allowable sea states assessment of the blade installation of offshore wind turbine

The methodology for developing α_R and assessing allowable sea states of marine operations have been presented in Ch. 4. In this chapter, a case study regarding blade installation of offshore wind turbines is conducted, to illustrate the procedure and the feasibility of the methodology. For the blade installation, the final mating phase is considered. In this phase, the blade is close to the nacelle and the dynamic properties of the system do not vary with time significantly. Therefore, the steady-state analysis of blade installation is performed. Numerical modelling related to the installation given in Sec. 5.1 together with uncertainty quantification of weather forecasts given in Sec. 5.2 are applied for generating α_R of relevant response limiting parameters. Both the crane tip motion and the blade root radial motion and velocity are regarded as the operational limiting response parameters for the installation process, to illustrate the methodology based on response analysis in frequency- and time-domain, respectively. Secs. 5.3 and 5.4 summarize the corresponding results of α_R factors and allowable sea states considering weather forecast uncertainty.

5.1 Numerical modelling of blade installation

The configuration of a semi-submersible crane vessel used to simulate the single blade installation is illustrated in Figure 5.1. As displayed, the numerical model consists of three main parts, i.e., a semi-submersible vessel, a crane and a blade. The semi-submersible vessel is assumed to be equipped with dynamic positioning (DP) systems to mitigate its slowly varying motions in surge, sway and yaw. The crane is modelled as a typical pedestal crane and the DTU 10 MW wind turbine blade [201] is used. For a detailed description of the model properties, refer to Zhao et al. [54]. Three coordinate systems are also shown in Figure 5.1. As displayed, there are three right-handed coordinate systems, i.e., a global coordinate system $O-XYZ$, a vessel-related coordinate system $O_v - X_vY_vZ_v$ and a blade-related coordinate system $O_b - X_bY_bZ_b$, whose origins are located at the mean sea surface, the center of the waterplane of the semi-submersible at rest and the center of gravity (COG) of the blade, respectively. X_v and X_b are in the longitudinal direction of the vessel and blade, respectively.

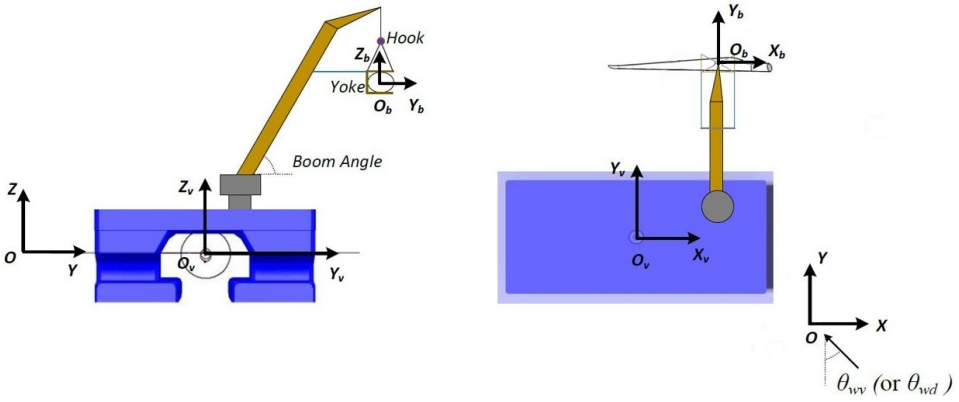

Figure 5.1: Schematic view of the offshore blade installation system (θ_{wv} is the incident wave angle and θ_{wd} is the wind inflow angle)

A fully coupled simulation method, the SIMO-RIFLEX-Aero [52], is applied to simulate the offshore blade installation in time-domain, which integrates three programs, i.e., SIMO (SINTEF Ocean [202]) , RIFLEX (SINTEF Ocean [203]) and Aero (Zhao et al. [53]). Among them, the hydrodynamic loads on the semi-submersible and structural dynamics (e.g., crane flexibility) are analyzed by SIMO and RIFLEX respectively, and they are integrated in the SIMA workbench [204]. The aerodynamic loads acting on the blade are calculated by the Aero code based on the cross-flow

principle [205, 206], in terms of the instantaneous blade displacement and velocity at each time step. It is coupled with SIMO and RIFLEX using the external dynamic link library (DLL) in SIMA.

To assess allowable sea states for the mating operation of blade installation, the critical events and the corresponding limiting parameters should first be identified. An illustration of the system is plotted in Figure 5.2, which was provided by Zhao [207]. According to her research, the critical events during the mating phase are excessive radial motion of the blade root and bent guide pins at the blade root. Correspondingly, the limiting parameters are the blade root radial motion and blade root radial velocity (i.e., motion and velocity in the $Y_bO_bZ_b$ plane), respectively. In addition, the crane tip motion is also regarded as a limiting parameter, in order to illustrate the methodology in frequency domain in the case study. To assess dynamic responses of the limiting response parameters, numerical simulations should be carried out under different environmental conditions. In the thesis, only irregular beam wind and wave condition is considered (i.e., θ_{wv} and θ_{wd} are zero in Figure 5.1) because they could induce relatively higher response of the system. In addition, the North Sea area is focused and the JONSWAP spectrum is used to describe the sea state. Besides, the simulation time is 10 min, which is consistent with the duration of the final mating phase of the blade installation.

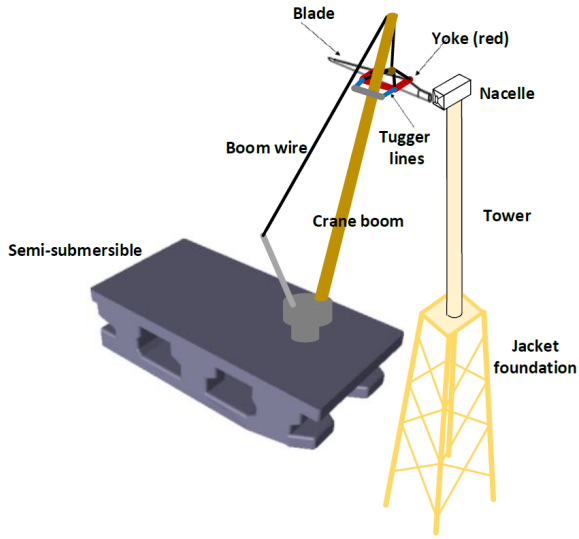

Figure 5.2: Illustration of the mating phase of offshore blade installation [207]

5.2 Uncertainty quantification of weather forecasts

Uncertainty of one-day-ahead H_s and T_p forecasts at the reference site is quantified in this section. TSML (ANN M-1 model is utilized) and PBML methods are adopted, which have been investigated in Ch. 2. Figures 5.3 and 5.4 show PDFs of ε_h and ε_t at different lead times. As displayed, the error seems to follow a Gaussian distribution, which is in line with its assumption. As the lead time increases, error distributions show more discrepancies, which proves the necessity of quantifying the weather forecast uncertainty. In addition, only forecasts of the total sea are considered and utilized for the uncertainty quantification analysis. For the wind-generated sea and swell, they are forecasted separately in Sec. 3.3.3, in which the corresponding uncertainty models are built. However, the effect of their forecast uncertainties on marine operations is not addressed in the thesis.

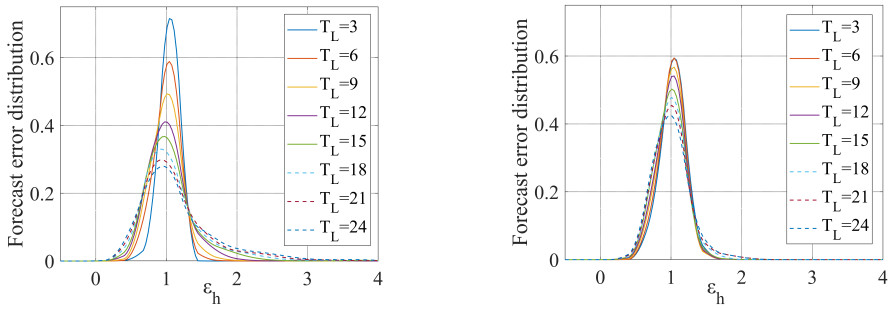

(a) ε_h distribution (TSML method) (b) ε_h distribution (PBML method)

Figure 5.3: Forecast error distribution of H_s at different lead times

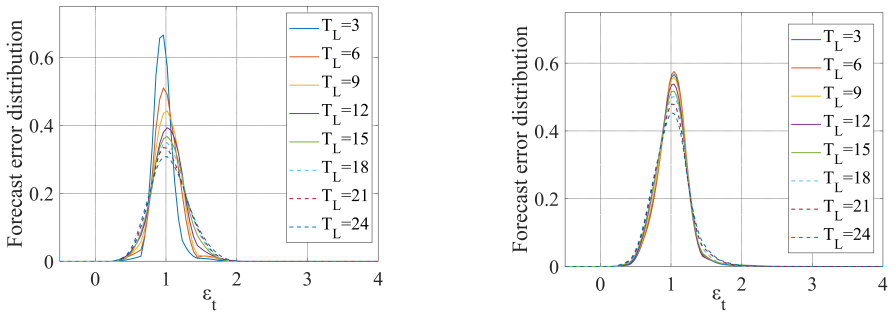

(a) ε_t distribution (TSML method) (b) ε_t distribution (PBML method)

Figure 5.4: Forecast error distribution of T_p at different lead times

As aforementioned, forecast error ratios should be analyzed with respect to the range of H_s and T_p. According to the scatter plot of sea states at the North Sea center (see Figure A.5 (c)), the interval of H_s groups is set to 0.5 m, and the group is named using the center value of the interval. For instance, the group '1.5 m' denotes forecasted H_s is between 1.25 m and 1.75 m. To ensure that there are sufficient data to fit uncertainty distributions in all groups, all errors with H_s lower than 0.75 m and higher than 3.75 m are classified as '0.5 m' and '4 m' groups, respectively. Likewise, T_p errors are categorized into different groups in terms of forecasted T_p with an interval of 1 s. All errors of T_p lower than 5.5 s and higher than 9.5 s are classified as '5 s' group and '10 s', respectively. These sea state ranges are site specific and need to be determined according to the characteristics of the target sea areas.

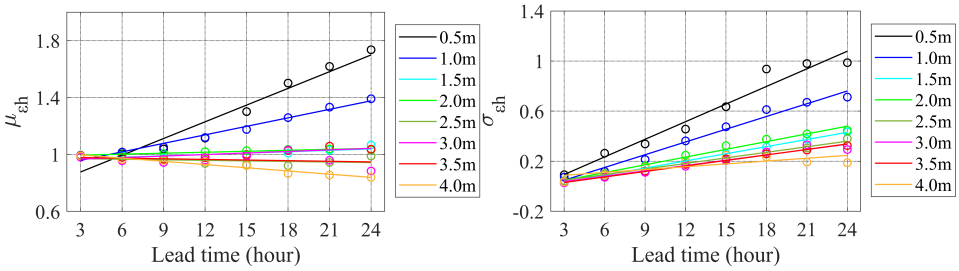

(a) $\mu_{\varepsilon h}$ (b) $\sigma_{\varepsilon h}$

Figure 5.5: Statistics of ε_h and trend line analysis for different lead times (TSML method)

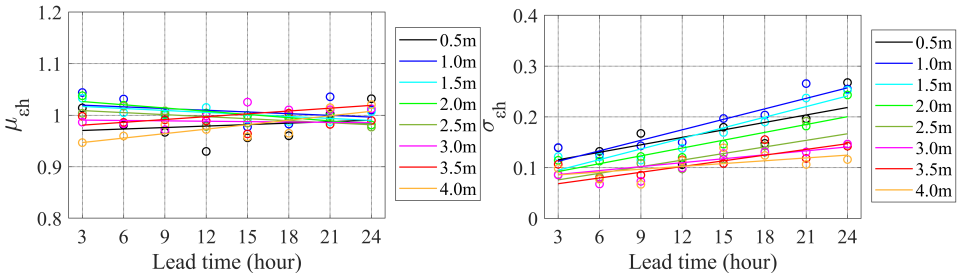

(a) $\mu_{\varepsilon h}$ (b) $\sigma_{\varepsilon h}$

Figure 5.6: Statistics of ε_h and trend line analysis for different lead times (PBML method)

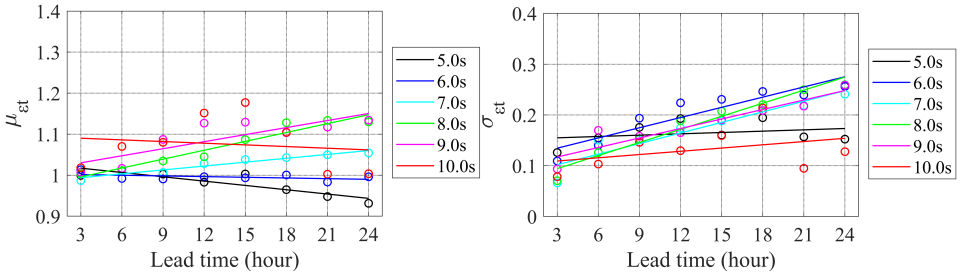

(a) $\mu_{\varepsilon t}$ (b) $\sigma_{\varepsilon t}$

Figure 5.7: Statistics of ε_t and trend line analysis for different lead times (TSML method)

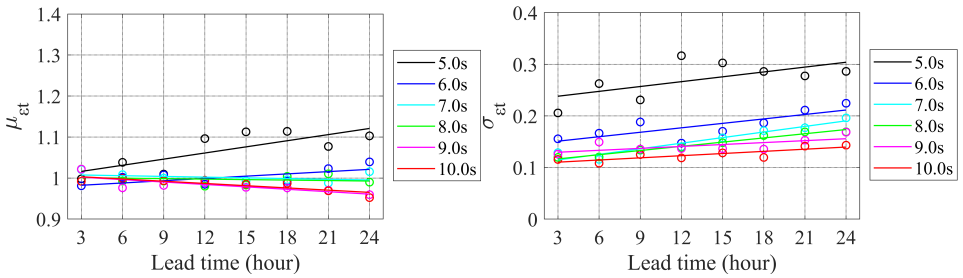

(a) $\mu_{\varepsilon t}$ (b) $\sigma_{\varepsilon t}$

Figure 5.8: Statistics of ε_t and trend line analysis for different lead times (PBML method)

Figures 5.5-5.8 present statistics of ε_h and ε_t (discrete points in different colors) in terms of different ranges of forecasted H_s and T_p, which are functions of the lead time T_L and generated by the TSML and PBML methods, respectively. It is evident that error statistics show certain fluctuations, caused by the statistical uncertainty due to the limited number of forecasts. This phenomenon can be observed especially in the cases with small significant wave height and short peak wave period. This may also be due to the fact that for the definition of the forecast error ratio, small values will have larger error ratio than the large values for the same absolute error. To eliminate these effects to a certain extent, the trend analysis is performed. The trend lines (linear type) of the discrete points in the above figures are estimated using the least-square fit algorithm, shown as solid lines in the corresponding figures. From the generated trend lines shown in Figures 5.5-5.8, one can observe that both $\mu_{\varepsilon h}$ and $\mu_{\varepsilon t}$ are close to one in different

groups, except for cases with H_s in the range of 0.5 to 1.0 m by the TSML method. Meanwhile, the level of $\sigma_{\varepsilon h}$ and $\sigma_{\varepsilon t}$ increase as T_L increases and the range decreases. By using statistics along trend lines, the PDF of actual sea states considering uncertainties can be generated, referring to Eqs. (4.18) and (4.19).

In addition to the machine learning-based forecasting models employed in the case study, physics-based wave models (such as WAM, SWAN and WATCH III) are another choice commonly used for the sea state forecasting. Various meteorological centers such as ECMWF and MetOffice are able to provide sea state forecasts based on the physics-based wave models. Their forecast performance is generally evaluated in terms of error measures like RMSE, bias, SI, etc. In order to deal with the corresponding forecast uncertainty and apply the results in the development of α_R, a slightly different uncertainty model should be developed. The aim of the model is to directly use error measures for uncertainty quantification analysis. A detailed example will show the work of it in the following part.

In this uncertainty model, the forecast error (defined as Eq. (2.45)) is used in the forecast uncertainty analysis. For H_s and T_p, Δ_h and Δ_t are expressed as Eqs. (5.1) and (5.2), respectively. Likewise, they are also modeled as random Gaussian variables, but considering all forecasted sea states. As a consequence, Δ_h and Δ_t are not functions of the sea state ranges, but only functions of the forecast lead time. This is different as compared to the forecast error ratios defined in Eqs. (4.10) and (4.11). To establish their distributions, the corresponding Gaussian parameters (i.e., the mean value μ_Δ and standard deviation σ_Δ) can be directly derived by means of RMSE and bias instead of statistical analysis of forecasted data. Their expressions can be seen in Eqs. (5.3) and (5.4), respectively. Table 5.1 lists statistics of Δ_h and Δ_t with respect to the one-day-ahead forecasts from six forecasting modelling institutions described in Sec. 3.4.

$$\Delta_h = h_s^f - H_s^t \tag{5.1}$$

$$\Delta_t = t_p^f - T_p^t \tag{5.2}$$

$$\mu_\Delta = bias \tag{5.3}$$

$$\sigma_\Delta = \sqrt{RMSE^2 - bias^2} \tag{5.4}$$

Table 5.1: Error mean and standard deviation of forecasts from different institutions (T_L=24 hours)

Forecast variable	Gaussian parameter	Forecast modelling institutions					
		ECMWF	MOF	MTF	SHM	DMI	MTN
H_s	$\mu_{\Delta h}$	-0.15	-0.08	-0.22	-0.27	-0.11	-0.17
	$\sigma_{\Delta h}$	0.28	0.24	0.36	0.35	0.25	0.24
T_p	$\mu_{\Delta t}$	-0.34	-0.08	-0.22	-0.44	-0.28	-0.26
	$\sigma_{\Delta t}$	0.77	0.84	1.00	0.72	1.23	0.80

According to the expressions of Δ_h and Δ_t, the conditional PDFs of actual H_s and T_p can be expressed as Eqs. (5.5) and (5.6) respectively. Then the conditional PDF of actual sea states can be calculated by Eq. (4.9). By doing this, the evaluation information of weather forecasts issued by different forecast modelling institutions can be used, and the forecast uncertainty quantification can be carried out. The quantification results can be further used in the following allowable sea state assessment. However, it should be emphasized that this is a relatively simple method since the error is constant within all ranges of the weather variable, and the error distribution are not expressed as a function in terms of h_s^f and t_p^f.

$$f_{H_s^t|H_s^f}(h_s^t \,|\, h_s^f) = N(h_s^f - \mu_{\Delta h}, \sigma_{\Delta h}^2) \tag{5.5}$$

$$f_{T_p^t|T_p^f}(t_p^t \,|\, t_p^f) = N(t_p^f - \mu_{\Delta t}, \sigma_{\Delta t}^2) \tag{5.6}$$

5.3 Crane tip motion (FD)

This section investigates the allowable sea states assessment in terms of the crane tip motion. For the blade installation by a semi-submersible, the motion of the crane tip is important. This is because wave-induced motion of the semi-submersible will contribute to a significant motion at the crane tip. The crane tip motion could further increase the motion of the blade and challenge the security of the blade mating operation. Given that the wave-induced vessel motion is the main source of the crane tip motion, the wave condition is of main interest and the wind condition is not considered in this section. Furthermore, frequency-domain response analysis approach is utilized for the advantage of the high cost efficiency.

5.3.1 Dynamic response analysis of the crane tip

Based on the frequency-domain response analysis approach, the motion of semi-submersible can be directly obtained by the motion transfer functions and wave spectra. The first-order motion transfer functions for the semi-submersible are obtained from the hydrodynamic code HydroD [208]. Based on the motion transfer functions of the semi-submersible and the relative coordinate of the crane tip to semi-submersible's COG, the motion transfer functions for the crane tip can be calculated.

5.3.1.1 Spectral analysis

In the beam sea condition, the transfer functions of the first-order motion of the crane tip in 3 degree-of-freedoms (DOFs) are shown in Figure 5.9. It is visible that the natural periods of the crane tip in X_b, Y_b and Z_b directions are relatively large (23-25 s). Given that the focus of T_p in weather uncertainty analysis is in the range of 5-10 s which are well smaller than these natural periods, the crane tip motion is mainly determined by wave-frequency motions. By applying the transfer functions together with wave spectra, the power spectra of crane tip motion can be generated. An example of a series of wave spectra and the resulting motion spectra of the crane tip are illustrated in Figure 5.10. In the figure, sea states are described by a JONSWAP spectrum with H_s =2 m and different T_p values (from 5 s to 10 s), and the motion spectra are generated by means of spectral analysis in frequency domain.

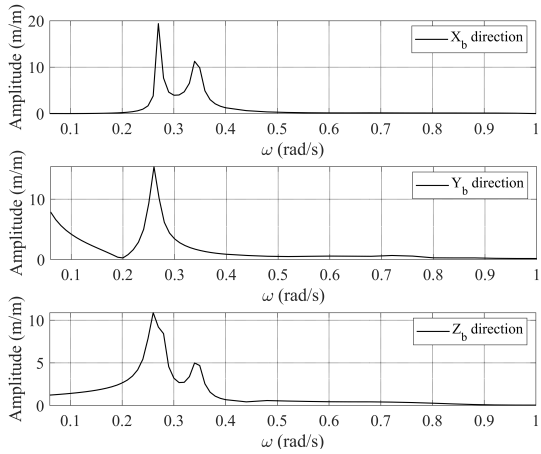

Figure 5.9: Motion transfer functions of the crane tip in the beam sea condition

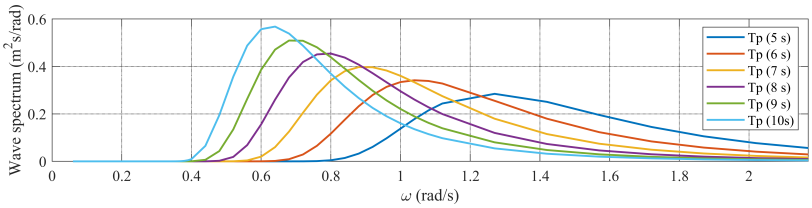

(a) Wave spectra

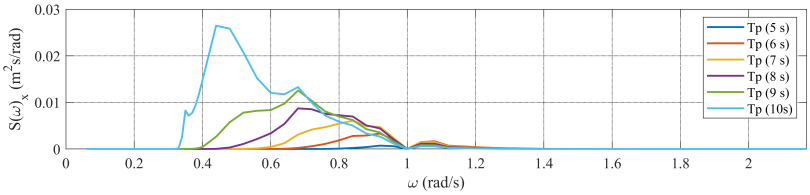

(b) Power spectra of crane tip motion (X_b direction)

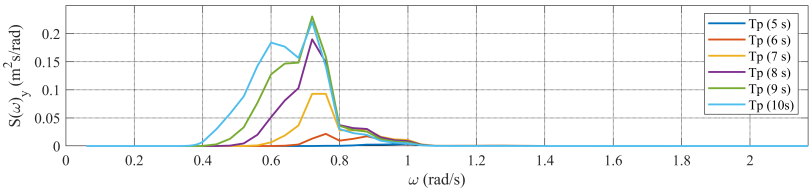

(c) Power spectra of crane tip motion (Y_b direction)

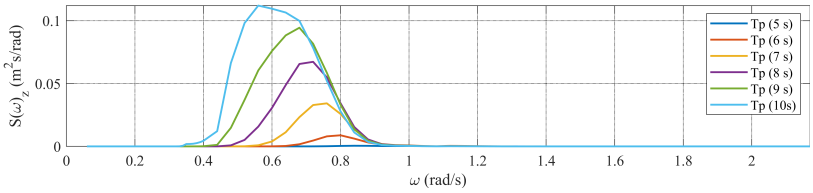

(d) Power spectra of crane tip motion (Z_b direction)

Figure 5.10: Wave spectra and power spectra of crane tip motion for different T_p (H_s=2 m)

As illustrated in Figure 5.10, for a given H_s, the shape of power spectra of crane tip motion is significantly affected by the selection of T_p. The spectrum peaks increase with increasing T_p values, which indicates that the crane tip motion is larger at sea state with larger T_p. This is because the relevant wave periods are well smaller than the natural periods of the crane tip motions and when the wave period increases, the motion of crane tip increases. In frequency domain, the motion spectra of the crane tip can give a complete description of its statistical properties, and a Gumbel dis-

tribution can be adopted to describe the 10-min extreme value. Thus, the characteristic value of the crane tip motion under a target exceedance probability can be identified from the simulation in FD, following the method described in Sec. 4.4. Figure 5.11 presents the characteristic values with an exceedance probability of 10^{-4}. The comparison among cases further proves the importance of T_p to crane tip motion when using a floating installation vessel. By comparing the crane tip motion in X_b, Y_b and Z_b directions, it is visible that the motion in Y_b direction is larger than that in other two directions in the beam sea condition. Hence, only Y_b direction is concerned, and the crane tip motion refers to its motion in Y_b direction in the following analysis.

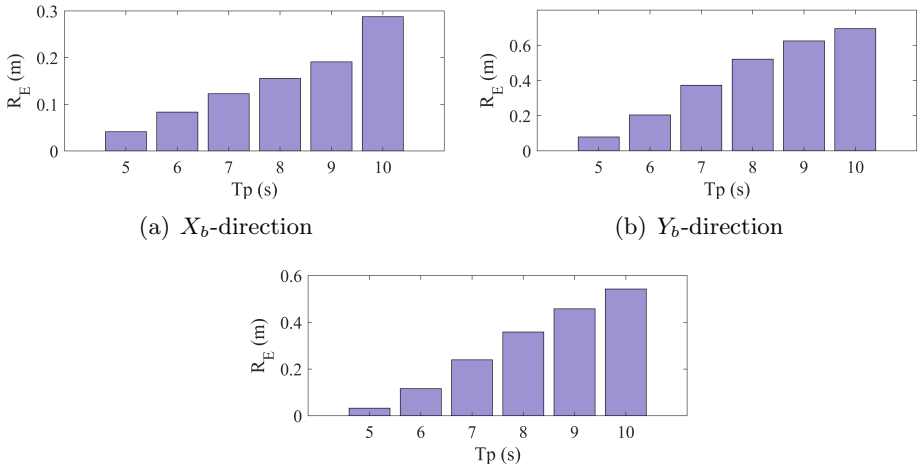

(a) X_b-direction

(b) Y_b-direction

(c) Z_b-direction

Figure 5.11: Characteristic values of crane tip motion for different T_p (H_s=2 m)

5.3.1.2 Extreme response analysis

To illustrate the effect of weather forecast uncertainty, Figure 5.12 gives an example of extreme value distributions of the crane tip motion with and without including weather forecast uncertainty. In this example, the TSML method is used in the sea state forecasting and T_L is 3 hours. The probability of exceedance of 10^{-4} is considered.

The obvious difference between blue and black lines in Figure 5.12 indicates that the uncertainty of sea state forecasts strongly affects the extreme value distribution. Since the weather forecast uncertainty is included, the

blue distribution is much more dispersed than the black one. Based on these two distributions, characteristic values corresponding to an exceedance probability of 10^{-4} are evaluated respectively. By dividing them, the relevant α_R can be established.

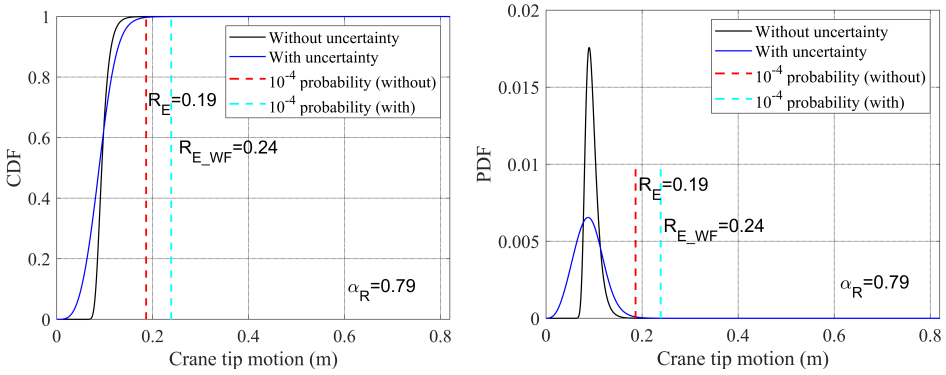

(a) CDF (b) PDF

Figure 5.12: Extreme response distributions with and without considering weather forecast uncertainty (H_s=1 m, T_p=7 s, TSML method, T_L=3 hours, 10^{-4} exceedance probability)

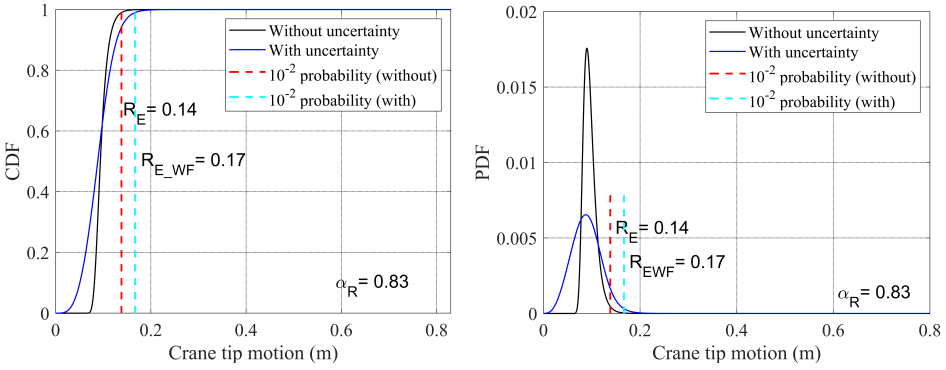

(a) CDF (b) PDF

Figure 5.13: Extreme response distributions with and without considering weather forecast uncertainty (H_s=1 m, T_p=7 s, TSML method, T_L=3 hours, 10^{-2} exceedance probability)

Generally, the characteristic value is determined from the extreme value distribution with a target exceedance probability, to ensure the safety of the

design with an acceptable low probability of damage or collapse. The target exceedance probability depends on the type of operation, the consequence of failure, etc. During the blade installation, since large crane tip motion may not lead to the operation failure, a larger probability of exceedance (i.e., 10^{-2}) can also be considered as well as 10^{-4} recommended in DNV standard. Figure 5.13 shows the relevant results with the 10^{-2} exceedance probability under the same condition as shown in Figure 5.12.

Following the same procedure, R_E and R_{E_WF} values regarding the crane tip motion with exceedance probabilities of 10^{-4} and 10^{-2} in different sea states can be estimated. Results with 10^{-4} exceedance probability are presented in Tables 5.2 and 5.3 for illustration. The R_{E_WF} values still correspond to the TSML method with T_L of 3 hours.

Table 5.2: R_E values (m) of the crane tip motion (10^{-4} exceedance probability)

H_s (m)	T_p (s)					
	5	6	7	8	9	10
0.5	0.02	0.05	0.09	0.13	0.16	0.17
1	0.04	0.10	0.19	0.26	0.31	0.35
1.5	0.06	0.15	0.28	0.39	0.47	0.52
2	0.08	0.20	0.37	0.52	0.62	0.70
2.5	0.10	0.26	0.47	0.65	0.78	0.87
3	0.12	0.31	0.56	0.78	0.94	1.04
3.5	0.14	0.36	0.65	0.91	1.09	1.22
4	0.16	0.41	0.75	1.04	1.25	1.39

By comparison of results in Tables 5.2 and 5.3, it is visible that the R_{E_WF} values are generally larger than the corresponding R_E values when forecast uncertainties in sea states are involved. The degree of this difference reflects the effect of weather forecast uncertainty on the dynamic response. Furthermore, characteristic values at other lead times can be calculated by the same procedure. Similar analysis can also be performed with respect to the forecasts by the PBML method.

Based on R_E and R_{E_WF} values, corresponding α_R factors can be calculated. This will be summarized and further analyzed in Sec. 5.3.2.

Table 5.3: R_{E_WF} values (m) of the crane tip motion (T_L=3 hours, TSML method, 10^{-4} exceedance probability)

H_s (m)	T_p (s)					
	5	6	7	8	9	10
0.5	0.07	0.10	0.11	0.14	0.18	0.33
1	0.15	0.20	0.24	0.28	0.38	0.70
1.5	0.23	0.31	0.36	0.43	0.57	1.05
2	0.31	0.42	0.50	0.59	0.78	1.42
2.5	0.38	0.51	0.60	0.72	0.96	1.69
3	0.46	0.61	0.72	0.85	1.14	1.94
3.5	0.54	0.72	0.84	1.00	1.34	2.19
4	0.64	0.87	1.02	1.22	1.61	2.43

5.3.2 α_R for the crane tip motion

For the definition of the response-based alpha-factor, an α_R of 1.0 presents the sea state forecast is completely correct. The farther it is from one, the greater the uncertainty implicit in the weather forecasts. Figures 5.14 and 5.15 show α_R factors for the crane tip motion with exceedance probability of 10^{-4}, using weather forecasts generated by the TSML and PBML methods, respectively. To investigate the effect of T_p forecast uncertainty on α_R, the variations of α_R with H_s in different T_p groups are plotted and displayed by solid lines with different colors. Besides, subfigures (a) and (b) in each figure show α_R at the lead time of 3 hours and 24 hours respectively, to explore the influence of the forecast horizon.

In addition to the α_R, the α-factors, extracted from the DNV standard [8], are plotted in figures for comparison. They correspond to the weather forecast Level C and are based on the work performed in JIP [146] during the years 2005 - 2007. According to the forecast horizon of the α-factors in the DNV standard, only results with the lead time of 24 hours are plotted in subfigures (b). Meanwhile, following the derivation process, α-factors are also calculated using the produced weather forecasts by TSML or PBML method, and are plotted in the corresponding figures. It should be noted that regarding the α-factor, H_{max} and H_{max_WF} are estimated from the extreme wave height distributions during a given sea state reference period, that is 3 hours in the case study. This implies that the difference between the

Table 5.4: Properties of the correction factors

Factor	α_R	α-factor 1	α-factor 2	α-factor 3
Forecast uncertainty in H_s	✓	✓	✓	✓
Forecast uncertainty in T_p	✓			
The effect of weather forecast uncertainty on dynamic response	✓			
Reference period to estimate the characteristic value	10 min	3 hours	10 min	3 hours
Forecasting methods	TSML or PBML	TSML or PBML	TSML or PBML	DNV standard

sea state reference period T_S and the operation duration T_E is not taken into account. For the sake of consistency, the α-factor generated by analyzing maximum wave heights during 10 mins (i.e., the duration corresponds to the mating operation) is calculated and displayed as well. The properties of the considered correction factors are summarized in Table 5.4.

The response-based alpha-factor is a complex indicator and both the extreme response of offshore structures and weather forecast uncertainty affect its value. According to the above extreme response analysis, the characteristic response of the crane tip motion increases significantly with increasing H_s and T_p. However, this effect is not equivalently reflected in the value of α_R. This is due to the fact that the α_R is a ratio of the extreme responses without and with the consideration of the weather forecast uncertainty for a given sea state. Since a frequency-domain approach is applied for motion analysis, the response of the system is approximately linear with respect to wave height. As a result, α_R does not change very much with H_s for a given T_p, as shown in Figures 5.14 and 5.15. By contrast, the α_R varies greatly among different T_p groups. Nevertheless, the dependency of the α_R on T_p is not necessary to be the same as that of the characteristic responses on T_p. As can be observed in Figure 5.11, for a given H_s, the characteristic response increases as T_p increases, while the α_R does not. The greatly contribution of the forecast uncertainty in T_p to the α_R might be the reason. For instance, as illustrated in Figure 5.8, the forecast uncertainty in the T_p groups with 5-6 s is higher than that in other groups. This causes a large difference between R_E and R_{E_WF}, and therefore making the α_R factors lower in these two groups, as shown in Figure 5.15.

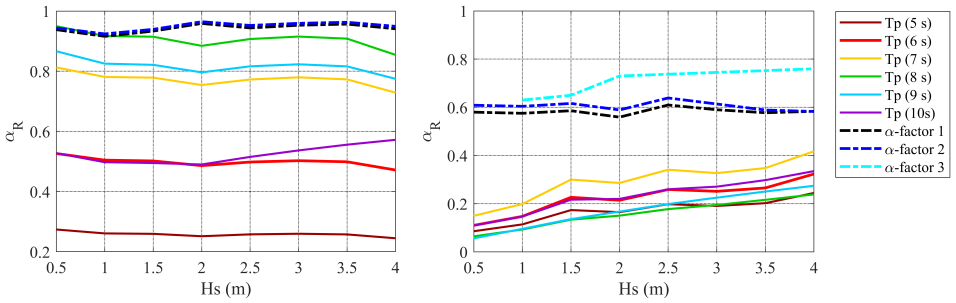

(a) T_L: 3 hours (b) T_L: 24 hours

Figure 5.14: α_R vs. H_s in different T_p groups (TSML method)

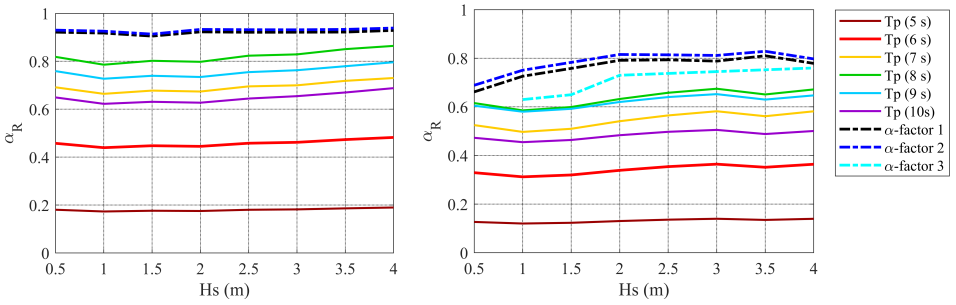

(a) T_L: 3 hours (b) T_L: 24 hours

Figure 5.15: α_R vs. H_s in different T_p groups (PBML method)

In general, a large difference of α_R factors is observed in different T_p groups with the same H_s, indicating that T_p is not a negligible variable in marine operations using a floating crane vessel. However, uncertainty in T_p forecasts is not reflected in the widely used α-factor. For instance, for the H_s group of 0.5 m in Figure 5.14 (a), the α-factor 1 and α-factor 2 are 0.938 and 0.944 respectively, which are independent of T_p. By comparison, α_R varies from 0.27 to 0.95 considering forecast uncertainty of T_p in different T_p groups. Furthermore, the α-factor is purely generated by analyzing weather data without considering their effect on the operation response. Comparison between subfigures (a) and (b) in the above two figures shows that although the α-factor decreases with the forecast horizon, the influence of the weather forecast uncertainty on the crane tip motion may not be clearly identified, especially when the forecast horizon is long. This is because the dynamic response is not totally proportional to H_s, and T_p is essential for operations

based on floating structures. Therefore, uncertainty in T_p forecasts should also be taken into account. Regarding the α_R, it reflects the influence of sea state forecast uncertainties on the dynamic response and a large lead time induce a smaller correction factor. In addition, the quality of weather forecasts is important to generate both the α-factor and the α_R. Compared to the PBML method, the TSML method makes the α_R decrease more when the lead time is extended to 24 hours. The comparison results related to the three α-factors can also implicitly reflect the forecast performance of machine learning-based methods and physics-based numerical methods to a certain extent. However, it still needs to be emphasized that this is not a strict comparison, because the conditions for generating the three α-factors are not exactly the same.

5.3.3 Allowable sea states assessment

Regarding the allowable sea states assessment, H_s-based alpha-factor derived by DNV can be used directly as a correction factor that is multiplied with the actual H_s limit of marine operations for decision-making when weather forecast uncertainty is considered. This is done by comparing the forecasted H_s with the new H_s limit with the alpha-factor. However, the response-based alpha-factor derived in the thesis cannot be directly used in combination with the forecasted values of H_s and T_p for decision-making of marine operations. This is because it is defined as a correction factor based on the response parameter, not on the wave height or H_s. Moreover, uncertainties in both H_s and T_p will play a role for the determination of the α_R. This is the drawback of using the response-based alpha-factor. However, one can inversely identify the allowable sea states in which a safe marine operation can be performed by comparing the extreme response with the allowable limit of response. This can also be done when using the forecast sea states and considering the forecast uncertainty. The procedure has been illustrated in Sec. 4.6 and the allowable sea states in terms of the crane tip motion are assessed in this section.

To assess the allowable sea states, the relevant allowable limit should be pre-defined. It is normally estimated based on structural damage criteria and reasonable assumptions. This is out of the scope of this thesis. In the thesis, the allowable limits are simply assumed to be constant values. Figures 5.16 and 5.17 illustrate the allowable sea states in terms of the crane tip motion with 10^{-4} and 10^{-2} exceedance probability, and the corresponding allowable limits are assumed to be 0.8 m and 0.4 m, respectively. For each selected exceedance probability, results based on TSML and PBML methods are separately provided.

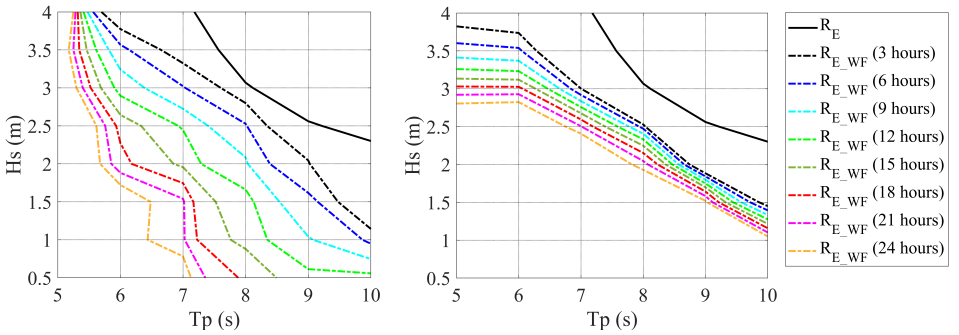

(a) TSML method (b) PBML method

Figure 5.16: Allowable sea states of the crane tip motion (allowable limit=0.8 m, 10^{-4} exceedance probability)

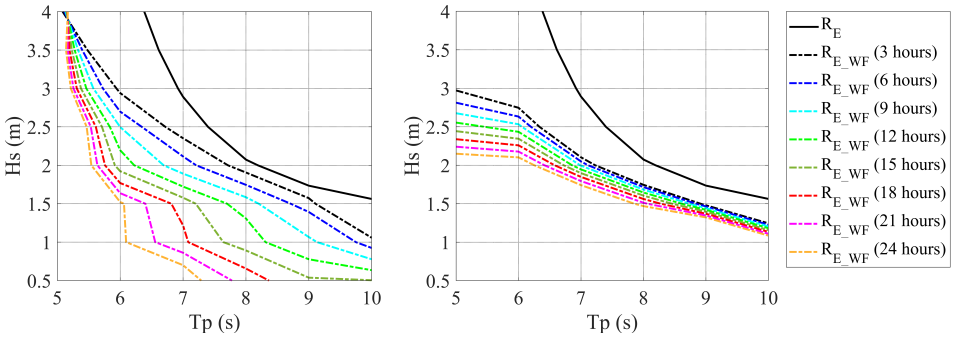

(a) TSML method (b) PBML method

Figure 5.17: Allowable sea states of the crane tip motion (allowable limit=0.4 m, 10^{-2} exceedance probability)

Similar to the description in Figure 4.2, the lines in Figures 5.16 and 5.17 represent the maximum allowable sea states, and all sea states below the lines are feasible. The black solid line denotes allowable sea state limits that does not include weather forecast uncertainty. The dash lines in different colors are allowable sea states considering forecast uncertainties at different lead times. It is visible that following the proposed method, allowable sea states at different lead times can be generated, which is convenient to assist decision-making during the execution of installation operation. The contour lines in two figures reveal that the allowable sea states gradually decrease as the forecast lead time increases. The sea state forecast uncertainties

induced by the two methods (i.e., TSML and PBML methods) result in different allowable sea states.

5.4 Blade root radial motion and velocity (TD)

In Sec. 5.3, a case study dealing with the motion response of the crane tip under wave conditions is carried out. For the challenging blade installation, in addition to wave loads, the nonlinear wind load acting on the blade is also important and needs to be considered. Thus, time-domain simulation is necessary to numerically model the actual installation process and assess the dynamic responses of the blade during the installation. In this section, the α_R factor with respect to the blade root radial motion and velocity will be derived on the basis of time-domain response analysis approach. The corresponding allowable sea states are assessed with emphasis on taking into account the uncertainty of weather forecasts by the PBML method.

5.4.1 Comparison between FD and TD analysis

The necessity of the response analysis in time domain (TD) is discussed and illustrated in this part through a comparison with the method in frequency domain (FD). Figure 5.18 shows the motion spectra of the crane tip under a typical beam sea (H_s =1 m and T_p =7 s).

As illustrated in Figure 5.18, in the beam sea condition, the crane tip motion in Y_b direction is relatively large. The 1^{st} order wave force dominant the motions, since the peak frequency in the motion spectrum is similar to the one of the wave spectrum. From a comparison with the results in FD and TD, a good agreement can be observed in the wave-frequency part. Nevertheless, the method in FD cannot capture the low frequency motions, which makes its power spectral density different from that of the motion obtained by the method in TD.

In Table 5.5, the advantages and disadvantages of the method in TD and FD are briefly listed. As shown above, the time domain analysis can capture the system motion which is subjected to wave loads more accurately by including nonlinear effects such as 2^{nd} order wave forces, lift wire tension formulation and geometrical nonlinearities for motion analysis. On the other hand, the nonlinear aerodynamic loads on the blade and the strong coupling between waves and wind are also important for the response of the installation system. However, these cannot be directly included by the method in FD. Therefore, although its computational efficiency is relatively low, the time-domain modelling is necessary to simulate the whole blade

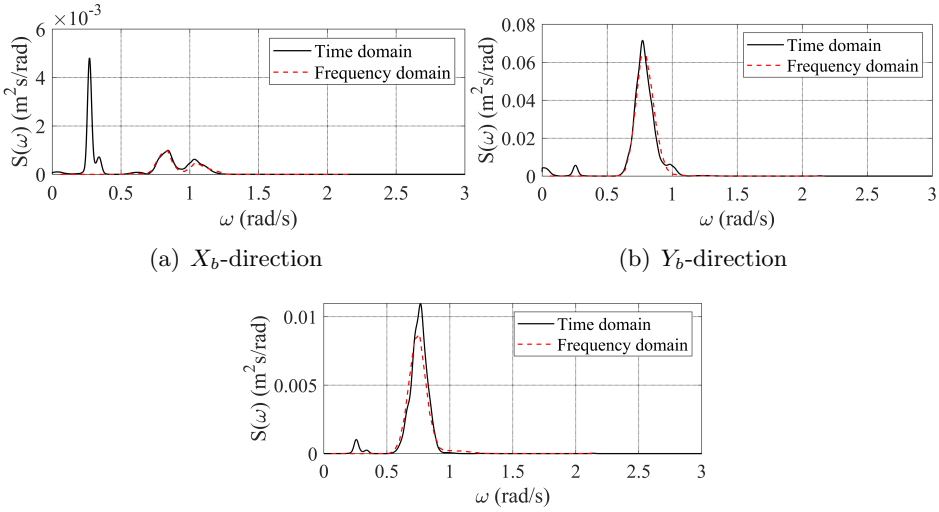

(a) X_b-direction (b) Y_b-direction

(c) Z_b-direction

Figure 5.18: Comparison of power spectra of crane tip motion using FD and TD methods (H_s =1 m, T_p =7 s)

installation process and perform dynamic response analysis.

5.4.2 Sensitivity analysis of wind loads

To establish the conditional distribution of the extreme response with a given sea state, the time domain simulation has to be repeated many times with different wave seeds. As a consequence, it is time-consuming compared with the simulation in frequency domain. Moreover, different combinations of wind and wave conditions should be considered. Given that under each combination multiple simulations are required, the computational cost of extreme response analysis will be heavily increased. To decrease the cost in TD, a sensitivity study on wind loads will be carried out.

In the sensitivity study, a constant H_s value of 2 m is applied, and T_p is selected as the mean value of the conditional distribution of T_p with the given H_s value, which is 7.5 s. The distribution is modelled as a Lognormal distribution, in which the Lognormal parameters are fitted using long-term time series of metocean variables at the North Sea center. Likewise, the joint distribution of U_w, H_s and T_p is fitted by data based on a simplified method proposed by Li et al. [209]. The joint distribution is used to determine the mean wind speed distribution with the given sea state. From the mean wind speed distribution, five typical U_w values (i.e., 1.9 m/s, 3.6 m/s, 5.3 m/s,

Table 5.5: Properties of TD and FD response analysis methods for blade installation

Response analysis methods	Time domain	Frequency domain
Advantage	Can simulate the whole blade installation process. Various terms can be included: - 2^{nd} order wave forces - Wind loads - Viscous loads - Nonlinear structural response	High computational efficiency
Disadvantage	Low computational efficiency	Only includes the 1^{st} order wave loads and the linear motion response
Properties of the modelling of blade	The actual blade root motion and velocity can be simulated, which are directly related to the operational criteria for installing blade	The crane tip motion is referred to, not the blade motion

7 m/s, 8.7 m/s) are selected to conduct the sensitivity study. It should be noted that the mean wind speed in the joint distribution is at the height of 10 m above the mean sea level. For the offshore wind turbine installation, the mean wind speed at the hub height is required and it can be calculated using a power law profile shown in Eq. (5.7).

$$U(z) = U_{10} \cdot \left(\frac{z}{10}\right)^{\alpha_U} \tag{5.7}$$

where z represents the hub height, that is 119 m of the DTU 10MW wind turbine. U_{10} is the mean wind speed at the reference height of 10 m. α_U is the power law exponent which is set to 0.14, based on IEC 61400-3 [210] for offshore wind field.

According to Eq. (5.7), U_w values at the hub height are obtained as 2.7 m/s, 5.1 m/s, 7.5 m/s, 9.9 m/s and 12.3 m/s. For each U_w, the 3D turbulent wind field is generated by TurbSim [211] using the IEC Kaimal model [212], and the turbulence intensity is defined as the class C. The wind load is incorporated into SIMA using DLL to simulate the blade installation in time domain. After simulations, the power spectra and standard deviation of the blade COG motion in 6 DOFs with different wind fields are shown in Figures 5.19 and 5.20, respectively. According to blade COG motion, the

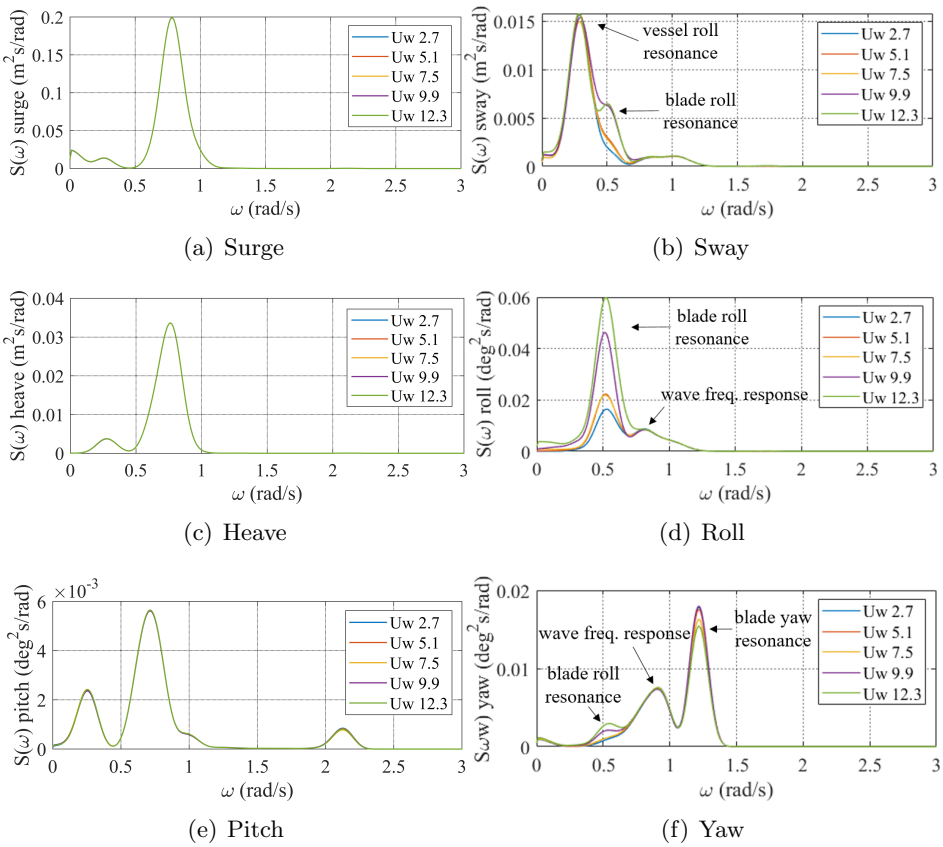

Figure 5.19: Power spectra of blade COG motion with different wind fields (H_s=2 m, T_p=7.5 s)

radial motion of the blade root can be obtained. The power spectra and standard deviations of the blade root radial motion are shown in Figure 5.21.

From Figures 5.19 and 5.20, it is visible that the surge, heave and pitch motions of the blade COG are almost irrelevant with the wind in the beam wind and wave condition, and the wave-induced motion is the main source of the blade motion in these 3 DOFs. By comparison, both aerodynamic loads and wave-induced motion contribute to the blade motion in sway, roll and yaw. Among them, the aerodynamic loads have significant effects on the blade roll motion and an obvious increase of the peak roll motion can be observed as the mean wind speed increases. Nevertheless, regarding radial motion of the blade root, it does not vary greatly under different

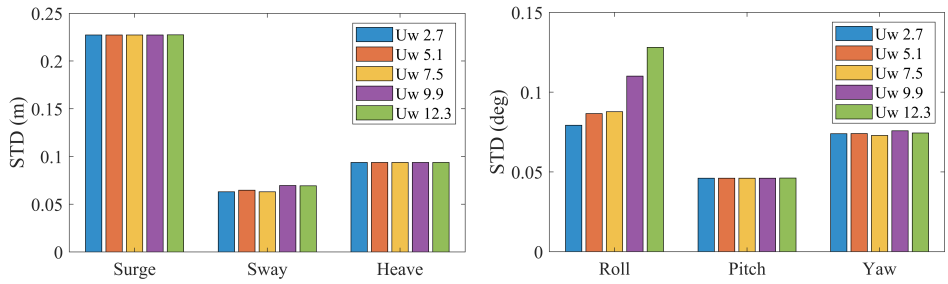

(a) Surge, Sway and Heave (b) Roll, Pitch and Yaw

Figure 5.20: Standard deviations of blade COG motion with different wind fields (H_s=2 m, T_p=7.5 s)

wind conditions. Figure 5.21 illustrates that the wave loads have a major contribution on the blade root radial motion while the aerodynamic loads have relatively less contributions.

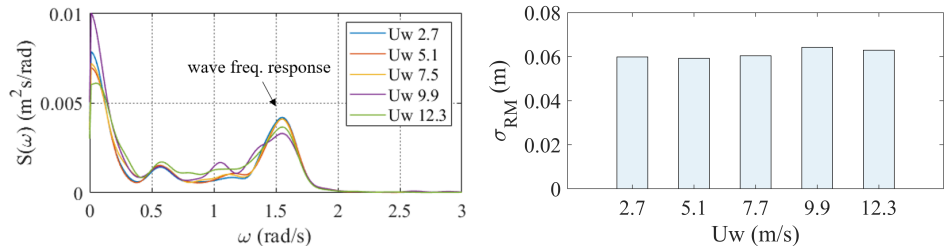

(a) Power spectra (b) Standard deviation

Figure 5.21: Comparison of blade root radial motions with different wind fields (H_s=2 m, T_p=7.5 s)

Overall, the sensitivity study demonstrates that the wave load dominates over the wind load. To illustrate the proposed methodology, the mean wind speed is simply selected as a constant value (8 m/s at 10 m height) in the case study, and the effect of different wind conditions on the blade installation is not considered in this thesis.

5.4.3 Extreme response analysis

Unlike the extreme response analysis based on response spectra in frequency domain, the extreme value distribution in time domain needs to be fitted using maxima values extracted from the response time series. Figure 5.22

shows a typical example of the extreme distribution of the blade root radial motion under a given sea state (H_s=2 m and T_p=5 s). To reduce statistical uncertainty in the tail of the fitted distribution, 50 10-min time-domain simulations are carried out with random wave seeds. The Gumbel distribution is utilized to fit the extracted 10-min extreme responses.

Under this sea state, the parameters (i.e., the location parameter γ and scale parameter β) of the Gumbel distribution are estimated by the maximum likelihood estimations (MLEs) method. Results shown in Figure 5.22 (a) indicate that the Gumbel distribution has a good performance to capture the extreme radial motion of the blade root. The characteristic value can therefore be obtained based on the distribution with a certain exceedance probability, as shown in Figure 5.22 (b). In the mating phase of the blade installation, a small exceedance probability (i.e., 10^{-4}) is considered since larger radial motion and velocity of the blade root may lead to the failure of installation.

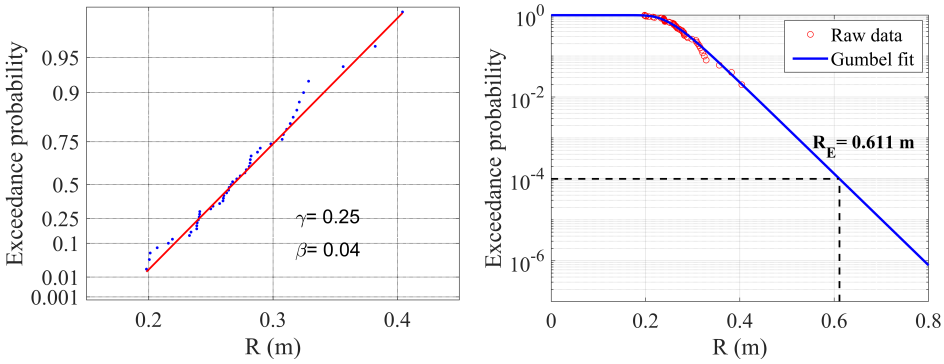

(a) Gumbel fitting (b) Exceedance probability

Figure 5.22: Extreme value distribution estimation of the blade root radial motion (H_s =2 m and T_p =5 s)

5.4.3.1 Statistical uncertainty

In the above extreme response analysis, only a limited number of simulations (i.e., 50 10-min) are conducted to estimate the characteristic values. The statistical uncertainty may exist when evaluating extreme responses. In this subsection, the accuracy of the estimated extreme values due to a limited number of simulations is addressed.

In Figure 5.23, the extreme distribution of the blade root radial motion under the given sea state (H_s=2 m and T_p=5 s) is further fitted, using

1000 simulations with different wave seeds. Based on the distribution, characteristic values with two exceedance probability levels, namely 10^{-2} and 10^{-4}, are estimated and displayed. For the 10^{-2} level, 1000 simulations can be considered as a reasonable choice, and the corresponding characteristic value is regarded as an accurate estimation for extreme responses. In this sensitivity study, the characteristic value with 10^{-4} level shown in Figure 5.23 is also taken as the reference value for the extreme response. Comparison between Figures 5.22 and 5.23 shows that there is a slight difference in the characteristic value estimated by different numbers of simulations.

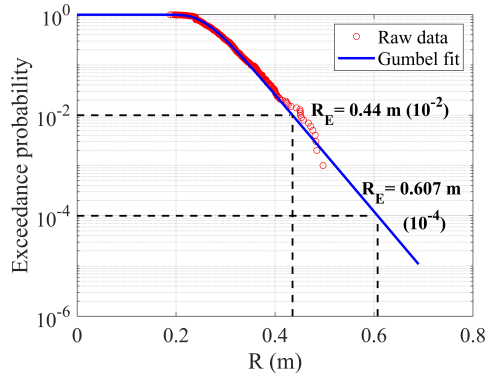

Figure 5.23: Fitted extreme distribution of the blade root radial motion (1000 simulations, H_s=2 m, T_p=5 s)

To investigate the effect of simulation numbers in the extreme response analysis, Figure 5.24 shows variation of the characteristic values of the blade root radial motion with different simulation numbers. Results for the exceedance probability of 10^{-2} and 10^{-4} are displayed in subfigure (a) and (b) separately.

It is visible that the number of simulations can affect the determination of fitting parameters for the Gumbel distribution, and thereby affect the estimation of the characteristic values. This phenomenon is especially obvious when the simulation number is less than 40. Compared with the case based on 1000 simulations, large uncertainty exists when only 5 simulations are used for the extreme response estimation. As expected, the statistical uncertainty decreases as the number of simulations increases. When the number of simulations is greater than 40, there is no significant difference in the results among different cases. Therefore, taking into account the computational efficiency, the number of simulations is selected as 50, which can give a reasonably good estimation of the characteristic response value.

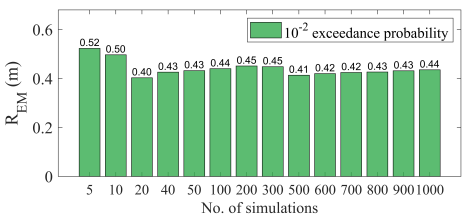

(a) Ten-min extreme response with a 10^{-2} exceedance probability

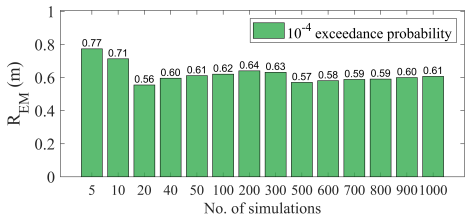

(b) Ten-min extreme response with a 10^{-4} exceedance probability

Figure 5.24: Variation of the characteristic with the number of simulations (H_s=2 m, T_p=5 s)

Moreover, the statistical uncertainty of the extreme response assessed by a fixed number of simulations (i.e., 50) is illustrated in Figure 5.25. In the figure, 10 sets of 50 time-domain simulations are selected randomly from 1000 simulations, and the extreme value in each set is estimated individually.

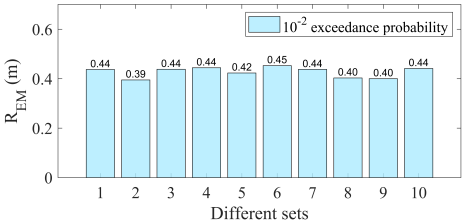

(a) Ten-min extreme response with a 10^{-2} exceedance probability

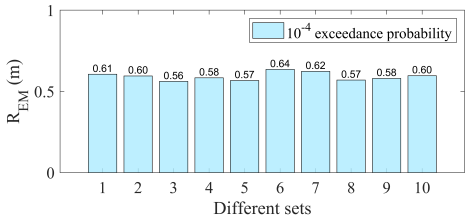

(b) Ten-min extreme response with a 10^{-4} exceedance probability

Figure 5.25: Variation of the characteristic values in different sets (H_s=2 m, T_p=5 s)

It can be found that the variation in characteristic values between different sets is small, further implying that 50 is a reasonable number for time-domain simulations under a given sea state. Furthermore, coefficient of variation (CoV), that is defined as Eq. (5.8) in terms of the mean value (μ_{R_E}) and standard deviation (σ_{R_E}) of characteristic values, is applied to measure the related statistical uncertainty. It is calculated based on 20 sets of 50 time-domain simulations and the relevant results are summarized in Table 5.6. The results show low statistical uncertainty, since small CoV values corresponding to 10^{-2} and 10^{-4} exceedance probability levels (i.e., 4% and 6%) are observed.

$$CoV = \frac{\mu_{R_E}}{\sigma_{R_E}} \tag{5.8}$$

Table 5.6: Statistical uncertainty in extreme response estimation (H_s=2 m, T_p=5 s)

Exceedance probability	μ_{R_E}	σ_{R_E}	CoV
10^{-2}	0.43	0.02	0.04
10^{-4}	0.60	0.03	0.06

Overall, the fitted distribution with 50 simulations for a sea state can give an overall good estimation of the extreme value and the statistical uncertainty is low. Therefore, the extreme responses of both the blade root radial motion and velocity in this thesis are assessed based on 50 time-domain simulations for each sea state.

5.4.3.2 Characteristic response values

By carrying out the extreme response analysis in TD, the R_E values of the blade root radial motion and velocity under different typical sea states are calculated and summarized in Tables 5.7 and 5.8, respectively.

As displayed in Tables 5.7 and 5.8, R_{EM} and R_{EV} increase significantly with H_s and T_p. This indicates that both H_s and T_p are important for assessing the dynamic responses of the blade and need to be considered before executing the blade installation. As aforementioned, the Gumbel parameters are functions of H_s and T_p. Figures 5.26 and 5.27 present the fitting surfaces of Gumbel parameters for extreme radial motion and velocity of the blade root, respectively.

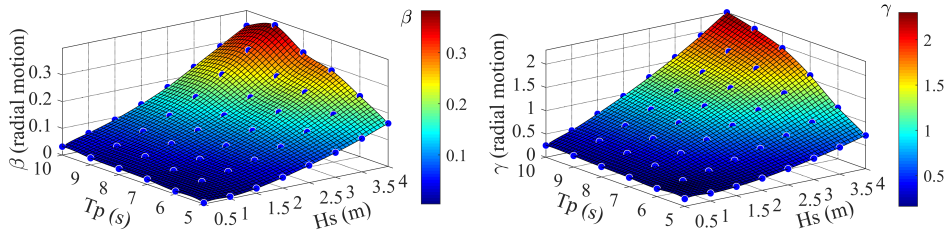

(a) β (b) γ

Figure 5.26: Fitting surface of Gumbel parameters as a function of H_s and T_p (blade root radial motion)

Table 5.7: R_E values (m) of the blade root radial motion (R_{EM})

Hs (m)	Tp (s)					
	5	6	7	8	9	10
0.5	0.20	0.27	0.37	0.42	0.47	0.54
1	0.23	0.46	0.60	0.80	0.88	1.03
1.5	0.36	0.71	0.96	1.26	1.42	1.55
2	0.61	1.03	1.41	1.76	2.02	2.16
2.5	0.93	1.44	1.95	2.35	2.75	2.86
3	1.30	1.93	2.62	3.06	3.64	3.68
3.5	1.72	2.53	3.37	3.90	4.62	4.56
4	2.20	3.18	4.21	4.87	5.68	5.46

Table 5.8: R_E values (m) of the blade root radial velocity (R_{EV})

Hs (m)	Tp (s)					
	5	6	7	8	9	10
0.5	0.13	0.18	0.25	0.27	0.31	0.33
1	0.22	0.36	0.47	0.58	0.61	0.64
1.5	0.32	0.53	0.70	0.88	0.92	0.96
2	0.43	0.70	0.92	1.19	1.22	1.29
2.5	0.54	0.88	1.16	1.505	1.53	1.62
3	0.66	1.06	1.40	1.82	1.84	1.94
3.5	0.78	1.24	1.66	2.15	2.17	2.28
4	0.90	1.43	1.92	2.48	2.49	2.63

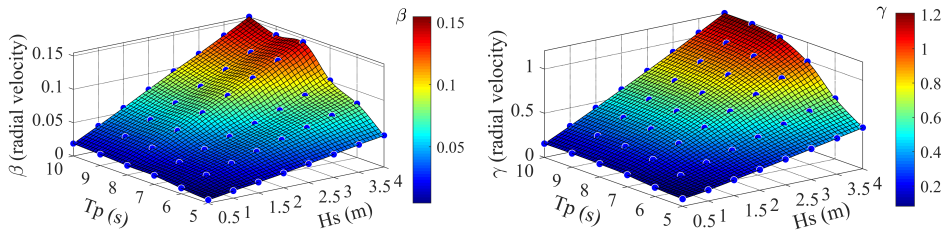

(a) β (b) γ

Figure 5.27: Fitting surface of Gumbel parameters as a function of H_s and T_p (blade root radial velocity)

In Figures 5.26 and 5.27, the blue points are Gumbel parameters fitted by the simulated response time series under typical sea states. They are utilized to evaluate the characteristic values without weather forecast uncertainty, i.e., R_E in Eq. (4.34). Based on these blue points, the surfaces of γ and β for different sea states are fitted by the piecewise cubic interpolation method [213] in Matlab. These surfaces are necessary to integrate the marginal distribution of the extreme response expressed in Eq. (4.36). Accordingly, the characteristic values R_{E_WF} can be calculated, accounting for weather forecast uncertainty by Eq. (4.37).

5.4.4 α_R for the final blade mating phase

Based on characteristic values of each limiting response parameter with and without weather forecast uncertainty, the response-based alpha-factors of the blade root radial motion (α_{RM}) and velocity (α_{RV}) can be estimated. Relevant results will be summarized and discussed in this section.

5.4.4.1 Blade root radial motion

Figure 5.28 shows an example of the α_{RM}, associated with weather forecast uncertainty of the PBML method with a lead time of 3 hours. It is clearly that the α_{RM} varies with sea states. Since the blade installation normally requires low sea states, Figure 5.29 further presents the variation of α_{RM} for different T_p and T_L, focusing on the results in H_s ranging from 0.5 m to 2.0 m.

From Figure 5.29, it can be found that the α_{RM} does not change significantly with the lead time, due to the good forecast performance of the PBML method on sea state forecasting. In contrast, by comparing α_{RM} in

different subfigures, a significant effect of forecast uncertainty in T_p is observed. Moreover, the effect of H_s can be found by comparing α_{RM} factors at each lead time for each subfigure. As shown, the α_{RM} varies with H_s, but the variation also depends on conditions of T_p and T_L.

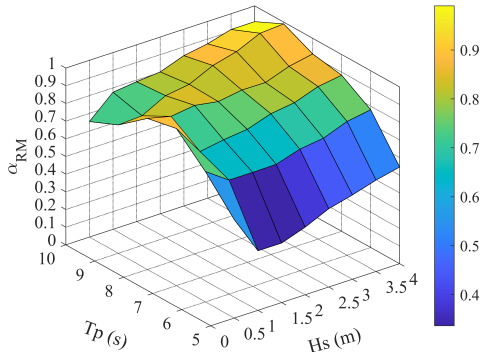

Figure 5.28: α_{RM} with a lead time of 3 hours

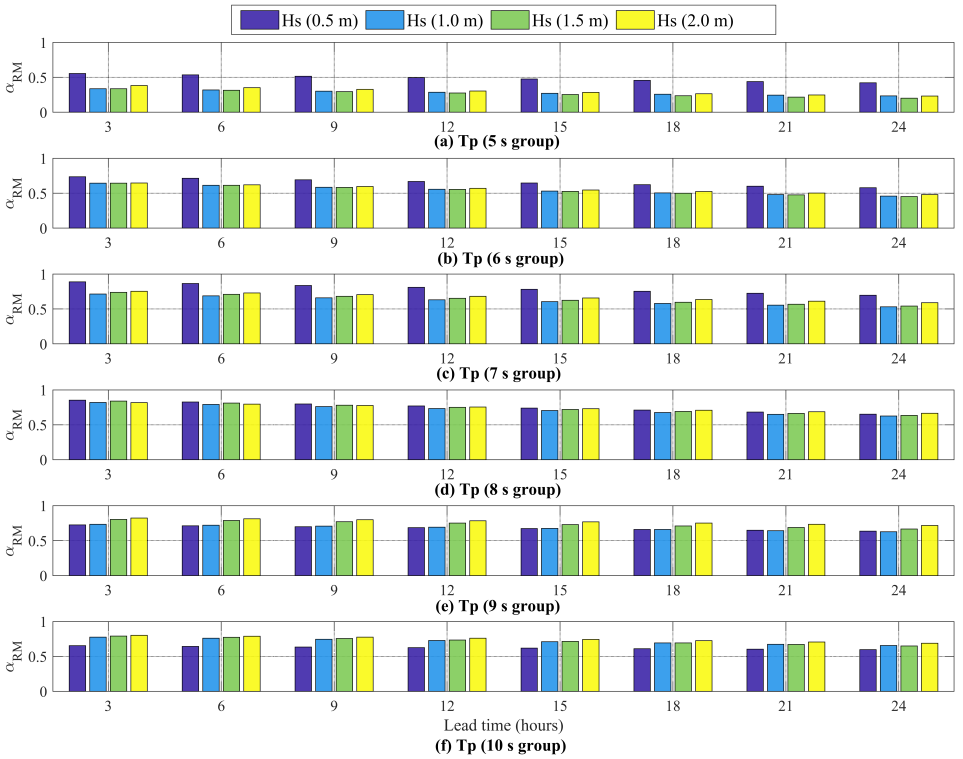

Figure 5.29: Variation of α_{RM} with lead times in different H_s groups

5.4.4.2 Blade root radial velocity

A similar analysis is conducted on the α_{RV}. α_{RV} with different H_s, T_p and T_L are presented in Figure 5.30. Likewise, only results in H_s groups between 0.5 m and 2.0 m are displayed.

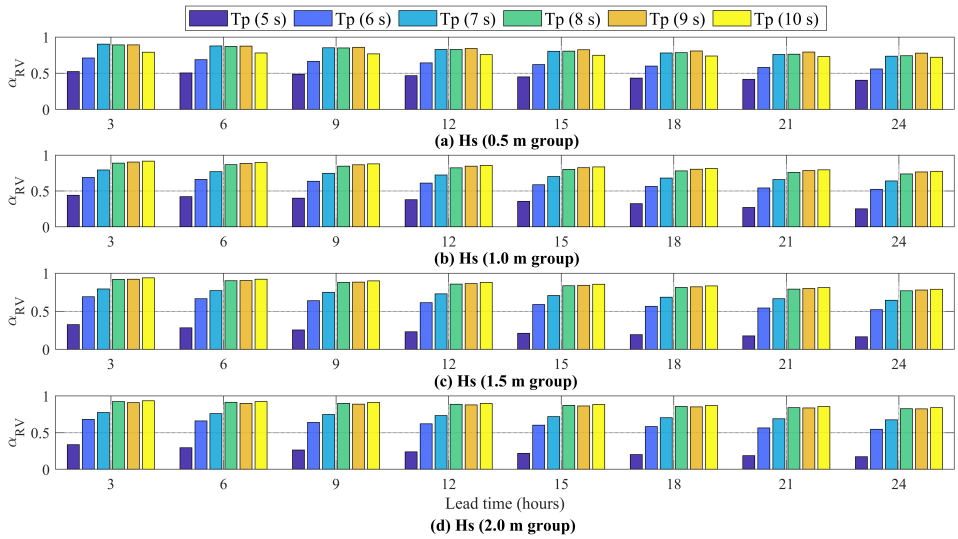

Figure 5.30: Variation of α_{RV} with lead times in different T_p groups

From Figure 5.30, the influence of T_p on the α_{RV} can be clearly found. For all lead times and H_s groups, α_{RV} are in the range of 0.16 to 0.52 for the T_p group of 5 s, and 0.52 to 0.99 for other T_p groups. By comparing Figures 5.29 and 5.30, it is noted that the variation observed in α_{RV} is different from that observed in α_{RM}. This reflects the characteristics of α_R, that is, it is specific to the operations and associated limiting response parameters.

Overall, results demonstrate that for the blade installation using a floating crane vessel, uncertainty in T_p forecasts is important and should not be neglected. Unlike the conventional alpha-factor that only relies on the uncertainty in H_s, α_R reflects forecast uncertainties in both H_s and T_p to guide marine operations.

5.4.5 Allowable sea state assessment

The allowable sea states are finally assessed through a comparison between the R_{E_WF} (adjusted by the α_R) and the corresponding allowable limits. Allowable sea states associated with the blade root radial motion and velocity are shown in the following separately. For the blade root radial motion,

the allowable limit is defined as the gap between the hub radius and the blade root radius during the mating phase. Figure 5.31 shows a sensitivity study on the allowable limit, in which $0.5R_{root}$, $0.3R_{root}$ and $0.2R_{root}$ are selected as the allowable limit, where R_{root} is the radius of blade root which is 2.69 m. For the blade root radial velocity, the allowable limit is normally related to the plastic bending in the guide pins. A reference velocity (0.7 m/s) proposed by Verma et al. [214] is applied as the allowable limit of the blade root radial velocity. Correspondingly, Figure 5.32 shows the allowable sea states using the blade root radial velocity as criterion. Both the allowable sea states with (dash lines) and without (solid lines) weather forecast uncertainty are presented at different lead times.

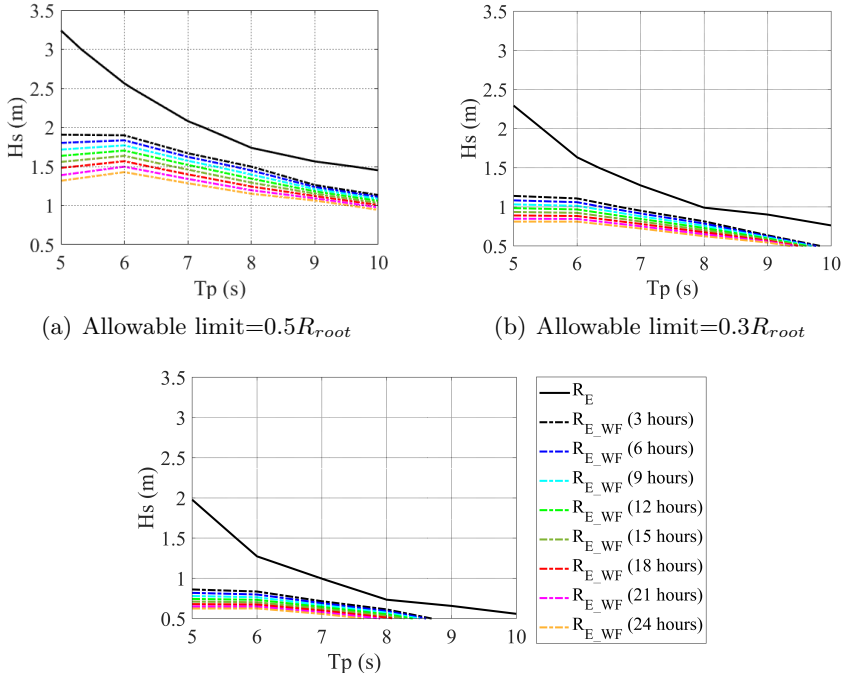

(a) Allowable limit=$0.5R_{root}$

(b) Allowable limit=$0.3R_{root}$

(c) Allowable limit=$0.2R_{root}$

Figure 5.31: Allowable sea states of the blade root radial motion

As displayed in Figures 5.31 and 5.32, the allowable sea state is significantly affected by the sea state forecast uncertainty, since an obvious discrepancy between the solid line and dash lines can be observed. Uncertainty in sea state forecasts decreases the allowable sea state, especially in the range of short T_p. Moreover, the comparison among the dash lines

in each figure indicates that the forecast horizon is another important parameter for determining the allowable sea states when the weather forecast uncertainty is taken into account. As expected, the allowable sea states gradually decrease with the forecast lead time T_L increases. This is reasonable since when the forecast lead time increases, the weather forecast becomes more uncertain, which reduces the α_R and therefore makes the allowable sea states more conservative. For instance, in Figure 5.31 (a), when T_p is 5 s, allowable H_s without forecast uncertainty is about 2 m, while allowable H_s with lead times of 3 and 24 hours are about 1.9 m and 1.3 m, respectively. In addition, the importance of the pre-determined allowable limit is also illustrated in Figure 5.31. The comparison among the three examples shows that small allowable limit requires a more accurate operation, and therefore, the allowable sea states will be reduced by high performance requirement.

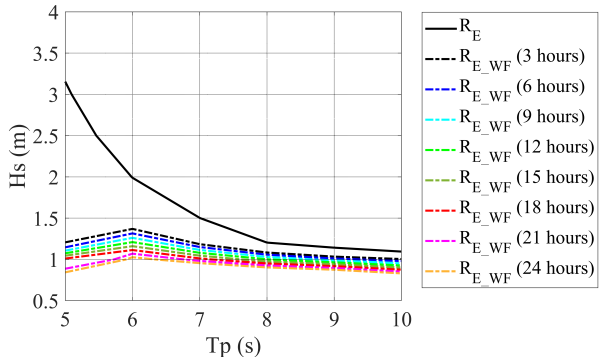

Figure 5.32: Allowable sea states of the blade root radial velocity

Furthermore, the workable weather windows for offshore blade installation can be identified by comparing the allowable sea states with weather forecasts. It is noted that if the operation is controlled by more than one limiting response parameter, identification of workable weather windows is relatively complicated. Regarding the final mating phase, the blade root radial motion and velocity should be considered simultaneously, and the overall weather window should be identified and selected considering the two corresponding windows. This also depends on the values of allowable limits. For instance, if the allowable limit of the blade root radial motion is selected as $0.5R_{root}$ (see Figure 5.31 (a)), the allowable sea states related to the blade root radial velocity are lower than those related to the blade root radial motion at every lead time. As a consequence, the overall workable weather window is decided by the blade root radial velocity. In

contrast, if the allowable limit of the blade root radial motion is $0.2R_{root}$ (see Figure 5.31 (c)), the corresponding weather windows will be shorter than that for the blade root radial velocity. In this case, the weather window for the blade root radial motion decide the overall workable weather windows. However, when the allowable limit of the blade root radial motion is $0.3R_{root}$ (see Figure 5.31 (b)), two weather windows should be taken into account simultaneously. Specifically, it is necessary to identify weather windows separately for each limiting parameter, and the overlap part will be the reference for the selection of overall workable weather windows.

Chapter 6

Conclusions and recommendations for future work

This thesis addresses the effect of weather forecast uncertainty on marine operations. First, different machine learning-based methods are developed for multi-step-ahead wave forecasting. Based on the wave forecasts, the forecast uncertainty quantification for different methods is carried out. A methodology for assessing allowable sea states of marine operations is subsequently proposed by means of a combination of the uncertainty quantification of weather forecasts and the dynamic response analysis of the operation. The methodology is used for the single blade installation of offshore wind turbines, with an aim to establish its allowable sea states considering weather forecast uncertainty. It should be emphasized that the methodology is a general process that can be used for other marine operations. The main conclusions, original contributions and recommendations for future work are presented in this final chapter.

6.1 Conclusions

The main conclusions of the thesis are summarized as follows:

- One-day-ahead forecasting of wave conditions was carried out by using time series-based machine learning (TSML) methods. Various TSML methods consisting of different combinations of pre-processing techniques, data-driven models and multi-step-ahead strategies are developed. Forecast uncertainty of different TSML methods is quan-

tified and compared. The results indicated that it is feasible to apply machine learning to forecast wave conditions. Typically, the TSML method can effectively produce accurate forecasts with short lead times. Nevertheless, all TSML methods are dependent on time series analysis, and an essential problem was encountered, that is, the forecast uncertainty would increase with the forecast horizon. This issue is difficult to be solved by changing data-driven models or developing more complicated TSML methods.

- A new machine learning-based forecasting method, called the physics-based machine learning (PBML) method was proposed to make multi-step-ahead forecasting of wave conditions. The method combines the physics-based wave model with machine learning technique. Specifically, it takes physical background into account by applying the primary inputs (i.e., initial wave boundary conditions and the future wind forcing) in physics-based wave models to design the model structure. Meanwhile, a machine learning algorithm is adopted to learn model. The results revealed that the PBML method can provide accurate one-day-ahead wave forecasts in a small domain. Compared with widely used physics-based wave models, high computational efficiency is its primary advantage.

- A new response-based correction factor, called the response-based alpha-factor α_R was proposed. It is used to reflect the effect of the weather forecast uncertainty on dynamic responses of the system used in operations. The α_R is defined as a ratio between the characteristic values of the operational limiting response parameter in the condition with and without considering the weather forecast uncertainty. It depends on the type and duration of marine operations, characteristics of dynamic system, weather forecasting method, forecast lead time, etc. To derive the α_R, the critical events and related limiting response parameters of an operation should be identified first. Dynamic responses of the limiting parameter are assessed by means of frequency- or time-domain response analysis approach that depends on the properties of the operation. Meanwhile, the weather forecast uncertainty quantification is performed by statistically analyzing forecast error ratios in terms of the range of sea states and forecast lead times. Based on the probabilistic assessment of dynamic responses with and without the uncertainty quantification result of weather forecasts, the α_R can therefore be established for different sea state forecast scenarios.

- A methodology for assessing the allowable sea states of marine oper-

ations was developed, with emphasis on accounting for the effect of weather forecast uncertainty. It includes the establishment of the α_R for a specific operation and the assessment of allowable sea states. After the α_R factors of the limiting response parameter for an operation are established, they are used to adjust the corresponding characteristic response values to make the operational limit more conservative. The allowable sea states are then assessed by comparing the adjusted characteristic values with corresponding allowable limits. This procedure is meaningful because the allowable sea states can be compared with weather forecasts in the execution phase to identify workable weather windows and further support operation decision-making.

- The proposed methodology was applied to assess the allowable sea states for single blade installation of offshore wind turbines. The crane tip motion and the blade root radial motion and velocity are regarded as the limiting response parameters for the installation process, to illustrate the methodology based on response analysis in frequency- and time-domain, respectively. When the blade installation is performed with a semi-submersible crane vessel, it was found that in addition to the forecast uncertainty of H_s, that of T_p is also critical and needs to be considered during the operation. Compared to the α-factor, the α_R takes sea state forecast uncertainties into account more comprehensive and reflects their effect on the system dynamic response. In addition, the quality of weather forecasts has a significant effect on the generation of the α_R. Comparison results of allowable sea states with and without weather forecast uncertainty demonstrated that weather forecast uncertainty plays an important role on the allowable sea states assessment. If the weather forecast uncertainty is not considered, the allowable sea states may be greatly over-estimated. As the forecast lead time increases, the allowable sea states gradually decrease.

6.2 Original contributions

The original contributions of the thesis are summarized below.

- **Evaluation and comparison of the forecast performance of different TSML methods**
  An uncertainty quantification analysis was carried out to evaluate and compare the forecast performance of 11 different TSML methods for multi-step-ahead wave forecasting. The comparison provides a reference for applying machine learning algorithms in weather forecast.

- **Development of a new forecasting method for wave forecasting**
  The physics-based machine learning (PBML) method is able to make use of the advantages of both physics-based wave models and machine learning algorithms. Due to the high forecast performance and low computational cost, the PBML method can be conceived as an efficient tool for the multi-step-ahead forecasting of wave conditions at least in a small domain, and thus has great potential to be applied for marine operations.

- **Development of a general methodology for assessing allowable sea states of marine operations**
  The methodology consists of quantification of weather forecast uncertainty, statistical analysis of dynamic responses of coupled system for marine operations and allowable sea states assessment by means of response-based criteria. It is able to provide an efficient way to investigate the effect of sea state forecast uncertainties on marine operations and assess their allowable sea states. The obtained allowable sea states can provide a good reference for the decision-making of the operation in the execution phase.

- **Establishment of the α_R factor for the single blade installation**
  The α_R factors with respect to the crane tip motion, blade root radial motion and velocity during the installation of offshore wind turbine blade were established separately in terms of sea state scenarios and forecast lead times. They are able to adjust corresponding characteristic responses for the blade installation by a semi-submersible crane vessel.

- **Assessment of allowable sea states for the blade installation of offshore wind turbines**
  Using the proposed methodology, the allowable sea states accounting for sea state forecast uncertainty regarding the final mating phase of the blade installation were assessed. The assessed allowable sea states are useful for executing the mating operation. By comparing the allowable sea states with weather forecasts, workable weather windows can be identified, which is important to ensure the safety and cost-efficiency of the installation.

6.3 Limitations and recommendations for future work

- *Validation of the machine learning-based forecasting methods via comparison with measurements*
  In the thesis, performance of the forecasting methods was validated by hindcast data. In practice, hindcast data may also have certain uncertainty. Thus, it is recommended to quantify the forecast uncertainty based on the comparison between forecasts and measurements. Moreover, the forecasting models developed in the thesis were based on hindcast data. If long-term measurements are available at the location of interest, they can be used to establish machine learning-based forecasting models.

- *Further development of the PBML method for T_p forecasting*
  The uncertainty of the PBML method for T_p forecasting is relatively higher than that for H_s due to the lower implicit relationships between the utilized input-output combination. For future works, more relevant factors can be involved in the T_p forecasting model to improve its forecast accuracy, such as wave directions, speeds and the distance from the position of the input to output. Moreover, feature selection techniques can also be adopted to further select and weight the relevant factors.

- *Development of the PBML method to forecast wind conditions*
  With regard to forecasting of wave conditions by the PBML method, the forecasted wind speeds and directions are required as inputs. It is therefore important to generate accurate wind forecasts. Future work can focus on development the related PBML method for wind forecasting.

- *Further comprehensive studies on the allowable sea states assessment for the blade installation*
  Regarding the blade installation of offshore wind turbines, only the beam sea condition is considered in the case study. In addition, the variation of wind fields are not considered due to the marginal effects of wind conditions on the installation system. In order to get more reliably α_R and further assess the allowable sea states for offshore blade installation with higher accuracy, more comprehensive studies can be carried out in future works.

- *Further subdivide sea states into wind-generated sea and swell, and*

consider their uncertainty on marine operations
In the thesis, wind-generated sea and swell are forecasted by means of the PBML method separately, to investigate the reasons for the larger forecast uncertainty in T_p. In practice, both wind-generated and swell components are essential to plan and execute marine operations. Thus, it is meaningful to investigate their forecast uncertainties separately in the proposed methodology for assessment of allowable sea states.

- *Extension of the methodology for allowable sea states assessment for other marine operations*
  In the thesis, only a case study focusing on the offshore blade installation was carried out. To further investigate the feasibility of the methodology, it can be used in other marine operations for allowable sea states assessment considering the effect of weather forecast uncertainty.

References

[1] D Validzic. Clean energy for all europeans-european union's new legislative framework. 2017.

[2] Mehmet Bilgili, Abdulkadir Yasar, and Erdogan Simsek. Offshore wind power development in europe and its comparison with onshore counterpart. *Renewable and Sustainable Energy Reviews*, 15(2):905–915, 2011.

[3] GWEC. Global offshore wind report 2020. `https://gwec.net/global-offshore-wind-report-2020/`. Accessed: 2020-12-09.

[4] IEA. Offshore wind outlook 2019. `https://www.iea.org/reports/offshore-wind-outlook-2019`. Accessed: 2020-12-09.

[5] IRENA. Future of wind. `https://irena.org/-/media/Files/IRENA/Agency/Publication/2019/Oct/IRENA_Future_of_wind_2019.pdf`, 2019. Accessed: 2020-12-09.

[6] Michael Liebreich. Bloomberg new energy finance summit. *London: Bloomberg New Energy Finance*, pages 1–10, 2013.

[7] L Ramírez, D Fraile, and G Brindley. Offshore wind in Europe: Key trends and statistics 2019. 2020.

[8] DNV. DNV-OS-H101: Marine Operations. *General, Offshore Standard*, 2011.

[9] StructuraeA. Troll A platform. `https://structurae.net/en/structures/troll-a-platform`. Accessed: 2021-02-02.

[10] Kongsberg. Rig move: Towing & tugging. `https://www.kongsberg.com/digital/models-and-examples/k-sim-offshore-solutions/rig-move-towing--tugging/`. Accessed: 2021-02-02.

[11] GLOBAL OFFSHORE ENGINEERING. Dry tow of a jack up rig. http://www.goe-group.com/goe_project/rig-moving-services/, 2018. Accessed: 2021-02-02.

[12] Shipsandoil. Summaries of major accident reports. http://www.shipsandoil.com/Picture%20of%20the%20Day%202012/2012%20Images/Kolskaya.html, 2012. Accessed: 2021-02-02.

[13] Tor Einar Berg, Ørjan Selvik, et al. Emergency towing operations in arctic waters. In *OTC Arctic Technology Conference*. Offshore Technology Conference, 2015.

[14] James G Speight and Pratima Jauhari. *Subsea and Deepwater Oil and Gas Science and Technology*. Gulf Professional, 2012.

[15] AkerSolutions. Subesa production systems. https://www.akersolutions.com/what-we-do/subsea-production-systems-and-lifecycle-services/subsea-production-systems/. Accessed: 2021-02-02.

[16] DNV. DNV-RP-H103: Modelling and analysis of marine operations. 2011.

[17] Ecosse IP. How weather conditions can impact subsea lifting operations. https://www.ecosse-ip.com/how-weather-conditions-can-impact-subsea-lifting-operations/. Accessed: 2021-02-02.

[18] Dong-Hoon Jeong, Myung-Il Roh, and Seung-Ho Ham. Lifting simulation of an offshore supply vessel considering various operating conditions. *Advances in Mechanical Engineering*, 8(6):1687814016654633, 2016.

[19] IREA IRENA. Renewable power generation costs in 2017. *Report, International Renewable Energy Agency, Abu Dhabi*, 2018.

[20] Kurt Thomsen. *Offshore wind: a comprehensive guide to successful offshore wind farm installation*. Academic Press, 2014.

[21] Zhiyu Jiang. Installation of offshore wind turbines: A technical review. *Renewable and Sustainable Energy Reviews*, 139:110576, 2021.

[22] Xiaoni Wu, Yu Hu, Ye Li, Jian Yang, Lei Duan, Tongguang Wang, Thomas Adcock, Zhiyu Jiang, Zhen Gao, Zhiliang Lin, et al. Foundations of offshore wind turbines: A review. *Renewable and Sustainable Energy Reviews*, 104:379–393, 2019.

[23] Wenbin Dong, Torgeir Moan, and Zhen Gao. Long-term fatigue analysis of multi-planar tubular joints for jacket-type offshore wind turbine in time domain. *Engineering structures*, 33(6):2002–2014, 2011.

[24] Tuukka Mäkitie, Allan D Andersen, Jens Hanson, Håkon E Normann, and Taran M Thune. Established sectors expediting clean technology industries? The Norwegian oil and gas sector's influence on offshore wind power. *Journal of cleaner production*, 177:813–823, 2018.

[25] SA Herman. Offshore wind farms: Analysis of transport and installation costs. 2002.

[26] Ballast Nedam. Supporting offshore wind - Alternative foundation installation. `https://www.flow-offshore.nl/images/flow-openbaar/alternative-foundation-installation.pdf`, 2011. Accessed: 2020-12-09.

[27] Offshore. UK leading offshore wind jacket foundation trend. `https://www.offshore-mag.com/field-development/article/14167727/uk-leading-offshore-wind-jacket-foundation-trend`, 2020. Accessed: 2021-03-03.

[28] BAM Infra. Gravity Base Foundation for Blyth. `https://www.baminfra.nl/projecten/gravity-base-foundation-for-blyth`. Accessed: 2021-03-03.

[29] Bjørn Skaare, Finn Gunnar Nielsen, Tor David Hanson, Rune Yttervik, Ole Havmøller, and Arne Rekdal. Analysis of measurements and simulations from the Hywind Demo floating wind turbine. *Wind Energy*, 18(6):1105–1122, 2015.

[30] Alexia Aubault, Christian Cermelli, Alireza Lahijanian, Alan Lum, Antoine Peiffer, and Dominique Roddier. WindFloat contraption: From conception to reproduction. In *International Conference on Offshore Mechanics and Arctic Engineering*, volume 44915, pages 847–853. American Society of Mechanical Engineers, 2012.

[31] Fons Huijs, Erik-Jan de Ridder, and Feike Savenije. Comparison of model tests and coupled simulations for a semi-submersible floating

wind turbine. In *ASME 2014 33rd International Conference on Ocean, Offshore and Arctic Engineering*. American Society of Mechanical Engineers Digital Collection, 2014.

[32] JH Koh, A Robertson, J Jonkman, F Driscoll, and EYK Ng. Building and calibration of a fast model of the sway prototype floating wind turbine. Technical report, National Renewable Energy Lab.(NREL), Golden, CO (United States), 2013.

[33] Armando Alexandre, Yohan Percher, Thomas Choisnet, Ricard Buils Urbano, and Robert Harries. Coupled analysis and numerical model verification for the 2MW Floatgen demonstrator project with IDEOL platform. In *ASME 2018 1st International Offshore Wind Technical Conference*. American Society of Mechanical Engineers Digital Collection, 2018.

[34] FLOW OCEAN. FLOW Concept - Proven technology, innovative design. `https://flowocean.com/flowconcept/`. Accessed: 2021-03-03.

[35] Michael Kausche, Frank Adam, Frank Dahlhaus, and Jochen Großmann. Floating offshore wind - Economic and ecological challenges of a TLP solution. *Renewable Energy*, 126:270–280, 2018.

[36] equinor. Hywind Demo. `https://www.equinor.com/en/what-we-do/floating-wind/hywind-demo.html`. Accessed: 2021-03-04.

[37] Yichao Liu, Sunwei Li, Qian Yi, and Daoyi Chen. Developments in semi-submersible floating foundations supporting wind turbines: A comprehensive review. *Renewable and Sustainable Energy Reviews*, 60:433–449, 2016.

[38] Dominique Roddier, Christian Cermelli, Alexia Aubault, and Alla Weinstein. Windfloat: A floating foundation for offshore wind turbines. *Journal of renewable and sustainable energy*, 2(3):033104, 2010.

[39] Dominique Roddier, Christian Cermelli, and Alla Weinstein. Windfloat: A floating foundation for offshore wind turbines—Part I: design basis and qualification process. In *International Conference on Offshore Mechanics and Arctic Engineering*, volume 43444, pages 845–853, 2009.

[40] Alexander J Coulling, Andrew J Goupee, Amy N Robertson, Jason M Jonkman, and Habib J Dagher. Validation of a FAST semi-submersible floating wind turbine numerical model with DeepCwind test data. *Journal of Renewable and Sustainable Energy*, 5(2):023116, 2013.

[41] Fukushima Offshore Wind Consortium. Fukushima Floating Offshore Wind Farm Demonstration Project (Fukushima FORWARD). `http://www.fukushima-forward.jp/pdf/pamphlet3.pdf`, 2014. Accessed: 2021-04-15.

[42] Main(e) International Consulting LLC. Floating Offshore Wind Foundations: Industry Consortia and Projects in the United States, Europe and Japan. `https://cdn.website-editor.net/073319e35fa34e6189750e64c2e99060/files/uploaded/Floating%252BOffshore%252BWind%252BPlatforms%252BConsortia%252Bfor%252Bweb.pdf`, 2012.

[43] eSubsea. Floating offshore wind foundations. `https://www.esubsea.com/floating-offshore-wind-foundations/#:~:text=A%20Tension%20leg%20platform%20(TLP,suction%20anchors%20or%20suction%20caissons.&text=TLP%20foundations%20are%20well%20suited%20for%20production%20at%20large%20sea%20depths.` Accessed: 2021-03-04.

[44] Thomas Hyland, Frank Adam, Frank Dahlias, Jochen Großmann, et al. Towing tests with the GICON®-TLP for wind turbines. In *The Twenty-Fourth International Ocean and Polar Engineering Conference*. International Society of Offshore and Polar Engineers, 2014.

[45] Emre Uraz. Offshore wind turbine transportation & installation analyses: Planning optimal marine operations for offshore wind projects. Master's thesis, Gotland University, 2014.

[46] Dang Ahn, Sung-chul Shin, Soo-young Kim, Hicham Kharoufi, and Hyun-cheol Kim. Comparative evaluation of different offshore wind turbine installation vessels for korean west–south wind farm. *International Journal of Naval Architecture and Ocean Engineering*, 9(1):45–54, 2017.

[47] Wei Wang and Yong Bai. Investigation on installation of offshore wind turbines. *Journal of Marine Science and Application*, 9(2):175–180, 2010.

[48] Arunjyoti Sarkar and Ove T Gudmestad. Study on a new method for installing a monopile and a fully integrated offshore wind turbine structure. *Marine structures*, 33:160–187, 2013.

[49] Wilson Guachamin Acero, Zhen Gao, and Torgeir Moan. Numerical study of a novel procedure for installing the tower and rotor nacelle assembly of offshore wind turbines based on the inverted pendulum principle. *Journal of Marine Science and Application*, 16(3):243–260, 2017.

[50] Lukas Kuijken. Single blade installation for large wind turbines in extreme wind conditions: A quasi-steady aeroelastic study in high wind speeds under different inflow angles. Master's thesis, DTU, 2015.

[51] Zhiyu Jiang, Zhen Gao, Zhengru Ren, Ye Li, and Lei Duan. A parametric study on the final blade installation process for monopile wind turbines under rough environmental conditions. *Engineering Structures*, 172:1042–1056, 2018.

[52] Yuna Zhao, Zhengshun Cheng, Peter Christian Sandvik, Zhen Gao, Torgeir Moan, and Eric Van Buren. Numerical modeling and analysis of the dynamic motion response of an offshore wind turbine blade during installation by a jack-up crane vessel. *Ocean Engineering*, 165:353–364, 2018.

[53] Yuna Zhao, Zhengshun Cheng, Peter Christian Sandvik, Zhen Gao, and Torgeir Moan. An integrated dynamic analysis method for simulating installation of single blades for wind turbines. *Ocean engineering*, 152:72–88, 2018.

[54] Yuna Zhao, Zhengshun Cheng, Zhen Gao, Peter Christian Sandvik, and Torgeir Moan. Numerical study on the feasibility of offshore single blade installation by floating crane vessels. *Marine Structures*, 64:442–462, 2019.

[55] Amrit Shankar Verma, Nils Petter Vedvik, and Zhen Gao. Numerical assessment of wind turbine blade damage due to contact/impact with tower during installation. In *IOP Conference Series: Materials Science and Engineering*, volume 276, page 012025. IOP Publishing, 2017.

[56] Amrit Shankar Verma, Yuna Zhao, Zhen Gao, and Nils Petter Vedvik. Explicit structural response-based methodology for assessment of

operational limits for single blade installation for offshore wind turbines. In *Proceedings of the Fourth International Conference in Ocean Engineering (ICOE2018)*, pages 737–750. Springer, 2019.

[57] Amrit Shankar Verma, Nils Petter Vedvik, and Zhen Gao. A comprehensive numerical investigation of the impact behaviour of an offshore wind turbine blade due to impact loads during installation. *Ocean Engineering*, 172:127–145, 2019.

[58] CADELER. Swire Blue Ocean intends to order new build vessel and invest in upgraded cranes for Pacific Orca and Pacific Osprey. `https://www.projectcargojournal.com/offshore/2020/09/21/swire-blue-ocean-plans-large-scale-fleet-upgrade/?gdpr=accept`. Accessed: 2021-02-10.

[59] Adnan Durakovic. Jan De Nul Group's Super-Sizes Floating Installation Crane Vessel. `https://www.offshorewind.biz/2019/11/26/jan-de-nul-orders-super-sized-floating-installation-vessel/`. Accessed: 2021-02-10.

[60] DNV GL. DNVGL-ST-N001: Marine operations and marine warranty. 2016.

[61] ISO. ISO 29400:2020 - Ships and marine technology—Offshore wind energy—Port and marine operations. 2020.

[62] DNV. DNV-RP-C205: Environmental conditions and environmental loads. 2010.

[63] DNV. DNV-OS-H202: Sea transport operations. 2015.

[64] DNV. DNV-OS-H205: Lifting Operations (VMO Standard-Part 2-5). 2014.

[65] DNV GL. DNVGL-ST-0119: Floating wind turbine structures, 2018.

[66] Wilson Guachamin Acero. *Assessment of marine operations for offshore wind turbine installation with emphasis on response-based operational limits*. PhD thesis, NTNU, 2016.

[67] Wilson Guachamin Acero, Lin Li, Zhen Gao, and Torgeir Moan. Methodology for assessment of the operational limits and operability of marine operations. *Ocean Engineering*, 125:308–327, 2016.

[68] Hui Zhu, L Li, and MC Ong. Study of lifting operation of a tripod foundation for offshore wind turbine. In *IOP Conference Series: Materials Science and Engineering*, volume 276, page 012012. IOP Publishing, 2017.

[69] Ben Hudson. Time-domain simulations of marine operations and their application to the offshore renewable energy sector. 2020.

[70] Lin Li, Carlos Parra, Xinying Zhu, and Muk Chen Ong. Splash zone lowering analysis of a large subsea spool piece. *Marine Structures*, 70:102664, 2020.

[71] MAAA Hassan and C Guedes Soares. Installation of pre-assembled offshore floating wind turbine using a floating vessel. In *Developments in Renewable Energies Offshore*, pages 461–468. CRC Press, 2020.

[72] Lin Li, Adham M Amer, and Xinying Zhu. Numerical analysis of an over-boarding operation for a subsea template. *Journal of Ocean Engineering and Science*, 6(2):146–159, 2021.

[73] Zhiyu Jiang, Rune Yttervik, Zhen Gao, and Peter Christian Sandvik. Design, modelling, and analysis of a large floating dock for spar floating wind turbine installation. *Marine Structures*, 72:102781, 2020.

[74] Frank Lemmer, Wei Yu, Kolja Müller, and Po Wen Cheng. Semi-submersible wind turbine hull shape design for a favorable system response behavior. *Marine Structures*, 71:102725, 2020.

[75] Ruifeng Chen and Ying Min Low. Reducing uncertainty in time domain fatigue analysis of offshore structures using control variates. *Mechanical Systems and Signal Processing*, 149:107192, 2021.

[76] Johyun Kyoung, Sagar Samaria, Jeffrey O'Donnell, and Sudhakar Tallavajhula. Advances in offshore structural analysis using response-based time-domain approach. In *Offshore Technology Conference*. OnePetro, 2021.

[77] Pierre Major, Houxiang Zhang, Hans Petter Hildre, and Mathieu Edet. Virtual prototyping of offshore operations: a review. *Ship Technology Research*, 68(2):84–101, 2021.

[78] Binbin Li. Operability study of walk-to-work for floating wind turbine and service operation vessel in the time domain. *Ocean Engineering*, 220:108397, 2021.

[79] Wilson Guachamin Acero, Zhen Gao, and Torgeir Moan. Methodology for assessment of the allowable sea states during installation of an offshore wind turbine transition piece structure onto a monopile foundation. *Journal of Offshore Mechanics and Arctic Engineering*, 139(6), 2017.

[80] Lin Li, Wilson Guachamin Acero, Zhen Gao, and Torgeir Moan. Assessment of allowable sea states during installation of offshore wind turbine monopiles with shallow penetration in the seabed. *Journal of Offshore Mechanics and Arctic Engineering*, 138(4), 2016.

[81] Amrit Shankar Verma, Zhiyu Jiang, Zhengru Ren, Zhen Gao, and Nils Petter Vedvik. Response-based assessment of operational limits for mating blades on monopile-type offshore wind turbines. *Energies*, 12(10):1867, 2019.

[82] Alice Goward Brown et al. Metocean Procedures Guide for Offshore Renewables. *Modern Transactions of the IMarEST*, 2018.

[83] World meteorological organization. Observations. `https://public.wmo.int/en/our-mandate/what-we-do/observations`. Accessed: 2021-03-07.

[84] Robert S Arthur. Wave forecasting and hindcasting. Technical report, University of California-Scripps institution of oceanography, 1951.

[85] Edwige Boudière, Christophe Maisondieu, Fabrice Ardhuin, Mickaël Accensi, Lucia Pineau-Guillou, and Jérémy Lepesqueur. A suitable metocean hindcast database for the design of marine energy converters. *International Journal of Marine Energy*, 3:e40–e52, 2013.

[86] Val R Swail and Andrew T Cox. On the use of NCEP–NCAR reanalysis surface marine wind fields for a long-term North Atlantic wave hindcast. *Journal of Atmospheric and oceanic technology*, 17(4):532–545, 2000.

[87] Ralf Weisse and Heinz Günther. Wave climate and long-term changes for the Southern North Sea obtained from a high-resolution hindcast 1958–2002. *Ocean Dynamics*, 57(3):161–172, 2007.

[88] Sarah Gallagher, Roxana Tiron, and Frédéric Dias. A long-term nearshore wave hindcast for Ireland: Atlantic and Irish Sea coasts (1979–2012). *Ocean Dynamics*, 64(8):1163–1180, 2014.

[89] Hajime Mase, Tomohiro Yasuda, and Nobuhito Mori. Real-time prediction of tsunami magnitudes in Osaka Bay, Japan, using an artificial neural network. *Journal of waterway, port, coastal, and ocean engineering*, 137(5):263–268, 2011.

[90] Alexis Mérigaud and John V Ringwood. Incorporating ocean wave spectrum information in short-term free-surface elevation forecasting. *IEEE Journal of Oceanic Engineering*, 44(2):401–414, 2018.

[91] Francesco Fusco. Short-term wave forecasting as a univariate time series problem. Technical report, Maynooth University, 2009.

[92] Hiroshi Kagemoto. Forecasting a water-surface wave train with artificial intelligence-A case study. *Ocean Engineering*, 207:107380, 2020.

[93] Tim Vasquez. *Weather Forecasting Red Book: Forecasting Techniques for Meteorology*. Weather Graphics Technologies, 2009.

[94] Robert Marc Friedman. *Appropriating the weather: Vilhelm Bjerknes and the construction of a modern meteorology*. Cornell University Press, 1993.

[95] Lewis Fry Richardson. *Weather prediction by numerical process*. Cambridge university press, 2007.

[96] Paul N Edwards. *A vast machine: Computer models, climate data, and the politics of global warming*. MIT Press, 2010.

[97] Jules G Charney, Ragnar Fjörtoft, and J von Neumann. Numerical integration of the barotropic vorticity equation. *Tellus*, 2(4):237–254, 1950.

[98] NOAA. Climate models. `https://celebrating200years.noaa.gov/breakthroughs/climate_model/modeling_schematic.html`. Accessed: 2019-04-25.

[99] Kristine Harper, Louis W Uccellini, Eugenia Kalnay, Kenneth Carey, and Lauren Morone. 50th anniversary of operational numerical weather prediction. *Bulletin of the American Meteorological Society*, 88(5):639–650, 2007.

[100] Philip Duncan Thompson. Dynamical prediction-The rational approach to weather forecasting. *Weatherwise*, 8(6):145–149, 1955.

[101] Atsunobu Ichikawa. *Global Warming-The Research Challenges: A Report of Japan's Global Warming Initiative*. Springer Science & Business Media, 2004.

[102] LM Leslie and GS Dietachmayer. Real-time limited area numerical weather prediction in Australia-A historical perspective. *Australian Meteorological Magazine*, 1992.

[103] James R Holton. An introduction to dynamic meteorology. *American Journal of Physics*, 41(5):752–754, 1973.

[104] Qingyun Duan, Florian Pappenberger, Andy Wood, Hannah L Cloke, and John Schaake. *Handbook of hydrometeorological ensemble forecasting*. Springer, 2019.

[105] Anders Persson and Federico Grazzini. User guide to ECMWF forecast products. *ECMWF*, 3:2, 2007.

[106] Peter W. White. Part IV: Physical processes (CY23R4). *ECMWF*, IFS Documentation Cycle, 2003.

[107] Peter Bauer, Alan Thorpe, and Gilbert Brunet. The quiet revolution of numerical weather prediction. *Nature*, 525(7567):47–55, 2015.

[108] Hendrik L Tolman. A third-generation model for wind waves on slowly varying, unsteady, and inhomogeneous depths and currents. *Journal of Physical Oceanography*, 21(6):782–797, 1991.

[109] The Wamdi Group. The WAM model-A third generation ocean wave prediction model. *Journal of Physical Oceanography*, 18(12):1775–1810, 1988.

[110] NRRC Booij, Roeland C Ris, and Leo H Holthuijsen. A third-generation wave model for coastal regions: 1. Model description and validation. *Journal of geophysical research: Oceans*, 104(C4):7649–7666, 1999.

[111] JMary E. Anderson Thomas C. Massey et al. STWAVE: Steady-state spectral wave model user's manual for STWAVE, version 6.0. Technical report, U.S. Army Corps of Engineers, 2011.

[112] George Lavidas and Vengatesan Venugopal. Application of numerical wave models at European coastlines: A review. *Renewable and Sustainable Energy Reviews*, 92:489–500, 2018.

[113] Francesco Fusco and John V Ringwood. Short-term wave forecasting with AR models in real-time optimal control of wave energy converters. In *2010 IEEE International Symposium on Industrial Electronics*, pages 2475–2480. IEEE, 2010.

[114] Yerai Pena-Sanchez and John Ringwood. A critical comparison of AR and ARMA models for short-term wave forecasting. In *Proceedings of the 12th European Wave and Tidal Energy Conference 27th Aug-1st Sept 2017*, number 961, pages 1–6. European Wave and Tidal Energy Conference 2017, 2017.

[115] Barbara G Brown, Richard W Katz, and Allan H Murphy. Time series models to simulate and forecast wind speed and wind power. *Journal of Applied Meteorology and Climatology*, 23(8):1184–1195, 1984.

[116] Philippe Poggi, Marc Muselli, Gilles Notton, Christian Cristofari, and Alain Louche. Forecasting and simulating wind speed in Corsica by using an autoregressive model. *Energy conversion and management*, 44(20):3177–3196, 2003.

[117] Ming Ge and Eric C Kerrigan. Short-term ocean wave forecasting using an autoregressive moving average model. In *2016 UKACC 11th International Conference on Control (CONTROL)*, pages 1–6. IEEE, 2016.

[118] Jose Luis Torres, Almudena Garcia, Marian De Blas, and Adolfo De Francisco. Forecast of hourly average wind speed with ARMA models in Navarre (Spain). *Solar energy*, 79(1):65–77, 2005.

[119] Ergin Erdem and Jing Shi. ARMA based approaches for forecasting the tuple of wind speed and direction. *Applied Energy*, 88(4):1405–1414, 2011.

[120] M Lydia, S Suresh Kumar, A Immanuel Selvakumar, and G Edwin Prem Kumar. Linear and non-linear autoregressive models for short-term wind speed forecasting. *Energy conversion and management*, 112:115–124, 2016.

[121] JD Agrawal and MC Deo. On-line wave prediction. *Marine structures*, 15(1):57–74, 2002.

[122] B Kamranzad, A Etemad-Shahidi, and MH Kazeminezhad. Wave height forecasting in Dayyer, the Persian Gulf. *Ocean engineering*, 38(1):248–255, 2011.

[123] Didit Adytia, Alif Rizal Yonanta, and Nugrahinggil Subasita. Wind wave prediction by using Autoregressive Integrated Moving Average model: Case study in Jakarta Bay. *International Journal on Information and Communication Technology (IJoICT)*, 4(2):33–42, 2018.

[124] Rajesh G Kavasseri and Krithika Seetharaman. Day-ahead wind speed forecasting using f-ARIMA models. *Renewable Energy*, 34(5):1388–1393, 2009.

[125] Mengjiao Qin, Zhihang Li, and Zhenhong Du. Red tide time series forecasting by combining ARIMA and deep belief network. *Knowledge-Based Systems*, 125:39–52, 2017.

[126] MC Deo and C Sridhar Naidu. Real time wave forecasting using neural networks. *Ocean engineering*, 26(3):191–203, 1998.

[127] Mc C Deo, Abhay Jha, AS Chaphekar, and K Ravikant. Neural networks for wave forecasting. *Ocean engineering*, 28(7):889–898, 2001.

[128] Iman Malekmohamadi, Bazargan-Lari, et al. Evaluating the efficacy of SVMs, BNs, ANNs and ANFIS in wave height prediction. *Ocean Engineering*, 38(2-3):487–497, 2011.

[129] S Mandal, Subba Rao, and DH Raju. Ocean wave parameters estimation using backpropagation neural networks. *Marine structures*, 18(3):301–318, 2005.

[130] DJ Peres, C Iuppa, L Cavallaro, A Cancelliere, and E Foti. Significant wave height record extension by neural networks and reanalysis wind data. *Ocean Modelling*, 94:128–140, 2015.

[131] Erasmo Cadenas and Wilfrido Rivera. Short term wind speed forecasting in La Venta, Oaxaca, México, using artificial neural networks. *Renewable Energy*, 34(1):274–278, 2009.

[132] P Flores, A Tapia, and G Tapia. Application of a control algorithm for wind speed prediction and active power generation. *Renewable Energy*, 30(4):523–536, 2005.

[133] Gong Li and Jing Shi. On comparing three artificial neural networks for wind speed forecasting. *Applied Energy*, 87(7):2313–2320, 2010.

[134] GW Chang, HJ Lu, YR Chang, and YD Lee. An improved neural network-based approach for short-term wind speed and power forecast. *Renewable energy*, 105:301–311, 2017.

[135] Pooja Jain and MC Deo. Real-time wave forecasts off the western Indian coast. *Applied ocean research*, 29(1-2):72–79, 2007.

[136] S Mandal and N Prabaharan. Ocean wave forecasting using recurrent neural networks. *Ocean engineering*, 33(10):1401–1410, 2006.

[137] Zaccheus O Olaofe. A 5-day wind speed & power forecasts using a layer recurrent neural network (LRNN). *Sustainable Energy Technologies and Assessments*, 6:1–24, 2014.

[138] Chenhua Ni, Xiandong Ma, and Yang Bai. Convolutional Neural Network based power generation prediction of wave energy converter. In *2018 24th International Conference on Automation and Computing (ICAC)*, pages 1–6. IEEE, 2018.

[139] Mehmet Özger and Zekai Şen. Prediction of wave parameters by using fuzzy logic approach. *Ocean Engineering*, 34(3-4):460–469, 2007.

[140] Adem Akpınar, Mehmet Özger, and Murat Ihsan Kömürcü. Prediction of wave parameters by using fuzzy inference system and the parametric models along the south coasts of the Black Sea. *Journal of Marine Science and Technology*, 19(1):1–14, 2014.

[141] Christos Stefanakos. Fuzzy time series forecasting of nonstationary wind and wave data. *Ocean Engineering*, 121:1–12, 2016.

[142] Mengning Wu, Christos Stefanakos, Zhen Gao, and Sverre Haver. Prediction of short-term wind and wave conditions for marine operations using a multi-step-ahead decomposition-ANFIS model and quantification of its uncertainty. *Ocean Engineering*, 188:106300, 2019.

[143] Sujit Basu, Abhijit Sarkar, K Satheesan, and CM Kishtawal. Predicting wave heights in the north Indian Ocean using genetic algorithm. *Geophysical research letters*, 32(17), 2005.

[144] Adil Ahmed and Muhammad Khalid. Multi-step ahead wind forecasting using nonlinear autoregressive neural networks. *Energy Procedia*, 134:192–204, 2017.

[145] Tong Niu, Jianzhou Wang, Kequan Zhang, and Pei Du. Multi-step-ahead wind speed forecasting based on optimal feature selection and a modified bat algorithm with the cognition strategy. *Renewable Energy*, 118:213–229, 2018.

[146] DNV JIP. Technical Report, Marine Operation Rules, Revised Alpha Factor-Joint Industry Project. *DNV, Oslo*, 2007.

[147] Sara Wilcken. Alpha factors for the calculation of forecasted operational limits for marine operations in the Barents sea. Master's thesis, University of Stavanger, Norway, 2012.

[148] Arthur L Samuel. Some studies in machine learning using the game of checkers. *IBM Journal of research and development*, 3(3):210–229, 1959.

[149] Nelson Morgan and Herve Bourlard. Continuous speech recognition using multilayer perceptrons with hidden markov models. In *International conference on acoustics, speech, and signal processing*, pages 413–416. IEEE, 1990.

[150] Janet M Baker, Li Deng, et al. Developments and directions in speech recognition and understanding, Part 1. *IEEE Signal processing magazine*, 26(3):75–80, 2009.

[151] Jaume Padrell-Sendra, Darío Martín-Iglesias, and Fernando Díaz-de María. Support vector machines for continuous speech recognition. In *2006 14th European Signal Processing Conference*, pages 1–4. IEEE, 2006.

[152] Jan Stadermann and Gerhard Rigoll. A hybrid SVM/HMM acoustic modeling approach to automatic speech recognition. In *8th International Conference on Spoken Language Processing, Jeju Island, South Korea*, 2004.

[153] Feng-Ping An. Medical image classification algorithm based on weight initialization-sliding window fusion convolutional neural network. *Complexity*, 2019.

[154] Alex Krizhevsky, Ilya Sutskever, and Geoffrey E Hinton. Imagenet classification with deep convolutional neural networks. *Advances in neural information processing systems*, 25:1097–1105, 2012.

[155] Gabriele Moser and Sebastiano B Serpico. Combining support vector machines and Markov random fields in an integrated framework for contextual image classification. *IEEE Transactions on Geoscience and Remote Sensing*, 51(5):2734–2752, 2012.

[156] Tianjun Xiao, Yichong Xu, Kuiyuan Yang, Jiaxing Zhang, Yuxin Peng, and Zheng Zhang. The application of two-level attention models in deep convolutional neural network for fine-grained image classification. In *Proceedings of the IEEE conference on computer vision and pattern recognition*, pages 842–850, 2015.

[157] M Bahadır. The analyse of precipitation and temperature in Afyonkarahisar (Turkey) in respect of Box-Jenkins technique. *Journal of Academic Social Science Studies*, 5(8):195–212, 2012.

[158] Sabine Hunsicker, Yu Chen, and Christian Federmann. Machine learning for hybrid machine translation. In *Proceedings of the seventh workshop on statistical machine translation*, pages 312–316, 2012.

[159] Christopher B Quirk, Arul A Menezes, Stephen D Richardson, and Robert C Moore. System and method for machine learning a confidence metric for machine translation, February 24 2009. US Patent 7,496,496.

[160] Yuliang Zhao, Sheng Dong, Fengyuan Jiang, and Atilla Incecik. Mooring tension prediction based on bp neural network for semi-submersible platform. *Ocean Engineering*, 223:108714, 2021.

[161] L Moreira and C Guedes Soares. Neural network model for estimation of hull bending moment and shear force of ships in waves. *Ocean Engineering*, 206:107347, 2020.

[162] Peng Chen, Lei Song, Jia-hao Chen, and Zhiqiang Hu. Simulation annealing diagnosis algorithm method for optimized forecast of the dynamic response of floating offshore wind turbines. *Journal of Hydrodynamics*, 33(2):216–225, 2021.

[163] D Cevasco, J Tautz-Weinert, AJ Kolios, and U Smolka. Applicability of machine learning approaches for structural damage detection of offshore wind jacket structures based on low resolution data. In *Journal of Physics: Conference Series*, volume 1618, page 022063. IOP Publishing, 2020.

[164] Zhiyu Jiang, Marius Bjørnholm, Jiamin Guo, Wenbin Dong, Zhengru Ren, and Amrit Shankar Verma. Damage identification of a jacket support structure for offshore wind turbines. In *2020 15th IEEE Conference on Industrial Electronics and Applications (ICIEA)*, pages 995–1000. IEEE, 2020.

[165] Xingxian Bao, Zhichao Wang, and Gregorio Iglesias. Damage detection for offshore structures using long and short-term memory networks and random decrement technique. *Ocean Engineering*, 235:109388, 2021.

[166] Agnieszka A Chojaczyk, Angelo P Teixeira, Luís C Neves, Joao B Cardoso, and C Guedes Soares. Review and application of artificial neural networks models in reliability analysis of steel structures. *Structural Safety*, 52:78–89, 2015.

[167] Yuliang Zhao and Sheng Dong. Probabilistic fatigue surrogate model of bimodal tension process for a semi-submersible platform. *Ocean Engineering*, 220:108501, 2021.

[168] Rasoul Hejazi, Andrew Grime, Mark Randolph, and Mike Efthymiou. A bayesian machine learning approach to rapidly quantifying the fatigue probability of failure for steel catenary risers. *Ocean Engineering*, 235:109353, 2021.

[169] Sagar S Jambhorkar and Mr Vijay S Jondhale. *Data Mining Technique: Fundamental Concept and Statistical Analysis*. Horizon Books (A Division of Ignited Minds Edutech P Ltd), 2015.

[170] GA Athanassoulis and Christos Stefanakos. A nonstationary stochastic model for long-term time series of significant wave height. *Journal of Geophysical Research: Oceans*, 100(C8):16149–16162, 1995.

[171] Christos Stefanakos. Nonstationary prediction of wind and waves in the pacific ocean using fuzzy inference systems. In *The 26th International Ocean and Polar Engineering Conference*. OnePetro, 2016.

[172] Christos Stefanakos and Erik Vanem. Climatic forecasting of wind and waves using fuzzy inference systems. In *ASME 2017 36th International Conference on Ocean, Offshore and Arctic Engineering*. American Society of Mechanical Engineers Digital Collection, 2017.

[173] Christos Stefanakos, GA Athanassoulis, et al. Multiscale time series modelling of significant wave height. In *The Twelfth International Offshore and Polar Engineering Conference*. International Society of Offshore and Polar Engineers, 2002.

[174] Christos Stefanakos, GA Athanassoulis, and SF Barstow. Time series modeling of significant wave height in multiple scales, combining

various sources of data. *Journal of Geophysical Research: Oceans*, 111(C10), 2006.

[175] Norden E Huang, Zheng Shen, et al. The empirical mode decomposition and the hilbert spectrum for nonlinear and non-stationary time series analysis. *Proceedings of the Royal Society of London. Series A: mathematical, physical and engineering sciences*, 454(1971):903–995, 1998.

[176] Matt Dyer Ben Byer Max Lambert, Andrew Engroff. Empirical mode decomposition. `https://www.clear.rice.edu/elec301/Projects02/empiricalMode/process.html`. Accessed: 2019-06-29.

[177] Frank Rosenblatt. The perceptron: a probabilistic model for information storage and organization in the brain. *Psychological review*, 65(6):386, 1958.

[178] Jamshid Nazari and Okan K Ersoy. Implementation of back-propagation neural networks with matlab. 1992.

[179] David E Rumelhart, Geoffrey E Hinton, and Ronald J Williams. Learning representations by back-propagating errors. *nature*, 323(6088):533–536, 1986.

[180] Caren Marzban, Scott Sandgathe, and Eugenia Kalnay. Mos, Perfect Prog, and Reanalysis. *Monthly weather review*, 134(2):657–663, 2006.

[181] Yoshua Bengio, Patrice Simard, and Paolo Frasconi. Learning long-term dependencies with gradient descent is difficult. *IEEE transactions on neural networks*, 5(2):157–166, 1994.

[182] Sepp Hochreiter and Jürgen Schmidhuber. Long short-term memory. *Neural computation*, 9(8):1735–1780, 1997.

[183] J-SR Jang. ANFIS: adaptive-network-based fuzzy inference system. *IEEE transactions on systems, man, and cybernetics*, 23(3):665–685, 1993.

[184] Per Undén, Laura Rontu, et al. HIRLAM-5 scientific documentation. *Swedish Meteorological and Hydrological Institute, Norrköping, Sweden*, 2011.

[185] Australia Government Bureau of Meteorology. Numerical weather and ocean prediction maps. `http://www.bom.gov.au/nmoc/ab_nmc_op.shtml`. Accessed: 2020-06-03.

[186] Government of Canada. Environment and climate change canada. `http://www.ec.gc.ca/`. Accessed: 2020-06-03.

[187] DWD. Deutscher Wetterdienst. `http://www.dwd.de/`. Accessed: 2020-06-03.

[188] Suranjana Saha, Shrinivas Moorthi, et al. The NCEP climate forecast system reanalysis. *Bulletin of the American Meteorological Society*, 91(8):1015–1058, 2010.

[189] Dick P Dee, S M Uppala, et al. The ERA-Interim reanalysis: Configuration and performance of the data assimilation system. *Quarterly Journal of the royal meteorological society*, 137(656):553–597, 2011.

[190] Y Gusdal, A Carrasco, BR Furevik, and Ø Sætra. Validation of the operational Wave Model WAM at met. no-Report 2010. *Report of the Norwegian Meteorological Institute-Oceanography*, (14), 2011.

[191] Eugen Rusu. Strategies in using numerical wave models in ocean/-coastal applications. *Journal of Marine Science and Technology-Taiwan*, 19(1):58–73, 2011.

[192] Wind Europe. Offshore wind in Europe. *Key trends and statistics*, 2019.

[193] National and Kapodistrian University of Athens (NKUA). Atmospheric modeling and weather forecasting group. `https://forecast.uoa.gr/en/group`. Accessed: 2021-03-09.

[194] Patrick Laloyaux, Eric de Boisseson, et al. CERA-20C: A coupled reanalysis of the twentieth century. *Journal of Advances in Modeling Earth Systems*, 10(5):1172–1195, 2018.

[195] Georgios Sylaios, Frédéric Bouchette, Vassilios A Tsihrintzis, and Cléa Denamiel. A fuzzy inference system for wind-wave modeling. *Ocean Engineering*, 36(17-18):1358–1365, 2009.

[196] Mengning Wu, Zhen Gao, Christos Stefanakos, and Sverre Haver. Comparison of machine-learning methods for multi-step-ahead prediction of wave and wind conditions. In *ITISE 2019. Proceedings of papers. Vol 2*, pages 1074–1093. 09 2019.

[197] Mengning Wu, Christos Stefanakos, and Zhen Gao. Multi-step-ahead forecasting of wave conditions based on a physics-based machine learning (PBML) model for marine operations. *Journal of Marine Science and Engineering*, 8(12):992, 2020.

[198] Jean-Raymond Bidlot. Intercomparison of operational wave forecasting systems against buoys: data from ECMWF, MetOffice, FNMOC, MSC, NCEP, MeteoFrance, BoM, SHOM, JMA, KMA, Puerto del Estado, DMI, NZM, METNO, SHN-SM. May 2017 to July 2017. `https://www.jcomm.info/index.php?option=com_oe&task=viewDocumentRecord&docID=20279`. Accessed: 2021-03-14.

[199] Asle Natskår, Torgeir Moan, and Per Ø Alvær. Uncertainty in forecasted environmental conditions for reliability analyses of marine operations. *Ocean Engineering*, 108:636–647, 2015.

[200] Sverre Haver. Metocean modelling and prediction of extremes. *Lecture notes in TMR4195-Design of Offshore Structures. Department of Marine Technology, NTNU*, 2017.

[201] Christian Bak, Frederik Zahle, et al. The DTU 10-MW reference wind turbine. In *Danish Wind Power Research 2013*, 2013.

[202] MARINTEK. SIMO-Theory Manual Version 4.0, 2012.

[203] SINTEF Ocean. RIFLEX 4.10.0 Theory Manual. *Trondheim, SINTEF Ocean*, 2017.

[204] SINTEF Ocean. SIMA 3.2 User Guide. Technical report, Technical report, 2015.

[205] SF Hoerner. Fluid-Dynamic Drag: Practical information on aerodynamic drag and hydrodynamic resistance. sf hoerner. *The Aeronautical Journal*, 80(788):371–371, 1976.

[206] SF Hoerner. Fluid-Dynamic Lift: Practical information on aerodynamic and hydrodynamic lift. *NASA STI/Recon Technical Report A*, 76:32167, 1975.

[207] Yuna Zhao. *Numerical Modelling and Dynamic Analysis of Offshore Wind Turbine Blade Installation.* PhD thesis, NTNU, 2019.

[208] GL DNV. Sesam user manual-wadam. *DNV GL Software*, 2017.

[209] Lin Li, Zhen Gao, and Torgeir Moan. Joint distribution of environmental condition at five European offshore sites for design of combined wind and wave energy devices. *Journal of Offshore Mechanics and Arctic Engineering*, 137(3), 2015.

[210] International Electrotechnical Commission et al. IEC 61400-3: Wind turbines-Part 3: Design requirements for offshore wind turbines. *International Electrotechnical Commission: Geneva, Switzerland*, 2009.

[211] Bonnie J Jonkman. TurbSim User's Guide: Version 1.50. Technical report, National Renewable Energy Lab.(NREL), Golden, CO (United States), 2009.

[212] International Electrotechnical Commission et al. IEC 61400-3: Wind turbines-Part 1: Design requirements for offshore wind turbines. *International Electrotechnical Commission, Geneva, Switzerland*, 64, 2005.

[213] Frederick N Fritsch and Ralph E Carlson. Monotone piecewise cubic interpolation. *SIAM Journal on Numerical Analysis*, 17(2):238–246, 1980.

[214] Amrit Shankar Verma, Zhiyu Jiang, Nils Petter Vedvik, Zhen Gao, and Zhengru Ren. Impact assessment of a wind turbine blade root during an offshore mating process. *Engineering Structures*, 180:205–222, 2019.

[215] Clark L Hull. The correlation coefficient and its prognostic significance. *The Journal of Educational Research*, 15(5):327–338, 1927.

[216] Kodi Arfer. Pearson correlation and prediction intervals. `https://upload.wikimedia.org/wikipedia/commons/a/a7/Pearson_correlation_and_prediction_intervals.svg`. Accessed: 2021-03-11.

Appendix A

Analysis of long-term metocean data

Hindcast data of H_s, T_p and U_w, extracted from the CERA-20C database from 2001 to 2009, are used for the data analysis.

A.1 Time series plot

Time series of H_s, T_p and U_w (one year three-hourly data) are presented in Figure A.1. The long-term time series provides an overview of the environment at the selected offshore site and three phenomena are found:

- There is no obvious trend exists in time series.
- There is a certain degree of seasonality.
- Due to characteristics of T_p (i.e., dominated by wind-generated waves or swells), its time series is not continuous.

A.2 Auto-correlation coefficient

The auto-correlation coefficient of the metocean variables is further calculated, to understand how well the future data can be affected from knowledge of the past data. The definition of the auto-correlation coefficient of a variable X is expressed in Eq. (A.1), in which $COV(X_t, X_{t+\tau})$ is the auto-covariance of X with the lag time τ. ρ_{XX} is in the range of [-1, 1], that provides a measure of the strength of statistical dependence.

$$\rho_{XX}(\tau) = \frac{COV(X_t, X_{t+\tau})}{\sigma_X^2} \tag{A.1}$$

The auto-correlation coefficients of H_s, T_p and U_w are displayed in Figure A.2. They are functions of the lag time (i.e., time interval between two data). All time series exhibit a strong temporal serial correlation. As shown in the figure, auto-correlation coefficients for small time intervals tend to be large for all three metocean variables, and they decrease rapidly as the time interval increases. Afterwards, they will not change greatly with the interval but remain at small values. As displayed, auto-correlation coefficients are more than 0.8 for H_s, T_p and U_w when the time interval is less than 9 hours. In contrast, as the time interval increases to one day, auto-correlation coefficients become lower than 0.6, 0.5 and 0.4, respectively.

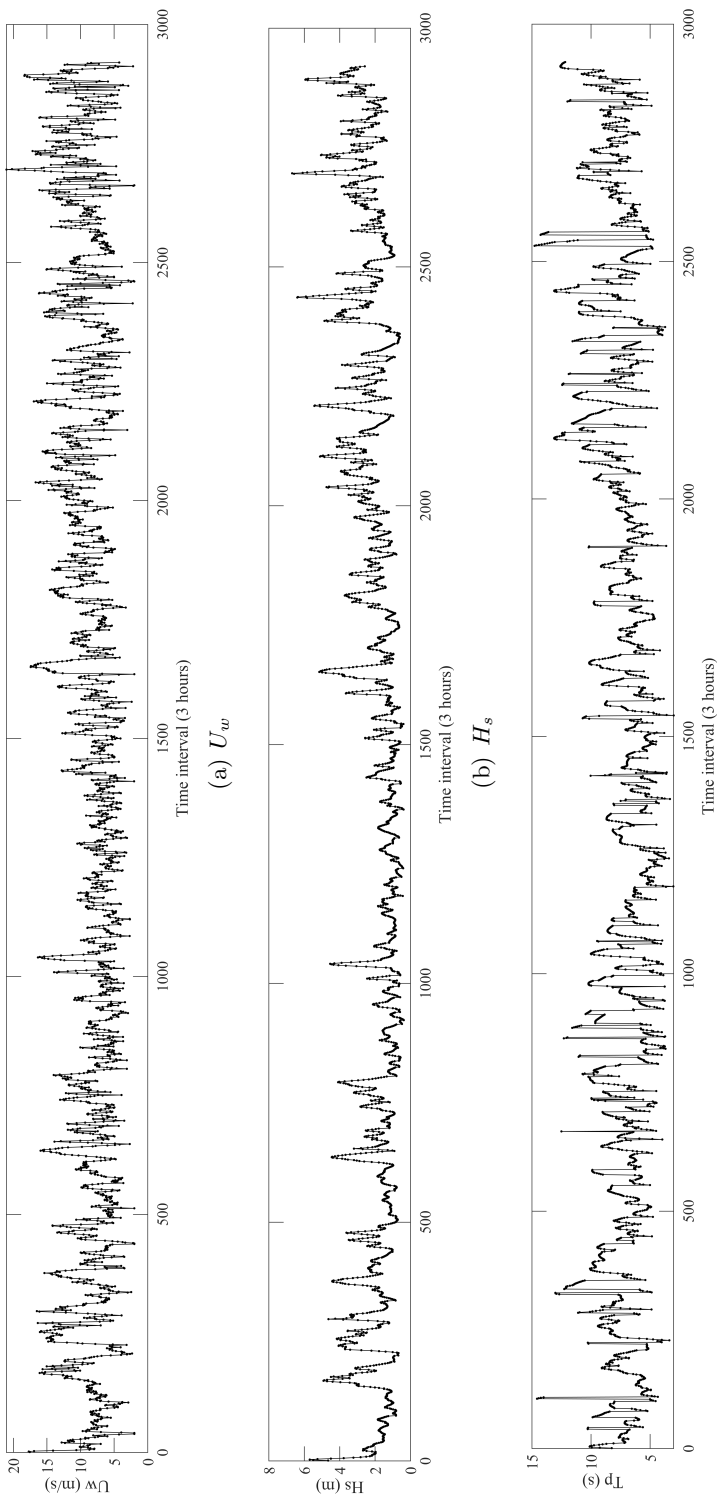

(a) U_w

(b) H_s

(c) T_p

Figure A.1: Time plot of metocean variables (one year)

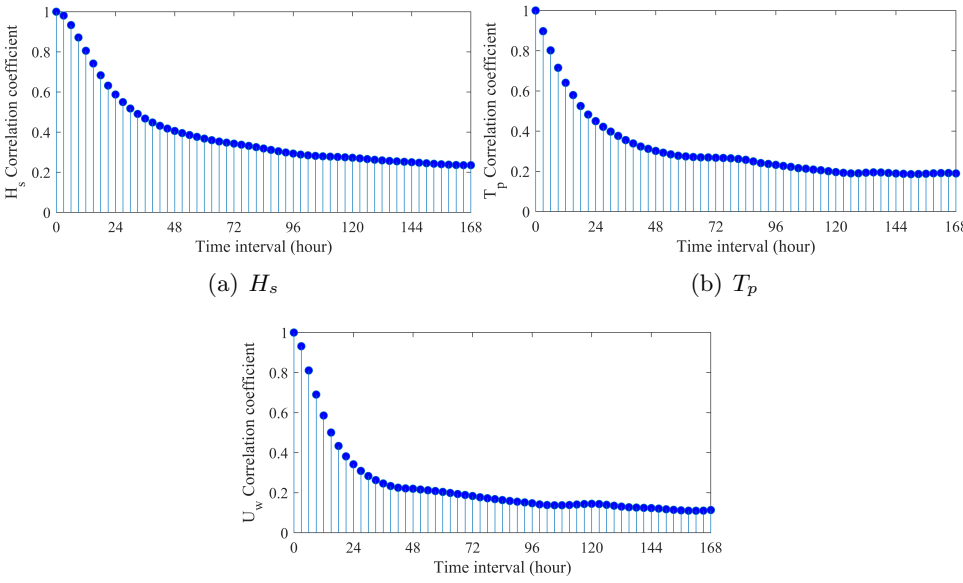

(a) H_s (b) T_p

(c) U_w

Figure A.2: Auto-correlation coefficient of metocean variables (one year)

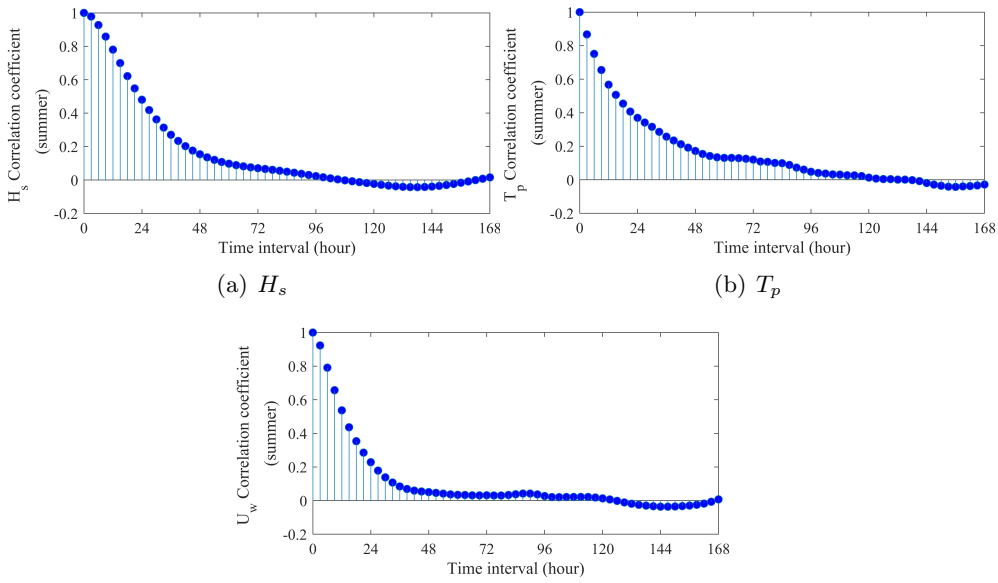

(a) H_s (b) T_p

(c) U_w

Figure A.3: Auto-correlation coefficient of metocean variables (summer)

The properties of auto-correlations depend to some extent on the season. Figures A.3 and A.4 show the results in summer (June to August) and winter (December to February), respectively. Compared with the results shown in Figure A.2, the auto-correlation coefficients decay to zero faster, but the difference is not obvious when the time interval is small. Overall, one metocean data in the time series has relatively high correlation with its 2 to 5 previous data, showing a certain degree of predictability.

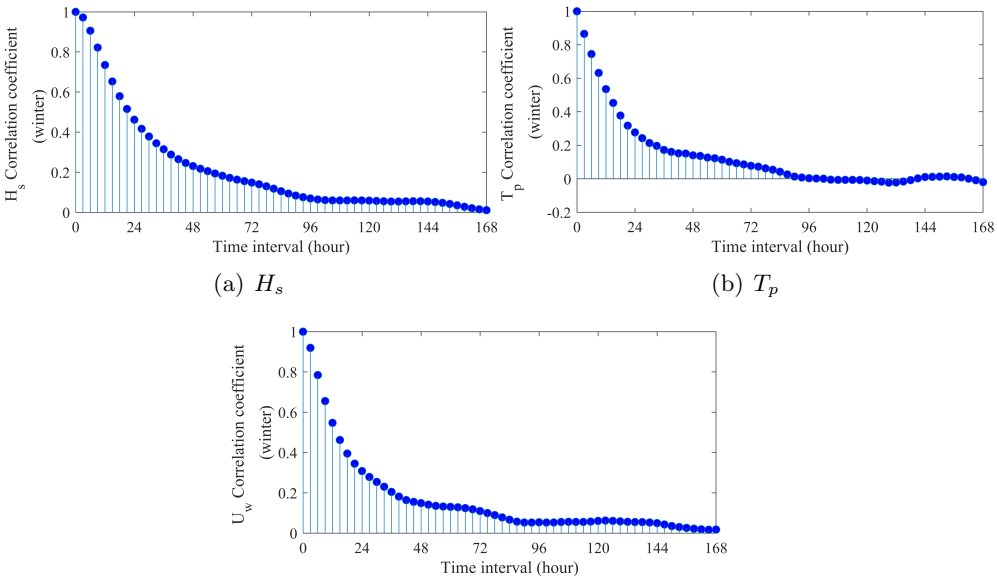

(a) H_s (b) T_p

(c) U_w

Figure A.4: Auto-correlation coefficient of metocean variables (winter)

A.3 Cross-correlation coefficient

In addition to analyzing auto-correlations in the time series of a single variable, it is also necessary to measure the relationship between different variables. Figure A.5 shows scatter plots of environmental variables. The color gives the probability of occurrence.

In general, positive relationships can be found between waves and wind. Among three subfigures in Figure A.5, the relationship between H_s and U_w is strongest (Figure A.5 (a)), while the relationships for other two cases are relatively low. To some extent, the figure indicates that wind conditions can be regarded as important input information for forecasting wave conditions.

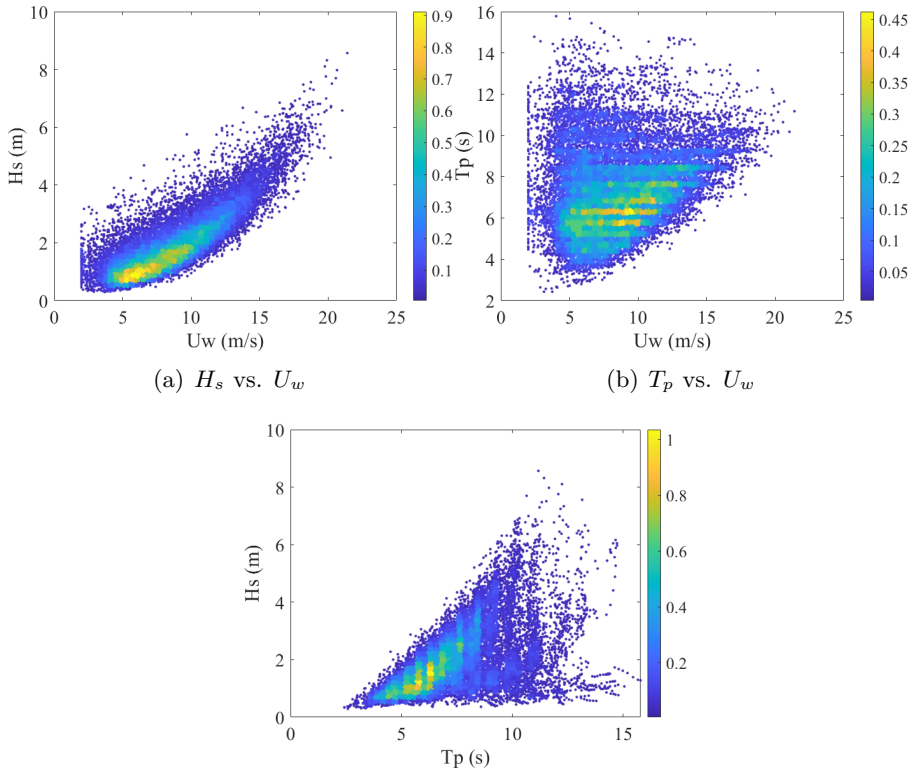

(a) H_s vs. U_w (b) T_p vs. U_w

(c) H_s vs. T_p

Figure A.5: Scatter plots of metocean data

Then cross-correlation coefficients are calculated between two variables, to measure their statistical relationship. The definition of the cross-correlation coefficient between variables X and Y is expressed as Eq. (A.2). Likewise, ρ_{XY} always ranges from -1 to 1. A value of 1 implies that a linear relationship while 0 implies that there is no linear correlation between two values. By checking ρ_{XY} for two metocean variables, what extent one variable can be used to determine the other variable can be revealed.

$$\rho_{XY}(\tau) = \frac{COV(X_t, Y_{t+\tau})}{\sigma_X \sigma_Y} \tag{A.2}$$

where $COV(X_t, Y_{t+\tau})$ is the covariance of X and Y.

In view of a strong relationship between H_s and U_w is observed in Figure A.5, the cross-correlation coefficient of H_s against U_w is displayed in Figure A.6. Obviously, the maximum value occurs at the time interval is zero, that is nearly 0.9, indicating that H_s has the greatest correlation with U_w at

the same time. Likewise, cross-correlations would also decrease as the time interval increases.

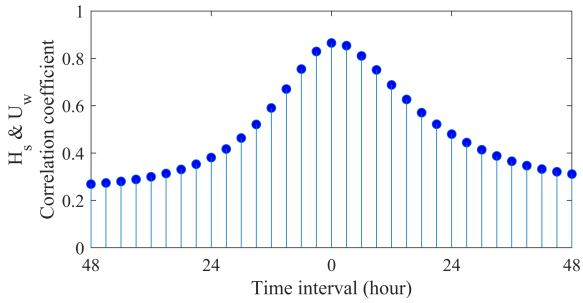

Figure A.6: Cross-correlation coefficient of H_s against U_w

A.4 Predictability

After checking correlations in time series, the amount of predictability in metocean data is measured according to the method proposed by Hull [215]. He defined a forecasting efficiency E in terms of the correlation coefficient ρ, showing the degree to which the past data can determine the future data. The E is expressed in Eq. (A.3) and illustrated in Figure A.7.

$$E = 1 - \sqrt{1 - \rho^2} \tag{A.3}$$

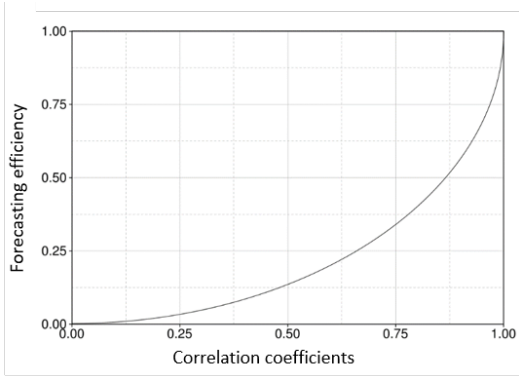

Figure A.7: Relation between the coefficient of correlation and forecasting efficiency [216]

For instance, with reference to Figures A.2 (a) and A.7, the probability of correct prediction using $H_s(t-1)$ to forecast $H_s(t)$ is about 65%. This

indicates that there is a certain short-term predictability in waves, using the most recent data of a wave variable to forecast its future value. By means of the same method, how well the future H_s can be forecasted from knowledge of U_w can be studied based on the results shown in Figure A.6. By calculation, it is found that when using $U_w(t)$ to forecast $H_s(t)$, the probability of correct prediction is about 56%. However, it must be emphasized that the forecast is still difficult if one wants to forecast environmental conditions for a long horizon, since the predictability would decrease significantly with increasing the time interval between data. For instance, when using $H_s(t-8)$ to forecast $H_s(t)$, the probability of correct prediction is only about 20%.

Appendix B

Forecasted and actual time series based on decomposition-ANFIS method

Forecasted time series of U_w, H_s and T_p during the testing period are presented in Figures B.1 to B.3, respectively. The actual and forecasted data are represented by black and red lines. In each figure, subfigures (a) and (b) depict the results that are based on the M-1 and M-1 slope models, and (c) depicts the results that are based on the M-N model.

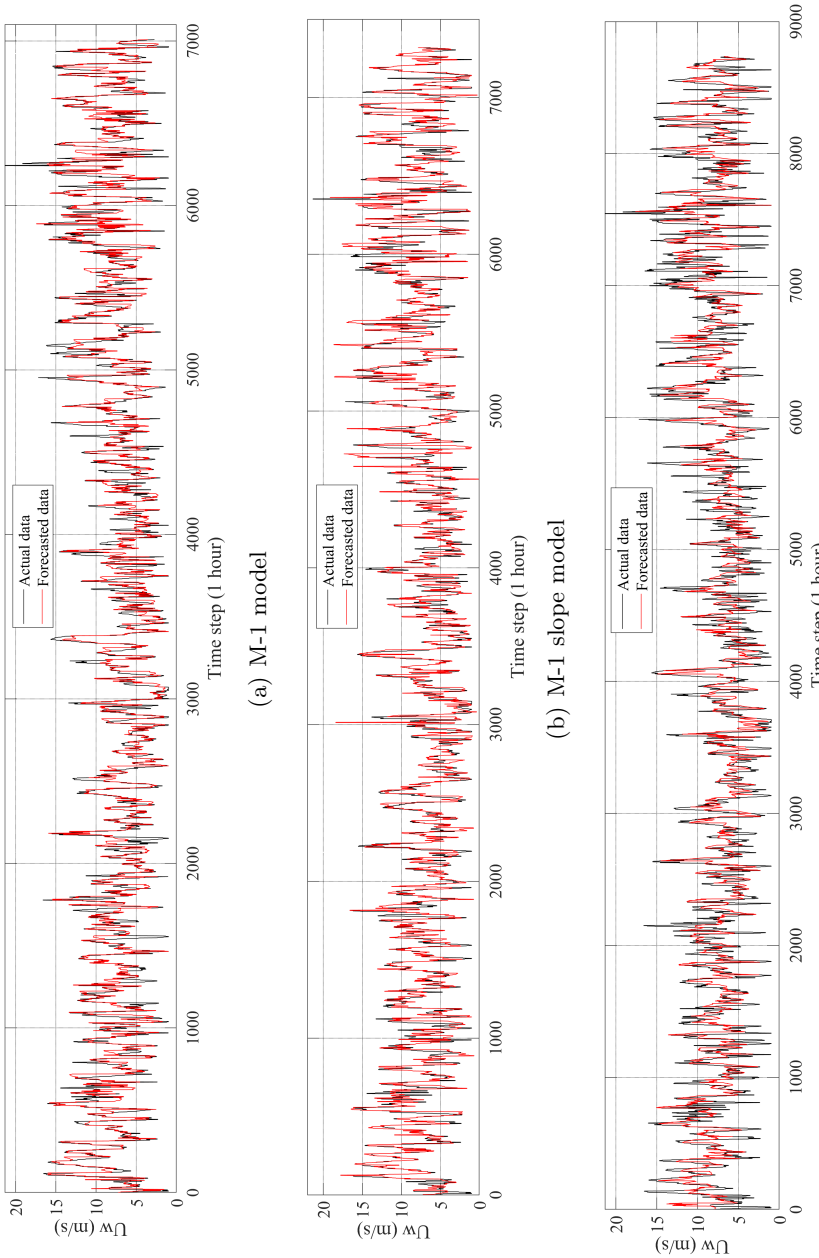

(a) M-1 model

(b) M-1 slope model

(c) M-N model

Figure B.1: Forecasted time series of U_w

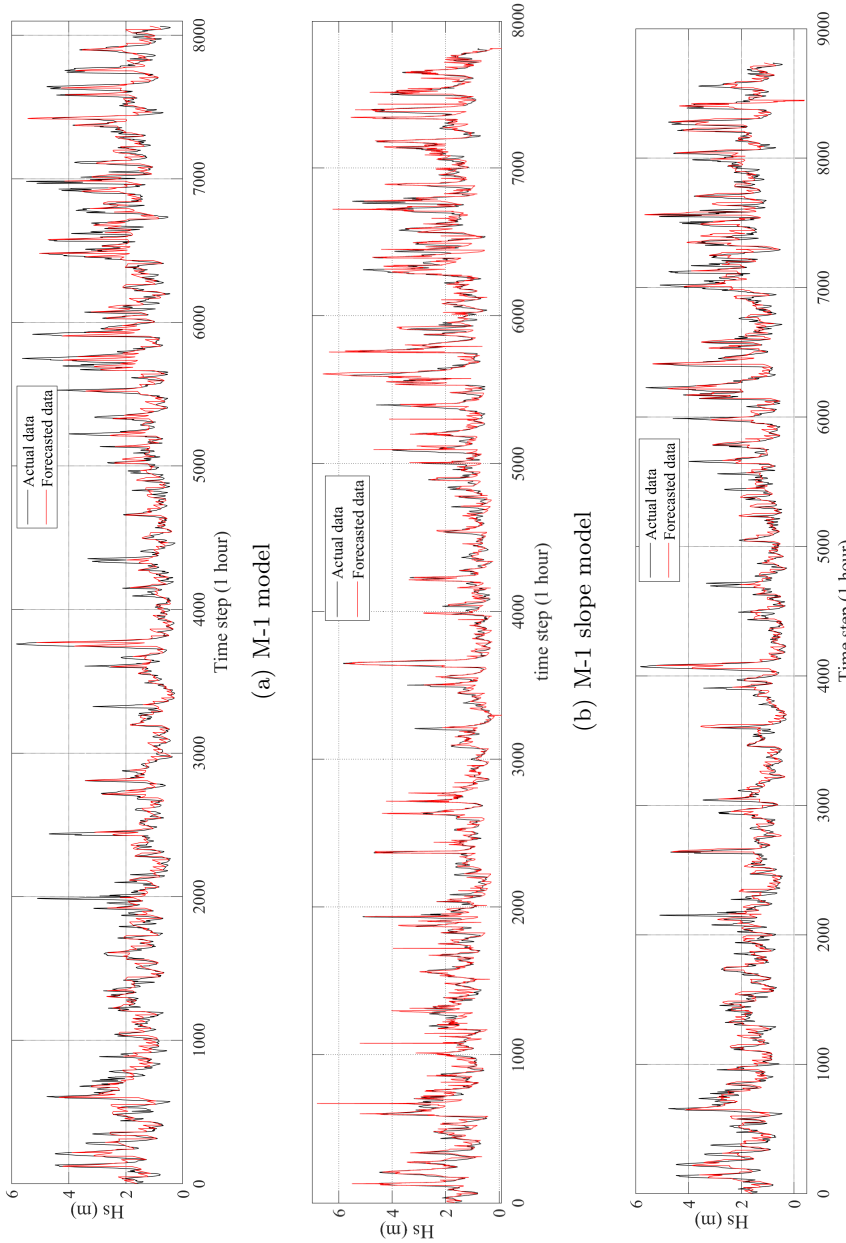

Figure B.2: Forecasted time series of H_s

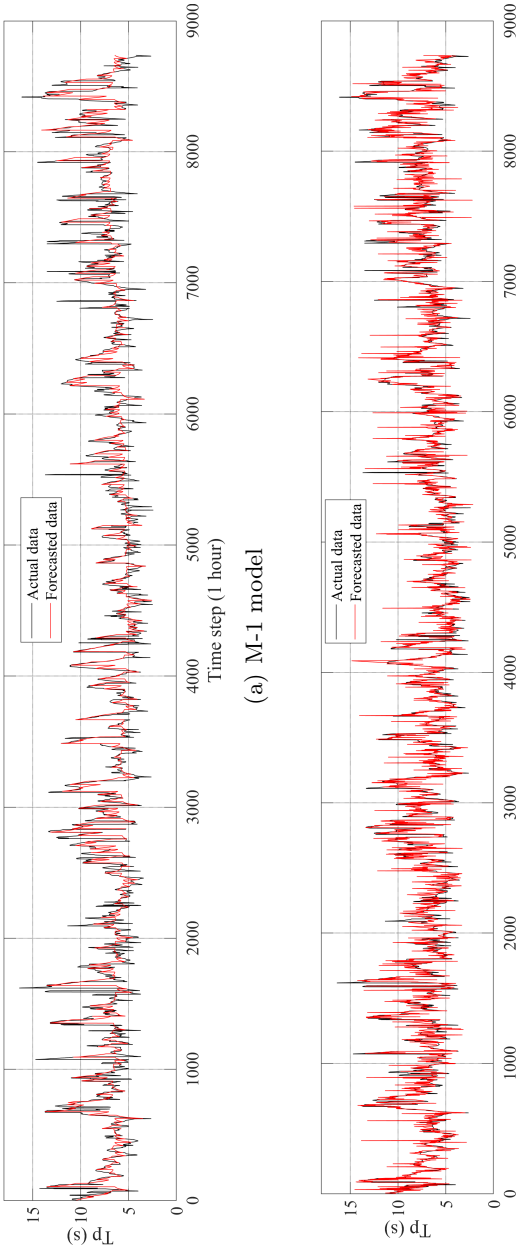

(a) M-1 model

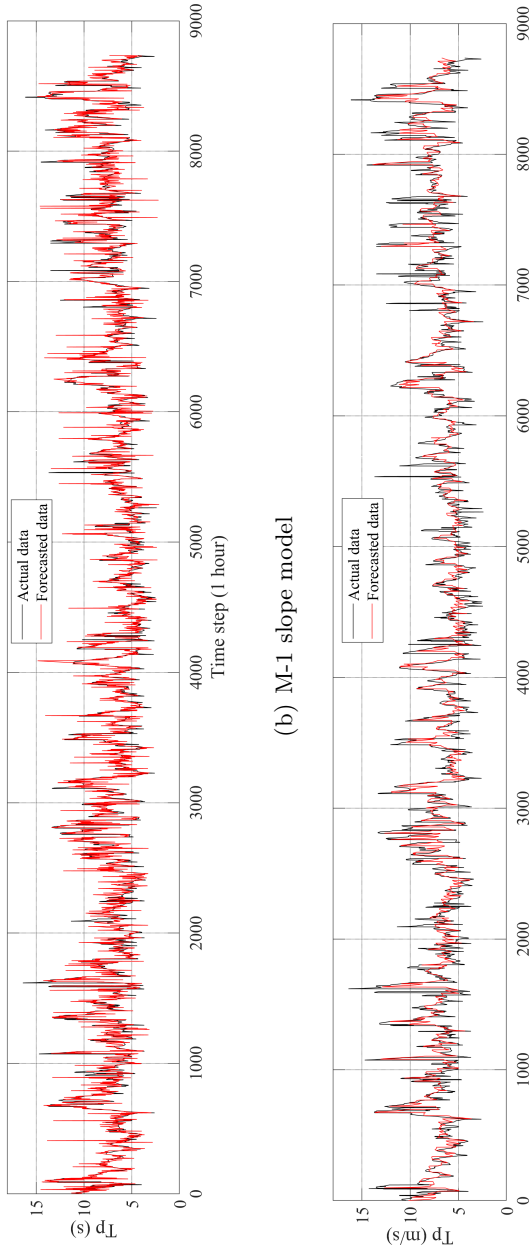

(b) M-1 slope model

(c) M-N model

Figure B.3: Forecasted time series of T_p

Appendix C

List of previous PhD theses at Dept. of Marine Tech.

Previous PhD theses published at the Department of Marine Technology (earlier: Faculty of Marine Technology) NORWEGIAN UNIVERSITY OF SCIENCE AND TECHNOLOGY

Report No.	Author	Title
	Kavlie, Dag	Optimization of Plane Elastic Grillages, 1967
	Hansen, Hans R.	Man-Machine Communication and Data-Storage Methods in Ship Structural Design, 1971
	Gisvold, Kaare M.	A Method for non-linear mixed -integer programming and its Application to Design Problems, 1971
	Lund, Sverre	Tanker Frame Optimalization by means of SUMT-Transformation and Behaviour Models, 1971
	Vinje, Tor	On Vibration of Spherical Shells Interacting with Fluid, 1972
	Lorentz, Jan D.	Tank Arrangement for Crude Oil Carriers in Accordance with the new Anti-Pollution Regulations, 1975
	Carlsen, Carl A.	Computer-Aided Design of Tanker Structures, 1975
	Larsen, Carl M.	Static and Dynamic Analysis of Offshore Pipelines during Installation, 1976
UR-79-01	Brigt Hatlestad, MK	The finite element method used in a fatigue evaluation of fixed offshore platforms. (Dr.Ing. Thesis)
UR-79-02	Erik Pettersen, MK	Analysis and design of cellular structures. (Dr.Ing. Thesis)
UR-79-03	Sverre Valsgård, MK	Finite difference and finite element methods applied to nonlinear analysis of plated structures. (Dr.Ing. Thesis)
UR-79-04	Nils T. Nordsve, MK	Finite element collapse analysis of structural members considering imperfections and stresses due to fabrication. (Dr.Ing. Thesis)
UR-79-05	Ivar J. Fylling, MK	Analysis of towline forces in ocean towing systems. (Dr.Ing. Thesis)
UR-80-06	Nils Sandsmark, MM	Analysis of Stationary and Transient Heat Conduction by the Use of the Finite Element Method. (Dr.Ing. Thesis)
UR-80-09	Sverre Haver, MK	Analysis of uncertainties related to the stochastic modeling of ocean waves. (Dr.Ing. Thesis)
UR-81-15	Odland, Jonas	On the Strength of welded Ring stiffened cylindrical Shells primarily subjected to axial Compression
UR-82-17	Engesvik, Knut	Analysis of Uncertainties in the fatigue Capacity of

		Welded Joints
UR-82-18	Rye, Henrik	Ocean wave groups
UR-83-30	Eide, Oddvar Inge	On Cumulative Fatigue Damage in Steel Welded Joints
UR-83-33	Mo, Olav	Stochastic Time Domain Analysis of Slender Offshore Structures
UR-83-34	Amdahl, Jørgen	Energy absorption in Ship-platform impacts
UR-84-37	Mørch, Morten	Motions and mooring forces of semi submersibles as determined by full-scale measurements and theoretical analysis
UR-84-38	Soares, C. Guedes	Probabilistic models for load effects in ship structures
UR-84-39	Aarsnes, Jan V.	Current forces on ships
UR-84-40	Czujko, Jerzy	Collapse Analysis of Plates subjected to Biaxial Compression and Lateral Load
UR-85-46	Alf G. Engseth, MK	Finite element collapse analysis of tubular steel offshore structures. (Dr.Ing. Thesis)
UR-86-47	Dengody Sheshappa, MP	A Computer Design Model for Optimizing Fishing Vessel Designs Based on Techno-Economic Analysis. (Dr.Ing. Thesis)
UR-86-48	Vidar Aanesland, MH	A Theoretical and Numerical Study of Ship Wave Resistance. (Dr.Ing. Thesis)
UR-86-49	Heinz-Joachim Wessel, MK	Fracture Mechanics Analysis of Crack Growth in Plate Girders. (Dr.Ing. Thesis)
UR-86-50	Jon Taby, MK	Ultimate and Post-ultimate Strength of Dented Tubular Members. (Dr.Ing. Thesis)
UR-86-51	Walter Lian, MH	A Numerical Study of Two-Dimensional Separated Flow Past Bluff Bodies at Moderate KC-Numbers. (Dr.Ing. Thesis)
UR-86-52	Bjørn Sortland, MH	Force Measurements in Oscillating Flow on Ship Sections and Circular Cylinders in a U-Tube Water Tank. (Dr.Ing. Thesis)
UR-86-53	Kurt Strand, MM	A System Dynamic Approach to One-dimensional Fluid Flow. (Dr.Ing. Thesis)
UR-86-54	Arne Edvin Løken, MH	Three Dimensional Second Order Hydrodynamic Effects on Ocean Structures in Waves. (Dr.Ing. Thesis)
UR-86-55	Sigurd Falch, MH	A Numerical Study of Slamming of Two-Dimensional Bodies. (Dr.Ing. Thesis)
UR-87-56	Arne Braathen, MH	Application of a Vortex Tracking Method to the Prediction of Roll Damping of a Two-Dimension Floating Body. (Dr.Ing. Thesis)

UR-87-57	Bernt Leira, MK	Gaussian Vector Processes for Reliability Analysis involving Wave-Induced Load Effects. (Dr.Ing. Thesis)
UR-87-58	Magnus Småvik, MM	Thermal Load and Process Characteristics in a Two-Stroke Diesel Engine with Thermal Barriers (in Norwegian). (Dr.Ing. Thesis)
MTA-88-59	Bernt Arild Bremdal, MP	An Investigation of Marine Installation Processes – A Knowledge - Based Planning Approach. (Dr.Ing. Thesis)
MTA-88-60	Xu Jun, MK	Non-linear Dynamic Analysis of Space-framed Offshore Structures. (Dr.Ing. Thesis)
MTA-89-61	Gang Miao, MH	Hydrodynamic Forces and Dynamic Responses of Circular Cylinders in Wave Zones. (Dr.Ing. Thesis)
MTA-89-62	Martin Greenhow, MH	Linear and Non-Linear Studies of Waves and Floating Bodies. Part I and Part II. (Dr.Techn. Thesis)
MTA-89-63	Chang Li, MH	Force Coefficients of Spheres and Cubes in Oscillatory Flow with and without Current. (Dr.Ing. Thesis
MTA-89-64	Hu Ying, MP	A Study of Marketing and Design in Development of Marine Transport Systems. (Dr.Ing. Thesis)
MTA-89-65	Arild Jæger, MH	Seakeeping, Dynamic Stability and Performance of a Wedge Shaped Planing Hull. (Dr.Ing. Thesis)
MTA-89-66	Chan Siu Hung, MM	The dynamic characteristics of tilting-pad bearings
MTA-89-67	Kim Wikstrøm, MP	Analysis av projekteringen for ett offshore projekt. (Licenciat-avhandling)
MTA-89-68	Jiao Guoyang, MK	Reliability Analysis of Crack Growth under Random Loading, considering Model Updating. (Dr.Ing. Thesis)
MTA-89-69	Arnt Olufsen, MK	Uncertainty and Reliability Analysis of Fixed Offshore Structures. (Dr.Ing. Thesis)
MTA-89-70	Wu Yu-Lin, MR	System Reliability Analyses of Offshore Structures using improved Truss and Beam Models. (Dr.Ing. Thesis)
MTA-90-71	Jan Roger Hoff, MH	Three-dimensional Green function of a vessel with forward speed in waves. (Dr.Ing. Thesis)
MTA-90-72	Rong Zhao, MH	Slow-Drift Motions of a Moored Two-Dimensional Body in Irregular Waves. (Dr.Ing. Thesis)
MTA-90-73	Atle Minsaas, MP	Economical Risk Analysis. (Dr.Ing. Thesis)
MTA-90-74	Knut-Aril Farnes, MK	Long-term Statistics of Response in Non-linear Marine Structures. (Dr.Ing. Thesis)
MTA-90-75	Torbjørn Sotberg, MK	Application of Reliability Methods for Safety Assessment of Submarine Pipelines. (Dr.Ing.

		Thesis)
MTA-90-76	Zeuthen, Steffen, MP	SEAMAID. A computational model of the design process in a constraint-based logic programming environment. An example from the offshore domain. (Dr.Ing. Thesis)
MTA-91-77	Haagensen, Sven, MM	Fuel Dependant Cyclic Variability in a Spark Ignition Engine - An Optical Approach. (Dr.Ing. Thesis)
MTA-91-78	Løland, Geir, MH	Current forces on and flow through fish farms. (Dr.Ing. Thesis)
MTA-91-79	Hoen, Christopher, MK	System Identification of Structures Excited by Stochastic Load Processes. (Dr.Ing. Thesis)
MTA-91-80	Haugen, Stein, MK	Probabilistic Evaluation of Frequency of Collision between Ships and Offshore Platforms. (Dr.Ing. Thesis)
MTA-91-81	Sødahl, Nils, MK	Methods for Design and Analysis of Flexible Risers. (Dr.Ing. Thesis)
MTA-91-82	Ormberg, Harald, MK	Non-linear Response Analysis of Floating Fish Farm Systems. (Dr.Ing. Thesis)
MTA-91-83	Marley, Mark J., MK	Time Variant Reliability under Fatigue Degradation. (Dr.Ing. Thesis)
MTA-91-84	Krokstad, Jørgen R., MH	Second-order Loads in Multidirectional Seas. (Dr.Ing. Thesis)
MTA-91-85	Molteberg, Gunnar A., MM	The Application of System Identification Techniques to Performance Monitoring of Four Stroke Turbocharged Diesel Engines. (Dr.Ing. Thesis)
MTA-92-86	Mørch, Hans Jørgen Bjelke, MH	Aspects of Hydrofoil Design: with Emphasis on Hydrofoil Interaction in Calm Water. (Dr.Ing. Thesis)
MTA-92-87	Chan Siu Hung, MM	Nonlinear Analysis of Rotordynamic Instabilities in Highspeed Turbomachinery. (Dr.Ing. Thesis)
MTA-92-88	Bessason, Bjarni, MK	Assessment of Earthquake Loading and Response of Seismically Isolated Bridges. (Dr.Ing. Thesis)
MTA-92-89	Langli, Geir, MP	Improving Operational Safety through exploitation of Design Knowledge - an investigation of offshore platform safety. (Dr.Ing. Thesis)
MTA-92-90	Sævik, Svein, MK	On Stresses and Fatigue in Flexible Pipes. (Dr.Ing. Thesis)
MTA-92-91	Ask, Tor Ø., MM	Ignition and Flame Growth in Lean Gas-Air Mixtures. An Experimental Study with a Schlieren System. (Dr.Ing. Thesis)
MTA-86-92	Hessen, Gunnar, MK	Fracture Mechanics Analysis of Stiffened Tubular Members. (Dr.Ing. Thesis)

MTA-93-93	Steinebach, Christian, MM	Knowledge Based Systems for Diagnosis of Rotating Machinery. (Dr.Ing. Thesis)
MTA-93-94	Dalane, Jan Inge, MK	System Reliability in Design and Maintenance of Fixed Offshore Structures. (Dr.Ing. Thesis)
MTA-93-95	Steen, Sverre, MH	Cobblestone Effect on SES. (Dr.Ing. Thesis)
MTA-93-96	Karunakaran, Daniel, MK	Nonlinear Dynamic Response and Reliability Analysis of Drag-dominated Offshore Platforms. (Dr.Ing. Thesis)
MTA-93-97	Hagen, Arnulf, MP	The Framework of a Design Process Language. (Dr.Ing. Thesis)
MTA-93-98	Nordrik, Rune, MM	Investigation of Spark Ignition and Autoignition in Methane and Air Using Computational Fluid Dynamics and Chemical Reaction Kinetics. A Numerical Study of Ignition Processes in Internal Combustion Engines. (Dr.Ing. Thesis)
MTA-94-99	Passano, Elizabeth, MK	Efficient Analysis of Nonlinear Slender Marine Structures. (Dr.Ing. Thesis)
MTA-94-100	Kvålsvold, Jan, MH	Hydroelastic Modelling of Wetdeck Slamming on Multihull Vessels. (Dr.Ing. Thesis)
MTA-94-102	Bech, Sidsel M., MK	Experimental and Numerical Determination of Stiffness and Strength of GRP/PVC Sandwich Structures. (Dr.Ing. Thesis)
MTA-95-103	Paulsen, Hallvard, MM	A Study of Transient Jet and Spray using a Schlieren Method and Digital Image Processing. (Dr.Ing. Thesis)
MTA-95-104	Hovde, Geir Olav, MK	Fatigue and Overload Reliability of Offshore Structural Systems, Considering the Effect of Inspection and Repair. (Dr.Ing. Thesis)
MTA-95-105	Wang, Xiaozhi, MK	Reliability Analysis of Production Ships with Emphasis on Load Combination and Ultimate Strength. (Dr.Ing. Thesis)
MTA-95-106	Ulstein, Tore, MH	Nonlinear Effects of a Flexible Stern Seal Bag on Cobblestone Oscillations of an SES. (Dr.Ing. Thesis)
MTA-95-107	Solaas, Frøydis, MH	Analytical and Numerical Studies of Sloshing in Tanks. (Dr.Ing. Thesis)
MTA-95-108	Hellan, Øyvind, MK	Nonlinear Pushover and Cyclic Analyses in Ultimate Limit State Design and Reassessment of Tubular Steel Offshore Structures. (Dr.Ing. Thesis)
MTA-95-109	Hermundstad, Ole A., MK	Theoretical and Experimental Hydroelastic Analysis of High Speed Vessels. (Dr.Ing. Thesis)
MTA-96-110	Bratland, Anne K., MH	Wave-Current Interaction Effects on Large-Volume Bodies in Water of Finite Depth. (Dr.Ing. Thesis)
MTA-96-111	Herfjord, Kjell, MH	A Study of Two-dimensional Separated Flow by a Combination of the Finite Element Method and

		Navier-Stokes Equations. (Dr.Ing. Thesis)
MTA-96-112	Æsøy, Vilmar, MM	Hot Surface Assisted Compression Ignition in a Direct Injection Natural Gas Engine. (Dr.Ing. Thesis)
MTA-96-113	Eknes, Monika L., MK	Escalation Scenarios Initiated by Gas Explosions on Offshore Installations. (Dr.Ing. Thesis)
MTA-96-114	Erikstad, Stein O., MP	A Decision Support Model for Preliminary Ship Design. (Dr.Ing. Thesis)
MTA-96-115	Pedersen, Egil, MH	A Nautical Study of Towed Marine Seismic Streamer Cable Configurations. (Dr.Ing. Thesis)
MTA-97-116	Moksnes, Paul O., MM	Modelling Two-Phase Thermo-Fluid Systems Using Bond Graphs. (Dr.Ing. Thesis)
MTA-97-117	Halse, Karl H., MK	On Vortex Shedding and Prediction of Vortex-Induced Vibrations of Circular Cylinders. (Dr.Ing. Thesis)
MTA-97-118	Igland, Ragnar T., MK	Reliability Analysis of Pipelines during Laying, considering Ultimate Strength under Combined Loads. (Dr.Ing. Thesis)
MTA-97-119	Pedersen, Hans-P., MP	Levendefiskteknologi for fiskefartøy. (Dr.Ing. Thesis)
MTA-98-120	Vikestad, Kyrre, MK	Multi-Frequency Response of a Cylinder Subjected to Vortex Shedding and Support Motions. (Dr.Ing. Thesis)
MTA-98-121	Azadi, Mohammad R. E., MK	Analysis of Static and Dynamic Pile-Soil-Jacket Behaviour. (Dr.Ing. Thesis)
MTA-98-122	Ulltang, Terje, MP	A Communication Model for Product Information. (Dr.Ing. Thesis)
MTA-98-123	Torbergsen, Erik, MM	Impeller/Diffuser Interaction Forces in Centrifugal Pumps. (Dr.Ing. Thesis)
MTA-98-124	Hansen, Edmond, MH	A Discrete Element Model to Study Marginal Ice Zone Dynamics and the Behaviour of Vessels Moored in Broken Ice. (Dr.Ing. Thesis)
MTA-98-125	Videiro, Paulo M., MK	Reliability Based Design of Marine Structures. (Dr.Ing. Thesis)
MTA-99-126	Mainçon, Philippe, MK	Fatigue Reliability of Long Welds Application to Titanium Risers. (Dr.Ing. Thesis)
MTA-99-127	Haugen, Elin M., MH	Hydroelastic Analysis of Slamming on Stiffened Plates with Application to Catamaran Wetdecks. (Dr.Ing. Thesis)
MTA-99-128	Langhelle, Nina K., MK	Experimental Validation and Calibration of Nonlinear Finite Element Models for Use in Design of Aluminium Structures Exposed to Fire. (Dr.Ing. Thesis)
MTA-99-	Berstad, Are J., MK	Calculation of Fatigue Damage in Ship Structures.

129		(Dr.Ing. Thesis)
MTA-99-130	Andersen, Trond M., MM	Short Term Maintenance Planning. (Dr.Ing. Thesis)
MTA-99-131	Tveiten, Bård Wathne, MK	Fatigue Assessment of Welded Aluminium Ship Details. (Dr.Ing. Thesis)
MTA-99-132	Søreide, Fredrik, MP	Applications of underwater technology in deep water archaeology. Principles and practice. (Dr.Ing. Thesis)
MTA-99-133	Tønnessen, Rune, MH	A Finite Element Method Applied to Unsteady Viscous Flow Around 2D Blunt Bodies With Sharp Corners. (Dr.Ing. Thesis)
MTA-99-134	Elvekrok, Dag R., MP	Engineering Integration in Field Development Projects in the Norwegian Oil and Gas Industry. The Supplier Management of Norne. (Dr.Ing. Thesis)
MTA-99-135	Fagerholt, Kjetil, MP	Optimeringsbaserte Metoder for Ruteplanlegging innen skipsfart. (Dr.Ing. Thesis)
MTA-99-136	Bysveen, Marie, MM	Visualization in Two Directions on a Dynamic Combustion Rig for Studies of Fuel Quality. (Dr.Ing. Thesis)
MTA-2000-137	Storteig, Eskild, MM	Dynamic characteristics and leakage performance of liquid annular seals in centrifugal pumps. (Dr.Ing. Thesis)
MTA-2000-138	Sagli, Gro, MK	Model uncertainty and simplified estimates of long term extremes of hull girder loads in ships. (Dr.Ing. Thesis)
MTA-2000-139	Tronstad, Harald, MK	Nonlinear analysis and design of cable net structures like fishing gear based on the finite element method. (Dr.Ing. Thesis)
MTA-2000-140	Kroneberg, André, MP	Innovation in shipping by using scenarios. (Dr.Ing. Thesis)
MTA-2000-141	Haslum, Herbjørn Alf, MH	Simplified methods applied to nonlinear motion of spar platforms. (Dr.Ing. Thesis)
MTA-2001-142	Samdal, Ole Johan, MM	Modelling of Degradation Mechanisms and Stressor Interaction on Static Mechanical Equipment Residual Lifetime. (Dr.Ing. Thesis)
MTA-2001-143	Baarholm, Rolf Jarle, MH	Theoretical and experimental studies of wave impact underneath decks of offshore platforms. (Dr.Ing. Thesis)
MTA-2001-144	Wang, Lihua, MK	Probabilistic Analysis of Nonlinear Wave-induced Loads on Ships. (Dr.Ing. Thesis)
MTA-2001-145	Kristensen, Odd H. Holt, MK	Ultimate Capacity of Aluminium Plates under Multiple Loads, Considering HAZ Properties. (Dr.Ing. Thesis)
MTA-2001-146	Greco, Marilena, MH	A Two-Dimensional Study of Green-Water

		Loading. (Dr.Ing. Thesis)
MTA-2001-147	Heggelund, Svein E., MK	Calculation of Global Design Loads and Load Effects in Large High Speed Catamarans. (Dr.Ing. Thesis)
MTA-2001-148	Babalola, Olusegun T., MK	Fatigue Strength of Titanium Risers – Defect Sensitivity. (Dr.Ing. Thesis)
MTA-2001-149	Mohammed, Abuu K., MK	Nonlinear Shell Finite Elements for Ultimate Strength and Collapse Analysis of Ship Structures. (Dr.Ing. Thesis)
MTA-2002-150	Holmedal, Lars E., MH	Wave-current interactions in the vicinity of the sea bed. (Dr.Ing. Thesis)
MTA-2002-151	Rognebakke, Olav F., MH	Sloshing in rectangular tanks and interaction with ship motions. (Dr.Ing. Thesis)
MTA-2002-152	Lader, Pål Furset, MH	Geometry and Kinematics of Breaking Waves. (Dr.Ing. Thesis)
MTA-2002-153	Yang, Qinzheng, MH	Wash and wave resistance of ships in finite water depth. (Dr.Ing. Thesis)
MTA-2002-154	Melhus, Øyvin, MM	Utilization of VOC in Diesel Engines. Ignition and combustion of VOC released by crude oil tankers. (Dr.Ing. Thesis)
MTA-2002-155	Ronæss, Marit, MH	Wave Induced Motions of Two Ships Advancing on Parallel Course. (Dr.Ing. Thesis)
MTA-2002-156	Økland, Ole D., MK	Numerical and experimental investigation of whipping in twin hull vessels exposed to severe wet deck slamming. (Dr.Ing. Thesis)
MTA-2002-157	Ge, Chunhua, MK	Global Hydroelastic Response of Catamarans due to Wet Deck Slamming. (Dr.Ing. Thesis)
MTA-2002-158	Byklum, Eirik, MK	Nonlinear Shell Finite Elements for Ultimate Strength and Collapse Analysis of Ship Structures. (Dr.Ing. Thesis)
IMT-2003-1	Chen, Haibo, MK	Probabilistic Evaluation of FPSO-Tanker Collision in Tandem Offloading Operation. (Dr.Ing. Thesis)
IMT-2003-2	Skaugset, Kjetil Bjørn, MK	On the Suppression of Vortex Induced Vibrations of Circular Cylinders by Radial Water Jets. (Dr.Ing. Thesis)
IMT-2003-3	Chezhian, Muthu	Three-Dimensional Analysis of Slamming. (Dr.Ing. Thesis)
IMT-2003-4	Buhaug, Øyvind	Deposit Formation on Cylinder Liner Surfaces in Medium Speed Engines. (Dr.Ing. Thesis)
IMT-2003-5	Tregde, Vidar	Aspects of Ship Design: Optimization of Aft Hull with Inverse Geometry Design. (Dr.Ing. Thesis)
IMT-	Wist, Hanne Therese	Statistical Properties of Successive Ocean Wave

2003-6		Parameters. (Dr.Ing. Thesis)
IMT-2004-7	Ransau, Samuel	Numerical Methods for Flows with Evolving Interfaces. (Dr.Ing. Thesis)
IMT-2004-8	Soma, Torkel	Blue-Chip or Sub-Standard. A data interrogation approach of identity safety characteristics of shipping organization. (Dr.Ing. Thesis)
IMT-2004-9	Ersdal, Svein	An experimental study of hydrodynamic forces on cylinders and cables in near axial flow. (Dr.Ing. Thesis)
IMT-2005-10	Brodtkorb, Per Andreas	The Probability of Occurrence of Dangerous Wave Situations at Sea. (Dr.Ing. Thesis)
IMT-2005-11	Yttervik, Rune	Ocean current variability in relation to offshore engineering. (Dr.Ing. Thesis)
IMT-2005-12	Fredheim, Arne	Current Forces on Net-Structures. (Dr.Ing. Thesis)
IMT-2005-13	Heggernes, Kjetil	Flow around marine structures. (Dr.Ing. Thesis
IMT-2005-14	Fouques, Sebastien	Lagrangian Modelling of Ocean Surface Waves and Synthetic Aperture Radar Wave Measurements. (Dr.Ing. Thesis)
IMT-2006-15	Holm, Håvard	Numerical calculation of viscous free surface flow around marine structures. (Dr.Ing. Thesis)
IMT-2006-16	Bjørheim, Lars G.	Failure Assessment of Long Through Thickness Fatigue Cracks in Ship Hulls. (Dr.Ing. Thesis)
IMT-2006-17	Hansson, Lisbeth	Safety Management for Prevention of Occupational Accidents. (Dr.Ing. Thesis)
IMT-2006-18	Zhu, Xinying	Application of the CIP Method to Strongly Nonlinear Wave-Body Interaction Problems. (Dr.Ing. Thesis)
IMT-2006-19	Reite, Karl Johan	Modelling and Control of Trawl Systems. (Dr.Ing. Thesis)
IMT-2006-20	Smogeli, Øyvind Notland	Control of Marine Propellers. From Normal to Extreme Conditions. (Dr.Ing. Thesis)
IMT-2007-21	Storhaug, Gaute	Experimental Investigation of Wave Induced Vibrations and Their Effect on the Fatigue Loading of Ships. (Dr.Ing. Thesis)
IMT-2007-22	Sun, Hui	A Boundary Element Method Applied to Strongly Nonlinear Wave-Body Interaction Problems. (PhD Thesis, CeSOS)
IMT-2007-23	Rustad, Anne Marthine	Modelling and Control of Top Tensioned Risers. (PhD Thesis, CeSOS)
IMT-2007-24	Johansen, Vegar	Modelling flexible slender system for real-time simulations and control applications
IMT-2007-25	Wroldsen, Anders Sunde	Modelling and control of tensegrity structures.

		(PhD Thesis, CeSOS)
IMT-2007-26	Aronsen, Kristoffer Høye	An experimental investigation of in-line and combined inline and cross flow vortex induced vibrations. (Dr. avhandling, IMT)
IMT-2007-27	Gao, Zhen	Stochastic Response Analysis of Mooring Systems with Emphasis on Frequency-domain Analysis of Fatigue due to Wide-band Response Processes (PhD Thesis, CeSOS)
IMT-2007-28	Thorstensen, Tom Anders	Lifetime Profit Modelling of Ageing Systems Utilizing Information about Technical Condition. (Dr.ing. thesis, IMT)
IMT-2008-29	Refsnes, Jon Erling Gorset	Nonlinear Model-Based Control of Slender Body AUVs (PhD Thesis, IMT)
IMT-2008-30	Berntsen, Per Ivar B.	Structural Reliability Based Position Mooring. (PhD-Thesis, IMT)
IMT-2008-31	Ye, Naiquan	Fatigue Assessment of Aluminium Welded Box-stiffener Joints in Ships (Dr.ing. thesis, IMT)
IMT-2008-32	Radan, Damir	Integrated Control of Marine Electrical Power Systems. (PhD-Thesis, IMT)
IMT-2008-33	Thomassen, Paul	Methods for Dynamic Response Analysis and Fatigue Life Estimation of Floating Fish Cages. (Dr.ing. thesis, IMT)
IMT-2008-34	Pákozdi, Csaba	A Smoothed Particle Hydrodynamics Study of Two-dimensional Nonlinear Sloshing in Rectangular Tanks. (Dr.ing.thesis, IMT/ CeSOS)
IMT-2007-35	Grytøyr, Guttorm	A Higher-Order Boundary Element Method and Applications to Marine Hydrodynamics. (Dr.ing.thesis, IMT)
IMT-2008-36	Drummen, Ingo	Experimental and Numerical Investigation of Nonlinear Wave-Induced Load Effects in Containerships considering Hydroelasticity. (PhD thesis, CeSOS)
IMT-2008-37	Skejic, Renato	Maneuvering and Seakeeping of a Singel Ship and of Two Ships in Interaction. (PhD-Thesis, CeSOS)
IMT-2008-38	Harlem, Alf	An Age-Based Replacement Model for Repairable Systems with Attention to High-Speed Marine Diesel Engines. (PhD-Thesis, IMT)
IMT-2008-39	Alsos, Hagbart S.	Ship Grounding. Analysis of Ductile Fracture, Bottom Damage and Hull Girder Response. (PhD-thesis, IMT)
IMT-2008-40	Graczyk, Mateusz	Experimental Investigation of Sloshing Loading and Load Effects in Membrane LNG Tanks Subjected to Random Excitation. (PhD-thesis, CeSOS)
IMT-2008-41	Taghipour, Reza	Efficient Prediction of Dynamic Response for Flexible amd Multi-body Marine Structures. (PhD-

		thesis, CeSOS)
IMT-2008-42	Ruth, Eivind	Propulsion control and thrust allocation on marine vessels. (PhD thesis, CeSOS)
IMT-2008-43	Nystad, Bent Helge	Technical Condition Indexes and Remaining Useful Life of Aggregated Systems. PhD thesis, IMT
IMT-2008-44	Soni, Prashant Kumar	Hydrodynamic Coefficients for Vortex Induced Vibrations of Flexible Beams, PhD thesis, CeSOS
IMT-2009-45	Amlashi, Hadi K.K.	Ultimate Strength and Reliability-based Design of Ship Hulls with Emphasis on Combined Global and Local Loads. PhD Thesis, IMT
IMT-2009-46	Pedersen, Tom Arne	Bond Graph Modelling of Marine Power Systems. PhD Thesis, IMT
IMT-2009-47	Kristiansen, Trygve	Two-Dimensional Numerical and Experimental Studies of Piston-Mode Resonance. PhD-Thesis, CeSOS
IMT-2009-48	Ong, Muk Chen	Applications of a Standard High Reynolds Number Model and a Stochastic Scour Prediction Model for Marine Structures. PhD-thesis, IMT
IMT-2009-49	Hong, Lin	Simplified Analysis and Design of Ships subjected to Collision and Grounding. PhD-thesis, IMT
IMT-2009-50	Koushan, Kamran	Vortex Induced Vibrations of Free Span Pipelines, PhD thesis, IMT
IMT-2009-51	Korsvik, Jarl Eirik	Heuristic Methods for Ship Routing and Scheduling. PhD-thesis, IMT
IMT-2009-52	Lee, Jihoon	Experimental Investigation and Numerical in Analyzing the Ocean Current Displacement of Longlines. Ph.d.-Thesis, IMT.
IMT-2009-53	Vestbøstad, Tone Gran	A Numerical Study of Wave-in-Deck Impact usin a Two-Dimensional Constrained Interpolation Profile Method, Ph.d.thesis, CeSOS.
IMT-2009-54	Bruun, Kristine	Bond Graph Modelling of Fuel Cells for Marine Power Plants. Ph.d.-thesis, IMT
IMT 2009-55	Holstad, Anders	Numerical Investigation of Turbulence in a Sekwed Three-Dimensional Channel Flow, Ph.d.-thesis, IMT.
IMT 2009-56	Ayala-Uraga, Efren	Reliability-Based Assessment of Deteriorating Ship-shaped Offshore Structures, Ph.d.-thesis, IMT
IMT 2009-57	Kong, Xiangjun	A Numerical Study of a Damaged Ship in Beam Sea Waves. Ph.d.-thesis, IMT/CeSOS.
IMT 2010-58	Kristiansen, David	Wave Induced Effects on Floaters of Aquaculture Plants, Ph.d.-thesis, CeSOS.

IMT 2010-59	Ludvigsen, Martin	An ROV-Toolbox for Optical and Acoustic Scientific Seabed Investigation. Ph.d.-thesis IMT.
IMT 2010-60	Hals, Jørgen	Modelling and Phase Control of Wave-Energy Converters. Ph.d.thesis, CeSOS.
IMT 2010- 61	Shu, Zhi	Uncertainty Assessment of Wave Loads and Ultimate Strength of Tankers and Bulk Carriers in a Reliability Framework. Ph.d. Thesis, IMT/ CeSOS
IMT 2010-62	Shao, Yanlin	Numerical Potential-Flow Studies on Weakly-Nonlinear Wave-Body Interactions with/without Small Forward Speed, Ph.d.thesis,CeSOS.
IMT 2010-63	Califano, Andrea	Dynamic Loads on Marine Propellers due to Intermittent Ventilation. Ph.d.thesis, IMT.
IMT 2010-64	El Khoury, George	Numerical Simulations of Massively Separated Turbulent Flows, Ph.d.-thesis, IMT
IMT 2010-65	Seim, Knut Sponheim	Mixing Process in Dense Overflows with Emphasis on the Faroe Bank Channel Overflow. Ph.d.thesis, IMT
IMT 2010-66	Jia, Huirong	Structural Analysis of Intect and Damaged Ships in a Collission Risk Analysis Perspective. Ph.d.thesis CeSoS.
IMT 2010-67	Jiao, Linlin	Wave-Induced Effects on a Pontoon-type Very Large Floating Structures (VLFS). Ph.D.-thesis, CeSOS.
IMT 2010-68	Abrahamsen, Bjørn Christian	Sloshing Induced Tank Roof with Entrapped Air Pocket. Ph.d.thesis, CeSOS.
IMT 2011-69	Karimirad, Madjid	Stochastic Dynamic Response Analysis of Spar-Type Wind Turbines with Catenary or Taut Mooring Systems. Ph.d.-thesis, CeSOS.
IMT - 2011-70	Erlend Meland	Condition Monitoring of Safety Critical Valves. Ph.d.-thesis, IMT.
IMT – 2011-71	Yang, Limin	Stochastic Dynamic System Analysis of Wave Energy Converter with Hydraulic Power Take-Off, with Particular Reference to Wear Damage Analysis, Ph.d. Thesis, CeSOS.
IMT – 2011-72	Visscher, Jan	Application of Particla Image Velocimetry on Turbulent Marine Flows, Ph.d.Thesis, IMT.
IMT – 2011-73	Su, Biao	Numerical Predictions of Global and Local Ice Loads on Ships. Ph.d.Thesis, CeSOS.
IMT – 2011-74	Liu, Zhenhui	Analytical and Numerical Analysis of Iceberg Collision with Ship Structures. Ph.d.Thesis, IMT.
IMT – 2011-75	Aarsæther, Karl Gunnar	Modeling and Analysis of Ship Traffic by Observation and Numerical Simulation. Ph.d.Thesis, IMT.

Imt – 2011-76	Wu, Jie	Hydrodynamic Force Identification from Stochastic Vortex Induced Vibration Experiments with Slender Beams. Ph.d.Thesis, IMT.
Imt – 2011-77	Amini, Hamid	Azimuth Propulsors in Off-design Conditions. Ph.d.Thesis, IMT.
IMT – 2011-78	Nguyen, Tan-Hoi	Toward a System of Real-Time Prediction and Monitoring of Bottom Damage Conditions During Ship Grounding. Ph.d.thesis, IMT.
IMT- 2011-79	Tavakoli, Mohammad T.	Assessment of Oil Spill in Ship Collision and Grounding, Ph.d.thesis, IMT.
IMT- 2011-80	Guo, Bingjie	Numerical and Experimental Investigation of Added Resistance in Waves. Ph.d.Thesis, IMT.
IMT- 2011-81	Chen, Qiaofeng	Ultimate Strength of Aluminium Panels, considering HAZ Effects, IMT
IMT- 2012-82	Kota, Ravikiran S.	Wave Loads on Decks of Offshore Structures in Random Seas, CeSOS.
IMT- 2012-83	Sten, Ronny	Dynamic Simulation of Deep Water Drilling Risers with Heave Compensating System, IMT.
IMT- 2012-84	Berle, Øyvind	Risk and resilience in global maritime supply chains, IMT.
IMT- 2012-85	Fang, Shaoji	Fault Tolerant Position Mooring Control Based on Structural Reliability, CeSOS.
IMT- 2012-86	You, Jikun	Numerical studies on wave forces and moored ship motions in intermediate and shallow water, CeSOS.
IMT- 2012-87	Xiang ,Xu	Maneuvering of two interacting ships in waves, CeSOS
IMT- 2012-88	Dong, Wenbin	Time-domain fatigue response and reliability analysis of offshore wind turbines with emphasis on welded tubular joints and gear components, CeSOS
IMT- 2012-89	Zhu, Suji	Investigation of Wave-Induced Nonlinear Load Effects in Open Ships considering Hull Girder Vibrations in Bending and Torsion, CeSOS
IMT- 2012-90	Zhou, Li	Numerical and Experimental Investigation of Station-keeping in Level Ice, CeSOS
IMT- 2012-91	Ushakov, Sergey	Particulate matter emission characteristics from diesel enignes operating on conventional and alternative marine fuels, IMT
IMT- 2013-1	Yin, Decao	Experimental and Numerical Analysis of Combined In-line and Cross-flow Vortex Induced Vibrations, CeSOS

IMT-2013-2	Kurniawan, Adi	Modelling and geometry optimisation of wave energy converters, CeSOS
IMT-2013-3	Al Ryati, Nabil	Technical condition indexes doe auxiliary marine diesel engines, IMT
IMT-2013-4	Firoozkoohi, Reza	Experimental, numerical and analytical investigation of the effect of screens on sloshing, CeSOS
IMT-2013-5	Ommani, Babak	Potential-Flow Predictions of a Semi-Displacement Vessel Including Applications to Calm Water Broaching, CeSOS
IMT-2013-6	Xing, Yihan	Modelling and analysis of the gearbox in a floating spar-type wind turbine, CeSOS
IMT-7-2013	Balland, Océane	Optimization models for reducing air emissions from ships, IMT
IMT-8-2013	Yang, Dan	Transitional wake flow behind an inclined flat plate-----Computation and analysis, IMT
IMT-9-2013	Abdillah, Suyuthi	Prediction of Extreme Loads and Fatigue Damage for a Ship Hull due to Ice Action, IMT
IMT-10-2013	Ramìrez, Pedro Agustìn Pèrez	Ageing management and life extension of technical systems- Concepts and methods applied to oil and gas facilities, IMT
IMT-11-2013	Chuang, Zhenju	Experimental and Numerical Investigation of Speed Loss due to Seakeeping and Maneuvering. IMT
IMT-12-2013	Etemaddar, Mahmoud	Load and Response Analysis of Wind Turbines under Atmospheric Icing and Controller System Faults with Emphasis on Spar Type Floating Wind Turbines, IMT
IMT-13-2013	Lindstad, Haakon	Strategies and measures for reducing maritime CO2 emissons, IMT
IMT-14-2013	Haris, Sabril	Damage interaction analysis of ship collisions, IMT
IMT-15-2013	Shainee, Mohamed	Conceptual Design, Numerical and Experimental Investigation of a SPM Cage Concept for Offshore Mariculture, IMT
IMT-16-2013	Gansel, Lars	Flow past porous cylinders and effects of biofouling and fish behavior on the flow in and around Atlantic salmon net cages, IMT
IMT-17-2013	Gaspar, Henrique	Handling Aspects of Complexity in Conceptual Ship Design, IMT
IMT-18-2013	Thys, Maxime	Theoretical and Experimental Investigation of a Free Running Fishing Vessel at Small Frequency of Encounter, CeSOS
IMT-19-2013	Aglen, Ida	VIV in Free Spanning Pipelines, CeSOS

IMT-1-2014	Song, An	Theoretical and experimental studies of wave diffraction and radiation loads on a horizontally submerged perforated plate, CeSOS
IMT-2-2014	Rogne, Øyvind Ygre	Numerical and Experimental Investigation of a Hinged 5-body Wave Energy Converter, CeSOS
IMT-3-2014	Dai, Lijuan	Safe and efficient operation and maintenance of offshore wind farms ,IMT
IMT-4-2014	Bachynski, Erin Elizabeth	Design and Dynamic Analysis of Tension Leg Platform Wind Turbines, CeSOS
IMT-5-2014	Wang, Jingbo	Water Entry of Freefall Wedged – Wedge motions and Cavity Dynamics, CeSOS
IMT-6-2014	Kim, Ekaterina	Experimental and numerical studies related to the coupled behavior of ice mass and steel structures during accidental collisions, IMT
IMT-7-2014	Tan, Xiang	Numerical investigation of ship's continuous- mode icebreaking in leverl ice, CeSOS
IMT-8-2014	Muliawan, Made Jaya	Design and Analysis of Combined Floating Wave and Wind Power Facilities, with Emphasis on Extreme Load Effects of the Mooring System, CeSOS
IMT-9-2014	Jiang, Zhiyu	Long-term response analysis of wind turbines with an emphasis on fault and shutdown conditions, IMT
IMT-10-2014	Dukan, Fredrik	ROV Motion Control Systems, IMT
IMT-11-2014	Grimsmo, Nils I.	Dynamic simulations of hydraulic cylinder for heave compensation of deep water drilling risers, IMT
IMT-12-2014	Kvittem, Marit I.	Modelling and response analysis for fatigue design of a semisubmersible wind turbine, CeSOS
IMT-13-2014	Akhtar, Juned	The Effects of Human Fatigue on Risk at Sea, IMT
IMT-14-2014	Syahroni, Nur	Fatigue Assessment of Welded Joints Taking into Account Effects of Residual Stress, IMT
IMT-1-2015	Bøckmann, Eirik	Wave Propulsion of ships, IMT
IMT-2-2015	Wang, Kai	Modelling and dynamic analysis of a semi-submersible floating vertical axis wind turbine, CeSOS
IMT-3-2015	Fredriksen, Arnt Gunvald	A numerical and experimental study of a two-dimensional body with moonpool in waves and current, CeSOS
IMT-4-2015	Jose Patricio Gallardo Canabes	Numerical studies of viscous flow around bluff bodies, IMT

IMT-5-2015	Vegard Longva	Formulation and application of finite element techniques for slender marine structures subjected to contact interactions, IMT
IMT-6-2015	Jacobus De Vaal	Aerodynamic modelling of floating wind turbines, CeSOS
IMT-7-2015	Fachri Nasution	Fatigue Performance of Copper Power Conductors, IMT
IMT-8-2015	Oleh I Karpa	Development of bivariate extreme value distributions for applications in marine technology,CeSOS
IMT-9-2015	Daniel de Almeida Fernandes	An output feedback motion control system for ROVs, AMOS
IMT-10-2015	Bo Zhao	Particle Filter for Fault Diagnosis: Application to Dynamic Positioning Vessel and Underwater Robotics, CeSOS
IMT-11-2015	Wenting Zhu	Impact of emission allocation in maritime transportation, IMT
IMT-12-2015	Amir Rasekhi Nejad	Dynamic Analysis and Design of Gearboxes in Offshore Wind Turbines in a Structural Reliability Perspective, CeSOS
IMT-13-2015	Arturo Jesùs Ortega Malca	Dynamic Response of Flexibles Risers due to Unsteady Slug Flow, CeSOS
IMT-14-2015	Dagfinn Husjord	Guidance and decision-support system for safe navigation of ships operating in close proximity, IMT
IMT-15-2015	Anirban Bhattacharyya	Ducted Propellers: Behaviour in Waves and Scale Effects, IMT
IMT-16-2015	Qin Zhang	Image Processing for Ice Parameter Identification in Ice Management, IMT
IMT-1-2016	Vincentius Rumawas	Human Factors in Ship Design and Operation: An Experiential Learning, IMT
IMT-2-2016	Martin Storheim	Structural response in ship-platform and ship-ice collisions, IMT
IMT-3-2016	Mia Abrahamsen Prsic	Numerical Simulations of the Flow around single and Tandem Circular Cylinders Close to a Plane Wall, IMT
IMT-4-2016	Tufan Arslan	Large-eddy simulations of cross-flow around ship sections, IMT

IMT-5-2016	Pierre Yves-Henry	Parametrisation of aquatic vegetation in hydraulic and coastal research,IMT
IMT-6-2016	Lin Li	Dynamic Analysis of the Instalation of Monopiles for Offshore Wind Turbines, CeSOS
IMT-7-2016	Øivind Kåre Kjerstad	Dynamic Positioning of Marine Vessels in Ice, IMT
IMT-8-2016	Xiaopeng Wu	Numerical Analysis of Anchor Handling and Fish Trawling Operations in a Safety Perspective, CeSOS
IMT-9-2016	Zhengshun Cheng	Integrated Dynamic Analysis of Floating Vertical Axis Wind Turbines, CeSOS
IMT-10-2016	Ling Wan	Experimental and Numerical Study of a Combined Offshore Wind and Wave Energy Converter Concept
IMT-11-2016	Wei Chai	Stochastic dynamic analysis and reliability evaluation of the roll motion for ships in random seas, CeSOS
IMT-12-2016	Øyvind Selnes Patricksson	Decision support for conceptual ship design with focus on a changing life cycle and future uncertainty, IMT
IMT-13-2016	Mats Jørgen Thorsen	Time domain analysis of vortex-induced vibrations, IMT
IMT-14-2016	Edgar McGuinness	Safety in the Norwegian Fishing Fleet – Analysis and measures for improvement, IMT
IMT-15-2016	Sepideh Jafarzadeh	Energy effiency and emission abatement in the fishing fleet, IMT
IMT-16-2016	Wilson Ivan Guachamin Acero	Assessment of marine operations for offshore wind turbine installation with emphasis on response-based operational limits, IMT
IMT-17-2016	Mauro Candeloro	Tools and Methods for Autonomous Operations on Seabed and Water Coumn using Underwater Vehicles, IMT
IMT-18-2016	Valentin Chabaud	Real-Time Hybrid Model Testing of Floating Wind Tubines, IMT
IMT-1-2017	Mohammad Saud Afzal	Three-dimensional streaming in a sea bed boundary layer
IMT-2-2017	Peng Li	A Theoretical and Experimental Study of Wave-induced Hydroelastic Response of a Circular Floating Collar
IMT-3-2017	Martin Bergström	A simulation-based design method for arctic maritime transport systems

IMT-4-2017	Bhushan Taskar	The effect of waves on marine propellers and propulsion
IMT-5-2017	Mohsen Bardestani	A two-dimensional numerical and experimental study of a floater with net and sinker tube in waves and current
IMT-6-2017	Fatemeh Hoseini Dadmarzi	Direct Numerical Simualtion of turbulent wakes behind different plate configurations
IMT-7-2017	Michel R. Miyazaki	Modeling and control of hybrid marine power plants
IMT-8-2017	Giri Rajasekhar Gunnu	Safety and effiency enhancement of anchor handling operations with particular emphasis on the stability of anchor handling vessels
IMT-9-2017	Kevin Koosup Yum	Transient Performance and Emissions of a Turbocharged Diesel Engine for Marine Power Plants
IMT-10-2017	Zhaolong Yu	Hydrodynamic and structural aspects of ship collisions
IMT-11-2017	Martin Hassel	Risk Analysis and Modelling of Allisions between Passing Vessels and Offshore Installations
IMT-12-2017	Astrid H. Brodtkorb	Hybrid Control of Marine Vessels – Dynamic Positioning in Varying Conditions
IMT-13-2017	Kjersti Bruserud	Simultaneous stochastic model of waves and current for prediction of structural design loads
IMT-14-2017	Finn-Idar Grøtta Giske	Long-Term Extreme Response Analysis of Marine Structures Using Inverse Reliability Methods
IMT-15-2017	Stian Skjong	Modeling and Simulation of Maritime Systems and Operations for Virtual Prototyping using co-Simulations
IMT-1-2018	Yingguang Chu	Virtual Prototyping for Marine Crane Design and Operations
IMT-2-2018	Sergey Gavrilin	Validation of ship manoeuvring simulation models
IMT-3-2018	Jeevith Hegde	Tools and methods to manage risk in autonomous subsea inspection,maintenance and repair operations
IMT-4-2018	Ida M. Strand	Sea Loads on Closed Flexible Fish Cages
IMT-5-2018	Erlend Kvinge Jørgensen	Navigation and Control of Underwater Robotic Vehicles

IMT-6-2018	Bård Stovner	Aided Intertial Navigation of Underwater Vehicles
IMT-7-2018	Erlend Liavåg Grotle	Thermodynamic Response Enhanced by Sloshing in Marine LNG Fuel Tanks
IMT-8-2018	Børge Rokseth	Safety and Verification of Advanced Maritime Vessels
IMT-9-2018	Jan Vidar Ulveseter	Advances in Semi-Empirical Time Domain Modelling of Vortex-Induced Vibrations
IMT-10-2018	Chenyu Luan	Design and analysis for a steel braceless semi-submersible hull for supporting a 5-MW horizontal axis wind turbine
IMT-11-2018	Carl Fredrik Rehn	Ship Design under Uncertainty
IMT-12-2018	Øyvind Ødegård	Towards Autonomous Operations and Systems in Marine Archaeology
IMT-13-2018	Stein Melvær Nornes	Guidance and Control of Marine Robotics for Ocean Mapping and Monitoring
IMT-14-2018	Petter Norgren	Autonomous Underwater Vehicles in Arctic Marine Operations: Arctic marine research and ice monitoring
IMT-15-2018	Minjoo Choi	Modular Adaptable Ship Design for Handling Uncertainty in the Future Operating Context
MT-16-2018	Ole Alexander Eidsvik	Dynamics of Remotely Operated Underwater Vehicle Systems
IMT-17-2018	Mahdi Ghane	Fault Diagnosis of Floating Wind Turbine Drivetrain- Methodologies and Applications
IMT-18-2018	Christoph Alexander Thieme	Risk Analysis and Modelling of Autonomous Marine Systems
IMT-19-2018	Yugao Shen	Operational limits for floating-collar fish farms in waves and current, without and with well-boat presence
IMT-20-2018	Tianjiao Dai	Investigations of Shear Interaction and Stresses in Flexible Pipes and Umbilicals
IMT-21-2018	Sigurd Solheim Pettersen	Resilience by Latent Capabilities in Marine Systems
IMT-22-2018	Thomas Sauder	Fidelity of Cyber-physical Empirical Methods. Application to the Active Truncation of Slender Marine Structures
IMT-23-2018	Jan-Tore Horn	Statistical and Modelling Uncertainties in the Design of Offshore Wind Turbines

IMT-24-2018	Anna Swider	Data Mining Methods for the Analysis of Power Systems of Vessels
IMT-1-2019	Zhao He	Hydrodynamic study of a moored fish farming cage with fish influence
IMT-2-2019	Isar Ghamari	Numerical and Experimental Study on the Ship Parametric Roll Resonance and the Effect of Anti-Roll Tank
IMT-3-2019	Håkon Strandenes	Turbulent Flow Simulations at Higher Reynolds Numbers
IMT-4-2019	Siri Mariane Holen	Safety in Norwegian Fish Farming – Concepts and Methods for Improvement
IMT-5-2019	Ping Fu	Reliability Analysis of Wake-Induced Riser Collision
IMT-6-2019	Vladimir Krivopolianskii	Experimental Investigation of Injection and Combustion Processes in Marine Gas Engines using Constant Volume Rig
IMT-7-2019	Anna Maria Kozlowska	Hydrodynamic Loads on Marine Propellers Subject to Ventilation and out of Water Condition.
IMT-8-2019	Hans-Martin Heyn	Motion Sensing on Vessels Operating in Sea Ice: A Local Ice Monitoring System for Transit and Stationkeeping Operations under the Influence of Sea Ice
IMT-9-2019	Stefan Vilsen	Method for Real-Time Hybrid Model Testing of Ocean Structures – Case on Slender Marine Systems
IMT-10-2019	Finn-Christian W. Hanssen	Non-Linear Wave-Body Interaction in Severe Waves
IMT-11-2019	Trygve Olav Fossum	Adaptive Sampling for Marine Robotics
IMT-12-2019	Jørgen Bremnes Nielsen	Modeling and Simulation for Design Evaluation
IMT-13-2019	Yuna Zhao	Numerical modelling and dyncamic analysis of offshore wind turbine blade installation
IMT-14-2019	Daniela Myland	Experimental and Theoretical Investigations on the Ship Resistance in Level Ice
IMT-15-2019	Zhengru Ren	Advanced control algorithms to support automated offshore wind turbine installation
IMT-16-2019	Drazen Polic	Ice-propeller impact analysis using an inverse propulsion machinery simulation approach
IMT-17-2019	Endre Sandvik	Sea passage scenario simulation for ship system performance evaluation

IMT-18-2019	Loup Suja-Thauvin	Response of Monopile Wind Turbines to Higher Order Wave Loads
IMT-19-2019	Emil Smilden	Structural control of offshore wind turbines – Increasing the role of control design in offshore wind farm development
IMT-20-2019	Aleksandar-Sasa Milakovic	On equivalent ice thickness and machine learning in ship ice transit simulations
IMT-1-2020	Amrit Shankar Verma	Modelling, Analysis and Response-based Operability Assessment of Offshore Wind Turbine Blade Installation with Emphasis on Impact Damages
IMT-2-2020	Bent Oddvar Arnesen Haugaløkken	Autonomous Technology for Inspection, Maintenance and Repair Operations in the Norwegian Aquaculture
IMT-3-2020	Seongpil Cho	Model-based fault detection and diagnosis of a blade pitch system in floating wind turbines
IMT-4-2020	Jose Jorge Garcia Agis	Effectiveness in Decision-Making in Ship Design under Uncertainty
IMT-5-2020	Thomas H. Viuff	Uncertainty Assessment of Wave-and Current-induced Global Response of Floating Bridges
IMT-6-2020	Fredrik Mentzoni	Hydrodynamic Loads on Complex Structures in the Wave Zone
IMT-7-2020	Senthuran Ravinthrakumar	Numerical and Experimental Studies of Resonant Flow in Moonpools in Operational Conditions
IMT-8-2020	Stian Skaalvik Sandøy	Acoustic-based Probabilistic Localization and Mapping using Unmanned Underwater Vehicles for Aquaculture Operations
IMT-9-2020	Kun Xu	Design and Analysis of Mooring System for Semi-submersible Floating Wind Turbine in Shallow Water
IMT-10-2020	Jianxun Zhu	Cavity Flows and Wake Behind an Elliptic Cylinder Translating Above the Wall
IMT-11-2020	Sandra Hogenboom	Decision-making within Dynamic Positioning Operations in the Offshore Industry – A Human Factors based Approach
IMT-12-2020	Woongshik Nam	Structural Resistance of Ship and Offshore Structures Exposed to the Risk of Brittle Failure
IMT-13-2020	Svenn Are Tutturen Værnø	Transient Performance in Dynamic Positioning of Ships: Investigation of Residual Load Models and Control Methods for Effective Compensation
IMT-14-2020	Mohd Atif Siddiqui	Experimental and Numerical Hydrodynamic Analysis of a Damaged Ship in Waves
IMT-15-2020	John Marius Hegseth	Efficient Modelling and Design Optimization of Large Floating Wind Turbines

IMT-16-2020	Asle Natskår	Reliability-based Assessment of Marine Operations with Emphasis on Sea Transport on Barges
IMT-17-2020	Shi Deng	Experimental and Numerical Study of Hydrodynamic Responses of a Twin-Tube Submerged Floating Tunnel Considering Vortex-Induced Vibration
IMT-18-2020	Jone Torsvik	Dynamic Analysis in Design and Operation of Large Floating Offshore Wind Turbine Drivetrains
IMT-1-2021	Ali Ebrahimi	Handling Complexity to Improve Ship Design Competitiveness
IMT-2-2021	Davide Proserpio	Isogeometric Phase-Field Methods for Modeling Fracture in Shell Structures
IMT-3-2021	Cai Tian	Numerical Studies of Viscous Flow Around Step Cylinders
IMT-4-2021	Farid Khazaeli Moghadam	Vibration-based Condition Monitoring of Large Offshore Wind Turbines in a Digital Twin Perspective
IMT-5-2021	Shuaishuai Wang	Design and Dynamic Analysis of a 10-MW Medium-Speed Drivetrain in Offshore Wind Turbines
IMT-6-2021	Sadi Tavakoli	Ship Propulsion Dynamics and Emissions
IMT-7-2021	Haoran Li	Nonlinear wave loads, and resulting global response statistics of a semi-submersible wind turbine platform with heave plates
IMT-8-2021	Einar Skiftestad Ueland	Load Control for Real-Time Hybrid Model Testing using Cable-Driven Parallel Robots
IMT-9-2021	Mengning Wu	Uncertainty of Machine Learning-Based Methods for Wave Forecast and its Effect on Installation of Offshore Wind Turbines